Universidade do Minho
Escola de Engenharia

Ana Rita Melo Ribeiro

Functionalization of multi-layer halochromic patch with cinnamaldehyde-containing lipid nano carriers for preventing wound chronicity

Novembro 2026

Functionalization of multi-layer halochromic patch with cinnamaldehyde-containing lipid nano carriers for preventing wound chronicity
Ana Rita Melo Ribeiro
UMinho | 2026

Universidade do Minho
Escola de Engenharia

Ana Rita Melo Ribeiro

Functionalization of multi-layer halochromic patch with cinnamaldehyde-containing lipid nano carriers for preventing wound chronicity

Tese de Doutoramento
Doutoramento em Engenharia Têxtil

Trabalho efetuado sob a orientação de:
Doutora Helena Prado Felgueiras
Professora Salette Reis
Doutora Catarina Leal Seabra

Novembro 2026

DIREITOS DE AUTOR E CONDIÇÕES DE UTILIZAÇÃO DO TRABALHO POR TERCEIROS

Este é um trabalho académico que pode ser utilizado por terceiros desde que respeitadas as regras e boas práticas internacionalmente aceites, no que concerne aos direitos de autor e direitos conexos.

Assim, o presente trabalho pode ser utilizado nos termos previstos na licença abaixo indicada.

Caso o utilizador necessite de permissão para poder fazer um uso do trabalho em condições não previstas no licenciamento indicado, deverá contactar o autor, através do Repositório UM da Universidade do Minho.

Licença concedida aos utilizadores deste trabalho



Atribuição-Não Comercial
CC BY-NC
https://creativecommons.org/licenses/by-nc/4.0/

AGRADECIMENTOS

Chegar ao fim deste percurso representa muito mais do que a conclusão de mais uma etapa académica. Representa crescimento, resiliência, dúvidas, conquistas e, acima de tudo, o apoio de muitas pessoas que caminharam comigo ao longo destes anos. Chegar até aqui não foi um caminho solitário, e é por isso que dedico esta tese a todos aqueles que, de uma forma ou de outra, fizeram parte desta jornada.

Às minhas orientadoras, Doutora Helena Felgueiras, Doutora Catarina Seabra e Professora Doutora Salette Reis, agradeço profundamente por toda a orientação, disponibilidade e confiança. Obrigada por me desafiarem a ser melhor, por me incentivarem a pensar de forma crítica e por me acompanharem ao longo de todo este processo. Também à Ana Isabel, pela exigência quando foi necessária, pelo apoio imensurável, mas também pela compreensão nos momentos de maior dificuldade.

Às minhas colegas de equipa, Marta e Tânia, e a todos os membros do centro de investigação, obrigada pelo ambiente de partilha, entreajuda e companheirismo. Pelas sugestões, pelas dúvidas partilhadas e até pelos momentos de descontração que tornaram os dias mais leves.

À minha família, o meu maior e mais profundo agradecimento. Por serem o meu apoio incondicional em todos os momentos, por acreditarem sempre em mim, mesmo quando eu própria duvidava. Obrigada pela paciência, pelo carinho, pelas palavras de incentivo e por estarem sempre presentes. Este doutoramento tem tanto de meu, como de vosso!

Ao Tiago. Por estares sempre ao meu lado, nos dias bons e nos mais difíceis. Pela paciência infinita, pelo apoio constante, por ouvires, por acalmares e por nunca me deixares desistir. Obrigada por acreditares em mim mesmo quando eu não conseguia.

Às minhas amigas, obrigada por serem um refúgio fora do mundo científico. Pelas conversas, pelas gargalhadas, pelos momentos de descontração e por me lembrarem sempre de manter o equilíbrio. A vossa presença foi essencial para manter a sanidade ao longo deste percurso.

A todos aqueles que, de forma direta ou indireta, contribuíram para a realização deste trabalho, deixo também o meu sincero agradecimento. Cada gesto, cada palavra e cada ajuda fizeram a diferença.

Por fim, a mim própria, por não ter desistido, mesmo quando parecia mais fácil fazê-lo.

STATEMENT OF INTEGRITY

I hereby declare having conducted this academic work with integrity. I confirm that I have not used plagiarism or any form of undue use of information or falsification of results along the process leading to its elaboration.

I further declare that I have fully acknowledged the Code of Ethical Conduct of the University of Minho.

University of Minho, April 2026
Full name: Ana Rita Melo Ribeiro

DECLARATION ON THE USE OF ARTIFICIAL INTELLIGENCE (AI) TOOLS

I hereby declare having acted this academic work with integrity and confirm that I have not resorted to any form of undue use of AI tools, nor to the falsification or omission of information, sources, data, results or processes in any of the stages leading to its elaboration. I further declare that any use of AI tools was done in a transparent and responsible manner, being duly noted in the work, and that I critically verified the accuracy of the content produced with their support, assuming full responsibility for what I submit. I further declare that I have fully acknowledged the Code of Ethical Conduct of the University of Minho, as well as the applicable standards of academic integrity and data protection.

University of Minho, April 2026
Full name: Ana Rita Melo Ribeiro

ABSTRACT

Chronic wounds remain a major clinical challenge due to impaired healing, persistent infections, and increased risk of complications. Among the microorganisms involved, fungi - particularly *Candida spp.*, the most frequently detected in chronic wounds - are often underestimated despite their contribution to delayed healing and secondary infections. To address the limited antifungal action of many current therapies, this work proposes an advanced multilayer dressing for simultaneous infection control and real-time wound monitoring. The system was engineered using electrospinning and electrospray and comprises an outer halochromic polycaprolactone/polyethylene glycol (PCL/PEG) layer containing red radish-derived anthocyanins for pH-responsive monitoring and an inner bioactive electrospun PCL layer functionalized with chitosan-coated nanostructured lipid carriers (Ch-NLCs) loaded with cinnamaldehyde (CN), a natural antifungal agent. The developed Ch-NLCs exhibited nanoscale dimensions (≈300-350 nm), high encapsulation efficiency (≈75%), and stable positive surface charge. The resulting multilayer mats presented high porosity (≈70-80%), fiber diameters around ≈ 1 μm, and mechanical properties suitable for skin applications. The systems displayed controlled wettability and permeability within the optimal range for wound healing, while PEG incorporation and nanoformulations enhanced swelling capacity and interfacial properties without compromising thermal stability. CN-loaded systems showed enhanced antifungal activity against *Candida spp.*, achieving reductions of up to ≈70-90% at early time points, whereas unloaded systems exhibited only modest effects. The patch also demonstrated antioxidant activity attributed to anthocyanins. Cytocompatibility and proliferation assays confirmed that the developed systems are non-cytotoxic toward L929 fibroblasts and HaCaT keratinocytes, maintaining cell viability above 90% under relevant conditions. In addition, the halochromic layer enabled clear color changes across physiologically relevant pH ranges, providing non-invasive wound monitoring without dressing removal. Overall, this work demonstrates a multifunctional dressing platform combining antifungal therapy, antioxidant protection, and real-time monitoring. The integration of electrospinning and electrospray enables precise control of structure–function relationships and supports the development of next-generation smart wound dressings for improved chronic wound management.

KEYWORDS: *Candida* spp.; chronic wounds; essential oils; halochromic monitoring; nanostructured lipid carriers.

RESUMO

As feridas crónicas continuam a representar um importante desafio clínico devido à cicatrização comprometida, frequentemente associada a infeções persistentes e maior risco de complicações. Entre os microrganismos envolvidos, os fungos - particularmente *Candida spp.,* os mais frequentemente detetados - são muitas vezes subvalorizados, apesar da sua contribuição para o atraso da cicatrização e para infeções secundárias. Para colmatar a limitada ação antifúngica de muitas terapias atuais, este trabalho propõe um penso multicamada avançado para controlo da infeção e monitorização em tempo real do estado da ferida. O sistema foi produzido por eletrofiação e electrospray e integra uma camada externa halocrómica de policaprolactona/polietileno glicol (PCL/PEG), contendo antocianinas derivadas de rabanete vermelho para monitorização responsiva ao pH, e uma camada interna bioativa de PCL eletrofiado funcionalizada com transportadores lipídicos nanoestruturados revestidos com quitosano (Ch-NLCs), carregados com cinamaldeído (CN), um agente antifúngico natural. Os Ch-NLCs apresentaram dimensões nanométricas (≈300-350 nm), elevada eficiência de encapsulação (≈75%) e carga superficial positiva estável. As membranas multicamada exibiram elevada porosidade (≈70-80%), diâmetros de fibra de ≈1 μm e propriedades mecânicas adequadas para aplicações cutâneas. Os sistemas demonstraram molhabilidade e permeabilidade adequadas à cicatrização, enquanto a incorporação de PEG e das nanoformulações aumentou a capacidade de intumescimento e as propriedades interfaciais sem comprometer a estabilidade térmica. Os sistemas contendo CN apresentaram atividade antifúngica superior contra *Candida spp.*, alcançando reduções de ≈70-90% em tempos iniciais, enquanto os sistemas sem CN revelaram apenas efeitos modestos. O penso demonstrou ainda atividade antioxidante atribuída às antocianinas. Os ensaios de citocompatibilidade e proliferação confirmaram a ausência de citotoxicidade para fibroblastos L929 e queratinócitos HaCaT, mantendo viabilidades celulares superiores a 90%. Adicionalmente, a camada halocrómica permitiu alterações de cor distintas em intervalos de pH fisiologicamente relevantes, possibilitando a monitorização não invasiva da ferida sem remoção do penso. Assim, este trabalho demonstra uma plataforma multifuncional que combina terapia antifúngica, proteção antioxidante e monitorização em tempo real. A integração de eletrofiação e electrospray permite o controlo preciso das relações estrutura–função e contribui para o desenvolvimento de pensos inteligentes de nova geração para a gestão de feridas crónicas.

PALAVRAS-CHAVE: *Candida spp.;* feridas crónicas; cinamaldeído; monitorização halocrómica; NLCs.

TABLE OF CONTENTS

Agradecimentos ii

STATEMENT OF INTEGRITY iii

DECLARATION ON THE USE OF ARTIFICIAL INTELLIGENCE (AI) TOOLS iv

ABSTRACT v

RESUMO vi

LIST OF FIGURES xii

LIST OF TABLES xvii

LIST OF SIMBOLS, ABBREVIATIONS AND ACRONYMS xix

Chapter I – Introduction 1

I.1 Motivation 1

I.2 Research Questions 3

I.3 Objectives 3

I.4 Thesis Structure 4

Chapter II – Literature overview 1

II.1 Chronic Wounds 2

II.2 Wound Dressings 4

II.3 Production of Nanofibers: Electrospinning Technique 8

II.4 Electrospinnable Polymers 12

II.4.1 Poly (ε-caprolactone) (PCL) 14

II.4.2 Polyethylene glycol (PEG) 15

II.5 Halochromic Molecules as pH-Sensors 17

II.5.1 Anthocyanins 18

II.5.2 Extraction, Detection and Quantification Methods 20

II.6 Nanoparticles for Biomedical Applications 24

II.6.1 Chitosan coated Nano-lipid Carriers (Ch-NLCs) 26

II.7 Essential Oils (EOs) as Nano-lipid Carriers Payloads 27

II.7.1 Cinnamaldehyde Essential Oil 29

Chapter III – Polycaprolactone/polyethylene glycol electrospun mats with pH-responsiveness for real-time sensing in chronic wound healing 32

III.1 Introduction 33

III.2 Materials and Methods 34

III.2.1 Materials 34

III.2.2 Natural Halochromic Extracts Properties 35

III.2.2.1 Visual pH grading 35

III.2.2.2 Chemical Composition through LC-MS/MS 35

III.2.2.3 Minimum Inhibitory Concentration (MIC) and Minimum Fungicidal Concentration (MFC) 37

III.2.2.4 Cell Culture Conditions and Viability Assessment 38

III.2.3 Production of Electrospun Mats 39

III.2.4 Immobilization of Halochromic Extracts 39

III.2.5 Characterization of Loaded and Unloaded Electrospun Mats 40

III.2.5.1 Field Emission Gun Scanning Electron Microscopy (FEG-SEM) 40

III.2.5.2 Fourier-transform Infrared Spectroscopy in Attenuated Total Reflectance Mode (ATR-FTIR) 40

III.2.5.3 Thermal Gravimetric Analysis (TGA) 40

III.2.5.4 Differential Scanning Calorimetry (DSC) 40

III.2.5.5 Mechanical Testing 41

III.2.5.6 Wettability and Surface Free Energy (SFE) 41

III.2.5.7 *In-vitro* Swelling and Degradation 42

III.2.5.7 Permeabilities 42

III.2.5.8 Diffuse Reflectance Spectroscopy 43

III.2.6 Mats Antioxidant Activity 44

III.2.7 Immobilized Electrospun Mats Cytocompatibility Testing 44

III.2.7.1 Cell Culture Conditions and Cell Viability Assessment 44

III.2.8 Statistical Analysis 44

III.3 Results and Discussion 44

III.3.1 Natural Extracts Characterization 44

III.3.2 Mats Morphology and Porosity 51

III.3.3 Chemical Analyses 55
III.3.4 Thermal Stability 58
III.3.5 Mechanical Performance 60
III.3.6 Wettability 62
III.3.7 *In-vitro* Swelling and Degradation 64
III.3.8 Air and Water Vapor Permeabilities 66
III.3.9 Antioxidant activity 68
III.3.10 Surface Color and Optical Properties 70
III.3.11 Cell Metabolic Activity of the Extract-Loaded Electrospun Mats 75
III.4 Practical Application and Clinical Relevance 76
III.5 Conclusions 77
Chapter Iv – Integration of Cinnamaldehyde Essential Oil onto Chitosan-coated Nanostructured Lipid Carriers on ε-Polycaprolactone Electrospun Mats: A Novel Approach for Antifungal Chronic Wound Healing 80
IV.1 Introduction 81
IV.2 Materials and Methods 82
IV.2.1 Materials 82
IV.2.2 Essential Oils Characterization 83
IV.2.2.1 Essential Oils Minimum Inhibitory and Fungicidal Concentrations 83
IV.2.3 Preparation of Nanostructured Lipid Carriers (NLCs) 84
IV.2.4 NLCs coated with Chitosan (Ch-NLCs) 84
IV.2.5 NLCs Characterization 84
IV.2.5.1 Particle Size, Polydispersity Index, and Zeta Potential 84
IV.2.5.2 Determination of Encapsulation Efficiency 85
IV.2.5.3 Storage Stability Studies 85
IV.2.6 Electrospinning and Electrospray Deposition 85
IV.2.7 Characterization of Electrospun Mats 86
IV.2.7.1 Field emission gun scanning electron microscopy (FEG-SEM) 86
IV.2.7.2 Fourier-transform Infrared Spectroscopy in Attenuated Total Reflectance Mode (ATR-FTIR) 86
IV.2.7.3 Thermal Gravimetric Analysis (TGA) 86
IV.2.7.4 Differential Scanning Calorimetry (DSC) 87

IV.2.7.5 Mechanical Testing 87
IV.2.7.6 Wettability and Surface Free Energy (SFE) 87
IV.2.7.7 *In-vitro* Swelling and Degradation 87
IV.2.7.8 Permeabilities 87
IV.2.8 Electrospun Mats Antifungal Efficiency 87
IV.2.8.1 Time-Kill Kinetics Evaluations 87
IV.2.9 Cell Culture Conditions and Viability Assessment 88
IV.2.10 Cytocompatibility Testing 89
IV.2.10.1 Cell Culture Conditions and Viability Assessment 89
IV.2.11 Statistical analysis 89
IV.3 Results and Discussion 89
IV.3.1 Essential Oils Properties 89
IV.3.2 Characterization of Unloaded and Loaded Ch-NLCs 91
IV.3.3 Mats Morphology 94
IV.3.4 Chemical Analysis 97
IV.3.5 Mats Thermal Stability 99
IV.3.6 Mechanical Properties 102
IV.3.7 Wettability 104
IV.3.8 *In-vitro* Swelling and Degradation 106
IV.3.9 Air and Water Permeabilities 108
IV.3.10 Antifungal Activity 110
IV.3.11 Cytocompatibility 113
IV.4 Conclusions 115
Chapter v – Monitoring cinnamaldehyde fungicidal action in diabetic wound-like environments by means of halochromic multi-layer electrospun/electrospray dressings 118
V.1 Introduction 119
V.2 Materials and Methods 121
V.2.1 Materials 121
V.2.2 Multi-Layer Dressing Production 121
V.2.3 Characterization of Multi-Layer Dressing 122
V.2.3.1 Field emission gun scanning electron microscopy (FEG-SEM) 122

V.2.3.2 Fourier-transform infrared spectroscopy in attenuated total reflectance mode (ATR-FTIR) 122
V.2.3.3 Thermal gravimetric analysis (TGA) 123
V.2.3.4 Differential Scanning Calorimetry (DSC) 123
V.2.3.5 Mechanical testing 123
V.2.3.6 *In-vitro* Swelling and Degradation 123
V.2.3.7 Permeabilities 124
V.2.4 Antioxidant Activity 125
V.2.5 Antifungal Efficiency 125
V.2.5.1 Time-kill Kinetics Evaluation 125
V.2.6 Cytocompatibility Testing 125
V.2.6.1 Cell Culture Conditions 125
V.2.6.2 Cell Viability Assessment 126
V.2.6.3 Cell Proliferation by MTT quantification 126
V.2.6.4 Cell Morphology observation by Brightfield Microscopy 127
V.2.7 Statistical Analysis 127
V.3 Results and Discussion 127
V.3.1 Multi-layer Dressing Characterization 128
V.3.2 Multi-layer System Thermal Behaviour 129
V.3.3 Mechanical Stability 131
V.3.4 *In-vitro* Swelling and Degradation 133
V.3.5 Permeabilities Study 136
V.3.6 Antioxidant Activity 137
V.3.7 Antifungal Activity 138
V.3.8 Cytocompatibility and Cell Viability 140
V.3.9 Cell Proliferation 143
V.3.10 Cell Morphology 144
V.4 Conclusions 147
Chapter VI – Conclusions and Future Perspectives 149
Supplementary Data 175

LIST OF FIGURES

Figure 1 - Differences between the healing process of an acute wound and a chronic wound. The chronic wound exhibits deregulated angiogenesis, sub-optimal inflammatory response and persistent bacterial and fungi colonization (adapted from [29]CC BY 4.0 permission). 2

Figure 2 - Different types of microorganisms organized according to the location in an example of chronic wound (adapted from [30] with CC BY 4.0 permission). 3

Figure 3 - Schematic representation of electrospinning equipment (adapted from [59] CC BY 4.0 permission). 9

Figure 4 - Common polymers used in the production of electrospun wound dressings (adapted from [58] with CC BY 4.0 permission). 14

Figure 5 - Anthocyanidin chemical structure. This figure was produced by ChemDraw 12.0 software. 19

Figure 6 - Representation of the color changes of anthocyanin-rich extracts at different pH values (adapted from [107] with CC BY 4.0 permission). 20

Figure 7 - Classes of NPs (adapted from [119] with CC BY 4.0 permission). 26

Figure 8 - Visual color grading of the three natural halochromic extracts at concentration of 5 mg/mL (RC, RR and PSP) in contact with pH solutions ranging from 4.0 to 10.0 (left to right).. 45

Figure 9 –(A) TPC shown in gallic acid equivalents. Data are reported as mean ± SD (n=3). Statistical significance was determined via Tukey's test applying multiple comparisons between the three natural extracts; no significant differences were reported. (B) DPPH scavenging activity (%) induced by halochromic extracts at 1, 2, 4, 6, 8 and 24 h. Trolox was used as a positive control and DMSO as a negative control (n =3). Statistical significance was determined via Tukey test, by applying multiple comparisons between concentrations for all extract types. Significance between RC 5 mg/mL and RC 10 mg/mL: $p<0.01$ at 24h; RC 2,5 mg/mL and RC 10 mg/mL: $p < 0.001$ at 24h. RR 5 mg/mL and RR 10 mg/mL: $p <0.001$ at 24h; RR 2,5 mg/mL and RR 10 mg/mL: $p < 0.0001$ at 24h. (C) Cytocompatibility studies were performed on (C.1) fibroblasts from mice (L929) and (C.2) human keratinocytes (HaCaT) for the three natural halochromic extracts. Data is reported as mean ± S.D. (n=3). Statistical significance was determined via Tukey test, by applying multiple comparisons between concentrations for all extract types (*$p < 0.05$; **$p < 0.01$; ***$p < 0.001$; ****$p < 0.0001$). 49

Figure 10 - FEG-SEM micrographs and diameter distribution histograms with the respective mean (M) and S.D. (n=3), for 100:0, 90:10 and 80:20 PCL/PEG mats, loaded with RC and RR extract and unloaded. Scale bars in micrographs represent 10 μm. 53

Figure 11 - ATR-FTIR spectra of (A) Free natural extracts RC and RR, (B) PCL/PEG combinations with RC and (C) PCL/PEG combinations with RR electrospun mats collected in the range of 4000 to 400 cm^{-1}. The standard FTIR spectra of RC and RR were used here for comparative purposes. 57

Figure 12 - (A.1) Thermal stability of individual components and polymer blends, and (A.2) extract-loaded electrospun mats was characterized based TGA thermograms. (B.1) DSC thermograms of individual components and (B.2) extract-loaded electrospun mats. Data reported as Heat Flow (mW) vs. Temperature (°C). 59

Figure 13 - Wettability of the electrospun mats by WCA measurements (n=3) using established ASTM and BS standardized methods. 64

Figure 14 - (A) Degree of swelling (%) of electrospun mats in PBS over 168 hours. All mats were incubated at 37 °C in PBS 1× 0.01M (pH 7.4). Data represent the mean ± SD(n = 4). (B) Mass loss (%) of electrospun mats over 28 days in PBS 1× 0.01M (pH 7.4). Negative values indicate water absorption rather than degradation. Data represent the mean ± SD (n = 4) Statistical significance was determined via Tukey test, by applying multiple comparisons between for all mat types. (*p < 0.05; **p < 0.01; ***p < 0.001; ****p < 0.0001). 65

Figure 15 - DPPH scavenging activity (%) induced by halochromic extracts (A) RC and (B) RR, immobilized on mats, after 1, 2, 4, 6 and 24h incubation. Trolox was used as a positive control and DMSO as a negative control. Data were reported as mean ± SD (n =3). Statistical significance was determined via Tukey test, by applying multiple comparisons between RC and RR loaded mats. No significant differences were reported. 69

Figure 16 - Cytocompatibility evaluation of extract-loaded electrospun mats. Cell metabolic activity (%) of (A) L929 fibroblasts and (B) HaCaT keratinocytes after 24 h of direct contact with electrospun mats composed of PCL and PCL/PEG blends (90:10 and 80:20), either unloaded or loaded with RC or RR extracts Data are presented as mean ± standard deviation (n = 9). Statistical significance was determined via Tukey's test applying multiple comparisons between the different combinations, reporting no significant differences. 76

Figure 17 - ATR-FTIR spectra of the three EOs (Ge, Ci, and CN) collected in the range of 4000 to 400 cm^{-1}. 91

Figure 18 – Storage stability of Ch-based nanoformulations over 8 weeks. (A) Size, (B) PDI, and (C) zeta potential of unloaded Ch-NLCs and loaded Ch-NLCs/CN monitored over 8 weeks, relative to the production week (week 0), when stored at RT or at 4 °C. (D) Entrapment efficiency (%) of CN in Ch-NLCs/CN during the same storage period under both storage conditions. Data are presented as mean ± standard deviation (n=3). Statistical significance was determined via Tukey's test, applying multiple comparisons between samples within the same timepoint, reporting no significant differences. 94

Figure 19 – (A) FEG-SEM micrographs at 5.000× and (B) 10.000 × magnitude of PCL+Ch-NLCs/CN architecture. (C) FEG-SEM micrographs at 5.000× and (D) 10.000 × magnitude of PCL+Ch-NLCs/CN+PCL architecture. Representative micrographs of the corresponding unloaded systems (without CN) exhibited similar morphological features to those presented in (A) and (B), indicating that CN incorporation did not significantly affect fiber morphology. Scale bars in micrographs represent 20 and 10 μm. 96

Figure 20 - ATR-FTIR spectra of (A) Ch-NLCs loaded and unloaded with CN, and of (B) PCL electrospun mats electrosprayed with Ch-NLCs loaded with CN and unloaded collected in the range of 4000 to 400 cm^{-1}. 99

Figure 21 - Thermal stability profiles of Ch-based nanoformulations and electrosprayed/electrospun PCL mats. (A) TGA profiles of unloaded and CN-loaded Ch-NLCs nanoformulations, as well as of CN-loaded and unloaded electrosprayed/electrospun PCL mats for both architectures. (B) DSC thermograms of unloaded and CN-loaded Ch-NLCs nanoformulations and of unloaded and CN-loaded electrosprayed PCL mats for both architectures. 102

Figure 22 - Wettability of neat PCL and the four PCL electrospun mats architectures electrosprayed with Ch-based nanoformulations by WCA measurements (n=5) using established ASTM standardized methods. 106

Figure 23 - (A) Degree of swelling (%) of electrosprayed electrospun mats in PBS over 168 hours. All mats were incubated at 37 °C in PBS. Data represent the mean ± SD (n = 4). (B) Mass loss (%) of electrospun mats over 28 days in PBS 1× 0.01M (pH 7.4). Negative values indicate water absorption rather than degradation. Data represent the mean ± SD (n = 4). Statistical significance was determined via the Tukey test, by applying multiple comparisons between all mat types, tested for the same time period (*p < 0.05; **p < 0.01; ***p < 0.001; ****p < 0.0001)..... 108

Figure 24 – Reduction of (A) C. albicans (B) C. tropicalis, and (C) C. parapsilosis number of fungi colonies in contact with the electrospun mats electrosprayed with Ch-based nanoformulations loaded and non-loaded with CN after 1, 2, 4, 6, and 24 h of incubation at 28 °C. Data are presented

as mean ± standard deviation (n = 3). Statistical significance was determined via Tukey's test applying multiple comparisons between the different combinations at the same time-points (*p < 0.05; **p < 0.01; ***p < 0.001; ****p < 0.0001)..... 112

Figure 25 - Cytocompatibility assessment of Ch-based nanoformulations and electrospun mats. (A) Viability of L929 fibroblasts and (B) metabolic activity of HaCaT keratinocytes after 24 h exposure to increasing lipid concentrations of CN-loaded and unloaded Ch-NLCs and free CN. (C) Viability of L929 fibroblasts and (D) metabolic activity of HaCaT keratinocytes after 24 h of direct contact with electrospun mats, either PCL or PCL incorporating Ch-NLCs and Ch-NLCs/CN for both architectures. Results are expressed as a percentage relative to untreated control cells. Data are presented as mean ± standard deviation (n=9). Statistical significance was determined via Tukey's test, applying multiple comparisons between the different combinations, reporting the absence of significant differences. 114

Figure 26 - (A) FEG-SEM micrograph of electrospun PCL fibers after electrospray deposition of Ch-NLCs/CN, showing surface roughness and nanoparticle localization. (B) FEG-SEM micrograph of electrospun PCL fibers without nanoformulations, exhibiting smooth and homogeneous fiber morphology. Both images are representative of all developed systems, indicating that neither nanoformulation incorporation nor multilayer assembly significantly altered the fibrous structure. (C) Macroscopic view of the final multi-layer dressing, displaying the two distinct external surfaces: the anthocyanin-loaded PCL/PEG layer (left) and the PCL layer functionalized with Ch-NLCs/CN (right). 128

Figure 27 - ATR-FTIR spectra of electrospun mats with different multi-layer architectures collected in the range of 4000–400 cm^{-1}..... 129

Figure 28 - Thermal stability profiles of multi-layer electrospun mats. (A) TGA profiles of PCL, PEG, PCL/PEG (90:10) and multi-layer electrospun mats. (B) DSC thermograms of PCL, PEG, PCL/PEG (90:10) and multi-layer mats. 131

Figure 29 - A) Degree of swelling (%) of controls and multi-layer electrospun mats in PBS over 168 hours. All mats were incubated at 37 °C in PBS. Data represent the mean ± SD (n=4). (B) Mass loss (%) of controls and multi-layer mats over 28 days in PBS 1× 0.01M (pH 7.4). Negative values indicate water absorption rather than degradation. Data represent the mean ± SD (n = 4). Statistical significance was determined via Tukey test, by applying multiple comparisons between all mat types, tested for the same time period (*p < 0.05; **p < 0.01; ***p < 0.001; ****p < 0.0001)..... 135

Figure 30 - DPPH scavenging activity (%) at 1, 2, 4, 6, 8 and 24 h. Trolox was used as a positive control and DMSO as a negative control (n=3). Statistical significance was determined via Tukey test, by applying multiple comparisons between timepoints. 138
Figure 31 - Reduction of (A) C. albicans (B) C. parapsilosis, and (C) C. tropicalis number of fungi colonies in contact with the electrospun mats after 1, 2, 4, 6, and 24 h of incubation at 28 °C. Data are presented as mean ± standard deviation (n=3). Statistical significance was determined via Tukey's test applying multiple comparisons between the different combinations at the same time-points (*p < 0.05; **p < 0.01; ***p < 0.001; ****p < 0.0001). 140
Figure 32 - Cytocompatibility assessment of multi-layer electrospun mats. (A) Viability of L929 fibroblasts and (B) metabolic activity of HaCaT keratinocytes after 24 h of direct contact with the electrospun mats. Results are expressed as a percentage relative to untreated control cells. Data are presented as mean ± standard deviation (n=9). Statistical significance was determined via Sidak's test, applying multiple comparisons between the different combinations. (*p < 0.05; **p < 0.01; ***p < 0.001; ****p < 0.0001). 142
Figure 33 - Cell proliferation of (A, B) L929 fibroblasts and (C, D) HaCaT keratinocytes after 24 h (A, C) and 48 h (B, D) of incubation in the presence of electrospun multi-layer mats. Results are expressed as percentage relative to untreated control cells. Data are presented as mean ± standard deviation (n=9). Statistical significance was determined via Sidak's test applying multiple comparisons between the different conditions (*p < 0.05; **p < 0.01; ***p < 0.001; ****p < 0.0001). 144

LIST OF TABLES

Table 1 - Characteristics that an ideal wound dressing must respect [43, 44]..... 5

Table 2 - Parameters that affect the production of nanofibers by the electrospinning technique [60]..... 9

Table 3 - Summary of the most common extraction methods used for anthocyanin extraction [103, 111]..... 22

Table 4 - Surface tension (γt) and dispersive (γd) and polar (γp) components for determining SFE, using the solvents: ultrapure water, ethylene glycol, and diiodomethane [167]. 42

Table 5 - Quantification, expressed as mg/kg, of the detected polyphenols and anthocyanidins in the natural extract samples. *Concentrations determined by alkaline hydrolysis of the extract to free anthocyanins from their corresponding sugar derivatives. 46

Table 6 – 100PCL, PCL/PEG and PCL/PEG + RC and RR solutions viscosity, conductivity, zeta potential and pH values. Data are reported as mean ± S.D. (n =3)..... 54

Table 7 – Young Modulus, elongation at break and break strength of loaded and unloaded PCL/PEG mats tested at a displacement rate of 10.0 mm/min (n =3). Statistical analysis showed on Table SD18 and SD19 on Supporting Information..... 62

Table 8 - WVTR, water vapor permeability index (I), air permeability rates and mats thicknesses (n =3)..... 67

Table 9 - CIELAB values and calculated ΔE* for 100PCL, PCL/PEG 90:10, and PCL/PEG 80:20 electrospun mats loaded with RC extract, after exposure to solutions across a pH range of 4.0–10.0. ΔE* indicates the total color difference from a reference color, and the corresponding color grading is visually represented below (n=3). 72

Table 10 - CIELAB values and calculated ΔE* for 100PCL, PCL/PEG 90:10, and PCL/PEG 80:20 electrospun mats loaded with RR extract, after exposure to solutions from pH 4.0 to 10.0. The visual color grading confirms a progressive halochromic response (n=3)..... 73

Table 11 - MIC and MFC values for the three EOs. Data are presented in mg/mL..... 91

Table 12 - PCL and Ch-NLCs loaded and unloaded aqueous solutions viscosity, conductivity, zeta potential, and pH values. Data are reported as mean ± S.D. (n=3)..... 97

Table 13 - Young Modulus, elongation at break, and break strength of the two PCL electrosprayed mat architectures and neat PCL mats tested at a displacement rate of 10.0 mm/min (n=3). . 104

Table 14 - WVTR, water vapor permeability index (I), air permeability rates, and mat thicknesses (n =3)..... 110

Table 15 - Young Modulus, elongation at break, and break strength of the PCL and PCL/PEG (90:10) mats and multi-layer architectures tested at a displacement rate of 10.0 mm/min (n=3). 132

Table 16 - Mat thicknesses, WVTR, water vapor permeability index (I) and air permeability rates (n=3). 137

Table 17 - Optical microscopy images of HaCaT keratinocytes and L929 fibroblasts after 24 h of incubation in direct contact with the electrospun multi-layer mats, compared with untreated control and Triton X-treated cells (positive control). Images highlight the interface between the mats (darker regions) and cells (lighter regions). 146

Table SD18 – Statistical comparison of the three parameters Young Modulus (N/mm), Elongation at Break (%) and Break Strength (MPa) between the selected control (100PCL loaded and non-loaded) (*p < 0.05; **p < 0.01; ***p < 0.001; ****p < 0.0001; ns: non-significant). 175

Table SD19 – Statistical comparison of the three parameters Young Modulus (N/mm), Elongation at Break (%) and Break Strength (MPa) between the selected control (non-loaded mats) against loaded mats (*p < 0.05; **p < 0.01; ***p < 0.001; ****p < 0.0001; ns: non-significant). 175

Table SD20 – Main DSC thermal events (T_o onset temperature, T_{peak} peak temperature and ΔH enthalpy). 176

Table SD21 - Detected compounds. Ionization mode, CAS number, retention time and MS/MS transitions. 176

Table SD22 - Main DSC thermal events (T_o onset temperature, T_{peak} peak temperature and ΔH enthalpy). 177

Table SD23 - Main DSC thermal events (T_o onset temperature, T_{peak} peak temperature and ΔH enthalpy). 178

LIST OF SIMBOLS, ABBREVIATIONS AND ACRONYMS

ATR-FTIR Fourier-transform Infrared Spectroscopy in Attenuated Total Reflectance Mode

Ci Citral

Ch Chitosan

CN Cinnamaldehyde

dH_2O Distilled water

DFUs Diabetic Foot Ulcers

DLS Dynamic light scattering

DS Degree of substitution

DSC Differential scanning calorimetry

ECM Extracellular matrix

EO Essential Oil

FDA Food and Drug Administration

G Gauge

Ge Geraniol

HPLC High-Performance Liquid Chromatography

LC-MS/MS Mass spectrometry

MFC Minimum fungicidal concentration

MIC Minimum inhibitory concentration

Mw Molecular weight

NLCs Nano Lipid Carriers

NPs Nanoparticles

PCL Polycaprolactone

PEG Polyethylene glycol

PSP Purple Sweet Potato

RC Red cabbage anthocyanin

RH Relative humidity

rpm Rotations per minute

RR Red radish anthocyanin

RT Room temperature

SEM Scanning electron microscopy

TGA Thermogravimetry

UV Ultraviolet

CHAPTER I

Introduction

CHAPTER I – INTRODUCTION

Abstract

This chapter presents the motivation for developing a multi-layer halochromic patch functionalized with cinnamaldehyde-containing lipid nanocarriers, aiming to prevent wound chronicity and promote an optimal healing environment. Subsequently, the main and specific objectives of the work are described, outlining the design, fabrication, and functionalization steps required to achieve the proposed patch. Finally, a brief overview of the thesis structure is provided, guiding the reader through the experimental steps and scientific basis of the selected strategy.

I.1 Motivation

Chronic wounds remain a major and growing healthcare challenge worldwide, with a particularly high burden in Europe. In 2025, more than 10 million individuals are estimated to be living with chronic wounds, generating annual healthcare costs that surpass €11 billion [1, 2]. Beyond the financial impact, these wounds severely reduce patients' quality of life, leading to persistent pain, psychological distress, and reduced mobility. Their chronic nature is associated with impaired healing capacity, prolonged inflammation, microbial colonization, and a heightened risk of complications such as infection and tissue necrosis. Chronic wounds are marked by a complex and heterogeneous environment, with variability in morphology, cellular response, and healing progression across patients [3, 4]. This heterogeneity makes it difficult to establish a universal treatment strategy, underscoring the importance of developing advanced, patient-tailored therapeutic approaches. Conventional management typically involves debridement, infection control, protective dressings, and frequent monitoring; yet, these measures often require repeated dressing changes that disrupt the wound bed, damage newly formed tissue, and increase reinfection risk [5]. Despite these measures, many wounds remain unhealed for extended periods, reinforcing the need for innovative solutions that integrate infection management, wound protection, and real-time monitoring. Microbial proliferation remains one of the most critical challenges in chronic wound care, as bacteria and fungi contribute to persistent inflammation and delayed tissue regeneration. Beyond bacterial colonization, fungi are now recognized as key players in delayed healing. Once considered secondary colonizers, fungi are now recognized as active contributors to deficient healing. *Candida spp.*, particularly *C. albicans*, *C. parapsilosis* and *C. tropicalis*, are frequently identified within chronic wound mycobiomes, often forming mixed bacterial-fungal biofilms that sustain inflammation and interfere with host immune responses. Such colonization is associated with increased wound chronicity and poorer outcomes [6, 7]. The ability of fungi to persist in biofilm states also complicates treatment, as conventional antifungal agents often display limited efficacy in these complex microenvironments. Conventional management is often hampered by biofilm-mediated tolerance and the risk that frequent dressing removal damages newly formed tissue and re-inoculates the site [8]. Amid concerns over antifungal resistance and the limitations of conventional agents in biofilm contexts, plant-derived essential oils are drawing renewed interest as broad-spectrum, multi-target antifungals with antibiofilm potential, even against difficult pathogens.

Plant-derived essential oils (EOs) contain bioactive compounds capable of disrupting fungal membranes, inhibiting quorum sensing, and reducing biofilm formation, and that can synergize with existing therapies [9, 10]. Their multi-target mechanisms of action make them particularly promising in combating antifungal resistance and in preventing chronic wound colonization [11]. Nevertheless, the volatility, hydrophobicity, and potential irritation of EOs pose challenges for their direct use. To overcome these limitations, nanostructured lipid carriers (NLCs), coated with chitosan (Ch-NLCs), have been explored as delivery platforms. Ch-NLCs offer muco-adhesion and sustained release that can concentrate EOs at the wound interface in a controlled manner, for fighting infections [12, 13].

In addition to antifungal management, continuous, non-invasive wound monitoring is another unmet clinical need. pH is a robust, clinically relevant wound biomarker, as chronic wounds tend to be more alkaline while healing wounds gradually shift toward acidic values. Thus, non-invasive, on-dressing pH readouts can reduce disturbance while informing timely interventions [14]. Smart dressings incorporating halochromic molecules, such as anthocyanins, have demonstrated the ability to provide visible, pH-dependent color changes, enabling clinicians and patients to track wound progression without frequent dressing removal. This reduces wound disturbance, minimizes reinfection risk, and improves patient comfort [15, 16]. The design of such multifunctional dressings depends strongly on the choice of polymers. Poly(ε-caprolactone) (PCL) offers excellent mechanical strength, structural integrity, and biodegradability, making it suitable as a scaffold material. However, its hydrophobicity and slow degradation can limit biological interactions [17, 18]. Poly(ethylene glycol) (PEG), by contrast, is hydrophilic, biocompatible, enhancing water uptake, exudate management, and antifouling behavior [19, 20]. When blended, PCL and PEG complement each other: PCL ensures mechanical stability, while PEG improves wettability. The resulting composites provide a balanced microenvironment for wound healing, combining resilience with functionality [21].

The electrospinning technique is particularly suited to process PCL/PEG blends into nanofibrous mats with high surface area, tunable porosity, and interconnected networks [22]. These structures mimic the extracellular matrix (ECM), supporting cell adhesion, proliferation, and tissue integration. Electrospinning also enables the integration of bioactive and responsive components, such as EO-loaded Ch-NLCs for antifungal activity and anthocyanins for real-time pH monitoring, without compromising scaffold morphology. In this way, electrospun PCL/PEG systems provide not only a physical barrier and structural support but also an intelligent platform for

controlled drug release and diagnostic feedback [23, 24]. Altogether, the integration of EO-loaded chitosan nanocarriers within PCL/PEG electrospun nanofibers, coupled with halochromic sensing functionality, represents a promising approach for the next generation of smart wound dressings. Bringing these threads together, a multilayer, halochromic wound patch that couples visible, pH-dependent colorimetric monitoring with controlled antifungal delivery of EO-loaded Ch-NLCs, directly addresses the three central challenges in chronic wound care: (i) early, non-invasive status assessment without dressing disturbance; (ii) targeted, sustained antifungal action; and (iii) materials aligned with safety and biocompatibility requirements. Such systems have the potential to shorten healing time, reduce dressing-change frequency, improve patient comfort, and optimize resource utilization in modern wound services.

I.2 Research Questions

Fundamental lines of questioning were proposed to address this research project:

1. Are anthocyanins extracted from red cabbage, red radish and purple sweet potato effective in monitoring pH variations?
2. Can electrospun mats of PCL and PEG meet the requirements for applications in wound dressings?
3. What is the most efficient method for blending anthocyanins within the polymeric solutions without compromising their halochromic features?
4. Is cinnamaldehyde essential oil effective against *Candida spp.*?
5. What is the effect of combining cinnamaldehyde and Ch-NLCs on the tested microorganisms?
6. Can the engineered multi-layer, pH-sensitive wound dressing guarantee antifungal performance while still meeting other chronic wound demands of breathability, flexibility, absorption, etc.?

I.3 Objectives

The main goal of this project is to develop an innovative multi-layer halochromic electrospun patch capable of combining real-time wound monitoring with controlled antifungal delivery. The system is composed of two functional layers: (i) an outer PCL/PEG layer modified with pH-sensitive halochromic molecules, enabling continuous, non-invasive colorimetric monitoring of wound status, and (ii) an inner bioactive PCL layer containing Ch-NLCs encapsulating cinnamaldehyde essential oil, designed for controlled local release and therapeutic action. The combination between the chitosan coating and the essential oil is expected to enhance antifungal efficacy, reduce microbial

colonization, and promote tissue regeneration. By combining halochromic sensing and targeted drug delivery in a single multifunctional dressing, this work seeks to improve patient outcomes, minimize dressing change frequency, and optimize clinical resources in chronic wound management.

Specific goals:

1. Chemical analysis, antioxidant activity and cytocompatibility screening of halochromic molecules, ensuring adequate color stability and pH-responsiveness for wound monitoring applications;
2. Fabrication and optimization of electrospun PCL/PEG mats, tuning fiber morphology and mechanical properties to achieve flexibility, exudate handling capacity, and structural integrity;
3. Functionalization of the outer layer with halochromic molecules and assessment of their pH-dependent colorimetric response under simulated pH wound conditions;
4. Synthesis and optimization of Ch-NLCs encapsulating cinnamaldehyde essential oil, including evaluation of encapsulation efficiency, particle characterization and stability, controlled release profile and potential synergistic effect of chitosan and cinnamaldehyde;
5. Integration of Ch-NLCs into electrospun PCL fibers to produce the bioactive inner layer, followed by characterization of morphology, physicochemical properties, and release kinetics;
6. Assembly of the complete multi-layer patch and evaluation of interlayer adhesion, stability, and degradation behavior under physiologically relevant conditions;
7. Assessment of antifungal performance, focusing on relevant chronic wound pathogens;
8. Biocompatibility and cytocompatibility testing of the final dressing to confirm its suitability for safe application on chronic wounds.

I.4 Thesis Structure

Chapter I. Introduction

This chapter highlights the motivation behind this study and outlines the objectives that guided the development of the work. In addition, it provides an overview of the thesis structure, offering a brief introduction to the content of each chapter.

Chapter II. Literature Overview

Chapter 2 provides a review of the essential concepts and technical background supporting this work. It begins with a definition of chronic wounds and an overview of current dressing strategies, highlighting the need for innovative approaches. The proposed multi-layer patch is then introduced, consisting of a halochromic PCL/PEG layer for pH-based monitoring and a bioactive PCL layer containing Ch-NLCs encapsulating essential oils. The design, advantages, and expected functionalities of this system are discussed. The electrospinning technique used for patch fabrication is briefly described, focusing on its principles and key parameters affecting fiber production. Finally, the therapeutic relevance of essential oils and the benefits of their encapsulation are reviewed, establishing the foundation for the experimental work.

Chapter III. Polycaprolactone/polyethylene glycol electrospun mats with pH-responsiveness for real-time sensing in chronic wound healing

This chapter presents the development and characterization of electrospun PCL/PEG mats functionalized with halochromic molecules. Their pH-responsiveness is evaluated to assess their potential as real-time, non-invasive wound monitoring systems through visible colorimetric changes. It includes a preliminary screening of the selected halochromic agents based on their safety and biocompatibility, ensuring their suitability for contact with living cells in wound healing applications.

Chapter IV. Development and Integration of Cinnamaldehyde loaded Chitosan coated Nano-Structured Lipid Carriers into Polycaprolactone Electrospun Mat: A Novel Approach for Antifungal Wound Healing

The focus of this chapter is on the production and optimization of Ch-NLCs encapsulating cinnamaldehyde essential oil and their incorporation into electrospun PCL mats. The chapter details the physicochemical characterization, encapsulation efficiency, release profile, and antifungal performance of the resulting bioactive dressing.

Chapter V. Monitoring cinnamaldehyde essential oil fungicidal action on chronic wounds by means of halochromic multi-layer electrospun dressing

Building on the previous results, this chapter evaluates the functionality of the multi-layer halochromic patch. The correlation between colorimetric response and local pH is analyzed and

the therapeutic effect of the cinnamaldehyde-loaded Ch-NLCs evaluated, demonstrating the patch's ability to provide combined treatment and real-time wound monitoring.

Chapter VI. Conclusions and Future Perspectives

This chapter summarizes the main findings of the work, highlighting the contribution of the multi-layer halochromic patch to the field of smart wound dressings. Future directions are proposed to further optimize the system and explore its translation into clinical applications.

CHAPTER II

Literature Overview

CHAPTER II – LITERATURE OVERVIEW

Abstract

Recently, biomedical engineering has seen significant advancements in nanomaterial-based scaffolds for tissue engineering and wound healing. Incorporating halochromic properties within these scaffolds has garnered substantial interest due to their real-time monitoring abilities for accessing tissue growth and regeneration. This chapter presents a comprehensive analysis of recent advancements in nanomaterial-based scaffolds with halochromic functionalities for skin applications. The discussion revolves around the various classes of nanomaterials used in scaffold fabrication, including but not limited to electrospun nanomaterials, polymeric nanomaterials (both of natural and synthetic origins), and nanomaterials based on bio-composites, each offering distinct advantages and limitations in terms of mechanical properties, biocompatibility, and tunability of halochromic response. Emphasis is placed on integrating halochromic moieties, such as pH-sensitive dyes, into the scaffold matrices, with a focus on maintaining optimal cytocompatibility and biofunctionality. A key focus is given to recent *in vitro* studies showcasing the potential of halochromic nanomaterial-based scaffolds in clinical applications. This study lies in providing a structured framework for understanding the interaction between halochromic nanomaterials and biomedical scaffolds, identifying challenges, and proposing future research directions to enhance their diagnostic and therapeutic potential.

This chapter is based on the following scientific publications:

- Ana R.M. Ribeiro, Bruna A.S. Oliveira, Ana Isabel Barbosa, Catarina L. Seabra, Salette Reis, Helena P. Felgueiras, Nanomaterial-based scaffolds endowed with halochromic properties for skin healing purposes, Journal of Drug Delivery Science and Technology, 108, 2025,https://doi.org/10.1016/j.jddst.2025.106950.
- Ana R. M. Ribeiro, Tavares T. D., Domingues J. M., Silva C., Antunes J. C., Catarina L. Seabra and Helena P. Felgueiras, "Electrospun nanofibrous composites for drug delivery applications". Handbook of Composite Materials for Advanced Biomedical Applications, Springer Nature (In Proof)

II.1 Chronic Wounds

During the evolution of humanity, the human body has developed a highly effective wound healing process through which specifically sequenced processes of inflammation, cell proliferation, migration, angiogenesis, deposition of new cell matrix, and remodeling occur with the purpose of repairing an injured tissue [25]. When that process becomes dysregulated, chronic lower extremity wounds may develop. Chronic wounds are biochemically different from acute wounds in their expression of growth factors, matrix metalloproteases, and various proteins [26]. This type of wound is defined by its failure in proceeding through an orderly and timely reparative set of stages in which anatomic and functional integrity is restored within a period of 3 months. To ensure a proper wound closure, its size must decrease by at least 0.7 mm per week, or the wound is labelled as chronic [26, 27]. Chronic wounds are also considered those when the renewal of the tissue does not allow the return of anatomical functionality.

Chronic wounds are characterized by events that tend to escalate sequentially: (1) barrier disruption and infection, (2) high oxidative stress induced by increased levels of reactive oxygen species, (3) neuropathy, (4) microvascular complications, and (5) chronic inflammatory response. In most cases, allied to these events are social life restrictions that compromise the psychological health of the patient. (Figure 1) [28, 29].

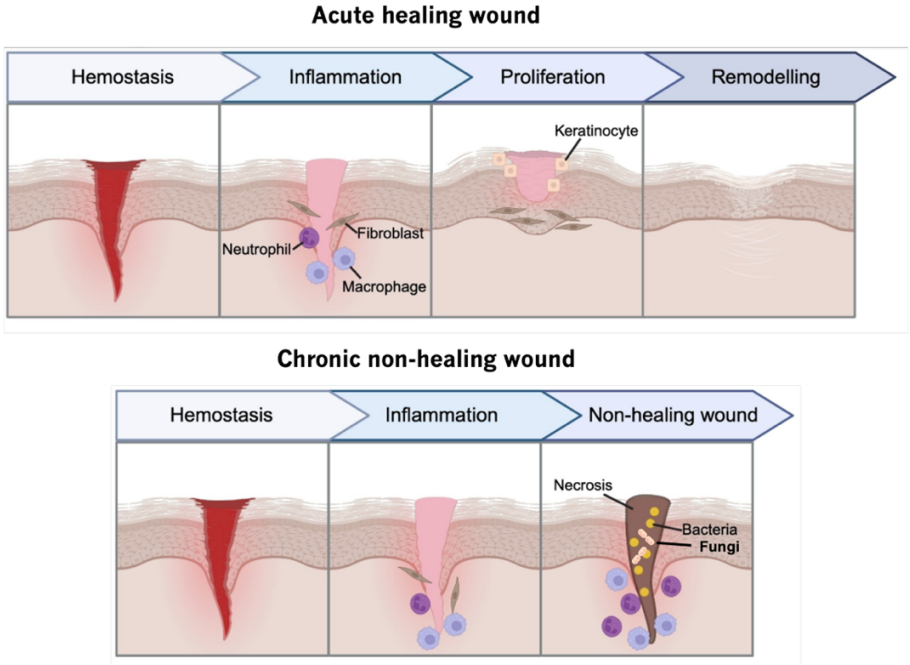


Figure 1 - Differences between the healing process of an acute wound and a chronic wound. The chronic wound exhibits deregulated angiogenesis, sub-optimal inflammatory response and persistent bacterial and fungi colonization (adapted from [29]CC BY 4.0 permission).

Considering the characteristics and nature of chronic wounds, the occurrence of infections is very common, negatively affecting the healing process, compromising vital functions. Infection is initiated by the colonization and multiplication of pathogenic microorganisms, often opportunistic, causing local tissue damage [25] Each wound has its microbiome, which differs from patient to patient mainly depending on the host's immune status and its physio pathological features. In addition to the presence of various types of bacteria, Gram-negative and Gram-positive, it is also possible to find anaerobic bacteria and fungi. Microorganisms in chronic wounds have "preferred locations" and the deep microbiota is more diverse and complex than the superficial skin microbiota and has a greater predominance of pathogenic bacteria and fungi. The colonization spot is defined by the amount of oxygen they take up when present. In contrast to anaerobes, which live deeper inside the niches given by aerobic oxygen intake, aerobic bacteria may be found at the surface where oxygen levels are significantly higher (Figure 2) [30, 31].

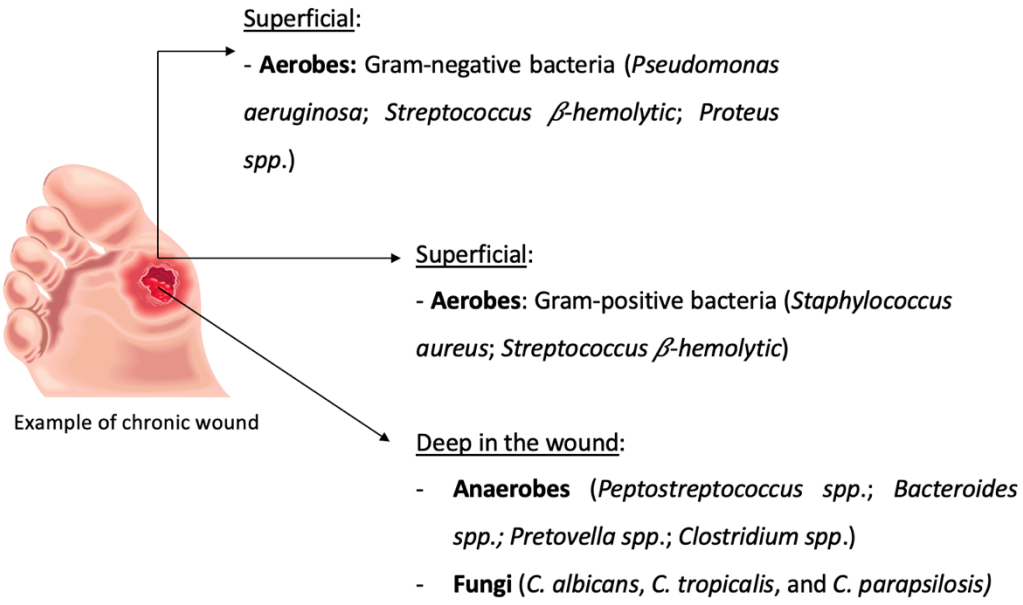


Figure 2 - Different types of microorganisms organized according to the location in an example of chronic wound (adapted from [30] with CC BY 4.0 permission).

Fungal infections in chronic wounds are not as investigated as bacterial; however, they play an important role in the development of infections and in the maintenance of biofilms that prevent the normal healing to occur [32, 33]. Despite the evidence for fungal infection in chronic wounds, clinicians and surgeons treat them as if they were only colonized by bacteria, resorting mainly to antibacterial agents. They often neglect fungal infections and do not explore the wound deep tissue for fungal culture and sensitivity (due to insufficient information in the literature) [34]. *Candida spp.*

are the most commonly isolated species of fungi in chronic wounds. These types of yeasts often belong to the normal microbiota of the skin around ulcers or may colonize wounds secondarily [35]. *Kandregula S. et al.* carried out a cross-section observational study in a tertiary care hospital, with a sample size of 60 DFUs, to find out the prevalence of fungi-derived infections. Microbiological analysis was done by swab culture and deep tissue culture. They concluded that the incidence of *C. albicans* (33.33 %), *C. tropicalis* (23.8 %), and *C. parapsilosis* (19%) were maximum compared to other microbes. Furthermore, two other *Candida* species (*C. glabrata* and *C. lustania*) were found together with another three fungi, the *Alternaria*, *Penicillium* and *Tricophyton* [35]. Fungal infections can be potentially fatal or lead to limb amputation if left untreated. Fungal cultures' research should be added to the treatment protocol in all long-standing chronic wounds, considering fungal-induced infections may not disappear despite adequate antimicrobial therapies being applied.

Traditional treatment strategies that resort to systemic antibiotics, conventional dressings, etc., have limited delivery to chronic wound sites, not preventing the growth of microorganisms and often interrupting the healing process and the formation of new tissue. As such, new therapies have been focused on topical delivery of drugs via systems that guarantee controlled release kinetics. The growing understanding of healing and regeneration mechanisms has helped to elucidate the best types of treatments that should be employed according to the situation; however, despite this, the successful management and treatment of chronic wounds continue to represent a significant therapeutic challenge. Management of chronic wounds requires extensive knowledge of their complexity. At first, wound debridement is made to remove thickened, dead, necrotic or infected tissue, followed by revascularization to assist in skin rebuilding and efficient antimicrobial protection through a combination of topical agents. In the end, to prevent the aggravation of infections after all these procedures, antibiotics are used as a traditional step in the healing of these wounds followed by appropriated dressing.

II.2 Wound Dressings

Wound healing is a complex process, with chronic wounds taking weeks to months to heal. It involves the simultaneous actuation of soluble mediators, blood cells, ECM and parenchymal cells, and is divided into homeostasis/coagulation, inflammation, proliferation (granulation tissue formation), re-epithelialization and remodeling phases. Usually, the transition between phases depends on the maturation and differentiation of keratinocytes, fibroblasts, mast cells and macrophages, which are the most important cells involved in the wound healing cascade [36, 37].

These steps do not follow a specific and rigorous timeline and may overlap. In patients with certain diseases like diabetes, these cellular and biophysical events are disrupted or delayed, giving rise to problems that prevent healing from progressing.

During the healing of a skin wound, dressings are used to protect the integrity of the dermal and epidermal tissues from further damage, shielding the wound from the external environment, promoting healing and reducing the risk of infection [38]. Currently, the manufacture of dressings has reached such a development that environments conducive to skin regeneration can be promoted [27]. There are two types of dressings: (1) the simplest, called traditional dressings, are only used with medicines that perform preventive actions and serve only to protect the wound; and (2) the advanced dressings, which provide site protection and, at the same time, promote tissue healing and regeneration [38]. In recent years, bioactive dressings have become systems with relevant importance as they combine the physical and biochemical properties of natural and synthetic polymers, with active compounds that have beneficial properties for the healing and regeneration of skin wounds [39, 40]. Polymeric (synthetic, semi-synthetic, or naturally derived) dressings are potentially useful in the treatment of local infections where achieving increased local concentrations of antibiotics may be ideal while avoiding high-systemic doses; thus, reducing patient exposure to an excess of drugs beyond the required at the wounded site. Composite dressings comprising both synthetic and naturally occurring polymers can also be used for controlled drug delivery. An ideal wound dressing must respond to several demands to guarantee a clean and moist environment around the injured site (Table 1) [41, 42].

Table 1 - Characteristics that an ideal wound dressing must respect [43, 44].

Absorb exudates and toxic components from the wound surface	Maintain a high humidity at the wound-dressing interface
Allow gas exchange between the wound and the environment	Control the pH
Mechanical stability	Protect the wound from the penetration of microorganisms and foreign particles
Be non-toxic or allergenic	Be biocompatible and biodegradable
Be easily and comfortably removed without causing trauma	Be cost-effective

The bioactive dressings derived from natural or synthetic polymers can be produced in the form of films, foams, alginates, hydrocolloids or hydrogels as long as they promote an effective barrier against microorganism permeation, maintain a moist environment, and allow gas exchanges [42]. These types of dressings are engineered for interacting with living components at the wound bed, delivering substances and participating actively in the healing process, for that reason, bioactive polymers and/or biomolecules must be present [43]. For instance, a wide variety of antibiotics can be immobilized directly onto nanofibrous dressings, namely triclosan, chlorhexidine, iodine, cetylpyridinium chloride, etc. However, the antibiotic resistance crisis allowed for other biomolecules to arise in drug delivery systems. Certain natural extracts have been highlighted for their intrinsic antibacterial, antifungal and insecticidal properties [44] moreover, lipid-based nanoparticles, such as solid lipid nanoparticles and nanostructured lipid carriers, have also been successfully incorporated into electrospun nanofibrous dressings to enhance their antibacterial performance [45]. More recently, EOs have emerged as promising alternatives to conventional antifungal and antibacterial agents due to their multi-target mechanisms of action, lower propensity for resistance development, and effective activity even against drug-resistant strains [46]. In a recent study conduct by *Yuan, X. et al.*, 98 essential oils were screened against *C. albicans* in the stationary phase, a condition associated with antifungal tolerance. Five essential oils - cinnamon, *Satureja montana*, palmarosa, lemon eucalyptus, and honey myrtle - exhibited potent antifungal activity, with minimal inhibitory concentrations (MICs) ≤ 0.0078 % and complete killing within short exposure times. Synergistic effects were also observed when certain essential oils were combined with amphotericin B [47]. *Emami et al.* developed a multifunctional bi-layer electrospun scaffold composed of collagen and poly(L-lactic acid) (PLLA), incorporating *Zataria multiflora (Z. multiflora)* essential oil for enhanced wound healing applications. In this system, the inner collagen layer provided a biocompatible surface that supported fibroblast adhesion and proliferation, while the outer PLLA layer ensured mechanical stability and controlled release of the bioactive oil. The incorporation of *Z. multiflora* essential oil endowed the scaffold with remarkable antibacterial, antifungal, and antioxidant properties, effectively inhibiting the growth of pathogenic microorganisms commonly associated with wound infections [48].

Multi-layered dressings have recently gained more significance compared to one-layer materials by offering different treatment approaches in one formulation and, thus, targeting many needs simultaneously. Indeed, these dressings are regarded as the ultimate wound protection and healing, via layer-by-layer approaches that merge multiple functions [49]. Most of the electrospun

nanofibrous dressings have been fabricated as single-layer structure mats. However, this design is less favorable for the effective healing of wounds because of the burst release effect of entrapped bioactive agents [50]. *Trinca, Rafael et al.,* developed a double-layer electrospun scaffold for skin lesions care, in which one layer acted as mechanical support, being composed of PCL or a PCL/cellulose acetate blend (PCL/CA) while the other layer performed the role of primary wound dressing, being constituted by a chitosan/poly(ethylene oxide) blend (CHI/PEO). Aside from guaranteeing oxygenation, moisture balance and exudates absorption, the scaffolds were non-cytotoxic towards fibroblasts (L929 cell line) and promoted adequate cell proliferation [51]. Similarly, *Saeed Seyed et al.* studied a strategy to improve the control of wound exudates, which remains a challenge, allied with an antibacterial profile. For that, a three-layer active electrospun wound dressing based on *e*-PCL, polyvinyl alcohol (PVA) and curcumin was investigated. They concluded that a three-layer dressing placed over an incision absorbs three times more exudates than traditional dressing options. Examinations also deemed the dressing containing 16% curcumin as antibacterial with no compromise to healthy cell viability [52]. In a recent study, *Erdogan, S. et al.* designed a multi-layer electrospun wound dressing composed of PCL and chitosan (Ch) nanofibrous scaffolds with tigecycline incorporated into the middle layer. The tri-layer structure, consisting of hydrophobic PCL outer and inner layers and a hydrophilic PCL-Ch-Tig middle layer, was tailored to mimic the extracellular matrix while enabling controlled drug delivery. SEM analysis revealed smooth, bead-free fibers while porosity and wettability were optimized by Ch incorporation. The dressing showed robust mechanical performance (tensile strength of 7.44 MPa), minimal degradation (<1.5 % over 14 days), and a biphasic tigecycline release profile, releasing ≈38 % of the drug in the first 60 min and sustaining release thereafter. Antibacterial tests confirmed significant inhibition against *E. coli* and *S. aureus*, and cytocompatibility assays demonstrated >95 % HUVEC viability, underscoring the scaffold's potential as a durable, bioactive platform for advanced wound healing applications [53]. More advanced formulations, capable of mapping the healing progression through environmental cues (pH, temperature, tissue oxygenation, moisture and even mechanical and electrical stimuli), have also gained interest [54]. *Brooker, C. and Tronci, G.* reported the development of a collagen-based theranostic wound dressing integrating bromothymol blue (BTB) for infection sensing. The prototype combined a collagen hydrogel contact layer with BTB introduced either by drop-casting or electrospinning, enabling rapid and reversible color changes in response to infection-associated alkaline pH (pH > 7). Remarkably, the drop-cast collagen/BTB constructs achieved a high dye loading efficiency (≈ 99 wt. %) and retained up to 97

% of the dye after 96 h in simulated wound fluids, ensuring durable infection-detection capability. The color shift was visible within 1 min and remained reversible over multiple acidic–alkaline cycles, while cytocompatibility assays confirmed high fibroblast viability (>90 %) [55]. Under the same topic, *Pakolpakçıl, A et al.*, developed a wound dressing for pH monitoring based on a sodium alginate (SA) and PVA nanofibrous mat modified with anthocyanins extracted from black carrot. The halochromic PVA/SA/black carrot nanofibrous mat showed a short response time presenting visibly distinguishable colors, especially at pH 4-6 and 8-10, which are consistent with the pH changes in the wound healing process [56]. The choice of a suitable dressing to manage chronic wounds remains of great importance in the medical field and can be guided by the wound features, patient requirements and costs.

II.3 Production of Nanofibers: Electrospinning Technique

Nowadays, nanotechnology has revolutionized the industry and science fields, having an overpowering impact on human life and the economy. The existence of a wide range of nanomaterials allows their application in several areas, such as biomedicine, textile industries, food packaging, electronics, etc. Nanomaterials are characterized by their nanosize, large surface area, good tensile strength, tunable morphology, topography and porosity, surface functionalization abilities, and overall stability [57]. Among the existing nanomaterials, nanofibers stand out for their excellent and broad advantages for applications in biomedicine, particularly in wound dressings. Micro and nanofiber-based scaffolds have gained much attention in tissue engineering, biomedicine, controlled drug delivery and wound care because of their large surface area, tailor ability, continuity, consistent diameter and ease of processing [43]. Nanofibers can be produced by several techniques such as drawing, melt blown, template synthesis, phase-separation, self-assembly, wet-spinning, melt-spinning, dry-spinning and electrospinning [58].

Compared to the other methods, electrospinning has been deemed the technique of choice for wound healing applications considering its economic competitiveness, high efficiency and time-saving abilities related to production rates. This technique is simple and effective and uses electrostatic force to produce nanoscale fibers from polymers of natural and synthetic origins. Its invention dates back 120 years, but it was only in the 1980s that it began to gain more attention due to its versatility, reproducibility, the scale at which it operates, volume-to-surface ratio, adjustable porosity, and the possibility of producing malleable fibers that adapt to a wide variety of sizes and shapes, and the ability to easily control the fiber composition to achieve desired properties and functionality.

In general, the operation of this technique is based on three fundamental principles (Figure 3): (1) the electrical power supply; (2) the use of a spinneret (the needle through which the polymer solution comes out to form the fiber); and (3) the collector [59]. Briefly, in electrospinning a polymeric solution is prepared in the appropriate solvents and introduced into a syringe connected directly to the spinneret. The next step is the application of a high electrical potential (kV) between the needle and the collector. When the applied electric field exceeds the surface tension of the droplet, a charged beam of polymer solution is expelled from the needle tip. This beam is called the "Taylor Cone", which acquires the shape of a cone as it leaves the needle, becoming longer and thinner depending on the high voltages applied, ending up being geometrically subdivided into bundles of nanofibers that are collected at an ideal distance, ending in the solidification of the polymers due to the evaporation of the solvent. Thus, the solidified nanofibers are deposited on the collector until they form a film with an appropriate thickness for the intended use [60].

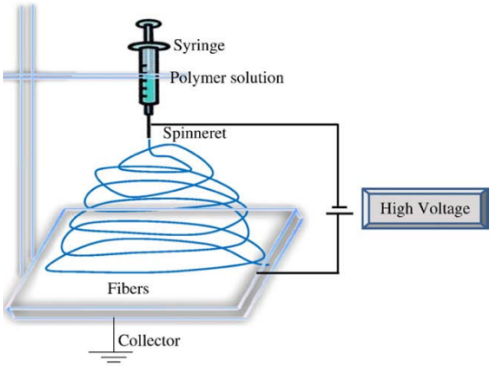


Figure 3 - Schematic representation of electrospinning equipment (adapted from [59] CC BY 4.0 permission).

Despite all its advantages, producing nanofibers using the electrospinning technique can be a challenging process. There are a variety of parameters that need to be controlled and optimized in order to obtain fibrous films with good fiber orientation and specific morphology and topography (Table 2). The ideal properties for nanofibrous films production, applied to the treatment of cutaneous wounds, should cover the following values: fiber diameter between 50-500 nm, a high volume to surface area ratio (i.e., high exudates absorbance), a high fiber porosity (60-90 %), and high mechanical strength (adaptable to different geometries and wound locations) [60].

Table 2 - Parameters that affect the production of nanofibers by the electrospinning technique [60].

Polymer Solution Parameters	**Operational Parameters**

Concentration	Applied voltage
Molecular weight	Flow
Viscosity	Needle diameter
Superficial tension	Collector shape
Conductivity	Distance to collector
Solvent volatility	Environmental conditions of the circulating environment (temperature, relative humidity)

The operational parameters are optimized during the electrospinning process by visualizing the stability of the beam generated. As far as the voltage is concerned, using higher values can increase the electrostatic repulsive forces on the jet and therefore the fiber diameter decreases, the solvent evaporates quickly, and aggregates do not form. The flow must also be adjusted depending on the polymer solution to be used; however, preferably, lower flows should be employed to allow evaporation of the solvent. The distance from the needle tip to the collector is used to control fiber morphology and diameter. Finally, the relative humidity (RH) of the air and the environment temperature of the place where the electrospinning equipment is located also affect the morphology and production of fibers as there is a direct correlation between solvent volatility and temperature. For example, the surface tension of the polymeric solution and the viscosity are affected by temperature [61]. On the other hand, the adjustment of the parameters to obtain a polymeric solution suitable for the production of nanofibers requires thorough prior knowledge of the chosen solvents and polymers. As for polymers, their concentration influences the shape of the nanofibers, while their molecular weight has a significant effect on viscosity, surface tension and conductivity. For example, a very low molecular weight solution tends to form aggregates rather than fibers. The viscosity (with a maximum between 1-215 poise) of the solution plays an important role in determining fiber size and morphology. It is necessary to reach an optimal balance since with very low viscosities there is no formation of a continuous fiber and with very high viscosities the polymeric solution has difficulties in being injected through the needle. The solvents are chosen for preparing the polymer solution also represent an important part of the success of the electrospinning technique. They must present good volatility, a low boiling point, be able to maintain the integrity of the solution even after dissolution is complete and must have an adequate pressure value so that the evaporation of the solvent at the time of injection is the fastest possible. At the same time, the surface tension must remain at low values, as high values cause instability of the

bundle, leading to the formation of droplets and consequently aggregates, contrary to the intended. Finally, it is concluded that solvents with highly conductive properties are unstable in the presence of an elevated electric field, leading to a wide distribution of the nanofibers' diameter [62].

Electrospinning allows for fibers with different organizations, compositions and structural arrangements to be achieved with a large surface area, which contributes significantly to their application in the biomedical field [39]. First, the structure can be similar to the natural ECM, which provides an ideal microenvironment for cell adhesion, proliferation, migration and differentiation. Secondly, the polymer matrix used for electrospinning can simultaneously combine the biocompatibility of natural polymers and the reliable mechanical strength of synthetic polymers. Furthermore, the nanofiber mats' wide surface area and the porous structure can be effectively modified with various biologically active compounds, including antibacterial drugs, inorganic NPs, vitamins and growth factors. The rate and time of drug release are controlled by adjusting the fiber structure and morphological size, thereby promoting effective healing of a wounded site [58, 63].

Different drug loading techniques can be applied to nanofibers, depending on the type of drug (small molecules, proteins, genes, etc.) and its physicochemical properties such as hydrophobicity, hydrophilicity and molecular weight. The choice of drug immobilization method in the nanofiber scaffold depends as well on the intended release kinetics, namely, increased initial burst, sustained release or prolonged circulation [64]. One of the most common functionalization approaches relies on the blending of bioactive agents with the polymeric solution prior to the electrospinning process. Co-electrospinning is a simple and single-step method. The characteristics of the polymeric blend are responsible for establishing the release pattern of the drug. To achieve an effective drug distribution, constant drug release and controllable release kinetics, the drug/polymer matrix must be compatible, being both hydrophobic and hydrophilic nature [65, 66]. In the case of co-axial electrospinning, the two components can be separated in different layers but are again ejected through the spinneret at the same time [65]. Co-axial electrospinning consists in two spinneret needles that separate two immiscible solutions and is used to produce nanofibers with core-shell structure, which are highly desirable for encapsulating bioactive agents at the core of the fiber, keeping them protected from external factors such as moisture and oxygen [65]. The hydrophobic shell serves as an outer protective layer to prevent initial burst release. Therefore, coaxial electrospinning is considered one of the most significant breakthroughs in the field of drug-sustained release [58, 65]. Other types of methods could also be applied after the electrospinning process. Surface immobilization is the simplest approach to bond a drug to the nanofibers' surface

by chemical (covalent bond) or physical (physisorption) means. When it comes to a covalent bond, during immobilization, stable complexes are formed between the functional groups of the substrate and the functional groups of the bioactive agent. The functional groups that participate in the reaction are the amino, carboxylic, thiol, imidazole, indole and hydroxyl groups. This method is seen as the most appropriate since the bioactive agents are covalently bonded to the fiber surface, so mass transfer limitations of the substrate to the bioactive agents active site that can occur with encapsulation or leaching as seen with adsorption, do not occur [67]. In the case of physisorption, the bioactive agent and the nanofiber substrate are placed in the solution for a fixed amount of time under dynamic conditions and then rinsed with buffer solution to remove any non-adsorbed bioactive agents. The mechanism for immobilization is based on weak interactions such as Van der Waals forces, and hydrophobic and electrostatic interactions. This is a simple, reagent free, low cost and easily reversible method, non-destructive to both the substrate and bioactive agent. However, because the bioactive agents are loosely bound to the polymer matrix, they can be easily desorbed from the nanofiber surface due to changes in temperature, pH and surface charge [67]. The immediate release of drugs from the nanofiber surface can enable facile dosage control of some therapeutic agents, suitable for fighting bacterial infection, for instance [68].

II.4 Electrospinnable Polymers

Biomaterials have received special attention from several researchers due to their potential in biomedicine. As wound dressings, these materials can target the inflammatory, proliferative or tissue remodeling phases, as well as modulate cell signaling pathways, triggering the growth, differentiation and overall function of the main agents of the healing process, namely the fibroblasts, keratinocytes, macrophages and endothelial cells. Within the wide range of biomaterials, biopolymers have been highlighted in wound healing for their excellent properties of biocompatibility, regeneration capacity, low antigenicity, ability to support cell growth, biodegradability and durability [69, 70]. One of the most essential prerequisites for defining a material as a biomaterial is its biocompatibility, that is, the ability of a material to function with an appropriate response towards the host without triggering cytotoxic events. The host response depends on several factors ranging from the chemical, physical and biological properties of the materials to the shape and structure of the scaffold used (three-dimensional structural organization). The properties inherent to biomaterials of polymeric origin that can affect their biocompatibility are the chemical characteristics of the polymer, molecular weight, solubility, shape

and structure, hydrophilic and hydrophobic properties, surface tension, water absorption capacity and degradation profile. The second most important pre-requisite is the biodegradability of the material and for that, the biocompatibility needs to be demonstrated over time. Polymeric scaffolds, when applied to living organisms, must persist without physical and chemical changes for a sufficient time to allow the formation of new tissue, but it is also essential for them to degrade in an approximate time frame [71].

Polymers of natural origin possess structural sequences or only monomers (i.e., amino acids, nucleic acids) that are linked by covalent bonds giving rise to peptides, polysaccharides, polyphenols, etc. They are produced naturally by living organisms such as plants, animals, fungi and algae, and among the most common we find cellulose, chitosan, alginate, hyaluronic acid, gelatin, silk fibroin, etc. (Figure 4) [72]. All these biopolymers have different medicinal properties, including anti-inflammatory effects, antimicrobial activity, healing power (intervention in different stages of the healing cascade), etc. Despite their biological benefits, their mechanical properties tend to be insufficient to withstand the mechanical movements and stresses inherent to many areas of the body, including the skin [73]. Blends with polymers of synthetic origin, such as PCL, polyvinylpyrrolidone (PVP), PEG, etc., offer multiple advantages in this regard, in addition to making their processing by nano and micro spinning techniques much easier. Synthetic polymers appear as a good option to fill some inherent flaws to the polymers of natural origin since they are recognized for their robust mechanical properties and are less expensive to both produce and process.

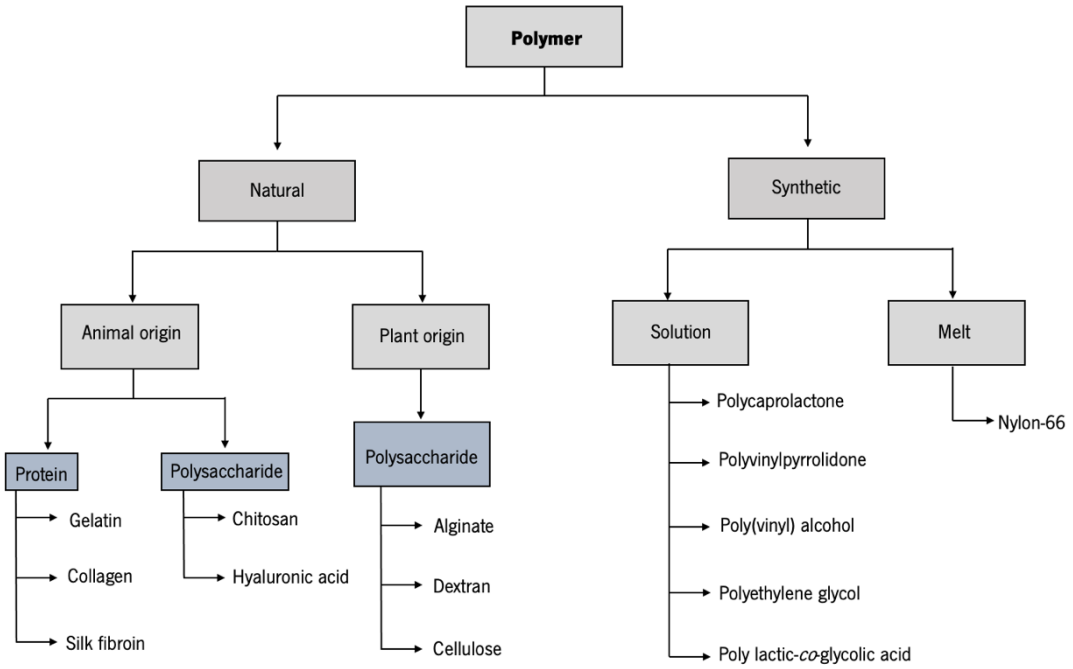


Figure 4 - Common polymers used in the production of electrospun wound dressings (adapted from [58] with CC BY 4.0 permission).

II.4.1 Poly (ε-caprolactone) (PCL)

PCL is a synthetic, biodegradable aliphatic polyester obtained through the ring-opening polymerization of ε-caprolactone using metal catalysts such as stannous octoate [74]. Owing to its excellent biocompatibility, processability, and mechanical properties, it has been widely investigated for biomedical applications, particularly in tissue engineering and wound healing. PCL's long aliphatic chains confer a semi-crystalline structure with a relatively low glass transition temperature ($T_g \approx -60$ °C) and low melting point ($T_m \approx 60$ °C), which makes it easy to process by various methods such as solvent casting, 3D printing, and electrospinning [75, 76]. Its slow hydrolytic degradation, driven by the cleavage of ester bonds, allows it to maintain structural integrity for extended periods, a characteristic that is especially useful in applications requiring long-term mechanical stability, including scaffolds for chronic wound dressings . The chemical and physical properties of PCL are influenced by its molecular weight, degree of crystallinity, and chain mobility. While its hydrophobicity limits water uptake and cell affinity, this same property contributes to its mechanical robustness and resistance to rapid degradation, making it a versatile base polymer for composite systems. PCL is thermoplastic, crease-resistant, and soluble in a variety of organic solvents, but exhibits low wettability and bioactivity in its pure form [76]. To

overcome these limitations, PCL is often chemically modified or blended with natural hydrophilic polymers (such as chitosan, cellulose derivatives, or collagen), thereby improving cell adhesion, moisture balance, and biofunctionality while retaining its mechanical strength [77]. Electrospun nanofibers of PCL have gained particular attention in wound healing research due to their fibrous morphology closely resembling the ECM, promoting cell migration and proliferation. PCL nanofibers are reported to exhibit high porosity, interconnected pore structures, and tunable fiber diameters, enabling adequate oxygen exchange and exudate management while serving as carriers for bioactive molecules [78]. However, electrospinning of pure PCL can yield dense, hydrophobic mats that limit cell interactions. To address this, PCL is frequently blended with hydrophilic polymers such as PEG or PVA, generating composite nanofibrous scaffolds that combine mechanical resilience with enhanced wettability and bioavailability [79, 80]. In wound care, PCL-based materials have been successfully functionalized with antimicrobial agents, growth factors, and natural bioactive compounds, highlighting their versatility as drug delivery vehicles and structural supports. Its slow degradation profile ensures prolonged therapeutic effect, while its compatibility with advanced fabrication techniques allows for the development of multilayer, multifunctional smart dressings tailored for chronic wound management [81]. For example, *Reyes-Guzmán et al.* incorporated a ChAgG nanocomposite (chitosan + silver + graphene) into PCL/ polyvinylpyrrolidone (PVP) electrospun fibers, demonstrating enhanced antimicrobial efficacy (including against fungi), good biocompatibility, and potential for wound dressings [82]. For instance, *Erdogan et al.* designed a multi-layer electrospun PCL/Ch scaffold for wound dressing applications, in which PCL provided mechanical support and slow degradation, while the Ch layers improved hydrophilicity and facilitated incorporation of antimicrobial agents. The composite scaffold exhibited sustained antibacterial activity, good biocompatibility, and potential for chronic wound management [83].

II.4.2 Polyethylene glycol (PEG)

PEG is a synthetic, hydrophilic, and biocompatible polyether obtained by the polymerization of ethylene oxide. It is one of the most widely used polymers in biomedical applications due to its non-toxic, non-immunogenic, and highly water-soluble nature, as well as its approval by the FDA for internal and external use [84, 85]. The physicochemical properties of PEG are highly dependent on its molecular weight (MW), which can range from a few hundred to several tens of thousands of g/mol. Low molecular weight PEGs (e.g., PEG 400–600) are liquid at room temperature and often used as plasticizers, solvents, or drug carriers, while high MW PEGs, such as PEG 20,000,

are solid, crystalline, and capable of forming more stable hydrogels and nanofibrous structures [86]. PEG is characterized by its flexible polyether backbone and abundance of hydroxyl terminal groups, which provide multiple sites for chemical functionalization. Its hydrophilicity and antifouling properties result in minimal protein adsorption and reduced bacterial adhesion, making it highly suitable for wound dressing applications [87–89]. However, PEG alone lacks mechanical robustness and structural stability, particularly in hydrated environments, which limits its direct use in load-bearing or long-term scaffolding systems. For this reason, it is often blended with other polymers such as PCL, PLA, or PVA, where it contributes to improved wettability, controlled degradation rates, and enhanced bioavailability of incorporated therapeutic agents [20]. Electrospinning of PEG and PEG-containing blends has been widely explored for wound healing applications. Although PEG's high water solubility can complicate the electrospinning process, the inclusion of high molecular weight PEG (e.g., PEG 20,000) increases solution viscosity, facilitates fiber formation, and improves the stability of electrospun mats [90, 91]. PEG-based nanofibers exhibit excellent moisture-retention capacity, high porosity, and interconnected pore networks, features that mimic the ECM and create a favorable environment for cell proliferation, nutrient diffusion, and exudate management [92]. Moreover, PEG's hydrophilic character enhances drug encapsulation and release efficiency, allowing for the sustained delivery of bioactive molecules such as essential oils, antibiotics, or growth factors. PEG is also extensively used to form hydrogels and semi-interpenetrating polymer networks that serve as wound dressings with controlled degradation and tailored mechanical properties. By varying molecular weight and crosslinking density, PEG hydrogels can be engineered to degrade over defined timeframes while maintaining adequate swelling and mechanical support. This tunability, combined with its excellent safety profile, makes PEG a highly versatile polymer for designing smart and multifunctional wound dressings [93]. *Mushtaq, F. et al.* studied chitosan conjugated with methoxy-PEG (mPEG) to form an injectable hybrid hydrogel system with good mechanical strength, *in situ* gelation, and sustained release behavior. The CH–mPEG hydrogels showed accelerated wound closure in full-thickness skin defect models in rats, enhanced re-epithelialization, collagen deposition, and angiogenesis, compared to controls. Crucially, the hydrogels were non-cytotoxic and promoted tissue regeneration while also allowing the possibility of incorporating antibacterial agents [94]. A recent study developed by *Katarina Virijević et al.* used an artificial intelligence approach to screen and optimize combinations of PCL and PEG in electrospun scaffolds. The optimized PCL/PEG scaffolds were further enriched with antibiotics and tested *in vivo*, demonstrating enhanced wound healing performance including

neo-vascularization and faster tissue repair. The work highlighted how PEG incorporation can help modulate scaffold properties (e.g. hydrophilicity, degradation) to achieve better biological outcomes [95].

II.5 Halochromic Molecules as pH-Sensors

The evolution of technology and the growing demand for more advanced and intuitive tools for the user have turned smart and functional textiles into a need of the future. Smart textiles are products that can receive and give responses to external stimuli so as to adapt themselves to changes in the surroundings, such as temperature, light, pressure, pH, etc. There are three types of smart textiles: (1) passive smart textiles, only able to sense the environment/user based on sensors; (2) active smart textiles, reactive sensors to stimuli from the environment, integrating an actuator function and a sensing device; and (3) very smart textiles, which are able to sense, react and adapt their behavior to the given circumstances [96]. pH-sensitive materials are an area of great interest that has recently been explored for the most varied applications. Colorimetric pH-responsive materials are most attractive because they do not require the use of expensive technologies as their lack of electrical components and simple designs do not involve complex equipment or skilled personnel for interpreting the collected data [97]. Halochromism is defined as a reversible color change arising from variations in pH, in which determination of alkaline or acidic conditions are the goal. Nanofiber scaffolds containing halochromic molecules can be defined as halochromic textiles, a subclass of smart textiles that change color depending on environmental pH alterations [98].

pH sensing for healthcare applications, like wound monitoring, requires materials with a high level of biocompatibility, sensitivity, reproducibility of data and stability to mechanical stresses, combined with low-cost fabrication technologies [97]. The application of halochromic textiles for wound dressings is an innovative way to evaluate the progression of the healing process by a pH-sensitive device that does not require removal for monitoring. The surrounding media of a wound, depending on the healing stage, displays different pH values [99]. The pH of chronic wounds has been measured within the range of 7.15-8.90. As the wound progresses towards healing, the pH moves to neutral and then becomes acidic. The normal skin surface exhibits a slightly acidic pH, ranging from 4.0 to 6.0 [56, 100]. These pH changes, accompanied by different colors, make it simpler to assess wound healing without jeopardizing its progression.

The halochromic molecules can be of two origins: natural or synthetic. When it comes to natural molecules, they can be categorized based on origin (vegetable, mineral and animal), the type of color presented (yellow, red, blue, purple, etc.), chemical constitution and application method, while synthetic dyes are simply classified as water-soluble (direct, basic, acid, reactive) and by their *in situ* color formation [101]. Natural origin halochromic molecules are preferable over synthetic since textiles prepared with synthetic halochromic indicators can be harmful to the human body considering their toxic and allergic inherent effects [102].

II.5.1 Anthocyanins

Anthocyanins are naturally occurring, water-soluble, flavonoid pigments, structurally composed by the α-or β-linkage of an anthocyanidin to a sugar moiety, derived from red-colored fruits or vegetable sources and are present in all tissues of higher plants, including leaves, stems, roots and flowers (Figure 5) [103]. These biomolecules have been extensively used, from industrial colorants and health promoting foods to renewable energies [103]. The concentration and chemical structure of anthocyanins vary according to the plant/fruit. According to pH change on the medium, they undergo reversible and irreversible transformations that result in low to high bathochromatic shifts, changing colors from red to purple and red to blue, respectively [56]. Anthocyanins contain a plethora of bioactive compounds, namely polyphenols, that are able to modulate different pathways and processes in our body and display antioxidant, anti-inflammatory, anticancer, glucose-regulating and neuroprotective activities, making them non-harmful for biomedical applications [104]. The stability of anthocyanins depends on the structure of their molecules (glycosylation, hydroxyl groups, acylation), the surrounding elements (pH, sugars, enzymes, co-pigments, metals), and external conditions (temperature, light, oxygen supply) [105].

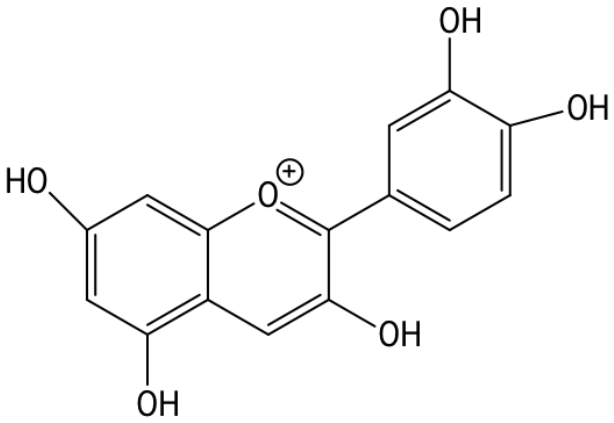


Figure 5 - Anthocyanidin chemical structure. This figure was produced by ChemDraw 12.0 software.

Anthocyanins extracted from plants can be used in the preparation of halochromic nanofibrous mats. However, most publications report only the use of red cabbage-originated anthocyanins for preparing electrospun nanofibrous pH sensors, since they are highly stable and tolerant to heat and light [105]. Red cabbage is grown as a vegetable and is rich in anthocyanin pigment. The anthocyanins in red cabbage are glycosides of anthocyanidin (cyanidin) with two different sugars and acylation with several aromatic acids [105, 106]. The color variation of the red cabbage anthocyanin (RC) extract from red to green/yellow is observed by a stepwise increase in pH from the acidic to the alkaline region (pH 2.0-12.0). At the lowest pH values (pH < 2.0), red dye caused by the flavylium cation is the predominant color. With a slight increase in pH (pH = 2.0-4.0), the color changes towards a purple/blue quinoidal base. Then, the colorless carbinol pseudo-base will become the dominant color by increasing pH from acidic to slightly acidic/near-neutral conditions. Further increase in pH (pH > 7) causes a gradual decrease in anthocyanins stability and generates a green–yellow color as a result of chalcone formation (Figure 6) [107].

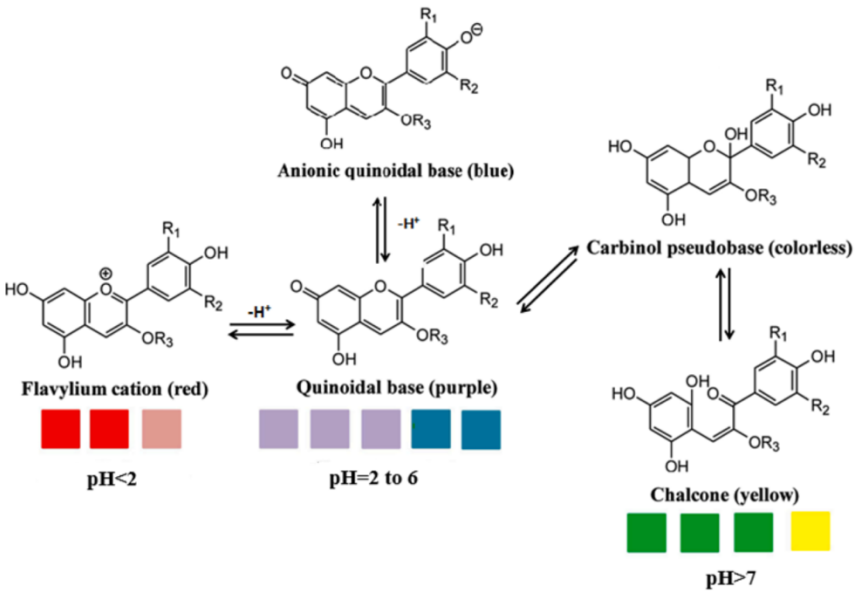


Figure 6 - Representation of the color changes of anthocyanin-rich extracts at different pH values (adapted from [107] with CC BY 4.0 permission).

Anthocyanins derived from red radish represent another versatile class of halochromic pigments beyond red cabbage. Red radish (RR) anthocyanins are typically more acylated, which can enhance their stability under varying pH, light, and heat conditions. Some studies have shown that RR anthocyanins maintain vivid color transitions across acidic to near-neutral pH ranges, making them suitable for incorporation into polymer matrices for pH sensing applications. In fact, *Chayavanich et al.* fabricated a pH-responsive nanofibrous membrane incorporating RR anthocyanin, which changed color in response to pH alterations, demonstrating that red radish extracts can serve as indicators in fibrous sensing platforms [108]. Similarly, purple sweet potato (PSP) is a rich source of anthocyanins that are valued for their high photostability and broad pH responsiveness. These pigments respond to pH changes by shifting hues (from red/pink at acidic pH to violet/blue at near-neutral and greenish/yellow in alkaline), lending themselves to use in colorimetric indicator systems [109].

II.5.2 Extraction, Detection and Quantification Methods

As anthocyanins are frequently found as secondary plant metabolites, it stands to reason that one of the main approaches used in their production is through extraction and isolation from plant tissues. However, the innate characteristics of these matrixes (e.g., uneven compound distribution and high enzymatic activity) may hinder the extraction process, as they can difficult the diffusion of compounds, allow for the simultaneous extraction of other elements and even lead to artifactual

changes in compounds. As such, the selection of an adequate extraction method gains particular relevance. There are many methods for anthocyanin extraction; however, the conventional method of solvent extraction is still considered the most effective and simpler (Table 3) [103].

Commonly used solvents are mainly divided into three categories: water, hydrophilic organic solvents and lipophilic organic solvents. During extraction process, a certain concentration of inorganic or organic acids is usually added to prevent the degradation of anthocyanins during extraction since anthocyanins are unstable in alkaline or neutral solutions. Anthocyanins in plants, food and agricultural samples are extracted with more hydrophilic solvents or with more prominent aqueous-based mixtures, like ethanol/methanol: water mixtures (70-95:30-5), and are usually acidified with hydrochloric acid, formic acid or other organic acids like citric acid [104, 110].

Table 3 - Summary of the most common extraction methods used for anthocyanin extraction [103, 111].

Nature of the method	Method	Definition	Advantages	Disadvantages
Conventional	Solid Liquid Extraction (SLE)	Classic approach is used to recover anthocyanins from plant tissues as their polarity facilitates dissolution into polar solvents (e.g., acidified methanol/ethanol and acetone).	Simple procedure; No need for specific equipment.	Long extraction time; Possibility of anthocyanin degradation upon contact with natural factors (air, light, etc.); High solvent consumption.
Non-conventional	Enzyme-Assisted Extraction (EAE)	Enzymes can be used as their extraction methods by EAE or as additional tools to other extraction processes to increase yields of extraction by weakening the vegetal cell walls and improving their disruptor.	Enzymes are highly selective and efficient; Moderate conditions of pressure and temperature; Environmentally friendly.	High associated costs; High process energy; Enzyme activity is highly dependent on pH, temperature, and nutrient availability; Difficulties in large-scale applications.
	Pulsed Electric Field Extraction (PEFE)	Cell membrane permeabilization technique that breaks down the cell wall of plants using electrical pulses. Application of an electric field of short duration pulses of moderate to high intensity, ranging from 0.1 to 0.3 kV/cm in batch mode and 20–80 kV/cm in continuous mode extraction at room temperature (RT).	Environmentally friendly; Easy to scale-up; Short extraction time (less than 1 s); Low energy and monetary costs.	Some compounds can be affected by high electric fields; Non-uniform distribution of the electric pulses.
	Microwave Assisted Extraction (MAE)	Uses microwaves to quickly, efficiently and evenly heat both solvent and the target tissue. In hydrated tissues, the water present absorbs the	Good reproducibility; Low solvent consumption; Low extraction time.	High temperatures may lead to anthocyanin degradation.

	energy with the resulting heat causing cell disruption.		
Pressurized Liquid Extraction	High pressure is used to maintain the liquid solvents at high temperatures (frequently temperatures above solvent boiling point), which improves the solubility of the compounds, sample wetting and matrix penetration.	Automation; Low extraction time; Low solvent consumption.	High temperatures may lead to anthocyanin degradation.
Supercritical Fluid Extraction (SFE)	Supercritical fluids (at vapor-liquid critical point) are used to extract the components of interest from a solid or even liquid matrix under absence of atmospheric O_2 and light and using pre-treatment of samples with supercritical CO_2 ($scCO_2$) that removes nonpolar components, reducing the amount of interferents.	Reduce exposure to air/light; Purest extract because it allows the removal of non-polar interferents; Inhibition of degrative enzymes.	High associated costs; Only allows the use of polar solvents; Requires CO_2.
Ultrasound Assisted Extraction (UAE)	The ultrasound frequencies are capable of facilitating the hydration of plant materials, which leads to the enlargement of cell wall pores and eventually causes the rupture of the cell wall. This promotes mass transfer, therefore increasing extraction yield.	Low solvent and energy consumption; Easy to scale-up; Safe for consumption of the extract.	High associated costs; Anthocyanin degradation may occur through heat dissipation.

After extraction, it is of interest to use methods to effectively detect the presence of anthocyanins within the extract and quantify their concentration. As a first assessment of the presence of anthocyanins in a given extract, a range of buffer solutions with varying pH is prepared and a specific amount of extract is combined. With this procedure, it is possible to confirm the presence of anthocyanins by following the changing of color of each buffer solution, according to a previously known colorimetric scale. For more accurate analyses, high-performance liquid chromatography (HPLC) can be used, providing high-resolution qualitative and quantitative data from small amounts of samples. Mass spectrometry (LC-MS) is also widely used for qualitative analysis of anthocyanins, being their category identifiable via molecular weight and structure information. To verify the anthocyanins' structure and chemical composition, nuclear magnetic resonance (NMR) spectroscope and other methods such as thin-layer chromatography, UV-visible spectroscopy and infrared spectrometry can be used as well [110]. For anthocyanin quantification, the single pH method, the subtraction method and the pH differential method are usually applied [110].

II.6 Nanoparticles for Biomedical Applications

The nanotechnology field applied to nanomedicine has gained great interest from the scientific community, combining pharmaceutical and biomedical sciences, with the ultimate goal of developing nanosystems with higher efficacy and improved safety and toxicological profiles [112]. However, it is a major challenge and crucial issue to achieve sustained and controlled delivery of active molecules or growth factors in many biomedical areas, including tissue regeneration. To fulfill this requirement, NPs-in-nanofibers (NPs-in-NFs) composites have been widely investigated as potential drug delivery systems for tissue regenerative medicine, wound management and even cancer treatments [113, 114]. NPs can be defined as three-dimensional (3D) structures with diameters ranging from 1 to 1000 nm, although NPs with a size smaller than 100 nm have shown higher efficacy, enhanced patient compliance, better biological distribution and site-specific drug delivery [115, 116]. Their size offers a high surface/volume ratio and correlation with structural sizes of biological components: they are small enough to pass through biological barriers [117], internalize target cells [118], and influence several cellular processes [119]. Some of the main limitations of a drug's delivery efficiency in the human body have to do with the fact that they are rapidly metabolized, sometimes even before reaching their target. The encapsulation method of conventional drugs changed the field of drug delivery systems by offering protection to the drug and, hence, maintaining its pharmaceutical properties. Loaded NPs can protect the cargo from

biodegradation, thus allowing drugs to retain their bioactivity, extending circulation times, enabling their controlled release, and ensuring their efficacy at the target site, requiring smaller doses than if the drugs were to be used in their free, unloaded form [116, 119]. The drug can be encapsulated within the NP core, entrapped in the polymer matrix, chemically conjugated with the polymer or bound to the NP surface.

The production method of different types of NPs depends on their final application. There are three types of NPs classes: lipid-based NPs, inorganic NPs and polymeric NPs (Figure 7). Lipid-based NPs are the most common class of FDA-approved nanomedicines. Usually have spherical forms comprising at least one lipid bilayer surrounding one internal aqueous compartment. As a delivery system, they offer many advantages including formulation simplicity, self-assembly, biocompatibility, high bioavailability, ability to carry large payloads and a range of physicochemical properties that can be controlled to modulate their biological characteristics [119]. The inorganic NPs are composed of inorganic materials such as gold, silver, iron, silica and copper. These are precisely formulated to have a wide variety of sizes, structures, and geometries. This class of NPs have unique physical, electrical, magnetic and optical properties, endowed by the base material they originated from. Organic NPs, templated from natural or synthetic organic molecules, are more easily recognized by the host [116]. Polymeric-based NPs have been particularly explored in medicine, for using natural-based materials in their formulation, avoiding known disadvantages of synthetic compounds such as poor clearance and associated susceptibility to chronic inflammation [120]. The most common forms of polymeric NPs are nanocapsules (cavities surrounded by a polymeric membrane or shell) and nanospheres (solid matrix systems). As drug delivery systems, polymeric NPs are also a great candidate because of their biodegradable, water-soluble, biocompatible and biomimetic profiles associated with great stability during storage. The easy manipulation of their surfaces makes them suitable for target-directed strategies [115, 119, 121].

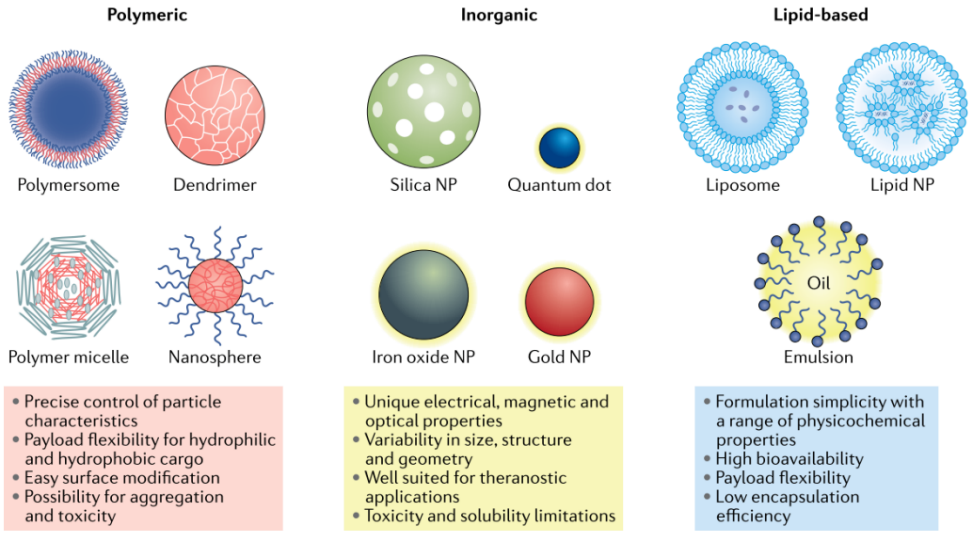


Figure 7 - Classes of NPs (adapted from [119] with CC BY 4.0 permission).

II.6.1 Chitosan coated Nano-lipid Carriers (Ch-NLCs)

Nano-lipid carriers (NLCs) represent a second-generation lipid-based nanocarrier system that was developed to overcome the limitations of solid lipid nanoparticles (SLNs). By blending solid and liquid lipids in their matrix, NLCs reduce crystallinity, improve drug incorporation, and provide more flexible release profiles, making them particularly suitable for poorly soluble or chemically labile compounds [122]. Despite these advantages, conventional NLCs may still encounter issues with colloidal stability, uncontrolled burst release, and quick clearance in biological systems in spite of these benefits. Surface modification with natural polymers has been extensively researched to address these drawbacks, and chitosan has emerged as one of the most promising options [123]. Chitosan, a biopolymer obtained by deacetylation of chitin, is well known for its cationic nature, biodegradability, muco-adhesion, and intrinsic antimicrobial activity. As a coating for NLCs, chitosan offers a protective barrier that stabilizes the lipid core in addition to imparting a positive surface charge that improves electrostatic interactions with negatively charged biological fluids and cellular membranes [124]. Chitosan-coated NLCs (Ch-NLCs) are a dual-action system that functions as a delivery vehicle and a bioactive material. This is achieved by combining the biological functionality of chitosan with the drug-loading and release-controlling benefits of lipid carriers. Several studies have demonstrated that Ch-NLCs exhibit enhanced encapsulation efficiency, improved physical stability during storage, prolonged release of active compounds, and increased penetration across epithelial and dermal barriers compared with uncoated NLCs [125, 126]. In the context of wound healing, these systems are particularly appealing because they can

simultaneously address infection control, inflammation, and tissue regeneration. Chitosan contributes with antimicrobial and antifungal activity that complements the loaded therapeutic agent, while its cationic surface promotes adhesion to the wound bed, retention of the formulation, and hemostatic effects [124, 127]. Moreover, NLCs provide a protective lipid environment for encapsulating sensitive molecules such as essential oils, polyphenols, peptides, or antibiotics, shielding them from degradation and ensuring a controlled local release. For example, recent work on astaxanthin-loaded Ch-NLCs for topical administration demonstrated improved tissue regeneration and antioxidant protection compared with free drug formulations [128]. Similarly, quercetin-loaded NLCs incorporated into chitosan hydrogel beads achieved high encapsulation efficiency (>95 %), prolonged stability, and enhanced permeation, highlighting the versatility of these hybrid systems for skin delivery [127]. According to recent reviews, Ch-NLCs multifunctionality is a result of both their biological performance and physicochemical stability. Chitosan has been demonstrated to stimulate collagen deposition, increase fibroblast proliferation, and modulate inflammatory responses, all of which are essential for wound closure and chronicity prevention. In this sense, Ch-NLCs act on two levels: the encapsulated bioactive combats infection or oxidative stress, while the chitosan coating actively contributes to the wound healing cascade [124]. Compared to traditional nanocarriers, which are frequently passive delivery systems, this dual functionality is a major improvement. Because Ch-NLCs stick to mucosal surfaces and shield medications from enzymatic breakdown, they are also being studied in more general biomedical contexts, such as oral, ocular, and transdermal delivery, in addition to direct wound applications [129, 130]. These studies offer mechanistic insights that can be applied to wound therapy and broaden the platform's potential applicability. However, there are still issues with the formulations' long-term stability, sterilization procedures, and large-scale reproducibility-all of which are crucial for clinical translation and regulatory approval [131]. The integration of Ch-NLCs into advanced wound dressings, such as electrospun fibers, hydrogel matrices, or multilayer patches, is an emerging strategy to enhance their handling, fluid management, and site-specific delivery, moving closer to clinically relevant wound care solutions.

II.7 Essential Oils (EOs) as Nano-lipid Carriers Payloads

Specialized drug delivery systems for treating bacterial and fungal infections have emerged as very promising tools in the war against antibiotic and antifungal resistance. For years, antibiotics were the most effective treatment against one of the biggest causes of death worldwide, systemic

infections, which are caused by a wide spectrum of microorganisms. However, in today's world, these are no longer fully effective solutions in fighting bacterial infections due to the development of resistance by both Gram-positive and Gram-negative bacteria [132]. Because of this concerning situation, there is now more interest in natural products that have inherent antimicrobial activity, especially EOs, which are secondary metabolites that come from plants and are well-known for their broad range of antibacterial, antifungal, antiviral, and antioxidant qualities. Despite extensive research on the powerful antimicrobial properties of EOs like eugenol, carvacrol, thymol, cinnamaldehyde, and tea tree oil, their clinical use has been hindered by their poor solubility, chemical instability, high volatility, and potential irritancy when applied directly to biological tissues [133]. To address these limitations, NLCs have been investigated as effective EOs delivery systems that offer defense against oxidative deterioration, enhance aqueous dispersibility, and permit controlled release at the infection site. By improving local bioavailability and allowing for prolonged exposure of pathogens to the bioactive components, the addition of EOs to NLCs not only improves their physicochemical stability but also amplifies their antimicrobial efficacy [134, 135]. The lipidic environment of the carrier helps to entrap hydrophobic essential oil constituents within its matrix, while the nanoscale size of the system enhances penetration across skin and mucosal barriers. This encapsulation strategy has also been shown to reduce cytotoxic side effects associated with direct application of concentrated essential oils, thereby improving their safety profile for therapeutic use [136, 137]. Several studies highlight the promising role of EO-loaded NLCs in wound healing and infection control. Cinnamaldehyde-loaded lipid nanoparticles, for instance, have demonstrated significant antibacterial activity against resistant *Staphylococcus aureus* strains while simultaneously modulating inflammatory pathways and accelerating tissue repair [138]. Similarly, carvacrol and thymol-loaded NLCs have been shown to improve drug retention in infected wounds and achieve synergistic antimicrobial activity when combined with conventional antibiotics [139]. Eugenol incorporated into NLCs have also exhibited prolonged antifungal activity against *Candida* species, which is particularly relevant for immunocompromised patients where fungal infections contribute significantly to wound chronicity [140]. EO-loaded NLCs have the potential to directly support tissue regeneration in addition to infection control. Numerous essential oils have antioxidant and anti-inflammatory properties that promote collagen synthesis and fibroblast proliferation while reducing oxidative stress at wound sites. These bioactive molecules can be embedded into NLCs to create multipurpose wound healing platforms that can target the microbial burden, lower inflammation, and promote repair mechanisms all at once. This multifunctionality is

becoming more widely acknowledged as a crucial pre-requisite for advanced wound therapies, particularly in diabetic and chronic wounds where dysregulated inflammatory responses and persistent infection frequently impede healing [141, 142]. Despite these promising findings, challenges remain for the translation of EO-loaded NLCs into clinical practice. Variability in essential oil composition depending on plant origin, extraction method, and seasonal factors can influence reproducibility and therapeutic consistency. Additionally, large-scale manufacturing, regulatory approval, and long-term stability of EO formulations must be addressed [143, 144]. However, growing evidence supports the potential of EO-loaded NLCs as a natural and sustainable alternative to conventional antimicrobial and antifungals, with the dual benefit of combating microbial resistance and promoting wound healing in complex clinical scenarios.

II.7.1 Cinnamaldehyde Essential Oil

Cinnamaldehyde (CN), the major bioactive component of cinnamon essential oil, has attracted attention as a payload in nano-lipid carriers due to its broad-spectrum antifungal and antibacterial activity, anti-inflammatory effects, and wound healing potential. It promotes wound healing by boosting blood vessel formation, reducing inflammation, and fighting infection. The healing process is accelerated by promoting angiogenesis, alleviating bacterial and fungal infections, and improving the skin's inflammatory response [145, 146]. When it comes to drug delivery, loading cinnamaldehyde into NLCs (or related lipid-based nanocarriers) offers several advantages: (i) the lipid matrix provides a hydrophobic environment suited to entrapment of CN and reduces volatilization or oxidative degradation; (ii) the nanoscale size enables improved permeation into tissues or across epidermal barriers; (iii) controlled release from the lipid core can sustain antifungal exposure over time, avoiding burst effects and reducing cytotoxicity; and (iv) biocompatibility of lipid excipients helps to mitigate irritation when applied to delicate or damaged tissues [147, 148]. In terms of wound healing and support of tissue repair, cinnamaldehyde has demonstrated anti-inflammatory, immunomodulatory, and pro-regenerative effects. For instance, in a murine skin-infection model, topical CN treatment reduced bacterial loads, suppressed pro-inflammatory cytokines (e.g. TNF-α, IL-6), decreased neutrophil infiltration, and accelerated re-epithelialization and collagen deposition in wounds contaminated with *S. aureus* [149]. Moreover, a cinnamaldehyde-based self-nanoemulsifying drug delivery system (CN-SNEDDS) applied to third-degree skin burns in rats significantly accelerated wound contraction, increased antioxidant enzyme activity, decreased inflammatory markers and microbial load compared to controls, indicating

beneficial interaction between the antimicrobial, antioxidant, and anti-inflammatory actions of CN in a wound scenario [150].

CHAPTER III

Polycaprolactone/polyethylene glycol electrospun mats with pH-responsiveness for real-time sensing in chronic wound healing

CHAPTER III – POLYCAPROLACTONE/POLYETHYLENE GLYCOL ELECTROSPUN MATS WITH PH-RESPONSIVENESS FOR REAL-TIME SENSING IN CHRONIC WOUND HEALING

Abstract

Constant monitoring of the healing process is crucial to prevent wound chronicity. In this study, we developed pH-responsive nanofibrous mats by incorporating anthocyanins extracted from red cabbage, red radish, and purple sweet potato into polycaprolactone (PCL)/polyethylene glycol (PEG) blends at 100:0, 90:10, and 80:20 v/v ratios via electrospinning. The natural extracts were characterized for phenolic content, antioxidant capacity, and halochromic response within pH 4.0–10.0, with red radish extract showing the highest color sensitivity and stability. Incorporation of PEG improved fiber morphology and hydrophilicity, with the 90:10 PCL/PEG ratio providing the optimal balance between mechanical strength and color response. Mats loaded with 5 mg/mL red radish extract exhibited a clear color shift from pink (pH 4.0–6.0) to purple/blue (pH 7.0–9.0) and green (pH ≥ 10.0), enabling straightforward visual discrimination across physiologically relevant pH ranges. Cytocompatibility assays indicated >80% cell viability, and antioxidant activity reached ≈50 %, suggesting additional therapeutic potential. These findings highlight the potential of the developed mats as wound dressings capable of real-time pH monitoring and supporting a more informed approach to wound management.

This chapter is based on the following scientific publication:

- Ana R. M. Ribeiro, Ana Isabel Barbosa, Maria Celeiro, Marta Lores, Catarina L. Seabra, Salette Reis, Helena P. Felgueiras, "Polycaprolactone/polyethylene glycol electrospun mats with pH-responsiveness for real-time sensing in chronic wound healing". Reactive and Functional Polymers, 222, 2026, https://doi.org/10.1016/j.reactfunctpolym.2026.106692.

III.1 Introduction

Monitoring wound healing through pH grading is a valuable and clinically relevant strategy, as variations in pH provide critical information about the wound microenvironment. Healthy skin typically exhibits an acidic pH between 4.0 and 6.0, which contributes to barrier function and protection against microbial colonization. During the healing process, however, wound pH often shifts toward more alkaline values (pH 7.0-8.0), particularly in the presence of inflammation or bacterial and/or fungal infection [151, 152]. A persistently alkaline environment is frequently associated with delayed healing and chronic wound formation, whereas a gradual return to acidic conditions is indicative of tissue regeneration and recovery. Therefore, non-invasive monitoring of wound pH can support early diagnosis of complications and guide timely therapeutic interventions, ultimately improving healing outcomes [153].

In this context, electrospinning has emerged as a highly suitable technique for the development of advanced wound dressings, owing to its cost-effectiveness, scalability, and high processing efficiency [154, 155]. This technique enables the fabrication of nanofibrous structures with tunable composition and morphology, providing high surface-area-to-volume ratios and structural versatility for biomedical applications [156, 157]. Importantly, electrospun fibers can mimic the architecture of the natural extracellular matrix (ECM), promoting cell adhesion, proliferation, and differentiation, which are essential for effective wound repair [158].

Among commonly used polymers, polycaprolactone (PCL) offers excellent mechanical stability and biocompatibility, while polyethylene glycol (PEG) contributes with biodegradability, non-toxicity, and enhanced hydrophilicity. The combination of these polymers allows the design of scaffolds with complementary mechanical and physicochemical properties, suitable for wound healing applications [159–161].

Anthocyanins are naturally occurring, water-soluble pigments belonging to the flavonoid family and are widely present in red and purple fruits and vegetables. Structurally composed of an anthocyanidin core linked to sugar moieties, anthocyanins exhibit pH-dependent structural transformations that result in visually perceptible color changes, typically transitioning from red under acidic conditions to purple or blue at neutral-to-alkaline pH [162] [163]. In addition to their halochromic behavior, anthocyanins are known for their antioxidant and anti-inflammatory properties, which may provide added benefits in wound healing environments [164]. The integration of pH-responsive molecules into electrospun matrices therefore represents a promising strategy for developing wound dressings capable of sensing and reporting physiological changes

during healing. Such systems enable real-time monitoring of wound status and facilitate clinical decision-making without the need for invasive procedures [165].

The novelty of the present work lies in the development of intrinsically halochromic electrospun mats based on PCL/PEG blends incorporating naturally derived anthocyanin-rich extracts (red cabbage, red radish, and purple sweet potato) for wound monitoring applications. While PCL ensures mechanical integrity and structural stability, PEG enhances hydrophilicity and porosity, favoring fluid exchange and improving the responsiveness of colorimetric transitions. Unlike many previously reported systems that rely on post-functionalization steps, synthetic dyes or drug-delivery-based approaches, this study adopts a single-step blending immobilization strategy, enabling the direct incorporation of natural halochromic compounds into the electrospun fibers. The resulting materials were characterized in terms of morphology, mechanical performance, physicochemical properties, cytocompatibility, antioxidant activity, and pH responsiveness. This sustainable and simplified approach, still poorly explored in the literature, provides a biocompatible and biodegradable platform for visual pH monitoring across a physiologically relevant range (pH 4.0–10.0), offering a promising alternative to conventional dressings for the management and monitoring of chronic wounds.

III.2 Materials and Methods

III.2.1 Materials

PCL (Mw 80.000) was purchased from PolySciences, Inc. (Valley Road, Warrington, USA), while PEG (Mw 20.000) was acquired from Sigma-Aldrich (Germany). All three natural extracts (red cabbage, red radish, purple sweet potato) were purchased in powder form from Yunnan Tonghai Yang Natural Products Co., Ltd (Yunnan Province, China). Chloroform (CHF) and dimethylformamide (DMF) were obtained from Riedel-de-Haen (Seelze, Germany) and PanReac AppliChem (Barcelona, Spain), respectively. Folin-Ciocalteu reagent, gallic acid, 2,2-Diphenyl-1-picrylhydrazyl (DPPH) and 6-Hydroxy-2,5,7,8-tetramethylchroman-2-carboxylic acid (Trolox) were purchased from Sigma-Aldrich (Germany). Sodium carbonate (Na_2CO_3) was purchased from Riedel-de Haën, Germany. Dimethyl sulfoxide (DMSO) and ethanol (99.8 %) were purchased from Fisher Scientific (United Kingdom). Polyphenols (3,4-dihydroxybenzoic acid, chlorogenic acid, caffeic acid, p-coumaric acid, trans-ferulic acid, kaempferol-O-glucoside) and anthocyanidins (delphinidin, cyanidin, pelargonidin) standards were purchased for Sigma-Aldrich (Steinheim, Germany). Mass grade water and methanol, formic acid and hydrochloric acid were obtained from Scharlau

(Barcelona, Spain). *Candida albicans*, C. *parapsilosis* and *C. tropicalis* were supplied by American Type Culture Collection (ATCC, Virginia, USA). For fungi growth, Sabouraud Dextrose Agar (SDA) and Sabouraud Dextrose Broth (SDB) were purchased from HiMedia Laboratories (India). Mouse fibroblast cell line (L929) was purchased from the European Collection of Authenticated Cell Cultures (ECACC, Salisbury, UK) and the human keratinocytes cell line (HaCaT) was purchased from Cell Lines Service GmbH (CLS, Eppelheim, Germany). Dulbecco's Modified Eagle Medium (DMEM, L-Glutamine) was purchased to Avantor VWR (Radnor, Pennsylvania, USA); Penicillin-streptomycin (10,000 U/mL), Trypsin-EDTA (0.25 % w/v) were purchased from Gibco Life Technologies (California, USA); Fetal Bovine Serum (FBS) was purchased from Biowest (Missouri, USA); and Trypan blue, Sodium resazurin, Triton X-100 were purchased from Sigma-Aldrich (St.Louis, Missouri, USA). The phosphate-buffered saline (PBS) used at 0.01 M was prepared at pH 7.4 from the combination of sodium chloride (NaCl; 8.00 g/L), potassium chloride (KCl; 0.20 g/L), sodium phosphate dibasic (Na_2HPO_4; 1.44 g/L) and monopotassium phosphate (KH_2PO_4; 0.24 g/L), all obtained from Sigma-Aldrich. Reagents were all used as commercially available, without additional chemical modifications. For clarity, the three natural extracts will hereafter be referred to as Red Cabbage (RC), Red Radish (RR), and Purple Sweet Potato (PSP).

III.2.2 Natural Halochromic Extracts Properties

III.2.2.1 Visual pH grading

The visual halochromic response of natural extracts to a range of Britton-Robinson buffer solutions with pH from 4.0 to 10.0 was carried out by adding 1 mL of aqueous extract solution at a concentration of 5 mg/mL (w/v) to 5 mL of buffer solution. The pH grading (visible color change) was recorded using an iPhone 14 Pro at 1× magnification and 10 cm distance from the sample.

III.2.2.2 Chemical Composition through LC-MS/MS

The quantification of the polyphenols and anthocyanidins present in the extracts was performed by LC-MS/MS using a Thermo Scientific (San Jose, CA, USA) instrument based on a TSQ Quantum Ultra™ triple quadrupole mass spectrometer equipped with a heated electrospray ionization (HESI) source, and an Accela Open autosampler with a 20 μL loop. For polyphenols, extracts were filtered through 0.22 μm polytetrafluoroethylene (PTFE) filters and directly injected into the LC-MS/MS system. For the determination of anthocyanidins, a previous acid hydrolysis (90 min at 100 °C in 10 % hydrochloric acid aqueous solution) was performed to release the free anthocyanidins from

the extract. Optimal instrumental conditions were previously optimized [166]. The chromatographic separation was performed employing a Kinetex C18 column (100 mm × 2.1 mm × 100 Å) obtained from Phenomenex (Torrance, CA, USA). The mobile phase was composed of water (A) and methanol (B), both with 0.1% formic acid. The eluted gradient started with 5% of B (held 5 min), it was increased to 90% of B in 11 min and kept constant for 3 min. Finally, initial conditions were reached in 9 min. The total run time was 20 minutes. Injection volume was 10 μL, with a flow rate of 0.2 mL min−1, and column temperature was set at 50 °C. Compound identification and detection were performed in Selected Reaction Monitoring (SRM) mode working simultaneously in negative and positive mode, monitoring two or three MS/MS transitions for each compound (see Table SD21 on Supporting Information). The MS/MS parameters for all studied compounds were optimized by individual direct infusion, and the most abundant collision-induced fragments were considered for quantification. Other HESI source parameters were the spray voltage: 3000 V, vaporizer temperature: 350 °C, sheath gas pressure: 35 au (arbitrary units), and ion sweep and auxiliar gas pressure: 0 and 10 au, respectively, and the capillary temperature: 320 °C. The system was operated by Xcalibur 2.2. and Trace Finder 3.1. software. The free radical scavenging activity of natural extracts were determined using the DPPH assay adapted for a 48-well plate. For this, 10 μL (diluted natural extracts) were incubated in 150 μL of DPPH stock solution (100 μM, 98 % EtOH), respectively, for 1, 2, 4, 6 and 24 h. The absorbance was measured in the respective time-points at 517 nm with a microplate reader (BioTek, SYNERGY H1M2, UK), to ensure that the reaction was completed (plateau state). The same DPPH solution was used as a negative control, and Trolox was used as a positive control and chemical reference for comparison. All measurements were made in triplicate. The results were expressed in terms of the percentage of reduced DPPH at steady state (% DPPHr) and were calculated following Eq. 1:

$$DPPHr\ (\%) = \frac{A_i - A_r}{A_i} \times 100 \qquad \text{Equation 1,}$$

in which A_r was the absorbance registered at steady state, and A_i was the initial absorbance registered at time 0 h.

The total content of phenolic compounds (TPC) was determined using an adaptation of the Folin-Ciocalteu method [167]. 2 μL of extract (1 mg/mL) dissolved in DMSO were combined with 10 μL of Folin's reagent and 120 μL of dH_2O, in the dark. The mixture was homogenized and further combined with 40 μL of Na_2CO_3 at 15 % (w/v) and 28 μL of dH_2O. After further homogenization, the microplate was kept in the dark for 2 h at room temperature (RT). Absorbance

was then measured at 750 nm (BioTek, SYNERGY H1M2, UK). The amount of phenolics was calculated using a standard gallic acid calibration curve and using DMSO as a negative control. Results were expressed in mg of gallic acid equivalents (GAE)/g of sample dry weight (mg GAE/g extract). TPC was determined using Eq. 2:

$$TPC = C_{GA} \times \frac{V}{m} \qquad \text{Equation 2,}$$

where CGA corresponds to the concentration of gallic acid obtained from the calibration curve (mg/mL), V represents the extract volume (mL), and m corresponds to the mass of the extract (g).

III.2.2.3 Minimum Inhibitory Concentration (MIC) and Minimum Fungicidal Concentration (MFC)

The natural extracts minimum inhibitory concentrations (MICs) and minimum fungicidal concentrations (MFCs) were determined using the broth microdilution method described by Wiegand et al. [168], which is an adaptation of the standard published by the Clinical and Laboratory Standards Institute (CLSI) and the European Committee on Antimicrobial Susceptibility Testing (EUCAST) [169]. Fungi inoculums were prepared from a single colony of *C. albicans*, *C. parapsilosis* and *C. tropicalis* and incubated overnight at RT and 150 rpm, in aerobic conditions in SDB broth. Tests were carried out using an initial concentration of ≈ 1.0 $\times 10^6$ CFUs/mL in SDB. Working solutions of 20.48 mg/mL were prepared for each natural extract in dH_2O. These were added to the first column of 96-well plates in a volume of 100 µL. Serial dilutions (1:2) were made with SDB in the consecutive wells, to a final volume of 50 µL. Then, to each of these wells, 50 µL of the fungi suspensions were added. Fungi suspensions and culture media were also used as controls. Absorbance readings at the wavelength of 640 nm (EZ READ 2000 Microplate Reader, Biochrom, UK) were made before and after plate incubation for 24 h at RT and 150 rpm. The MIC for each natural extract/fungi combination was established as the concentration at which fungi did not show any growth, determined visually and confirmed by differences in absorbance readings (between 0 and 24 h). The MFC were established by culturing the fungi suspensions at MIC (if identified) and the concentrations at its vicinity (concentration higher and lower than MIC value) and counting the number of grown colonies. Briefly, aliquots of 10 µL of each of these cell suspensions, diluted from 10^{-1} to 10^{-4} in PBS, were cultured in SDA for 48 h at 28 °C. The absence of colonies established the MFC. The 24-hour incubation period for MIC determination was selected to allow sufficient time for fungal cells to undergo at least one complete growth cycle under

standard conditions, enabling accurate detection of growth inhibition by the extracts. In contrast, MFC determinations were performed after a 48-hour incubation to ensure that any surviving fungal cells, including those in a lag phase or with slower metabolic activity, could be detected. This extended incubation period provides a more reliable assessment of the fungicidal potential of the extracts by confirming the absence of viable colonies.

III.2.2.4 Cell Culture Conditions and Viability Assessment

The cytocompatibility of the three natural extracts towards mouse fibroblast cell line (L929) and human keratinocytes cell line (HaCaT) were evaluated using direct contact assay. The murine fibroblast cell line (L929) and the human keratinocyte cell line (HaCaT) were selected to ensure a comprehensive assessment of the cytocompatibility of the developed materials. L929 cells are widely accepted as a reference model in preliminary biocompatibility evaluations, in accordance with ISO 10993-5 standards, due to their reproducibility and sensitivity in detecting cytotoxic responses. Conversely, HaCaT cells provide a more clinically relevant model, reflecting the physiological behavior of human skin cells and enabling a translational evaluation of potential cutaneous interactions. The combined use of these cell lines strengthens the reliability and applicability of the biological performance data for chronic wound healing applications. The cytocompatibility testing (metabolic activity) was performed according to the international standard ISO 10993-5:2009. Cells were thawed and sub-cultured in DMEM medium supplemented with 10 % (v/v) heat inactivated FBS and 1 % (v/v) penicillin-streptomycin, at 37 °C in a humidified atmosphere of 5 % CO_2, until reaching 90 % confluence. Thereafter, cells were chemically detached from cell culture flasks using trypsin-EDTA at 0.25 % (w/v). The number of cells was determined using a Neubauer Chamber, labelling cells with trypan blue (ratio 1:1 v/v) and cells were counted using a Motic® Inverted Microscope (Motic, Barcelona, Spain). Cells were seeded in 96-well tissue culture polystyrene (TCPS, VWR®, Pennsylvania USA) plates, at the density of 4×10^4 cells per well and incubated for 24 h at 37 °C in a humidified atmosphere of 5 % CO_2. The experiments were performed using fibroblast-like cells in passage 18–23 and keratinocytes cell line in passage 32–365. After 24 h of incubation, the metabolic activity of the cells was evaluated by resazurin staining. Briefly, 0.01 mg/mL of sodium resazurin in complete DMEM was added to the wells containing the natural extracts and incubated for 2 h at 37 °C and 5 % CO_2 atmosphere. Afterwards, 100 µL of supernatant were transferred to a black 96-well plate (Falcon®, Arizona, USA) and the fluorescence was measured (λ_{ex} = 560 and λ_{em} = 590 nm) using a microplate fluorometer (Cytation

5 Cell Imaging Reader - BioTek Instruments, Vermont, USA). The percentage of metabolic activity was evaluated by Eq. 3 as an indicator of cells viability:

$$Metabolic\ activity\ (\%) = \frac{Flu_s - Flu_{nc}}{Flu_{pc} - Flu_{nc}} \times 100 \qquad \text{Equation 3,}$$

where the Flu_s is the fluorescence of the samples, Flu_{nc} is the fluorescence of the negative control cells treated with 2 % (v/v) Triton X-100 solution, and Flu_{pc} is the fluorescence of the positive control cells treated only with DMEM.

III.2.3 Production of Electrospun Mats

Separated polymeric solutions of PCL/PEG were prepared at 14 % and 10 % (w/v) respectively, in CHF/DMF (9:1 v/v). These solutions were continuously stirred at 50 °C for 4 h and 1 h, respectively. PCL and PEG were combined at varying ratios: 100/0 (also labeled as 100PCL), 90:10 and 80:20 (v/v). Their viscosity was assessed using a viscometer Brookfield DV-II + Pro (spindle 21, 50 rpm at RT during 5 min, with 30 s time points), while their conductivity was determined using a Thermo Scientific Benchtop Meter (Orion Versa Star Pro). Electrospinning was conducted with a fixated voltage of 12 kV applied to the steel capillary needle with an inner diameter of 18 Gauge (G). The distance between the needle tip and the aluminum collector was 17 cm. The solution feeding rate was set at 0.7 mL/h. RT and relative humidity (RH) were controlled and maintained at 20–22 °C and 65–70%, respectively. After production, electrospun mats were stored in a desiccator.

III.2.4 Immobilization of Halochromic Extracts

Solutions of natural extracts were prepared at varying concentrations (2.5-25.0 mg/mL (w/v) and directly blended into polymeric solutions of 100:0, 90:10, and 80:20 PCL/PEG (v/v). Based on the polymer ratio, each extract was pre-dissolved in 2.0, 1.8, and 1.6 mL of DMF, respectively, before being incorporated into the final solution without compromising the final polymer concentration. The mixtures were stirred at 150 rpm at RT overnight to ensure homogeneity. Visual confirmation of the color change according with different Britton-Robinson buffers pH (4.0 - 10.0) on the immobilized mats were carried out by adding 100 μL of each buffer solution directly into the electrospun mats. The pH grading (visible color change) was recorded using an iPhone 14 Pro at 1× magnification and 10 cm distance from the sample.

III.2.5 Characterization of Loaded and Unloaded Electrospun Mats

III.2.5.1 Field Emission Gun Scanning Electron Microscopy (FEG-SEM)

Micrographs (NOVA 200 Nano SEM, FEI Company) were collected with an accelerating voltage of 10 kV. Mats were initially coated with a thin film (10 nm) of Au-Pd (80-20 wt.%) using a 208HR high-resolution sputter coater (Cressington Company, Watford WD19 4BX, UK) coupled to an MTM-20 Cressington High-Resolution Thickness Controller. The average fiber diameter of the loaded and unloaded electrospun mats were determined by conducting 100 fiber measurements on three micrographs of each PCL and PCL/PEG ratios with and without extracts, at a magnitude of 50.000 ×, simulating the diameter distribution with a log-normal function. Images were processed using the ImageJ® software (version 1.53a, National Institutes of Health, USA). The porosity of the mats was analyzed using the same ImageJ® software and methodology as reported in [170].

III.2.5.2 Fourier-transform Infrared Spectroscopy in Attenuated Total Reflectance Mode (ATR-FTIR)

To identify the chemical groups presented on the loaded and unloaded PCL and PCL/PEG mats, ATR-FTIR spectra were collected using an IRAffinity-1S, SHIMADZU spectrophotometer (Kyoto, Japan), with a diamond crystal, applied at a spectral resolution of 4 cm^{-1}, for 200 scans, over a range of 4000–400 cm^{-1}.

III.2.5.3 Thermal Gravimetric Analysis (TGA)

The electrospun mats thermal degradation behavior was assessed by weight loss monitoring with increasing temperature in the range of 25-600 °C, at a heating rate of 10 °C/min under a dynamic nitrogen atmosphere and flow rate of 200 mL/min (inert environment) on a STA 7200 Hitachi® (Fukuoka, Japan), using aluminum pans. The initial mass of each sample was 5 ± 2 mg. Results were plotted as percentage of Weight Loss vs temperature.

III.2.5.4 Differential Scanning Calorimetry (DSC)

Thermal properties were also evaluated using a DSC 822 Mettler Toledo (Columbus, USA). Samples were submitted to a first heating step (25-500 °C) (to remove absorbed and adsorbed water), followed by cooling and then to a second heating step from 0 to 250 °C at a rate of 10

°C/min, under a dynamic nitrogen atmosphere, and flow rate of 20 mL/min (inert environment). DSC curves were plotted with Heat flow vs. Temperature.

III.2.5.5 Mechanical Testing

Elongations at break and breaking strength of the anthocyanin loaded and unloaded electrospun mats were measured using a uniaxial tensile test. Samples were prepared with dimensions 1 × 3 cm. The gauge length was set to 25 mm. Hounsfield Universal Testing Machine (Hounsfield UTM) with a 250 N load cell was used to run the tensile test at RT applying displacement rates of 10 mm/min. Prior to testing, a low tare load was applied to establish a consistent zero position. Three experiments were conducted.

III.2.5.6 Wettability and Surface Free Energy (SFE)

Water contact angle (WCA) measurements were conducted in a Contact Angle OCA 200, Data Physics apparatus (Filderstadt, Germany) connected to a video-based drop shape analyzer OCA15 plus software (version 1.2), following the standard ASTM-D7334–08. Droplets of 5 μL of ultrapure water at a velocity of 5 μL/s were used to evaluate the electrospun mats wettability via the sessile drop measuring method. Five measurements were performed per type of sample. Angles were recorded immediately after the droplet contacted with the surface. In turn, the surface free energy (SFE) was calculated based on the angles obtained with ultrapure water (polar solvent), ethylene glycol (nonpolar solvent) and diiodomethane (nonpolar solvent) using 5 μL drops (solvent information in Table 4). Once again 5 measurements were carried out on the surface of the samples at 22-23 °C and relative humidity of ≈ 50 %, for each liquid and sample type. The Owens and Wendt method was used to calculate the SFE (Eq. 4):

$$\frac{\gamma(1+\cos\theta)}{2\sqrt{\gamma^d}} = \sqrt{\gamma s^{p^*}}\left(\frac{\sqrt{\gamma^p}}{\gamma^d}\right) + \sqrt{\gamma s^d} \qquad \text{Equation 4,}$$

where γ is the total surface tension of the sample liquid with dispersive γd and polar γp components, and γs is the surface free energy of a solid with dispersive γsd and polar γsp components. θ is the contact angle between the liquid and solid surface of the sample (average of 5 measurements).

Table 4 - Surface tension (γt) and dispersive (γd) and polar (γp) components for determining SFE, using the solvents: ultrapure water, ethylene glycol, and diiodomethane [167].

Liquid	γ^d (mN/m)	γ^p (mN/m)	γ^t (mN/m)
Ultrapure water	21.8	51.0	72.8
Ethylene glycol	29.0	19.0	48.0
Diiodomethane	50.8	0.0	50.8

III.2.5.7 *In-vitro* Swelling and Degradation

Samples of 11 mm of diameter were cut and dried overnight at 37 °C for complete elimination of residual water molecules. Posteriorly, they were weighted (m_d in mg) and incubated in 1 mL of PBS 0.01 M (PBS, pH 7.4) at 37 °C for 1, 2, 4, 6, 24, 48, 72, 120 and 168 h under static conditions. At each specified interval, samples were collected, the excess of solution removed, and the wet weight measured (m_w). The degree of swelling (%) was determined using the following Eq. 5:

$$DS\ (\%) = \frac{(m_w - m_d)}{md} \times 100 \qquad \text{Equation 5,}$$

where m_w (mg) is the weight of the fibers after sample immersion and m_d (mg) is the weight of the dried fibers before immersion.

Degradation profile was also assessed in PBS by incubating 11 mm samples of each type of mat, at 37 °C for up to 7 days. After 7 days of incubation, samples were weighted. Mass loss was determined using the following Eq. 6 [171]:

$$mass\ loss\ (\%) = \frac{mi - mf}{mi} \times 100 \qquad \text{Equation 6,}$$

in which mi (mg) represents the weight of the hydrated mats at time 0 h (mats were initially hydrated for 1 h in dH_2O, until saturation) and mf (mg) corresponds to the mats weight after each incubation period.

III.2.5.7 Permeabilities

To assess the electrospun mats capacity for air exchange and moisture retention, air and water/vapor permeability studies were conducted according to BS 7209:1990 and ASTM D 737–

96. In the first, air pressure of 100 Pa was applied on three samples of each polymer ratio, selected transversely along the mats, and the permeability was measured. On the water vapor permeability (WVP) examination, samples were placed on top of cylindrical cups containing 46 mL of dH_2O for 24 h. The evaporation of water through the test membrane was determined by weighing the cup before and after the testing period. Examinations were performed at 37 °C and 65 % RH. An open cup was used as reference. Measurements were conducted in triplicate. The water vapor transmission rate (WVTR) and the WVP index (I) were determined using Eq. 7 and 8:

$$WVTR = \frac{24\Delta W}{A\Delta t} \qquad \text{Equation 7,}$$

$$I = \frac{WVP_s}{WVP_r} \times 100 \qquad \text{Equation 8,}$$

where ΔW is the difference in the water weight (g) before and after the 24 h test, A is the inner area of the cup (mm), Δt is the exposure time (h), WVP_s is the water vapor permeability of the samples and WVP_r is the water vapor permeability of reference (a cup without any sample on top, mimicking a wound without cover and completely exposed to the surrounding environment). The experiment was performed in triplicate.

III.2.5.8 Diffuse Reflectance Spectroscopy

The chromatic attributes of the loaded electrospun mats were quantified utilizing a Konica Minolta CM-2600d (Konica Minolta, Chiyoda, Japan) diffuse fibre optic reflectance spectrophotometer, in the range between 400 and 700 nm, at standard illuminate D65 (LAV/Spec. Incl., d/8, D65/10°). Three areas on each sample were measured in various positions, and the results presented as average values with up to 1% variation. The responses analysed were the colour characteristics: K/S, L*, a*, b*. K/S is the colour strength calculated using Kubelka-Munk's equation ($K/S = (1-R)^2/2 \times R$, where R is the reflectance). L*, a*, and b* are the coordinates of the colour in the cylindrical colour space, based on the theory that colour is perceived by black white (L*, lightness), red-green (a*), and yellow-blue (b*) sensations. The lightness, L*, represents the darkest black at L* = 0 and the brightest white at L* = 100. The colour channels, a* and b*, represent true neutral grey values at a* = 0 and b* = 0. The red/green opponent colors are represented along the a* axis, with green at negative a* values and red at positive a* values. The yellow/blue opponent colours are represented along the b* axis, with blue at negative b* values and yellow at positive b* values [172].

III.2.6 Mats Antioxidant Activity

The free radical scavenging activity of electrospun mats immobilized with the natural extracts were determined using the DPPH assay adapted for a 48-well plate as mentioned on 2.2.3 section on a 1 × 1 cm sample.

III.2.7 Immobilized Electrospun Mats Cytocompatibility Testing

III.2.7.1 Cell Culture Conditions and Cell Viability Assessment

The cytocompatibility of electrospun mats typologies towards mouse fibroblast cell line (L929) and human keratinocytes cell line (HaCaT) were evaluated using direct contact assay as described on section 2.2.5.

III.2.8 Statistical Analysis

Data was treated using GraphPad Prism Software (v10.2.1, GraphPad Software Inc., USA). All assays were conducted three or more times and data was expressed as mean ± standard deviation (SD). Statistically significant was determined as having $p < 0.05$.

III.3 Results and Discussion

III.3.1 Natural Extracts Characterization

Three natural-origin halochromic extracts were analyzed for their color grading in contact with solutions with a 4.0-10.0 range of pH, , chemical profile, total phenolic compound (TPC), antifungal activities, antioxidant activity and cellular viability. On the other hand, the pH sensitivity of the three natural halochromic extracts was clearly demonstrated through distinct and visually perceptible color transitions across a pH range from 4.0 to 10.0 (Figure 8). All extracts showed gradual changes in hue, indicating their potential for use as natural pH indicators. Among them, PSP exhibited the most pronounced and vibrant color shifts, ranging from pink at acidic pH to deep blue under alkaline conditions. Similarly, RC and RR also displayed color changes, although the transitions between pH in RR were less intense. These results confirm that these anthocyanin-rich extracts are highly responsive to pH variations, with color changes driven by structural transformations in anthocyanin molecules [173]. Anthocyanins exist in different ionic forms depending on the pH of the medium: at acidic pH they are predominantly present as flavylium cations, responsible for the red to pink coloration, whereas at neutral to alkaline pH they undergo

hydration, tautomerization, and subsequent deprotonation steps leading to the formation of quinoidal bases (purple/blue) and, at higher pH values, chalcone forms (yellowish tones). This dynamic equilibrium explains the progressive and visually distinct color changes observed in Figure 8 [174] This property highlights their applicability in diagnostic tools where visual pH detection is desired.



Figure 8 - Visual color grading of the three natural halochromic extracts at concentration of 5 mg/mL (RC, RR and PSP) in contact with pH solutions ranging from 4.0 to 10.0 (left to right).

The chemical composition of the three natural extracts was assessed by LC-MS/MS, and results are summarized in Table 5. The analysis revealed distinct phenolic and anthocyanidin profiles, highlighting the diversity of bioactive molecules naturally present in these halochromic sources. PSP showed high levels of chlorogenic acid (119.0 ± 2.0 mg/kg), a compound widely associated with antioxidant and anti-inflammatory activity, while also containing *p*-coumaric acid [175, 176]. RC was found to be particularly rich in *p*-coumaric acid (162.0 ± 2.0 mg/kg) and cyanidin (19,699.0 ± 384.0 mg/kg), consistent with its well-documented pigmentation with the intense radish coloration at low pH and the lighter tones observed as pH increases, and antioxidant potential [177–179]. RR, on the other hand, displayed a more complex profile of hydroxycinnamic

acids, including caffeic (25.0 ± 1.0 mg/kg), *p*-coumaric (146.0 ± 11.0 mg/kg), sinapic (61.0 ± 2.0 mg/kg) and trans-ferulic acid (895.0 ± 8.0 mg/kg) that may contribute to color stabilization through co-pigmentation effects, further modulating the visible response. Interestingly, RR also exhibited an exceptionally high concentration of pelargonidin (209,920.0 ± 1,498.0 mg/kg), which is strongly linked to intense red coloration and robust halochromic behavior [180, 181]. These compositional differences provide a clear validation for the distinct color transitions observed among the extracts when exposed to different pH conditions. The predominance of cyanidin in RC and pelargonidin in RR suggests variable sensitivity to pH shifts, while the abundance of phenolic acids across all extracts contributes to additional antioxidant protection [182, 183]. Together, these results corroborate that the colorimetric performance of the extracts is a direct consequence of the structural re-arrangements of anthocyanins and the synergistic effect of other phenolics, highlighting their potential for application in pH-sensitive sensing systems.

Table 5 - Quantification, expressed as mg/kg, of the detected polyphenols and anthocyanidins in the natural extract samples.

*Concentrations determined by alkaline hydrolysis of the extract to free anthocyanins from their corresponding sugar derivatives.

Compounds	Purple Sweet Potato	Red Cabbage	Red Radish
Benzoic Acids			
3-4-dihydroxybenzoic acid	-	9.0 ± 3.0	-
Hydroxycinnamic acids			
Chlorogenic acid	119.0 ± 2.0	-	-
Caffeic acid	-	-	25.0 ± 1.0
p-coumaric acid	-	162.0 ± 2.0	146.0 ± 11.0
Sinapic acid	-	-	61.0 ± 2.0
Trans-ferulic acid	-	-	895.0 ± 8.0
Flavanols			
Kaempferol-*O*-glucoside	-	5.0 ± 1.0	3.0 ± 1.0
Anthocyanidins*			
Delphynidin	-	-	-
Cyanidin	-	19699.0 ± 384.0	-
Pelargolin	-	-	209920.0 ± 1498.0

The TPC analysis revealed that all extracts were rich in phenolic compounds, with PSP showing the highest value (704.2 mg GAE/g), followed by RC (610.0 mg GAE/g) and RR (602.0 mg GAE/g) (Figure 9 (A)), validating the previous observations on chemical profile. The antioxidant activity, assessed via DPPH radical scavenging, displayed concentration-dependent and extract-specific behaviors (Figure 9 (B)). At 24 h, RC at 5 mg/mL exhibited the highest and most stable antioxidant effect, maintaining values above 60 % DPPH reduction. PSP reached relatively high activity at 2.5 mg/mL, but all PSP concentrations eventually stabilized below 50 %. RR showed moderate activity, with 2.5 and 5 mg/mL concentrations outperforming 10 mg/mL, which consistently presented the weakest effect. Statistical comparisons at 24 h confirmed significant differences between intermediate and high concentrations for RC (5 vs. 10 mg/mL, $p < 0.01$; 2.5 vs. 10 mg/mL, $p < 0.001$) and RR (5 vs. 10 mg/mL and 2.5 vs. 10 mg/mL, $p < 0.0001$). These findings reinforce that antioxidant performance is not linearly correlated with concentration; in fact, higher doses such as 10 mg/mL may undergo saturation or aggregation, leading to reduced radical scavenging efficiency. The case of PSP further illustrates this complexity, as despite its higher TPC, it did not outperform RC or RR, emphasizing that qualitative aspects of the phenolic profile are as important as quantitative differences. Although high TPC values are generally correlated with stronger antioxidant capacity, this relationship is not strictly linear, as antioxidant activity also depends on the molecular composition, stability, and interactions of phenolics within each extract [184, 185]. Indeed, PSP's higher TPC did not translate into superior antioxidant performance compared with RC and RR.

The antifungal properties of extracts RC, RR and PSP were evaluated by determining MIC and MFC against *Candida* species (*C. albicans*, *C. parapsilosis* and *C. tropicalis).* Based on the analysis conducted, none of the natural halochromic extracts in test exhibited antifungal activity, thus preventing MIC and MFC determination. This lack of antifungal effect may be attributed to the specific chemical composition of the extracts (Table 5), which, although all samples were rich in phenolic compounds - particularly cyanidin in RC and pelargonidin in RR- anthocyanins are primarily known for their antioxidant and anti-inflammatory properties, with limited evidence of direct antifungal action. Furthermore, other phenolic acids detected, such as *p*-coumaric, trans-ferulic, and chlorogenic acids, are reported to display only mild inhibitory effects at concentrations considerably higher than those quantified in the present extracts. The absence of other bioactive classes commonly associated with antifungal activity, such as saponins, alkaloids, or specific

flavonoids that are typically required to disrupt fungal cell structures or metabolic processes, likely explains the lack of growth inhibition observed, [186, 187].

Cytocompatibility assays were performed to evaluate the biological safety of the extracts in solution. The metabolic activity of L929 fibroblasts and HaCaT keratinocytes exposed for 24 h to different extract concentrations (0.08–10 mg/mL) was measured using the resazurin reduction assay (Figure 9 (C)). All extracts were well tolerated at lower concentrations, with L929 fibroblasts maintaining metabolic activity up to 2.5 mg/mL and HaCaT keratinocytes up to 1.25 mg/mL for PSP and 2.5 mg/mL for RC and RR. At higher concentrations, a dose-dependent decline in metabolic activity was observed, particularly at 10 mg/mL, where RC reduced fibroblast viability to ≈ 30 %. HaCaT cells displayed slightly higher sensitivity than fibroblasts, confirming their greater susceptibility to extract-induced stress. Among the extracts, PSP exhibited the strongest cytotoxic effect, significantly reducing metabolic activity at lower concentrations compared with RC and RR. This behavior may be linked to its high pigment load and phenolic profile, which, although beneficial for antioxidant activity, may interfere with cellular metabolism and membrane integrity. At elevated concentrations, these molecules can generate pro-oxidant effects, leading to the production of reactive oxygen species (ROS) and oxidative stress. This imbalance can disrupt mitochondrial function, impair energy metabolism, and compromise membrane integrity, ultimately reducing cell viability [188]. Taken together, these results support the selection of 5 mg/mL as the optimal concentration for further applications, as it ensures a balance between effective antioxidant activity, stable halochromic response, and acceptable cytocompatibility. Given its higher cytotoxicity and weaker antioxidant performance despite high TPC, PSP was excluded from subsequent steps. RC and RR, in contrast, demonstrated robust halochromic properties, good cytocompatibility, and suitable antioxidant efficiency, justifying their use in the immobilization process for the development of halochromic electrospun mats.

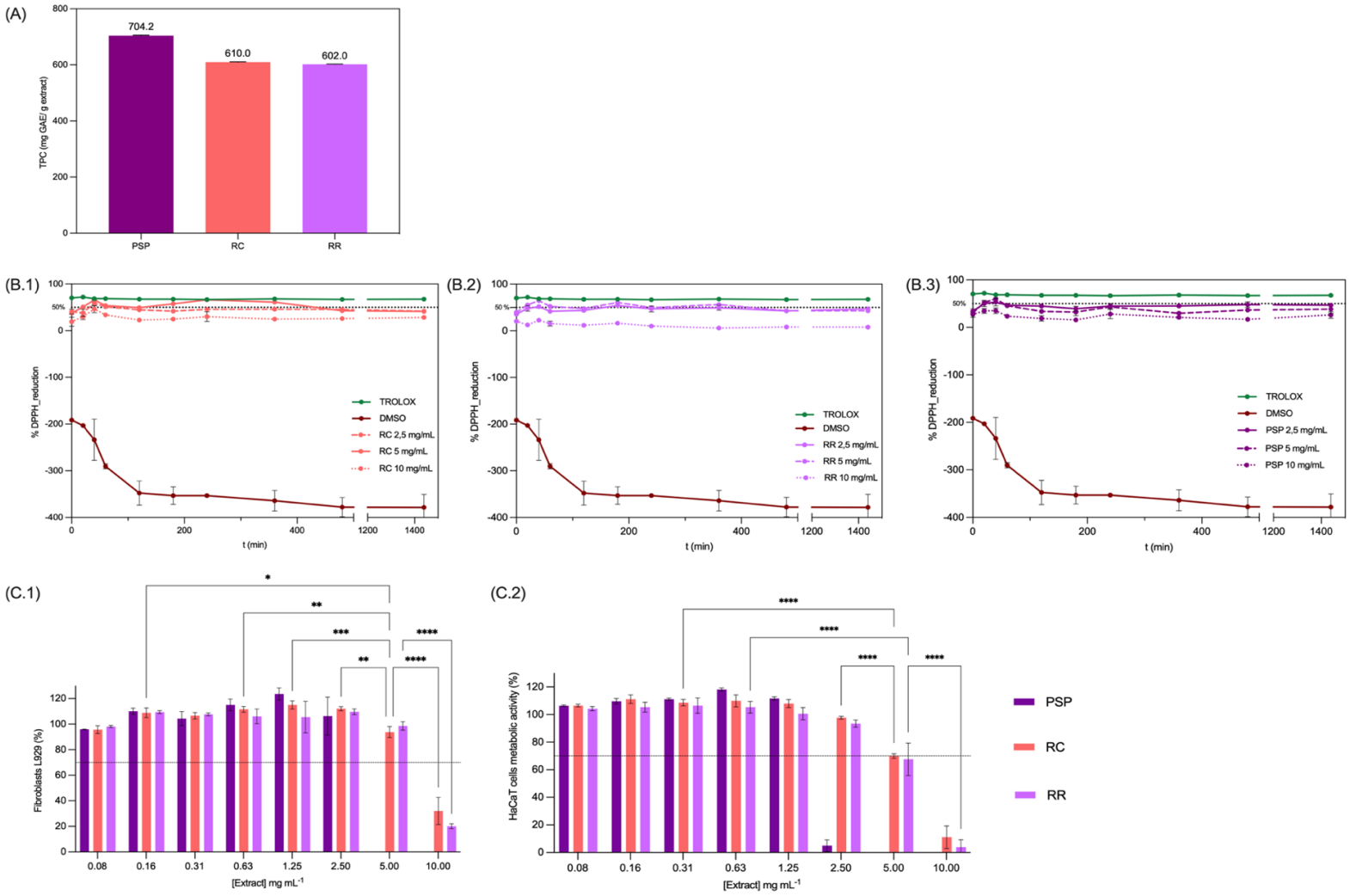


Figure 9 –(A) TPC shown in gallic acid equivalents. Data are reported as mean ± SD (n=3). Statistical significance was determined via Tukey's test applying multiple comparisons between the three natural extracts; no significant differences were reported. (B) DPPH scavenging activity (%) induced by halochromic extracts at 1, 2, 4, 6, 8 and 24 h. Trolox was used as a positive control

and DMSO as a negative control (n =3). Statistical significance was determined via Tukey test, by applying multiple comparisons between concentrations for all extract types. Significance between RC 5 mg/mL and RC 10 mg/mL: $p<0.01$ at 24h; RC 2,5 mg/mL and RC 10 mg/mL: $p < 0.001$ at 24h. RR 5 mg/mL and RR 10 mg/mL: $p <0.001$ at 24h; RR 2,5 mg/mL and RR 10 mg/mL: $p < 0.0001$ at 24h. (C) Cytocompatibility studies were performed on (C.1) fibroblasts from mice (L929) and (C.2) human keratinocytes (HaCaT) for the three natural halochromic extracts. Data is reported as mean ± S.D. (n=3). Statistical significance was determined via Tukey test, by applying multiple comparisons between concentrations for all extract types (*$p < 0.05$; **$p < 0.01$; ***$p < 0.001$; ****$p < 0.0001$).

III.3.2 Mats Morphology and Porosity

SEM micrographs showed that all electrospun mats exhibited a continuous, bead-free, and randomly oriented fibrous morphology. Pure PCL mats (100PCL) presented the thickest fibers, with a mean diameter of 1331.5 ± 180.8 nm, consistent with the higher viscosity (1.678 ± 0.149 Pa·s) and lower conductivity (0.123 ± 0.005 µS/cm) of its precursor solution. Incorporation of PEG led to a progressive reduction in fiber diameter: PCL/PEG 90:10 exhibited a mean diameter of 896.3 ± 91.2 nm, and PCL/PEG 80:20 further decreased to 853.0 ± 88.9 nm. This trend aligns with the decreasing viscosity and increasing conductivity of the solutions (Table 6), enhancing the stretching of the polymer jet during electrospinning [189, 190]. The addition of RC and RR halochromic extracts further influenced fiber diameter and surface morphology. For RC-loaded mats, all formulations showed thinner and more uniform fibers compared to their extract-free counterparts. Notably, PCL/PEG 90:10 + RC exhibited the smallest mean diameter (787.8 ± 66.1 nm), likely due to enhanced solution conductivity (0.320 ± 0.005 µS/cm) and moderate viscosity (1.660 ± 0.005 Pa·s), which promoted jet elongation. 100PCL + RC also showed a significant reduction in diameter (885.5 ± 147.4 nm) compared to pure 100PCL, despite a similar viscosity, likely due to the increased conductivity (0.181 ± 0.004 µS/cm) introduced by the extract. RR-containing mats displayed the lowest mean diameters among all groups. The combination of PCL/PEG 80:20 + RR resulted in the thinnest fibers (810.3 ± 106.3 nm) with the highest solution conductivity (0.717 ± 0.009 µS/cm) and viscosity (2.358 ± 0.193 Pa·s). In addition to morphological observations, fiber diameter and arrangement are closely linked to the porosity of the electrospun mats. Generally, mats composed of thicker and less uniform fibers, such as those from 100PCL, exhibited lower porosity due to denser packing and reduced inter-fiber spacing. As PEG was incorporated and its concentration increased, fiber diameter decreased and fiber distribution became more homogeneous, contributing to enhanced porosity. This trend was further intensified again by the addition of halochromic extracts. Mats loaded with RC and RR extracts displayed more porous structures, as evidenced by their thinner and more uniformly distributed fibers. Particularly, the PCL/PEG 90:10 + RC and RR as well as PCL/PEG 80:20 + RR formulations, which showed the smallest mean fiber diameters (787.8 ± 66.1 nm and 810.3 ± 106.3 nm, respectively), and, consequently, the highest porosity among all groups. Furthermore, the enhanced conductivity and optimized viscosity of these solutions promoted better jet elongation during electrospinning, leading to a more open fibrous network and improved pore interconnectivity that are advantageous for wound healing applications, as they facilitate oxygen diffusion, moisture

retention, and exudate absorption [190, 191] Overall, the synergistic effect of PEG and halochromic extracts not only modulated fiber diameter but also significantly influenced the porosity of the mats, which is a critical parameter for their potential use in real-time wound monitoring systems.

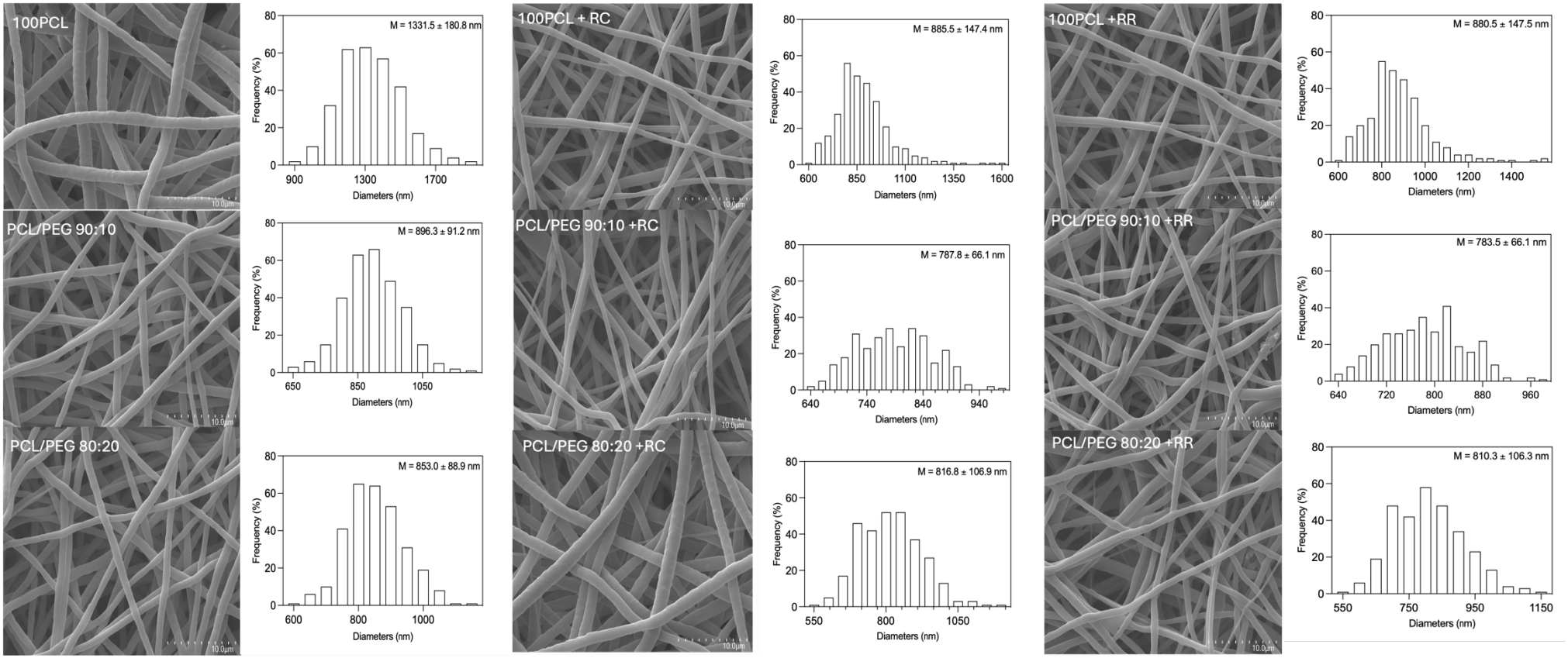


Figure 10 - FEG-SEM micrographs and diameter distribution histograms with the respective mean (M) and SD. (n=3), for 100:0, 90:10 and 80:20 PCL/PEG mats, loaded with RC and RR extract and unloaded. Scale bars in micrographs represent 10 μm.

The physicochemical properties of the electrospinning solutions were significantly influenced by both PEG content and extract incorporation (Table 6). Increasing PEG concentration from 10 % to 20 % led to a systematic reduction in viscosity and a slight increase in conductivity, indicating enhanced polymer chain mobility and charge transport. These changes are indicative of enhanced polymer chain mobility and charge transport [192]. The addition of RC and RR extracts further increased conductivity and, in most formulations, viscosity, particularly in PCL/PEG 80:20 solutions, where viscosity exceeded 2.0 Pa·s. This effect is attributed to the presence of anthocyanins and other polar compounds capable of interacting with PEG and PCL chains through hydrogen bonding, leading to increased chain entanglement [193]. Zeta potential measurements confirmed a shift towards more negative values after extract addition, reaching −29.011 ± 0.004 mV for PCL/PEG 80:20 + RR, likely due to ionizable groups present in the extracts. This enhanced surface charge likely derives from the ionizable groups in the halochromic molecules and is beneficial for colloidal stability and potential biological interaction (e.g., protein adsorption, wound exudate interaction) [194]. These changes in solution properties directly translated into the morphology of the electrospun mats, producing thinner fibers and more homogeneous structures compared with unloaded formulations. The pH of extract-free solutions was near-neutral to slightly basic (7.10-7.98), influenced by the polymeric matrix. In contrast, extract-loaded solutions showed a slight decrease in pH (6.5-7.2), consistent with the acidic nature of anthocyanins. This pH range remains compatible with physiological conditions, supporting the potential of these materials for wound monitoring where pH fluctuation is a key marker of infection or healing state.

Table 6 – 100PCL, PCL/PEG and PCL/PEG + RC and RR solutions viscosity, conductivity, zeta potential and pH values. Data are reported as mean ± SD. (n =3).

Polymeric Solutions	Viscosity (Pa·s)	Conductivity (μS/cm)	Zeta Potential (mV)	pH
100PCL	1.678 ± 0.149	0.123 ± 0.005	-10.980 ± 0.002	7.100 ± 0.001
PCL/PEG 90:10	0.976 ± 0.006	0.644 ± 0.003	-12.050 ± 0.002	7.340 ± 0.006
PCL/PEG 80:20	0.819 ± 0.047	0.670 ± 0.005	-13.231 ± 0.004	7.980 ± 0.003
100PCL + RC	1.673 ± 0.092	0.181 ± 0.004	-22.345 ± 0.004	6.830 ± 0.001
PCL/PEG 90:10 + RC	1.660 ±0.005	0.320 ± 0.005	-26.761 ± 0.004	6.500 ± 0.005
PCL/PEG 80:20 + RC	2.093 ± 0.055	0.367 ± 0.004	-21.075 ± 0.004	7.000 ± 0.001
100PCL + RR	0.375 ± 0.091	0.191 ± 0.010	-28.167 ± 0.007	7.200 ± 0.001
PCL/PEG 90:10 + RR	1.767 ± 0.002	0.418 ± 0.015	-28.631 ± 0.004	6.780 ± 0.005

PCL/PEG 80:20 + RR	2.358 ± 0.193	0.717 ± 0.009	-29.011 ± 0.004	6.900 ± 0.002

III.3.3 Chemical Analyses

ATR-FTIR spectroscopy was used to identify the chemical groups detectable on the electrospun mats and to confirm the successful incorporation of halochromic extracts into the PCL and PCL/PEG matrices (Figure 11). The spectra of 100PCL, PCL/PEG 90:10, and PCL/PEG 80:20 display characteristic bands associated with polycaprolactone. The strong absorption band at around 1720 cm^{-1} corresponds to the stretching vibration of the ester carbonyl group (C=O), while the peaks near 2940 cm^{-1} and 2865 cm^{-1} are assigned to asymmetric and symmetric CH_2 stretching vibrations, respectively. The bands at 1294 cm^{-1}, 1173 cm^{-1}, and 1108 cm^{-1} are attributed to C–O and C–C stretching, typical of the aliphatic polyester backbone of PCL [195]. The incorporation of PEG slightly modified the spectral profiles by increasing the intensity of bands around 1100–1050 cm^{-1}, corresponding to C–O–C stretching vibrations from the ether linkages in PEG [196]. This effect is more pronounced in PCL/PEG 80:20, confirming greater PEG content in the blend. In the RC-loaded mats (100PCL + RC, PCL/PEG 90:10 + RC, and PCL/PEG 80:20 + RC), the main PCL and PEG bands remain visible, indicating that the polymer backbone remains intact. However, subtle new features and broadening of bands are observed, particularly in the 3200–3500 cm^{-1} range (not shown clearly but expected), which may indicate O–H stretching from anthocyanins and other phenolic compounds present in RC extract correlating with the chemical profile of the extracts (Table 5) and their total phenolic content [174]. Minor changes near 1600–1650 cm^{-1} may also reflect C=C aromatic vibrations or carbonyl contributions from the anthocyanins. These spectral shifts support the successful incorporation of RC within the fibers and potential weak interactions (e.g., hydrogen bonding) between extract constituents and the polymer matrix. RR components (mainly anthocyanins and possible glucosinolates) likely contribute to the broadening of O–H and N–H regions (≈ 3200–3400 cm^{-1}) and potential intensity changes in the 1600 cm^{-1} region. The spectra of PCL/PEG 80:20 + RR, in particular, show subtle but noticeable changes compared to the unloaded formulation, suggesting good dispersion of the extract into the polymer matrix without major structural disruption [197]. The standard FTIR spectra of RC and RR highlight their chemical profiles. All show broad O–H stretches (3200–3400 cm^{-1}), C=O stretches near 1700 cm^{-1}, and complex fingerprint regions (<1500 cm^{-1}), corresponding to polyphenols, sugars, and acids. These reference spectra provide a chemical basis

for identifying extract-related features in the loaded mats. With these results, we can conclude that the chemical integrity of the PCL and PCL/PEG matrices after electrospinning was maintained as well as the successful incorporation of RC and RR extracts, evidenced by subtle spectral changes, likely non-covalent interactions (hydrogen bonding) between extract molecules and the polymer matrix [194]. These findings reinforce the potential of the electrospun mats to retain halochromic activity without compromising polymer structure.

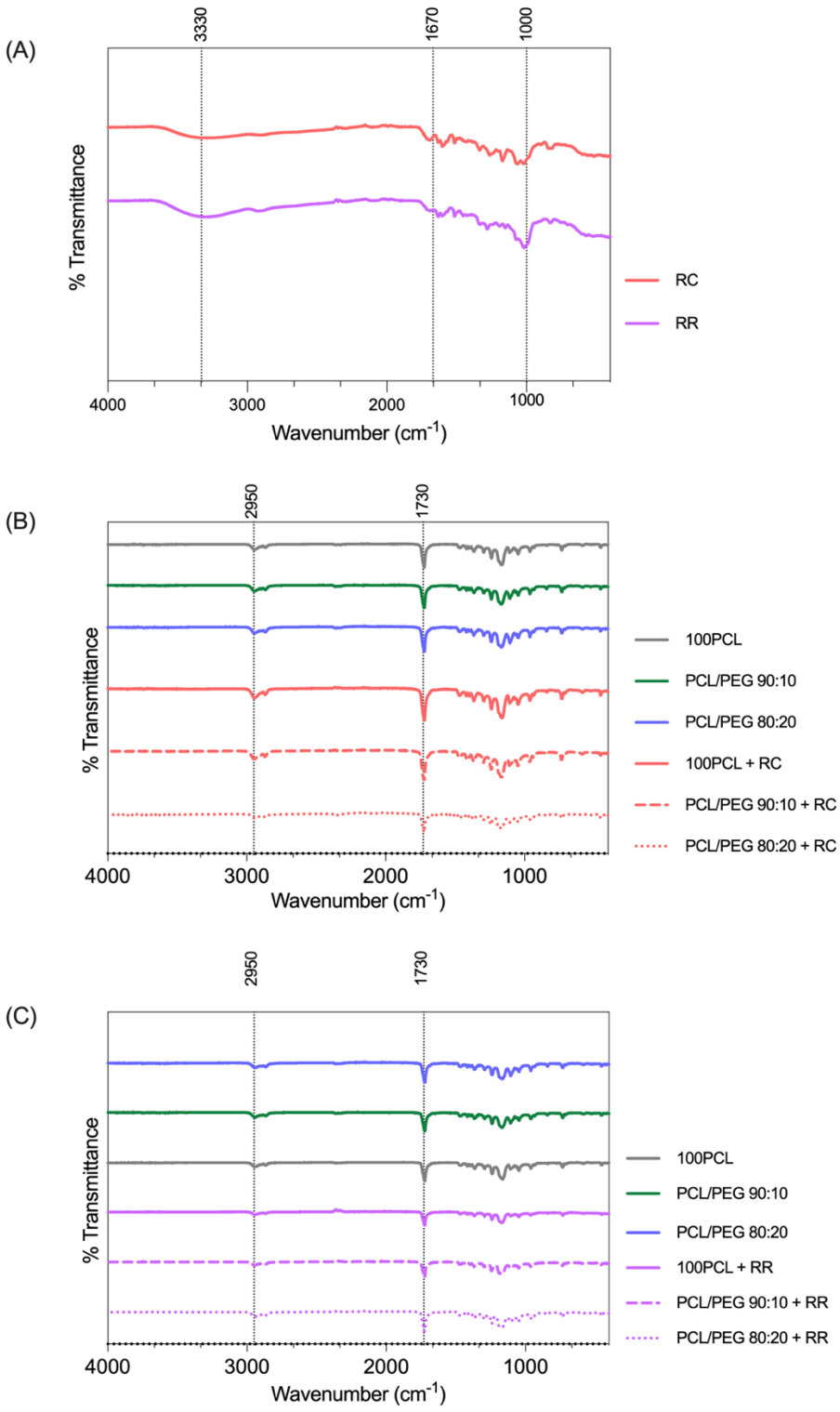


Figure 11 - ATR-FTIR spectra of (A) Free natural extracts RC and RR, (B) PCL/PEG combinations with RC and (C) PCL/PEG combinations with RR electrospun mats collected in the range of 4000 to 400 cm^{-1}. The standard FTIR spectra of RC and RR were used here for comparative purposes.

III.3.4 Thermal Stability

TGA provides insights into the degradation mechanisms and thermal stability of the individual components, polymer blends, and extract-loaded electrospun mats. Figure 12 (A) displays the TGA thermograms for the isolated extracts (RC and RR), the neat polymers (PCL and PEG), their binary blends, and the final mats containing the bioactive extracts. The natural extracts displayed gradual and continuous mass loss starting from RT up to ≈ 350 °C, with no distinct degradation steps. Both extracts lost approximately 40–60 % of their mass within this range. This profile reflects the presence of moisture, volatile compounds, and thermally labile constituents such as anthocyanins, sugars, and other plant metabolites [198–200]. The absence of sharp degradation events indicates a broad compositional complexity typical of crude plant extracts. Among the neat polymers, PCL powder and 100PCL mat samples exhibited a single-step degradation beginning at ≈230 °C, with rapid mass loss up to ≈350 °C, characteristic of polyester thermal decomposition via ester bond cleavage [201, 202]. In contrast, PEG powder began degrading much earlier, around 150 °C, and followed a two-step degradation process. This early thermal degradation is consistent with the known low thermal stability of PEG due to its ether bonds and chain-end scission, resulting in ≈ 60 % mass loss by ≈ 300 °C [203]. When blended, the PCL/PEG 90:10 and 80:20 samples showed a moderate shift toward lower degradation temperatures compared to pure PCL, especially in the 80:20 formulation. This is attributed to the plasticizing effect of PEG, which increases chain mobility and reduces the overall thermal resistance of the blend [204]. However, both blends retained a single, prominent degradation step between 200-350 °C, suggesting miscibility and a dominant degradation mechanism governed by the PCL matrix. The incorporation of RC and RR extracts into the PCL-based matrices (bottom panel of Figure 12 (A)) had only a minor effect on the thermal degradation profile of the resulting electrospun mats. All extract-loaded mats maintained the characteristic single-step degradation between 200-350 °C, similar to the unloaded polymer systems, indicating that the presence of extracts did not introduce additional degradation stages or significantly alter thermal stability. For example, both 100PCL + RC and 100PCL + RR mats exhibited nearly identical degradation curves to pure PCL, with onset temperatures slightly below 230 °C and complete decomposition by 350 °C. Also, the PCL/PEG 90:10 and 80:20 mats with either extract followed similar degradation trends to their control counterparts. Slight decreases in thermal stability were observed with increasing PEG content, particularly in the PCL/PEG 80:20 + RC mat, which showed an earlier onset of degradation, consistent with the lower thermal resistance of PEG and possible interactions between PEG and extract constituents. Notably, the thermal

degradation profiles of the extract-loaded mats were significantly sharper and more defined than those of the pure extracts alone, suggesting that the immobilization of the extracts within the fibrous polymer matrix stabilizes their thermal behavior. The matrix appears to act as a barrier to early decomposition of the bioactives, preventing premature volatilization or thermal breakdown below 200 °C [21]. These results demonstrate that while the natural extracts themselves are thermally less stable and degrade gradually across a broad temperature range, their incorporation into PCL or PCL/PEG blends via electrospinning does not compromise the thermal integrity of the polymer matrix. The mats retain the thermal stability characteristic of PCL-based systems and are therefore suitable for applications that involve moderate thermal exposure, such as biomedical scaffolds. Additionally, the fact that the extracts do not introduce new thermal degradation stages implies a homogeneous dispersion and compatibility with the polymer blends.

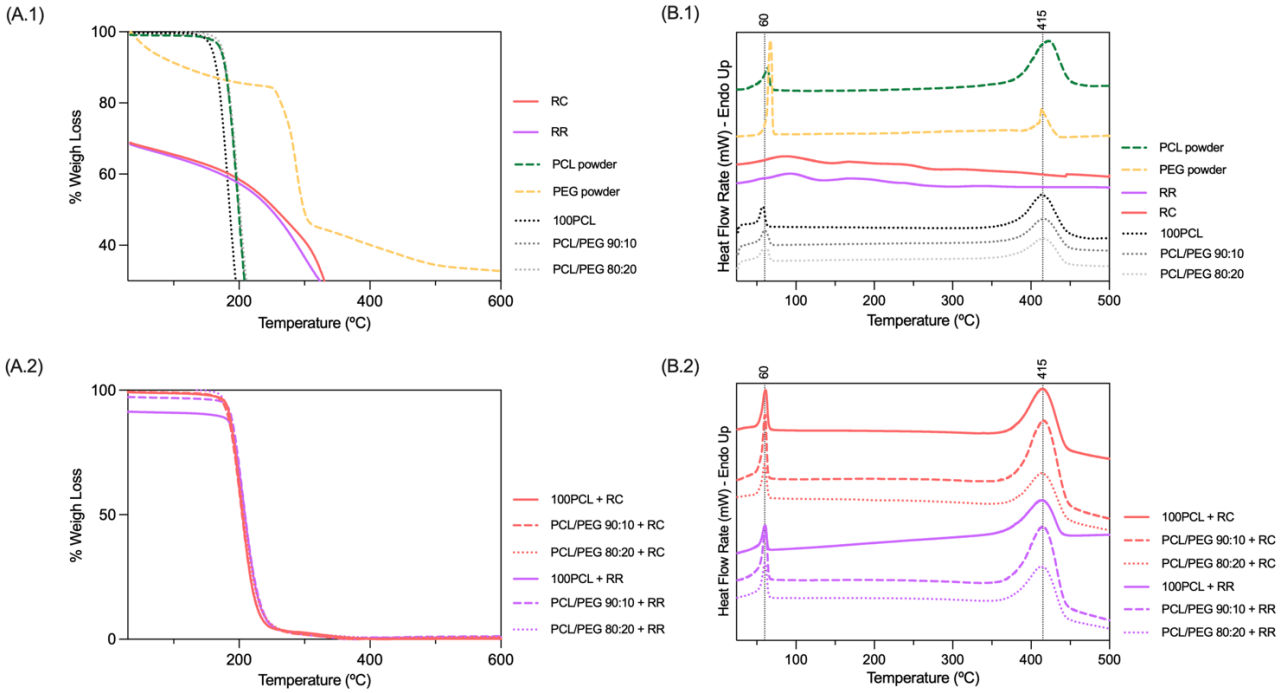


Figure 12 - (A.1) Thermal stability of individual components and polymer blends, and (A.2) extract-loaded electrospun mats was characterized based TGA thermograms. (B.1) DSC thermograms of individual components and (B.2) extract-loaded electrospun mats. Data reported as Heat Flow (mW) vs. Temperature (°C).

To complement the TGA data, DSC analysis was performed to assess thermal transitions, crystallinity, and the thermal behavior of individual components, blends, and extract-loaded mats. The resulting thermograms are shown in Figure 12 (B) (Main DSC thermal events: T_o onset

temperature, and ΔH enthalpy in SI – Table SD20). As expected, the neat polymers, PCL and PEG, exhibited their characteristic endothermic peaks. PCL powder displayed a sharp melting endotherm at ≈ 60 °C and a secondary peak at ≈ 415 °C, associated with thermal degradation. PEG showed a prominent melting event at ≈ 60 °C, in line with its lower thermal resistance. The natural extracts exhibited broad and less intense transitions across the measured temperature range, with no clear melting peaks. This suggests their amorphous or heterogeneous composition, typical of crude plant extracts rich in anthocyanins, phenolics, and sugars [205]. The absence of sharp transitions further confirms their low crystallinity and thermal complexity. When incorporated into the electrospun mats, the thermal behavior of the polymer blends remained largely unchanged. All PCL/PEG compositions, both unloaded and extract-loaded, retained the primary melting transition of PCL around ≈ 60 °C, confirming the preservation of the crystalline structure. A slight depression in melting temperature and peak intensity was observed with increasing PEG content, attributed to the plasticizing effect and reduction in crystallinity. The addition of RC and RR extracts caused no significant shift in the melting point or additional transitions, indicating that the extracts were well dispersed within the polymer matrix and did not disrupt crystallization. Extract-loaded mats showed slightly broadened endothermic peaks, particularly in the PEG-rich formulations, possibly due to weak interactions between anthocyanins and the polymer chains, which could slightly delay chain packing. DSC results corroborate TGA findings, reinforcing that the incorporation of halochromic extracts into PCL or PCL/PEG matrices does not compromise the thermal behavior of the base materials.

III.3.5 Mechanical Performance

The mechanical behavior of the electrospun mats was assessed through the evaluation of Young's modulus, elongation at break, and break strength, providing insights into their flexibility, stiffness, and tensile resistance, all critical parameters for wound dressing applications where conformability and mechanical durability are essential (Table 7). Incorporating PEG into the PCL matrix influenced the mechanical profile of the mats significantly. The 100PCL formulation exhibited the highest elongation at break (310.89 ± 20.16 %) and a relatively low breaking strength (0.054 ± 0.010 MPa), consistent with its flexible, ductile nature. As PEG content increased, both elongation and breaking strength gradually decreased, with PCL/PEG 80:20 showing the lowest elongation (141.56 ± 19.71 %) and a breaking strength of 0.045 ± 0.013 MPa. This reduction in stretchability suggests increased fiber fragility with higher PEG proportions, likely due to reduced

molecular entanglement and fiber cohesion [206]. Young's modulus values also reflected this trend: PCL/PEG 90:10 and PCL/PEG 80:20 reported 0.171 N/mm and 0.318 N/mm, respectively, indicating a shift toward increased stiffness as elongation declined.

The incorporation of RC extract led to a further decrease in flexibility, particularly in 100PCL + RC, where the elongation at break dropped by over 59 % compared to neat PCL (126.78 ± 39.14 %) and the breaking strength sharply declined to 0.016 ± 0.001 MPa. This stiffening effect can be attributed to phenolic compound-polymer interactions that reduce chain mobility and potentially induce localized crosslinking or crystallinity as seen on DSC results [207]. PEG-containing RC-loaded formulations showed moderately higher tensile resistance compared to 100PCL + RC. Both PCL/PEG 90:10 + RC and PCL/PEG 80:20 + RC showed increased Young's modulus (0.421 and 0.463 N/mm, respectively), along with reduced elongation and modest breaking strengths (0.043 and 0.047 MPa). This behavior supports the notion that RC compounds act as reinforcing agents in the fiber matrix, enhancing stiffness at the cost of flexibility [208]. Similarly, RR extract increased the stiffness of the electrospun mats. The most substantial effect was observed in PCL/PEG 80:20 + RR, which exhibited the lowest elongation at break (85.78 ± 15.26 %) and an elevated Young's modulus of 0.443 N/mm, despite a lower breaking strength (0.038 ± 0.003 MPa). Compared to RC-loaded samples, RR-loaded mats maintained slightly higher tensile strength while still exhibiting similar elasticity. Interestingly, 100PCL + RR maintained a high breaking strength (0.054 ± 0.011 MPa) and elongation comparable to the neat PCL mat, suggesting a milder stiffening effect in the absence of PEG. This difference may arise from varying affinities between the extract constituents and polymer chains. In the neat polymer system, PEG acts as a plasticizer: increasing PEG content lowers Young's modulus and increases elongation, consistent with enhanced chain mobility. When halochromic extracts are added, this trend is partially counterbalanced by phenolic–polymer interactions (e.g., hydrogen bonding/physical crosslinking) and improved chain entanglement, which lead to an increase in stiffness (higher Young's modulus) with a modest loss of flexibility. PEG is retained in the formulation because it improves electrospinnability (lower viscosity, more uniform jets), promotes homogeneous dispersion/retention of the extracts within the PCL matrix, and increases hydrophilicity, which is advantageous for exudate management and subsequent biological interaction. Thus, any reduction of the plasticizing effect upon extract addition is offset by gains in fiber uniformity, extract integration, and mechanical robustness required for the targeted application. These effects were more pronounced with RC than RR, likely due to the different phenolic or pigment profiles of the extracts. Such mechanical tuning is advantageous in designing

smart wound dressings, where a balance between flexibility (for comfort and movement) and stiffness (for handling and durability) is needed.

Table 7 – Young Modulus, elongation at break and break strength of loaded and unloaded PCL/PEG mats tested at a displacement rate of 10.0 mm/min (n=3). Statistical analysis showed on Table SD18 and SD19 on Supporting Information.

Electrospun Mats	Young Modulus (N/mm)	Elongation at break (%)	Break strength (MPa)
100PCL	0.174 ± 0.070	310.89 ± 20.160	0.054 ± 0.010
PCL/PEG 90:10	0.171 ± 0.034	274.44 ± 10.730	0.047 ± 0.011
PCL/PEG 80:20	0.318 ± 0.055	141.56 ± 19.712	0.045 ± 0.013
100PCL + RC	0.126 ± 0.022	126.78 ± 39.145	0.016 ± 0.001
PCL/PEG 90:10 + RC	0.421 ± 0.102	102.22 ± 38.300	0.043 ± 0.001
PCL/PEG 80:20 + RC	0.463 ± 0.988	101.44 ± 14.637	0.047 ± 0.011
100PCL + RR	0.440 ± 0.077	122.78 ± 11.170	0.054 ± 0.011
PCL/PEG 90:10 + RR	0.454 ± 0.062	110.11 ± 18.120	0.050 ± 0.005
PCL/PEG 80:20 + RR	0.443 ± 0.092	85.78 ± 15.261	0.038 ± 0.003

III.3.6 Wettability

The wettability of the electrospun mats was evaluated by WCA measurements using established ASTM and BS standardized methods, which are widely adopted for the evaluation of wound dressing materials. All measurements were performed in triplicate (Figure 13). This analysis provides insight into the surface hydrophobicity or hydrophilicity, a critical parameter influencing cell adhesion, fluid exchange, and the overall performance of wound dressings [209]. Neat PCL mats exhibited a high contact angle of 134.0° ± 2.59, confirming their intrinsically hydrophobic nature due to the low surface energy of the polymer. Upon incorporation of PEG, which is known for its hydrophilic character, the WCA significantly decreased. For instance, the PCL/PEG 90:10 and 80:20 blends showed contact angles of 94.9° ± 8.92 and 76.7° ± 1.86, respectively. This progressive reduction in contact angle with increasing PEG content reflects improved wettability and suggests more favorable surface characteristics for wound healing. The addition of natural halochromic extracts further modified the surface properties. RC-loaded mats generally showed a modest reduction in WCA compared to their extract-free counterparts: 100PCL + RC exhibited a WCA of 109.5° ± 4.43, while PCL/PEG 90:10 + RC and PCL/PEG 80:20 + RC showed contact angles of 88.9° ± 2.43 and 64.2° ± 0.84, respectively. These values indicate enhanced

hydrophilicity due to the presence of hydrophilic anthocyanins and phenolic compounds from the extract, which may alter surface polarity [210]. Similarly, mats incorporating RR also demonstrated reduced contact angles compared to the neat PCL. 100PCL + RR reached 111.1° ± 2.73, while PCL/PEG 90:10 + RR and PCL/PEG 80:20 + RR showed 89.6° ± 1.87 and 63.5° ± 1.53, respectively. These results suggest that the impact of the RR extract on wettability is comparable to that of RC, with both promoting more hydrophilic surfaces when combined with PEG, especially in higher PEG content formulations. These results show that PEG is the key driver of surface hydrophilicity in these mats. In neat PCL, the high WCA (≈134°) reflects low surface energy. Upon electrospinning with PEG, PEG chains preferentially segregate to the fiber surface and orient their ether/terminal hydroxyl groups outward, which lowers the surface energy and increases the polar component, decreasing WCA. When halochromic extracts are included, PEG further acts as a molecular spacer/bridge: hydrogen bonding between PEG and anthocyanin-rich phenolics prevents their aggregation inside the fiber and promotes their presentation at the interface. The exposure of ionizable phenolic –OH groups, together with the hydrophilic PEG layer, enhances interfacial hydration, yielding additional WCA reductions. Thus, PEG is required not only to render PCL-based mats sufficiently hydrophilic, but also to correctly position the extract molecules at the fiber surface, enabling rapid fluid uptake and reliable activation of the halochromic response in use. The most hydrophilic surfaces were observed in the PEG-rich formulations, particularly PCL/PEG 80:20 loaded with natural extracts. This indicates that even at lower PEG content, the combination of PEG and the anthocyanin-rich RR extract effectively enhances surface hydrophilicity. Such moderately hydrophilic characteristics are beneficial for wound healing applications [211].

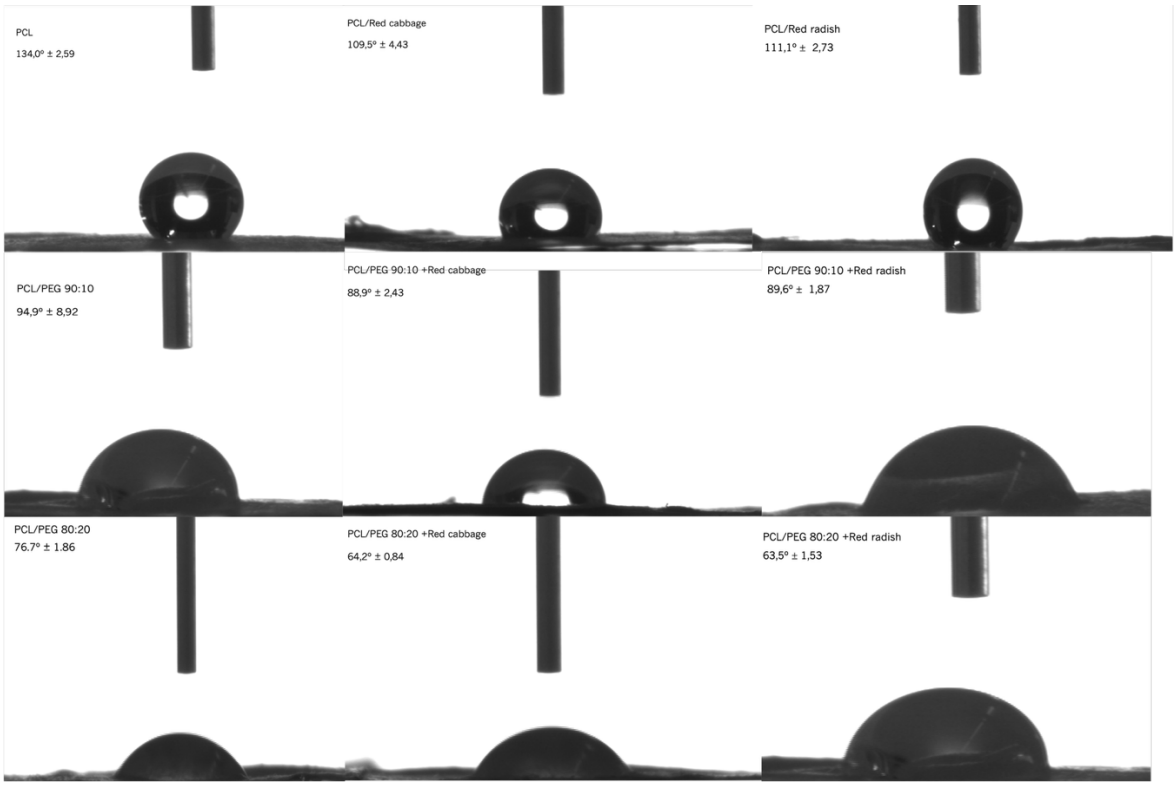


Figure 13 - Wettability of the electrospun mats by WCA measurements (n=3) using established ASTM and BS standardized methods.

III.3.7 *In-vitro* Swelling and Degradation

The degree of swelling and degradation profiles of the developed electrospun mats were evaluated to assess their suitability as wound dressings, where moisture absorption and gradual biodegradability are essential features. As shown in Figure 14 (A), all mat formulations exhibited rapid swelling within the first few hours of PBS incubation, stabilizing after 24 h. The incorporation of PEG enhanced the swelling capacity compared to pure PCL (100PCL), attributed to PEG's hydrophilic nature. The PCL/PEG 90:10 and 80:20 blends reached higher swelling degrees (≈ 85–95 %) consistently across all time points, while 100PCL remained significantly lower (≈ 60–75 %). Among the extract-loaded mats, the RR-loaded formulations (particularly PCL/PEG 90:10 + RR and 80:20 + RR) showed slightly reduced swelling compared to extract-free counterparts, possibly due to physical interactions between anthocyanins and the polymer matrix, restricting water uptake. This behavior likely arises from hydrogen bonding between anthocyanin phenolic –OH/sugar moieties and PEG ether/PCL carbonyl groups, which sequesters PEG and masks polar domains in the bulk, thereby limiting water uptake even when surface wettability increases. Interestingly, RC-loaded mats maintained comparable swelling behavior to extract-free ones, suggesting less interference with hydrophilic domains [212].

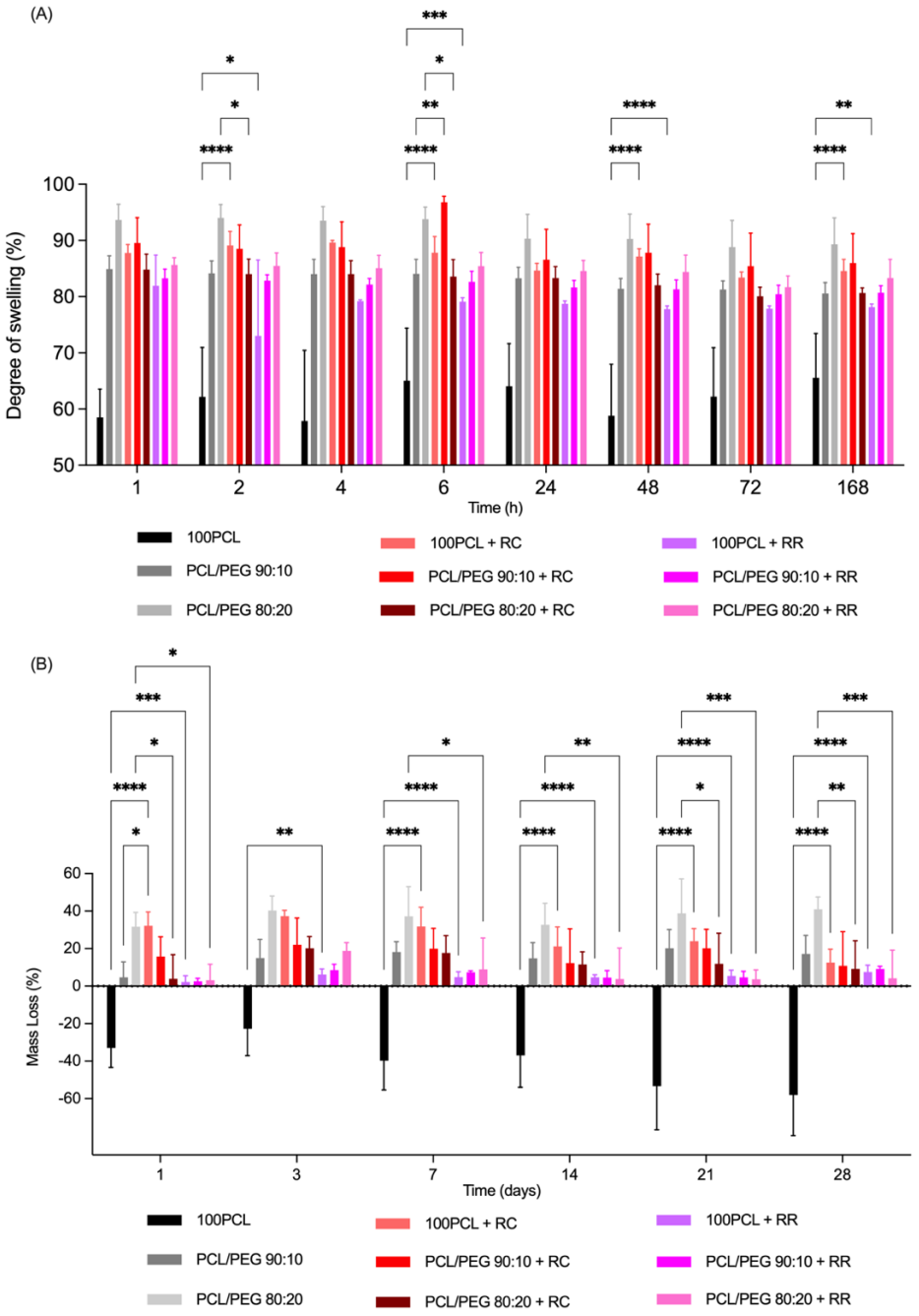


Figure 14 - (A) Degree of swelling (%) of electrospun mats in PBS over 168 hours. All mats were incubated at 37 °C in PBS 1× 0.01M (pH 7.4). Data represent the mean ± SD(n = 4). (B) Mass loss (%) of electrospun mats over 28 days in PBS 1× 0.01M (pH 7.4). Negative values indicate water absorption rather than degradation. Data represent the mean ± SD (n = 4) Statistical significance was determined via Tukey test, by applying multiple comparisons between for all mat types. (*p < 0.05; **p < 0.01; ***p < 0.001; ****p < 0.0001).

The mass loss study (Figure 14 (B)) over 28 days in PBS revealed distinct degradation trends. The 100PCL mats exhibited negative mass loss values, indicating water retention rather than material degradation. Conversely, PEG-containing mats showed increased degradation, with PCL/PEG 80:20 displaying the highest weight loss (≈ 35-50 %), consistent with PEG's faster solubility and leaching [213]. In agreement with mechanical results, PEG introduces discontinuities in the PCL chains, generating labile junctions that accelerate fragmentation and mass loss in PBS. The presence of anthocyanin extracts further enhanced the degradation rate, particularly in RC-loaded mats, likely due to acidic moieties and phenolic content destabilizing polymer chains. Among all formulations, PCL/PEG 80:20 + RC exhibited the highest mass loss by day 28, highlighting its potential for faster degradation in moist environments. RR-loaded mats showed more moderate degradation, maintaining higher structural stability over time. This difference reflects the extracts' profiles: RC, richer in cyanidin-based anthocyanins, increases hydrophilicity and promotes PEG leaching, accelerating hydrolytic mass loss, whereas RR-containing higher levels of hydroxycinnamic acids (e.g., trans-ferulic, *p*-coumaric; Table 5)-forms stronger hydrogen bonding with PCL/PEG and, together with its antioxidant capacity, moderates chain scission and slows degradation. Overall, the combination of PCL with PEG, especially at a 90:10 ratio and loaded with RR, offered a promising balance between swelling capacity, controlled degradation, and extract retention, supporting its suitability as a functional wound dressing capable of both moisture management and real-time pH monitoring.

III.3.8 Air and Water Vapor Permeabilities

Permeability analyses were performed to assess the suitability of electrospun mats for wound healing applications, where appropriate moisture and gas exchange are essential for tissue regeneration (Table 8). The base 100PCL mat showed the highest WVTR (16,646.46 ± 1019.83 g/m^2·day), which was slightly reduced upon PEG addition in PCL/PEG 90:10 (15,687.38 ± 370.99 g/m^2·day) but remained comparable in PCL/PEG 80:20 (16,554.86 ± 1096.83 g/m^2·day). Incorporating halochromic extracts caused modest variation in WVTR values. The RC-loaded mats showed a slight reduction in permeability for PCL/PEG 80:20 + RC (14,941.14 ± 1301.96 g/m^2·day), while PCL/PEG 90:10 + RC actually increased in WVTR (16,810.80 ± 919.48 g/m^2·day), indicating that extract addition can modulate vapor transport depending on composition. RR samples, particularly PCL/PEG 80:20 + RR, maintained high WVTR values (16,627.60 ± 172.84 g/m^2·day) and the lowest water vapor permeability index (85.78 ± 15.26

%), highlighting an improved moisture barrier compared to other groups. The fact that the assay was performed at 37 °C and 50 % RH-conditions that mimic advanced wound microclimates-yielded high WVTR, suggesting suitability for heavily exuding lesions such as venous ulcers, where moisture control prevents maceration and promotes re-epithelialization. The permeability index (I), a relative indicator of how effectively the material regulates moisture, was highest in 100PCL (310.89 ± 20.16 %) and declined with both PEG and extract addition. The lowest indices were observed in extract-loaded PEG-rich formulations (PCL/PEG 90:10 + RC: 102.22 ± 38.30 %; PCL/PEG 80:20 + RR: 85.78 ± 15.26 %), suggesting more controlled moisture release, likely due to tighter fiber packing and reduced mat porosity. This behavior is also consistent with the wettability data-PEG lowers WCA-so increased hydrophilicity enhances sorption–desorption of water molecules at the fiber surface, moderating vapor flux. Air permeability values ranged from 0.016 to 0.054 mL/cm²/s. As expected, 100PCL + RC exhibited the lowest air permeability (0.016 ± 0.001 mL/cm²/s), likely due to denser fiber packing and thicker individual fibers (as seen in Figure 10) . PEG incorporation slightly decreased air permeability in extract-free samples (PCL/PEG 90:10: 0.047 ± 0.011; PCL/PEG 80:20: 0.045 ± 0.013 mL/cm²/s), correlating with reduced thickness and smaller fiber diameters. Among extract-loaded groups, PCL/PEG 80:20 + RR had the lowest air permeability (0.038 ± 0.003 mL/cm²/s), while 100PCL + RR maintained high values similar to the neat PCL mat (0.054 ± 0.011 mL/cm²/s), suggesting that RR did not significantly hinder gas exchange in PCL-only formulations. Mat thickness was also found to influence permeability behavior. Thicker mats (e.g., 100PCL: 0.091 ± 0.001 mm) showed higher WVTR and air permeability, while thinner mats (PCL/PEG 80:20 and extract-loaded formulations) exhibited lower air permeability and lower permeability indices. Together, these findings demonstrate that PEG content and halochromic extract incorporation finely tune the balance between moisture retention, vapor transmission and air exchange. Formulations like PCL/PEG + RR offer particularly favorable properties for chronic wound dressings, maintaining high WVTR while reducing water loss rate and gas penetration, all critical for wound hydration and biochemical sensing [214].

Table 8 - WVTR, water vapor permeability index (I), air permeability rates and mats thicknesses (n =3).

Electrospun Mats	Thickness (μm)	WVTR (g/m².day)	I (%)	Air permeability (mL/s)
100PCL	91 ± 1 μm	16646.46 ± 1019.830	310.89 ± 20.160	0.054 ± 0.010
PCL/PEG 90:10	60 ± 2 μm	15687.38 ± 370.990	274.44 ± 10.730	0.047 ± 0.011

PCL/PEG 80:20	49 ± 4 µm	16554.86 ± 1096.830	141.56 ± 19.710	0.045 ± 0.013
100PCL + RC	58 ± 8 µm	16231.58 ± 653.620	126.78 ± 39.140	0.016 ± 0.001
PCL/PEG 90:10 + RC	55 ± 5 µm	16810.80 ± 919.480	102.22 ± 38.300	0.043 ± 0.001
PCL/PEG 80:20 + RC	81 ± 2 µm	14941.14 ± 1301.960	101.44 ± 14.630	0.047 ± 0.011
100PCL + RR	47 ± 6 µm	15269.81 ± 471.980	122.78 ± 11.170	0.054 ± 0.011
PCL/PEG 90:10 + RR	52 ± 3 µm	16148.05 ± 235.220	110.11 ± 18.120	0.050 ± 0.005
PCL/PEG 80:20 + RR	53 ± 3 µm	16627.60 ± 172.84	85.78 ± 15.26	0.038 ± 0.003

III.3.9 Antioxidant activity

The antioxidant activity of PCL/PEG-based electrospun mats was evaluated using the DPPH radical scavenging assay over a 24 h period. Figure 15 illustrates the DPPH reduction profiles of mats loaded with RC (top) and RR (bottom) across different polymer blend ratios (100PCL, PCL/PEG 90:10, and PCL/PEG 80:20). After immobilization, the antioxidant profile was preserved: RC-loaded mats consistently showed higher radical-scavenging than RR, reflecting the behavior of the free extracts (Fig. 3B). Notably, fibers containing RC demonstrated a gradual increase in DPPH reduction, stabilizing near 50 % after ≈ 6 h, regardless of PEG content. While initial variability was observed, particularly in PEG-rich blends (e.g., PCL/PEG 80:20), the overall antioxidant effect was preserved. This sustained antioxidant activity is likely due to the controlled release of phenolic compounds from the mat, facilitated by PEG's hydrophilicity enhancing extract diffusion and rapid mat degradation. In contrast, RR-loaded fibers exhibited less consistent DPPH reduction, with values occasionally dropping below zero, especially in PEG-containing formulations. Phenolic –OH/COO^- groups bind PEG (ether O) and PCL (C=O) via H-bonding, transiently sequestering antioxidants and tightening hydrophilic domains-explaining the delayed DPPH response and moderated bulk swelling despite higher surface wettability. The negative DPPH values seen at early time points could be indicative of artefacts presence and limited extract accessibility-e.g., radical adsorption to the fibrous matrix and delayed release/solubilization of phenolics. As wetting and equilibration progress, more antioxidant compounds become available in the medium and activity is detected. Notably, RC-loaded formulations consistently overtook RR, in line with the higher anthocyanin content and reported antioxidant potency of *Brassica oleracea* extracts [215–217]. The fabrication process and polymer ratios did not markedly impair functionality, indicating that these mats-particularly PCL or moderate-PEG blends-can deliver immediate and sustained antioxidant action relevant to chronic wound management. Moreover, the antioxidant capacity of

RC remained effective across different fiber compositions, suggesting that the fabrication process and polymer ratios did not significantly impair extract functionality. RC-loaded mats, particularly in PCL or moderate PEG blends, show potential for delivering immediate and prolonged antioxidant activity, an essential property for reducing oxidative stress in chronic wounds and supporting the healing process.

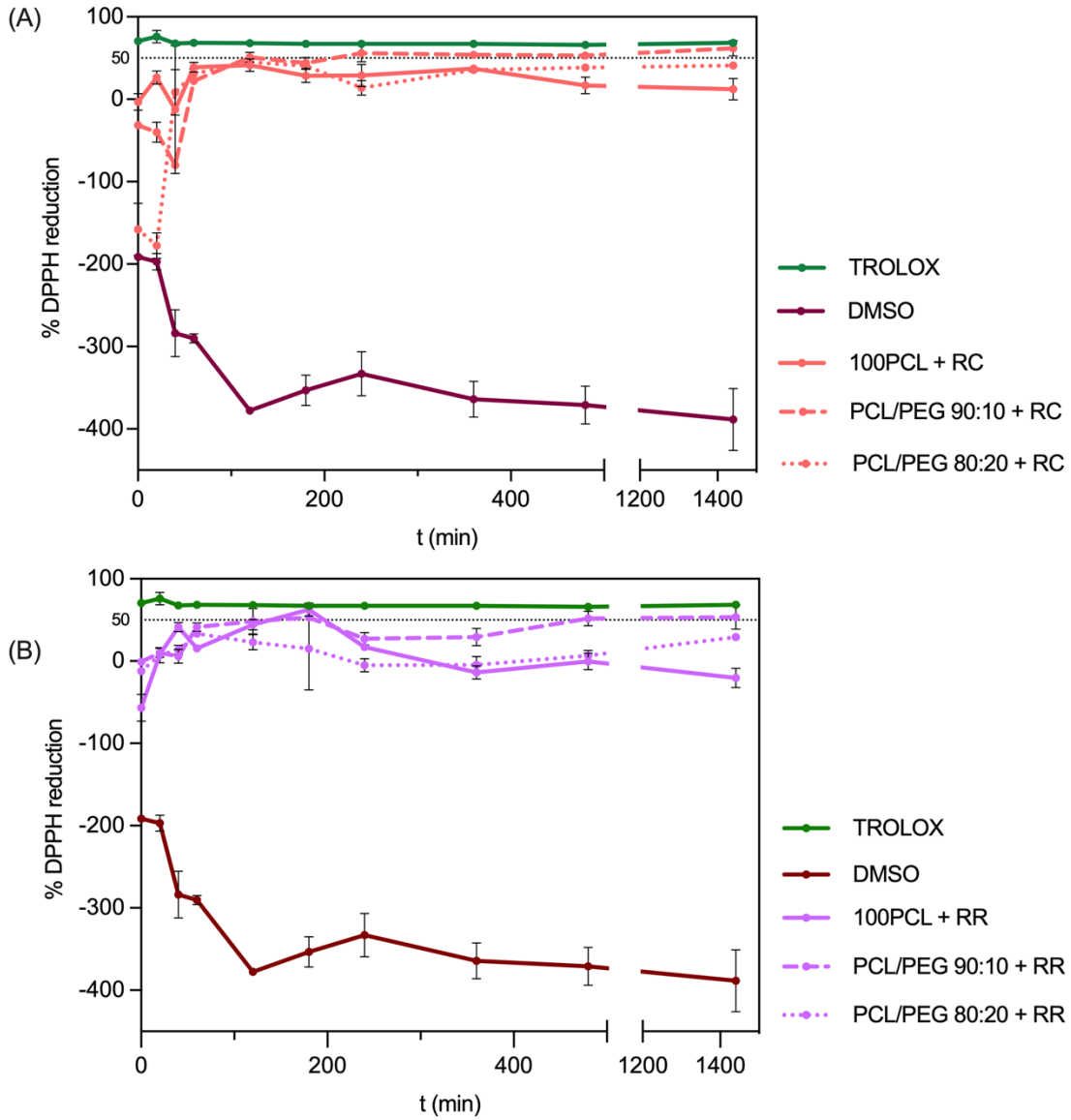


Figure 15 - DPPH scavenging activity (%) induced by halochromic extracts (A) RC and (B) RR, immobilized on mats, after 1, 2, 4, 6 and 24h incubation. Trolox was used as a positive control and DMSO as a negative control. Data were reported as mean ± SD (n=3). Statistical significance was determined via Tukey test, by applying multiple comparisons between RC and RR loaded mats. No significant differences were reported.

III.3.10 Surface Color and Optical Properties

The halochromic behavior of the developed electrospun mats was evaluated through colorimetric analysis using the CIELAB system, which quantifies perceptual color differences by tracking changes in L* (lightness), a* (green–red axis), and b* (blue–yellow axis) coordinates across a pH range from 4.0 to 10.0. The total color difference (ΔE*) was calculated using the standard ΔE equation, offering a comprehensive measure of visible color variation under different pH conditions [172]. The visual response was additionally supported by qualitative color grading blocks representing observed mat coloration. Table 9 and 10 shows the colorimetric response of RC and RR-loaded electrospun mats. All tested formulations exhibited noticeable pH-responsive behavior. Among these, the PCL/PEG 90:10 blend demonstrated the most consistent and perceptible chromatic progression across the entire pH range, with ΔE* values exceeding 10 starting from pH 5.0 and reaching a peak of 18,29 at pH 8.0. In comparison, 100PCL mats displayed only moderate ΔE* values (≈ 8-11 up to pH 7.0), with more significant changes occurring under alkaline conditions (ΔE* > 20 at pH 9.0 and 10.0). Meanwhile, PCL/PEG 80:20 also showed substantial responsiveness, particularly at pH 9.0 and 10.0, although the transitions were slightly less uniform across intermediate pH values. These results confirm the suitability of PEG-containing matrices for halochromic integration, with 90:10 providing a strong balance between responsiveness and visual clarity. For 100PCL + RR, ΔE* values were already high from pH 4.0 ahead and exceeded 30 units at alkaline pH, but the material showed excessive sensitivity and instability in intermediate pH ranges. In contrast, PCL/PEG 90:10 + RR exhibited a well-distributed and progressive color response across the entire spectrum, with ΔE* values ranging from 4,07 at pH 4.0 to 36,55 at pH 10.0. Importantly, color transitions remained perceptible and distinguishable at each pH step. PCL/PEG 80:20 + RR, although also responsive (ΔE* > 10 across the board), showed more variable performance, particularly in the neutral range, where differences were less distinguishable. The extracted ΔL*, Δa*, and Δb* values further confirmed that RR-loaded mats exhibited prominent transitions along both chromatic axes (a*, b*), reflecting anthocyanin-based shifts from reddish to purplish-blue hues. This behavior aligns with known anthocyanin responses in mildly acidic to basic environments and supports real-time pH monitoring in physiological conditions [162, 193]. In summary, PCL/PEG 90:10 loaded with RR extract consistently outperformed other formulations in terms of visible, quantifiable, and gradual color transitions from pH 4.0 to 10.0. This further reinforces its selection as a potential candidate for halochromic sensing layers in smart wound dressings, capable of detecting wound status shifts through non-invasive color grading. The

halochromic behavior of the electrospun mats was validated through a combination of visual pH grading and quantitative diffuse reflectance spectroscopy, enabling correlation between observable color changes and objective chromatic parameters. This dual qualitative–quantitative approach ensures the reliability of the pH-sensing performance across the physiologically relevant range.

Table 9 - CIELAB values and calculated ΔE* for 100PCL, PCL/PEG 90:10, and PCL/PEG 80:20 electrospun mats loaded with RC extract, after exposure to solutions across a pH range of 4.0–10.0. ΔE* indicates the total color difference from a reference color, and the corresponding color grading is visually represented below (n=3).

		pH 4.0	pH 5.0	pH 6.0	pH 7.0	pH 8.0	pH 9.0	pH 10.0
100 PCL + RC	L*	-4,11	-1,96	-3,50	-8,38	-11,67	-20,51	-18,58
	a*	-5,44	-7,44	-7,94	-7,77	-8,23	-5,04	-12,09
	b*	4,96	7,70	6,90	2,07	-1,24	-12,75	-9,16
	ΔE*	8,43	10,88	11,08	11,61	14,34	24,67	23,98
	Color Grading							
PCL/PEG 90:10 + RC	L*	-14,78	-10,52	-12,95	-10,30	-16,66	-16,51	-13,62
	a*	6,84	3,97	1,67	-1,43	-2,08	-2,99	-6,39
	b*	-3,24	-2,51	-2,87	-1,34	-7,28	-5,45	-3,75
	ΔE*	16,61	11,52	13,37	10,49	18,29	17,64	15,51
	Color Grading							
PCL/PEG 80:20 + RC	L*	-5,28	-11,72	-15,03	-15,05	-14,06	-17,05	-20,50
	a*	-0,47	3,43	3,48	-0,32	-3,78	-4,83	-8,88
	b*	5,96	0,18	-4,74	-4,23	-4,41	-8,73	-7,97
	ΔE*	7,98	12,21	16,14	15,63	15,22	19,76	23,72

	Color Grading	

Table 10 - CIELAB values and calculated ΔE* for 100PCL, PCL/PEG 90:10, and PCL/PEG 80:20 electrospun mats loaded with RR extract, after exposure to solutions from pH 4.0 to 10.0. The visual color grading confirms a progressive halochromic response (n=3).

		pH 4.0	pH 5.0	pH 6.0	pH 7.0	pH 8.0	pH 9.0	pH 10.0
100 PCL + RR	L*	-14,74	-13,66	-22,07	-20,58	-25,32	-35,41	-31,56
	a*	8,47	4,62	7,50	4,49	0,16	-1,39	-7,42
	b*	-3,07	-7,94	-11,33	-15,66	-19,69	-15,52	-25,42
	ΔE*	17,28	16,46	25,92	26,25	32,07	38,69	41,20
	Color Grading							
PCL/PEG 90:10 + RR	L*	-3,31	-13,14	-15,01	-17,19	-28,62	-33,10	-29,44
	a*	1,98	8,52	6,52	2,70	8,87	2,85	-5,42
	b*	1,29	-4,95	-8,26	-11,45	-16,12	-18,91	-20,97
	ΔE*	4,07	16,42	18,33	20,83	34,03	38,23	36,55
	Color Grading							
PCL/PEG 80:20 + RR	L*	-8,99	-11,30	-12,22	-12,67	-15,86	-11,74	-14,93
	a*	5,22	6,12	6,70	3,15	1,36	-8,00	-10,62

b*	5,67	2,60	-1,34	-1,55	-5,64	-5,15	-8,01
ΔE*	11,84	13,11	14,00	13,15	16,89	15,11	20,00
Color Grading							

III.3.11 Cell Metabolic Activity of the Extract-Loaded Electrospun Mats

Following the selection of RC and RR as the most cytocompatible extracts in solution, their incorporation into electrospun PCL/PEG mats was evaluated in terms of biological safety. As shown in Figure 16, all formulations, whether extract-free or loaded with RC or RR, demonstrated cell metabolic activities above the 70 % threshold in both mouse fibroblasts (L929, Figure 16 (A)) and human keratinocytes (HaCaT, Figure 16 (B)), confirming their cytocompatibility according to ISO 10993-5:2009 guidelines [169]. For both cell lines, extract-free mats (100PCL, PCL/PEG 90:10, and PCL/PEG 80:20) exhibited high metabolic activity, serving as a robust baseline for comparison. PCL and PEG are widely reported as biocompatible polymers for biomedical use, including wound dressings, with hydrolytic by-products being generally reported as non-cytotoxic at the levels released from electrospun mats [212]. In line with this evidence, extract-free PCL/PEG mats maintained L929 and HaCaT metabolic activity above the 70 % threshold. Even in formulations showing greater mass loss due to PEG, the leachates did not depress cell metabolism, indicating that polymer fragments remained below cytotoxic levels. Upon extract incorporation, slight decreases in cell metabolic activity were noted, particularly for PEG-rich formulations, but the values remained within the acceptable range. Among the extract-loaded groups, mats containing RC maintained the highest cytocompatibility overall, especially in HaCaT cells. RR-loaded mats showed slightly lower viability values, particularly in the PCL/PEG 80:20 composition, although still above 70 %. No statistically significant cytotoxic effects were observed upon extract immobilization, indicating that the encapsulation of RC and RR within the polymeric matrix mitigates any potential toxicity seen at higher extract concentrations in solution. These results confirm that the selected polymer ratios and extract concentrations used in the final mats (approximately 0.14 mg/mL) are within the safe range for both cell lines and that the incorporation of halochromic extracts does not compromise cytocompatibility supporting the suitability of RC and RR-loaded electrospun mats for biomedical use. Cytocompatibility was evaluated following the ISO 10993-5 standard, using both L929 fibroblasts and HaCaT keratinocytes as representative skin-related cell models. The reliability of the results was ensured through the use of appropriate positive and negative controls, triplicate measurements, and statistical analysis, allowing robust assessment of cellular metabolic activity.

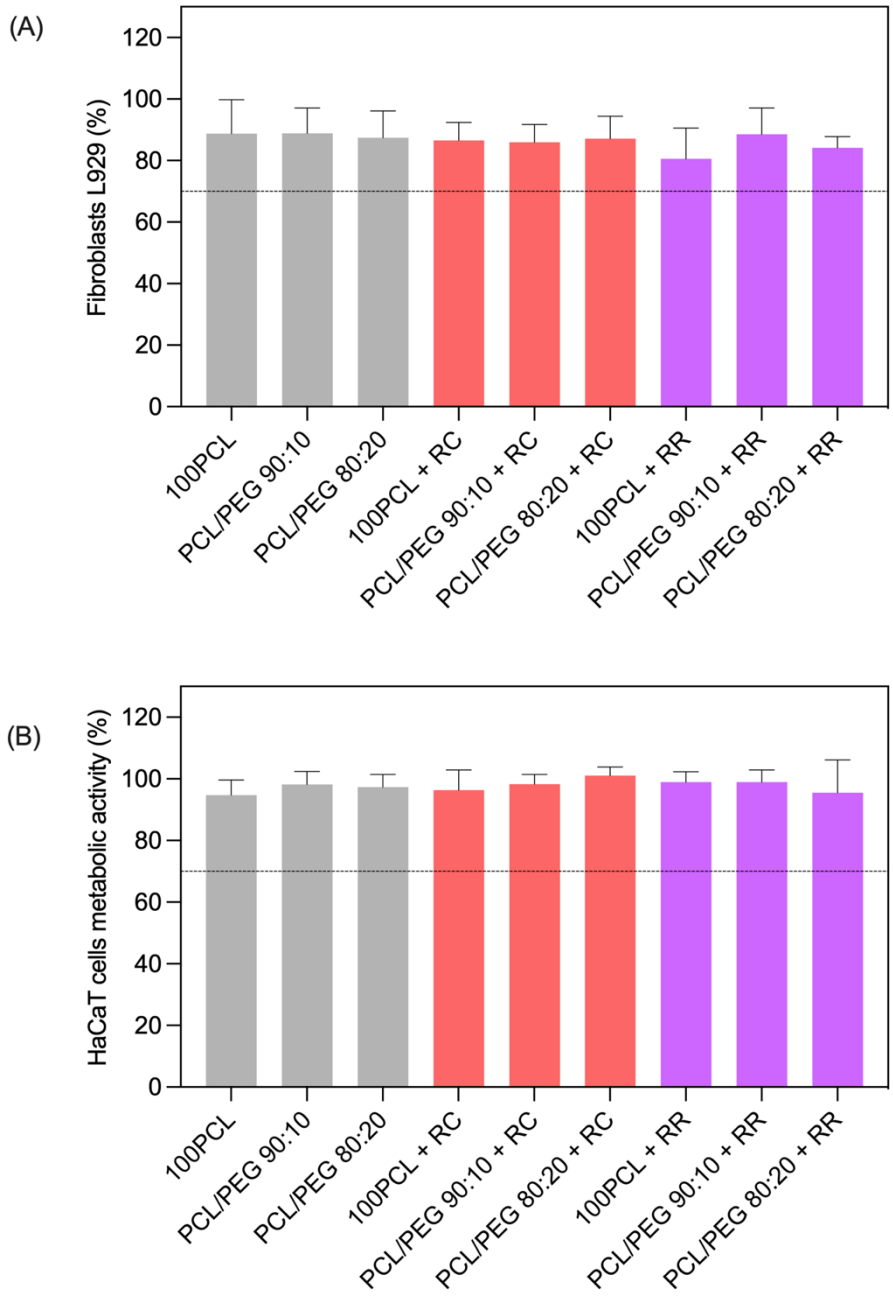


Figure 16 - Cytocompatibility evaluation of extract-loaded electrospun mats. Cell metabolic activity (%) of (A) L929 fibroblasts and (B) HaCaT keratinocytes after 24 h of direct contact with electrospun mats composed of PCL and PCL/PEG blends (90:10 and 80:20), either unloaded or loaded with RC or RR extracts Data are presented as mean ± standard deviation (n = 9). Statistical significance was determined via Tukey's test applying multiple comparisons between the different combinations, reporting no significant differences.

III.4 Practical Application and Clinical Relevance

The developed halochromic electrospun mats are intended for use as advanced wound dressings capable of non-invasive, real-time monitoring of chronic wound status. By visually

indicating local pH variations through distinct and easily interpretable color changes, these materials allow healthcare professionals and caregivers to rapidly assess wound progression without the need for specialized equipment or invasive sampling. In practical terms, the dressing can be applied directly to the wound bed in a manner similar to conventional polymeric wound dressings. Color transitions from acidic to alkaline ranges provide immediate feedback on infection risk, inflammation, or delayed healing, enabling timely clinical intervention, dressing replacement, or adjustment of treatment strategies. The use of biocompatible and biodegradable polymers, combined with naturally derived halochromic compounds, supports safe skin contact and reduces environmental and regulatory concerns associated with synthetic dyes or drug-loaded systems. As such, the proposed system is particularly suited for chronic wounds requiring frequent monitoring, including diabetic ulcers, pressure ulcers, and venous leg ulcers, as well as for use in outpatient settings or home-based wound care.

III.5 Conclusions

This study developed halochromic electrospun nanofibrous mats by directly incorporating natural anthocyanin-rich extracts into PCL/PEG blends, enabling real-time, visual pH monitoring targeted at chronic wound care applications.

- A systematic evaluation of polymer ratios and extract incorporation demonstrated that the PCL/PEG 90:10 formulation loaded with RR extract represents the most promising system, offering an optimal balance between structural performance, biological compatibility, and functional responsiveness.
- The selected formulation exhibited high swelling capacity, supporting effective wound exudate absorption, alongside moderate and controlled degradation rates, ensuring mechanical stability during prolonged application without premature loss of integrity.
- Enhanced surface wettability and hydrophilicity were achieved through PEG incorporation, promoting favorable conditions for cell adhesion, moisture regulation, and interaction with the wound environment.
- The optimized mats showed a clear, visually distinguishable halochromic response across a physiologically relevant pH range (4.0–10.0), allowing straightforward discrimination between acidic, neutral, and alkaline wound conditions associated with healing progression or chronicity.

- The developed materials maintained high cytocompatibility with both fibroblasts and keratinocytes, together with measurable antioxidant activity, supporting their suitability for contact with wounded skin.

Based on the results obtained, the PCL/PEG 90:10 + RR electrospun mat is recommended as a promising candidate for advanced wound dressings capable of non-invasive, real-time pH monitoring. Future studies should focus on long-term stability, *in vivo* validation, and integration into clinically relevant dressing formats.

CHAPTER IV

Integration of Cinnamaldehyde Essential Oil onto Chitosan-coated Nanostructured Lipid Carriers on ε-Polycaprolactone Electrospun Mats: A Novel Approach for Antifungal Chronic Wound Healing

CHAPTER IV – INTEGRATION OF CINNAMALDEHYDE ESSENTIAL OIL ONTO CHITOSAN-COATED NANOSTRUCTURED LIPID CARRIERS ON ε-POLYCAPROLACTONE ELECTROSPUN MATS: A NOVEL APPROACH FOR ANTIFUNGAL CHRONIC WOUND HEALING

Abstract

Chronic wounds pose a significant healthcare challenge due to their susceptibility to microbial infections, particularly fungal pathogens. Traditional antifungal treatments often exhibit limitations such as systemic toxicity and poor wound penetration. Herein, we present a novel approach for antifungal wound healing by integrating the essential oil (EO) cinnamaldehyde (CN) onto nanostructured lipid nanocarriers (NLCs) coated with chitosan (Ch) and then electrosprayed onto ε-polycaprolactone (PCL) electrospun mats. Spherical nanoparticles of ≈ 350 nm with ≈ 75 % EO efficient encapsulation were obtained via ultrasonication. CN possesses well-documented antifungal properties and was encapsulated within lipid nanocarriers based on cetyl palmitate and coated with Ch (Ch-NLCs/CN) to enhance stability and controlled release. Electrospun PCL mats with a fiber diameter of ≈ 1050 nm, porosity of ≈ 70-80 %, and Young's modulus of ≈ 0.17 N/mm provide a scaffold for wound dressing applications with a high surface area-to-volume ratio and modifiable mechanical properties, while maintaining adequate flexibility and tensile strength for skin-contact applications. Data confirmed the successful incorporation of the Ch-NLCs/CN without compromising the fibrous structure. Antifungal efficacy against three *Candida* strains was evaluated for all systems, with CN-loaded mats generally exhibiting higher antifungal activity, particularly at early time points (1-6 h), reaching reductions of up to ≈ 90-100 %. Additionally, *in vitro* cytocompatibility studies demonstrated the biocompatibility of the integrated system against a human keratinocyte cell line (HaCaT) and a mouse fibroblast cell line (L929). Overall, the combination of Ch-NLCs/CN onto PCL electrospun mats offers a promising approach for antifungal wound healing, providing sustained release and biocompatibility.

This chapter is based on the following scientific publication:

- Ana R. M. Ribeiro, Ana Isabel Barbosa, Catarina L. Seabra, Salette Reis, Helena P. Felgueiras, "Integration of Cinnamaldehyde Essential Oil onto Chitosan-coated Nanostructured Lipid Carriers on ε-Polycaprolactone Electrospun Mats: A Novel Approach for Antifungal Chronic Wound Healing". Colloids and Surfaces B: Biointerfaces (In Proof)

IV.1 Introduction

Throughout human evolution, the body has developed an efficient wound healing system. This system follows a precise sequence of steps: inflammation, cell growth, migration, the formation of new blood vessels, the deposition of a new cellular matrix, and tissue remodeling, all aimed at repairing damaged tissue [218, 219]. However, if this process is disrupted, it can lead to chronic wounds, particularly in the lower extremities. Conventional treatment methods, by means of systemic antibiotics and standard dressings, have shown limited effectiveness in reducing wound chronicity. These approaches often fail to prevent microbial growth and can even disrupt the healing process and the formation of new tissue [220, 221]. Advances in the understanding of the mechanisms of healing and regeneration have shed light on more appropriate treatments for chronic situations. Despite these developments, effectively managing and treating chronic wounds remains a major therapeutic challenge [222].

Among the major complications associated with chronic wounds is microbial infection, with fungal pathogens, particularly *Candida* species, emerging as significant contributors to wound persistence and delayed healing [223, 224]. Fungal infections can thrive in the moist environment of chronic wounds and are often resistant to conventional antifungal agents [225]. Moreover, systemic antifungal treatments frequently present limitations such as low bioavailability at the wound site, potential cytotoxicity, and disruption of local tissue regeneration [226]. Therefore, there is an urgent need for localized, biocompatible antifungal therapies that can enhance wound healing while minimizing adverse side effects.

In recent years, bioengineered wound dressings that combine antimicrobial activity with regenerative properties have gained increasing attention. Among natural compounds, essential oils (EOs) have shown promising antimicrobial, antioxidant, and anti-inflammatory effects [227, 228]. Cinnamaldehyde (CN), a major component of cinnamon oil, has demonstrated potent antifungal activity against a broad spectrum of fungal species, including drug-resistant *Candida* strains [229]. However, the clinical application of EOs is limited by their volatility, instability, and easy oxidative degradation [230]. Encapsulation within nanocarriers has emerged as a viable strategy to overcome these drawbacks, enhancing EO stability and allowing for sustained release at the target site [231, 232]. Nanostructured lipid carriers (NLCs) have shown potential as delivery vehicles for lipophilic biomolecules like CN due to their high loading capacity, biocompatibility, and ability to protect sensitive compounds from physicochemical degradation [233–235]. Coating these carriers with chitosan (Ch), a natural polysaccharide known for its antifungal and wound-healing features,

can further enhance their stability, bio-adhesion, and controlled release characteristics [235, 236]. This multi-functional approach influences both the antimicrobial activity of CN and the bioactivity of Ch to generate a synergistic antifungal effect [237–239]. Electrospun polymeric mats, particularly those based on ε-polycaprolactone (PCL), offer an ideal scaffold for wound dressings due to their high surface area, porosity, and mechanical tunability [240, 241]. By integrating Ch-coated NLCs loaded with CN via electrospraying onto electrospun PCL mats, a multifunctional wound dressing can be fabricated that combines antifungal activity with structural support for tissue regeneration [242, 243]. In this study, we report the development and characterization of an innovative system and evaluate its antifungal efficacy and cytocompatibility *in vitro*. This novel approach holds significant potential for advancing localized antifungal therapy in chronic wound care.

IV.2 Materials and Methods

IV.2.1 Materials

PCL (Mw 80,000) was purchased from PolySciences, Inc. (Valley Road, Warrington). Chloroform (CHF) and dimethylformamide (DMF) were obtained from Riedel-de-Haen (Seelze, Germany) and PanReac AppliChem (Barcelona, Spain), respectively. Chitosan (Ch; Low molecular weight) was purchased from Sigma-Aldrich (USA). Tween® 80 was purchased from Sigma-Aldrich (USA). Cetyl palmitate pellets were kindly given by Gattefossé SAS (Saint-Priest Cedex, France). Citral (Ci), Geraniol (Ge), and Cinnamaldehyde (CN) EOs with ≥ 96, 97, and 95 % purity, respectively, were acquired from Sigma-Aldrich (USA). Acetic acid and ethanol 90 % were purchased from VWR (USA) and Fisher Scientific (Pittsburgh, Pennsylvania, USA), respectively. Fungal strains, *Candida albicans (C. albicans)*, *parapsilosis (C. parapsilosis),* and *tropicalis (C. tropicalis)* were supplied by American Type Culture Collection (ATCC, Virginia, USA). For fungi growth, Sabouraud Dextrose Agar (SDA) and Sabouraud Dextrose Broth (SDB) were purchased from HiMedia Laboratories (India). The phosphate-buffered saline solution (PBS) used at 0.01 M was prepared at pH 7.4 from the combination of sodium chloride (NaCl; 8.00 g/L), potassium chloride (KCl; 0.20 g/L), sodium phosphate dibasic (Na_2HPO_4; 1.44 g/L), and monopotassium phosphate (KH_2PO_4; 0.24 g/L), all obtained from Sigma-Aldrich. Mouse fibroblast cell line (L929) was purchased from the European Collection of Authenticated Cell Cultures (ECACC, Salisbury, UK), and the human keratinocyte cell line (HaCaT) was purchased from Cell Lines Service GmbH (CLS, Eppelheim, Germany). Dulbecco's Modified Eagle Medium (DMEM, high glucose, GlutaMAX, pyruvate) was acquired at

Avantor VWR (Radnor, Pennsylvania, USA); Penicillin-streptomycin (10,000 U/mL) and Trypsin-EDTA (0.25 % w/v) were purchased from Gibco Life Technologies (California, USA); Fetal Bovine Serum (FBS) was obtained from Biowest (Missouri, USA); Trypan blue, Sodium resazurin, and Triton X-100 were purchased from Sigma-Aldrich (St.Louis, Missouri, USA). Reagents were all used as commercially available, without additional chemical modifications.

IV.2.2 Essential Oils Characterization

IV.2.2.1 Essential Oils Minimum Inhibitory and Fungicidal Concentrations

Ci, Ge, and CN minimum inhibitory concentrations (MICs) were determined using the broth microdilution method described by Wiegand et al. [168], which is an adaptation of the standard published by the Clinical and Laboratory Standards Institute (CLSI) and the European Committee on Antimicrobial Susceptibility Testing (EUCAST) [169]. Fungal inocula were prepared from a single colony of *C. albicans*, *C. parapsilosis,* and *C. tropicalis* and incubated overnight at room temperature (RT) and 150 rpm, in aerobic conditions in SDB broth. Tests were carried out using an initial concentration of ≈ 1.0×10^5 CFUs/mL in SDB. Working solutions of 20.48 mg/mL were prepared for each EO in distilled water. These were added to the first column of 96-well plates in a volume of 100 μL. Serial dilutions (1:2 v/v) were made with SDB in the consecutive wells, to a final volume of 50 μL. Then, to each of these wells, 50 μL of the fungi suspensions were added. EO-free fungi suspensions and culture media were also used as controls, respectively positive and negative for fungi growth. Absorbance readings at the wavelength of 640 nm (EZ READ 2000 Microplate Reader, Biochrom, UK) were made before and after plate incubation for 24 h at RT and 150 rpm. The MIC for each EO/fungi combination was established as the concentration at which fungi did not show any growth, determined visually and confirmed by differences in absorbance readings (between 0 and 24 h). The minimal fungicidal concentrations (MFC) were established by culturing the fungi suspensions at MIC and the concentrations in its vicinity (concentrations higher and lower than the MIC value) and counting the number of grown colonies. Briefly, aliquots of 10 μL of each of these cell suspensions, diluted from 10^{-1} to 10^{-4} in PBS, were cultured in SDA for 48 h at 28 °C. The absence of colonies established the MFC. The 24-hour incubation period for MIC determination was selected to allow sufficient time for fungal cells to undergo at least one complete growth cycle under standard conditions, enabling accurate detection of growth inhibition by the extracts. In contrast, MFC determinations were performed after a 48-hour incubation to ensure that any surviving fungal cells, including those in a lag phase or with slower metabolic activity, could be

detected. This extended incubation period provides a more reliable assessment of the fungicidal potential of the EOs by confirming the absence of viable colonies.

IV.2.3 Preparation of Nanostructured Lipid Carriers (NLCs)

The preparation of the NLCs was performed according to the hot ultrasonication method previously developed by Vieira et al. [244, 245]. The lipid phase containing the cetyl palmitate (150 mg) lipid and EO (50 mg) was heated to 75 °C until complete solubilization of the EO in the lipid matrix. The solution of surfactant (Tween® 80, 50 mg) in double-deionized water was previously heated in a water bath at the same temperature. The aqueous phase containing the surfactant (7 mL) was added to the lipid phase with EO, and then it was homogenized using a probe sonicator (VCX130; Sonics & Materials, Inc., Newtown, CT, USA), at 80 % amplitude for 5 min. The obtained nanosuspension was rapidly cooled in an ice bath with continuous stirring. Control NLCs were similarly prepared but without the EO.

IV.2.4 NLCs coated with Chitosan (Ch-NLCs)

Unloaded and EO-loaded NLCs were coated with Ch by a gentle physical adsorption procedure [245]. Here, low molecular weight Ch was initially dissolved at 10 mg/mL in 2 % (v/v) acetic acid and filtered using a 0.8 μm filter to remove any impurities. NLCs were then immersed in the Ch solution and left for 24 h at RT under gentle shaking to promote Ch binding and a complete coating.

IV.2.5 NLCs Characterization

IV.2.5.1 Particle Size, Polydispersity Index, and Zeta Potential

The particle size, polydispersity index (PDI), and zeta potential of Ch-NLCs and Ch-NLCs/EO were determined using a Particle Size Analyzer (Brookhaven Instruments Corporation, Software: Particle Sizing v.5 Brookhaven Instruments; Holtsville, NY, USA), operating at a scattering angle of 90°, at 25 °C. Zeta potential (ZetaPALS, Brookhaven Instruments Corporation, Software: PALS Zeta Potential Analyzer v.5, Brookhaven Instruments; Holtsville, NY, USA) was also determined at the same testing conditions. Samples were diluted in double-deionized ultrapure water (1:100 v/v) for analysis.

IV.2.5.2 Determination of Encapsulation Efficiency

Entrapment efficiency (EE %) of EO in the nanoformulations was determined by UV-spectrophotometry. A dilution of the NLCs (1:20 v/v) in double-deionized water was centrifuged (Allegra® X-15R, Beckman Coulter, California, USA) through centrifugal filter units (Amicon® Ultra Centrifugal Filters, Ultracel-50 KDa, Darmstadt, Germany) at 3500 rpm, 20 °C, during 10 min or until complete separation between the NLCs retained in the filter unit and the aqueous phase corresponding to the filtrate with lose EO. The collected supernatant was quantified by UV–vis spectrophotometry (Jasco V-660 Spectrophotometer, Piscataway, NJ, USA) at 288 nm. The amount of EO incorporated was quantified against a calibration curve of the EO in ethanol: water (9:1 v/v), ranging from 0.5 to 12.0 μg/mL (Abs = 0.204 × [EO] + 0.0274, R^2 = 0.9979), and following Equation 2:

$$EE\ \% = \frac{m_{EO\ total} - m_{EO\ unnentraped}}{m_{EO\ total}} \qquad \text{Equation 2}$$

IV.2.5.3 Storage Stability Studies

The storage stability of the Ch-NLCs and Ch-NLCs/EO was studied over an 8 week-period, with three independent batches of each type of developed formulation. Physicochemical parameters described in section 2.4.1 and EO quantification described in 2.4.2 were monitored weekly and compared to the starting point (production time or week zero). Particles were stored protected from light both at RT and 4 °C.

IV.2.6 Electrospinning and Electrospray Deposition

PCL polymeric solution was prepared at 14 % w/v in CHF/DMF (9:1) (v/v). The solution was continuously stirred at 50 °C for 4 h. Viscosity was assessed using a viscometer Brookfield DV-II + Pro (spindle 21, 50 rpm at RT during 5 min, with 30 s time points), while conductivity was determined using a Thermo Scientific Benchtop Meter (Orion Versa Star Pro). Electrospinning was conducted with a fixed voltage of 12 kV applied to the steel capillary needle with an inner diameter of 18 Gauge (G). The distance between the needle tip and the aluminum collector was 17 cm. The solution feeding rate was set at 0.7 mL/h. RT and relative humidity (RH) were controlled and maintained at 20-22 °C and 65-70 %, respectively. The electrospray deposition of the Ch-NLCs onto the PCL fibers was performed using aqueous suspensions of the particles for 1 h deposition (lipid weight). The suspensions were electrosprayed on the surface of the PCL electrospun mat.

The electrospinning conditions were a fixed voltage of 16 kV applied to the steel capillary needle with an inner diameter of 20 Gauge (G). The distance between the needle tip and the aluminum collector was 10 cm. The solution feeding rate was set at 1.2 mL/h. RT and RH were controlled and maintained constant. After production, the fibrous mats were stored in a desiccator for complete elimination of potential solvent residues.

IV.2.7 Characterization of Electrospun Mats

IV.2.7.1 Field emission gun scanning electron microscopy (FEG-SEM)

Micrographs (NOVA 200 Nano SEM, FEI Company) were collected with an accelerating voltage of 10 kV. Mats were initially coated with a thin film (10 nm) of Au–Pd (80-20 wt. %) using a 208HR high-resolution sputter coater (Cressington Company, Watford WD19 4BX, UK) coupled to an MTM-20 Cressington High-Resolution Thickness Controller. The average fiber diameter of the electrospun mats was determined by conducting 100 fiber measurements on three micrographs of PCL at a magnification of 10.000 ×, simulating the diameter distribution with a log-normal function. Images were processed using the ImageJ® software (version 1.53a, National Institutes of Health, USA). The porosity of the mats was analyzed using the same ImageJ® software and methodology as reported in [170].

IV.2.7.2 Fourier-transform Infrared Spectroscopy in Attenuated Total Reflectance Mode (ATR-FTIR)

To examine the chemical groups presented on the EOs, nanoformulations, and electrospun mats, ATR-FTIR spectra were collected by ATR-FTIR, following the protocol presented in section 2.5.2. from chapter III.

IV.2.7.3 Thermal Gravimetric Analysis (TGA)

Thermal degradation behavior was assessed by weight loss monitoring with the increase of temperature in the range of 25–600 °C, at a heating rate of 10 °C/min under a dynamic nitrogen atmosphere and flow rate of 200 mL/min (inert environment) on a STA 7200 Hitachi® (Fukuoka, Japan), using aluminum pans. The initial mass of each sample was 5 ± 2 mg. Results were plotted as the percentage of weight loss vs. temperature.

IV.2.7.4 Differential Scanning Calorimetry (DSC)

Thermal properties were also evaluated using a DSC 822 Mettler Toledo (Columbus, USA). Samples were submitted to a first heating step (0-100 °C) (to remove absorbed and adsorbed water), followed by cooling and then to a second heating step from 0 to 500 °C at a rate of 10 °C/min, under a dynamic nitrogen atmosphere, and a flow rate of 20 mL/min (inert environment). DSC curves were plotted with heat flow vs. temperature.

IV.2.7.5 Mechanical Testing

The mechanical performance of electrospun mats was evaluated by determining their maximum elongations at break and breaking strength, following the protocol described in section 2.5.4. from chapter III.

IV.2.7.6 Wettability and Surface Free Energy (SFE)

Water contact angle measurements and surface free energy calculations were conducted according with the protocol described in section 2.5.6. from chapter III.

IV.2.7.7 *In-vitro* Swelling and Degradation

Electrospun mats hydrating properties was analyzed by determining the DS of each mat typology, as described in section 2.5.7. from chapter III. In order to evaluate the stability of such mats when exposed to physiological media, the degradation profile of the fibers was analyzed, also following the procedure presented in section 2.5.7. from chapter III.

IV.2.7.8 Permeabilities

To assess the electrospun mats' capacity for air exchange and moisture retention, air and water/vapor permeability studies were conducted according with the protocol described in section 2.5.8. from chapter III.

IV.2.8 Electrospun Mats Antifungal Efficiency

IV.2.8.1 Time-Kill Kinetics Evaluations

Mat samples of 11 mm of diameter, electrosprayed with unloaded and EO-loaded Ch-NLCs, were tested for their killing abilities against *C. albicans*, *C. parapsilosis,* and *C. tropicalis* fungi suspensions, adjusted to 1.0×10^5 CFUs/mL in SDB broth (adaptation of ASTM-E2149-01).

Electrospun mats/fungi solutions were incubated at 28 °C and 150 rpm. After 0 (before agent action), 1, 2, 4, 6, and 24 h of incubation, fungi were serially diluted (10^{-1} to 10^{-4} in PBS), cultured on SDA plates, and further incubated for another 48 h at 28 °C. Fungal reduction determinations were made between control suspensions (without a sample) and mats containing the unloaded and EO-loaded Ch-NLCs. Colonies of surviving fungi were counted and reported as fungi reduction % ± standard deviation (S.D.).

IV.2.9 Cell Culture Conditions and Viability Assessment

The cytocompatibility of all nanoformulations towards mouse fibroblast cell line (L929) and human keratinocytes cell line (HaCaT) were evaluated using direct contact assay. The cytocompatibility testing was performed according to the international standard ISO 10993-5:2009. Cells were thawed and sub-cultured in DMEM medium supplemented with 10 % (v/v) FBS and 1 % (v/v) penicillin-streptomycin, at 37 °C in a humidified atmosphere of 5 % CO_2, until reaching 90 % confluence. Thereafter, cells were chemically detached from cell culture flasks using trypsin-EDTA at 0.25 % (w/v). The number of cells was determined using a Neubauer Chamber, labelling cells with trypan blue (ratio 1/1) and cells were counted using a Motic® Inverted Microscope (Motic, Barcelona, Spain). Cells were seeded in 96-well tissue culture polystyrene plates for nanoformulations' cytocompatibility, and 48-well tissue culture polystyrene (TCPS, VWR®, Pennsylvania USA) plates for mats cytocompatibility, at the densities of 5×10^4 and 12×10^4 cells per well, respectively, and incubated for 24 h at 37 °C in a humidified atmosphere of 5 % CO_2. The experiments were performed using fibroblast cells in passage 120-17 and keratinocytes cells line in passage 26–31.

After 24 h of incubation, the metabolic activity of the cells was evaluated by resazurin staining. Briefly, 0.01 mg/mL of sodium resazurin in medium solution was added to the wells and incubated for 2 h at 37 °C and 5 % CO_2 atmosphere. Afterwards, 100 µL of supernatant were transferred to a black 96-well plate (Falcon®, Arizona, USA) and the fluorescence was measured (λ_{ex} = 560 and λ_{em} = 590 nm) using a microplate fluorometer (Cytation 5 Cell Imaging Reader - BioTek Instruments, Vermont, USA). The percentage of metabolic activity was evaluated by Equation 1 as an indicator of cells viability:

$$Metabolic\ activity\ (\%) = \frac{Flu_s - Flu_{nc}}{Flu_{pc} - Flu_{nc}} \times 100 \qquad \text{Equation 1}$$

where the Flus is the fluorescence of the samples, Flu_{nc} is the fluorescence of the negative control, the untreated cells, and Flu_{pc} is the fluorescence of the positive control, the treated cells with 2 % (v/v) Triton X-100 solution.

IV.2.10 Cytocompatibility Testing

IV.2.10.1 Cell Culture Conditions and Viability Assessment

The cytocompatibility of electrospun mats towards the mouse fibroblast cell line (L929) and human keratinocyte cell line (HaCaT) was evaluated using direct contact assay as described in section 2.2.2.

IV.2.11 Statistical analysis

Data were treated using GraphPad Prism Software (v7.03, GraphPad Software Inc., USA). All assays were conducted at least three independent times, and data were expressed as mean ± S.D. Statistically significant was determined as having $p < 0.05$.

IV.3 Results and Discussion

IV.3.1 Essential Oils Properties

CN, Ci, and Ge were selected as representative EO and subjected to a preliminary screening to identify the most suitable antifungal agent for incorporation into an NLC. These compounds were chosen as model molecules due to their well-documented antifungal activity and structural diversity, namely two monoterpenes (Ge and Ci) and one aromatic aldehyde (CN), all containing conjugated double bonds that are known to enhance reactivity and biological activity [246]. These structural features have been associated with the ability to interact with fungal membranes, making them promising candidates for the treatment of infected wounds. Furthermore, these EOs have been reported to exhibit both antifungal and anti-inflammatory properties, which are highly relevant in wound healing applications [247]. The EOs were initially characterized by ATR-FTIR (Figure 17 (A)) to confirm their chemical identity. Ge displayed the characteristic O–H stretching band around 3300 cm^{-1}, together with aliphatic C–H stretching vibrations near 2900 cm^{-1} and C=C stretching bands, consistent with its monoterpenoid alcohol structure. Ci exhibited intense absorption bands associated with the aldehydic C=O stretching at approximately 1670–1690 cm^{-1}, in addition to C=C stretching and aliphatic C–H vibrations, in agreement with its α, β-unsaturated aldehyde structure. CN showed a well-defined conjugated aldehyde C=O stretching band around 1680 cm^{-1},

along with aromatic C=C stretching vibrations near 1600 and 1500 cm^{-1} and characteristic fingerprint-region bands, confirming its aromatic aldehyde structure [248]. Although the three compounds share unsaturated functional groups, their distinct chemical structures (alcohol, aliphatic aldehyde, and aromatic aldehyde) are expected to influence their biological activity and interaction with cellular membranes. As summarized in Table 11, Ge and Ci presented relatively high MIC and MFC against *C. albicans*, *C. parapsilosis*, and *C. tropicalis*, indicating moderate antifungal activity. In contrast, CN exhibited substantially lower MIC and MFC, particularly against *C. albicans* and *C. tropicalis*, revealing a significantly higher antifungal potency. These differences can be explained by the distinct mechanisms of action of the EOs. In general, EOs exhibit antifungal activity primarily through disruption of fungal cell membranes, leading to increased permeability, leakage of intracellular components, and ultimately cell death. Additionally, they may interfere with ergosterol biosynthesis, a key component of fungal membranes, thereby compromising membrane integrity and function. CN has been widely reported to exhibit strong antifungal activity due to its ability to penetrate fungal cells and react with intracellular proteins and enzymes, disrupting metabolic processes and inducing oxidative stress. Also, its conjugated aldehyde group can interact with nucleophilic groups in cellular components, leading to protein denaturation and inhibition of essential cellular pathways. In contrast, Ge and Ci, although capable of interacting with lipid membranes, generally show weaker antifungal effects, which may explain their higher MIC and MFC values [249]. The superior antifungal activity of CN clearly distinguished it from Ge and Ci, leading to its selection as the most promising candidate for subsequent nanoencapsulation and integration into the developed systems.

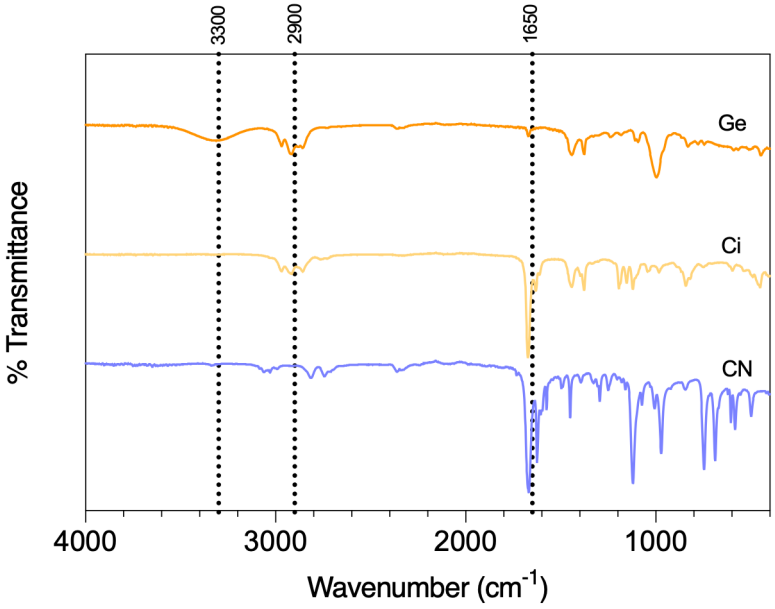


Figure 17 - ATR-FTIR spectra of the three EOs (Ge, Ci, and CN) collected in the range of 4000 to 400 cm^{-1}.

Table 11 - MIC and MFC values for the three EOs compounds, Ge, Ci and CN. Data are presented in mg/mL.

	MIC (mg/mL)			MFC (mg/mL)		
	C. albicans	*C. parapsilosis*	*C. tropicalis*	*C. albicans*	*C. parapsilosis*	C. tropicalis
Ge	10.24	10.24	5.12	10.24	10.24	10.24
Ci	10.24	10.24	5.12	10.24	10.24	10.24
CN	0.40	6.40	0.20	1.60	6.40	0.40

IV.3.2 Characterization of Unloaded and Loaded Ch-NLCs

The prepared nanoformulations were first physicochemically characterized in terms of hydrodynamic diameter, PDI, and zeta potential by DLS, as well as EE % of the selected essential oil, CN, to confirm the successful formation of the system prior to stability assessment. Before the Ch coating, the lipid nanoparticles presented mean diameters of approximately 220 nm, which is consistent with typical NLC systems [250]. Following Ch adsorption, particle size increased to approximately 300-350 nm (Figure 18 (A)), indicating a formation of a polymeric shell around the lipid core. This increase in size is widely reported for Ch-coated lipid nanoparticles and is attributed to the deposition of the polymer layer onto the nanoparticle surface [251, 252] [37]. In parallel, the zeta potential shifted toward highly positive values after coating, reflecting the presence of protonated amine groups from chitosan and confirming successful surface modification. Such a positive surface charge is particularly advantageous for colloidal stability, as it promotes

electrostatic repulsion between particles and prevents aggregation. Consistently, the zeta potential remained strongly positive (typically within the +25 to +35 mV range) (Figure 18 (C)), which is commonly considered indicative of stable dispersions and effective surface coverage by Ch [38, 39][253]. Additionally, PDI values were generally below ≈ 0.30 (Figure 18 (B)), indicating moderately narrow size distributions and acceptable homogeneity, which is a key requirement for nanoparticle-based delivery systems [36,38]. Regarding encapsulation efficiency, CN entrapment remained consistently high, with EE values around ≈ 75 % (Figure 18 (D)), confirming the high affinity of this lipophilic compound for the mixed solid–liquid lipid matrix and supporting the effectiveness of the formulation strategy. Such values agree with those reported for EO-loaded NLCs and are generally associated with improved retention of volatile compounds within the lipid core [252, 254]. After confirming the successful formation of nanoformulations with suitable physicochemical properties, their stability was evaluated over an 8-week period under two storage conditions (RT and 4 °C). Overall, CN entrapment remained relatively stable throughout the storage period, maintaining values close to ≈ 75 %, indicating that the lipid matrix effectively retained the EO over time. Similarly, zeta potential values remained strongly positive (Figure 18 (C)), suggesting that the Ch coating was preserved and continued to provide electrostatic stabilization. PDI values also remained below ≈ 0.30 for all conditions (Figure 18 (B)), indicating that no significant aggregation or broadening of size distribution occurred during storage. Despite the general favorable charge and PDI profiles, a formulation-dependent difference emerged in the evolution of particle size: Ch-NLCs/CN progressively increased in diameter over time, whereas the unloaded Ch-coated controls remained comparatively stable (Figure 18 (A)). This divergence suggests that the presence of CN introduces additional structural dynamics that can manifest as gradual growth of the hydrodynamic diameter during storage. A size increase in lipid nanoparticles upon storage is a common observation and can arise from several, potentially concurrent mechanisms, including lipid polymorphic transitions (re-organization toward more ordered crystalline forms), partial expulsion or re-distribution of the encapsulated compound [250, 254]. The physicochemical properties of CN may further contribute to this behavior. As a small, reactive, and partially volatile aromatic aldehyde, CN can interact with both the lipid matrix and the surrounding aqueous environment, potentially affecting interfacial tension and lipid packing over time. Such interactions may promote gradual particle growth, even in systems where surface charge remains sufficiently high to prevent aggregation. Similar trends have been reported for EO-loaded NLCs, where certain bioactive compounds induce measurable changes in particle size during storage, highlighting that

EO incorporation can influence nanoparticle stability [255]. Furthermore, temperature-dependent increases in particle size have also been described for CN-loaded lipid systems, reinforcing the role of both storage conditions and payload properties in long-term behavior [256]. Notably, the absence of significant size changes in unloaded Ch-NLCs indicates that Ch coating itself does not compromise stability, and that the observed effects are primarily associated with the presence of CN within the lipid core [257]. From an application standpoint, the observed size increase in Ch-NLCs/CN at later storage times was not considered a critical limitation for the intended study. In practice, these dispersions are used within the first 2–3 weeks after preparation to functionalize the electrospun mats. Within this period, the formulations maintain a positive zeta potential, acceptable PDI, and stable CN entrapment, supporting their suitability for processing and short-term handling. Moreover, once deposited into the fibrous matrices, the nanoparticles are effectively transferred from a colloidal state to a solid or semi-solid immobilized state, which mitigates the relevance of long-term dispersion stability as a product constraint. This justification is supported by composite nanofiber strategies reported in the literature, where Ch-coated lipid nanoparticles embedded in electrospun fibers can be stored/handled as a solid system [258]. Therefore, while the CN-loaded dispersions show signs of reduced long-term colloidal stability relative to unloaded controls, their performance within the operational timeframe and their subsequent immobilization in the final fibrous construct support their practical robustness for the proposed application.

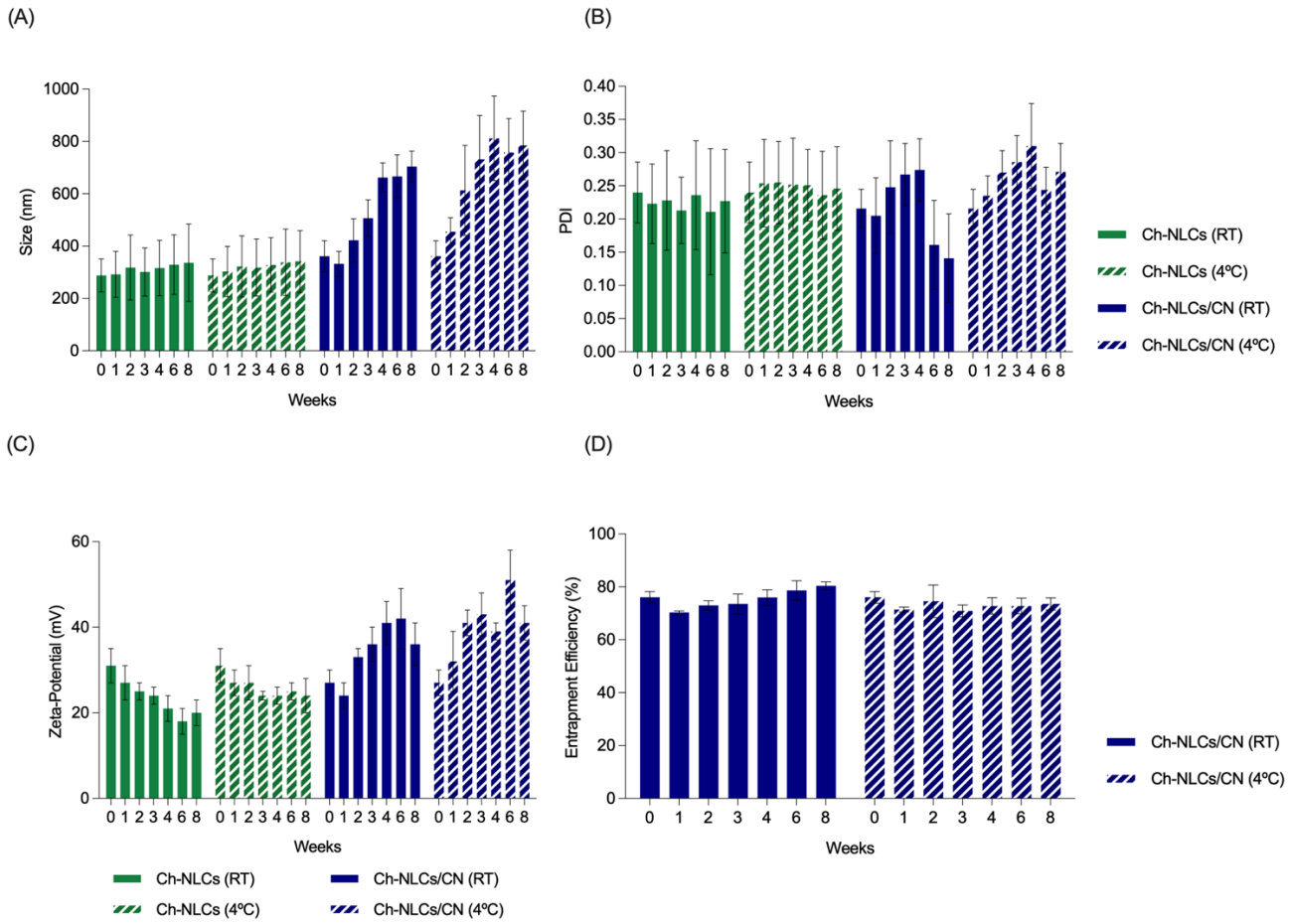


Figure 18 – Storage stability of Ch-based nanoformulations over 8 weeks. (A) Size, (B) PDI, and (C) zeta potential of unloaded Ch-NLCs and loaded Ch-NLCs/CN monitored over 8 weeks, relative to the production week (week 0), when stored at RT or at 4 °C. (D) Entrapment efficiency (%) of CN in Ch-NLCs/CN during the same storage period under both storage conditions. Data are presented as mean ± standard deviation (n=3). Statistical significance was determined via Tukey's test, applying multiple comparisons between samples within the same timepoint, reporting no significant differences.

IV.3.3 Mats Morphology

Following the selection and stabilization of the CN-loaded nanoformulations, their integration into PCL mats was investigated, with particular emphasis on how the deposition strategy influenced fiber morphology and supported the intended dressing concept. Importantly, the Ch-NLCs loaded and unloaded with CN were not blended into the polymeric spinning solution. Instead, the nanoformulations were deposited by electrospray directly onto the surface of the electrospun PCL mats. This approach was deliberately chosen to preserve the physicochemical integrity of the nanoparticles and to spatially localize the antifungal component at the surface of the fibrous substrate, where interaction with the wound environment is most relevant. Four different fibrous

architectures were explored within a sandwich-like dressing design: a PCL + Ch-NLCs/CN loaded and unloaded (control without EO) layer intended to be in direct contact with the skin, and a PCL + Ch-NLCs/CN loaded and unloaded + PCL configuration, in which an additional PCL electrospun layer partially covers the electrosprayed nanoparticles. FEG-SEM micrographs (Figure 19) confirmed that all architectures resulted in continuous, randomly oriented fibrous networks without bead formation, with fiber diameters of ≈ 1050 ± 380.2 nm with 0.135 ± 0.013 mm and 0.143 ± 0.006 mm thickness, respectively, and demonstrated that the electrospraying step did not compromise the underlying electrospun structure. In the PCL + Ch-NLCs/CN and without CN architecture (Figure 19 (A,B)), fibers exhibited a slightly roughened surface with localized deposits and irregularities, which can be attributed to the presence of Ch-coated nanoparticles deposited onto the fiber surface during electrospraying. Similar morphologies have been reported in electrospun mats functionalized by post-deposition of nanoparticles, where surface roughness and particulate features are considered indicative of successful surface functionalization rather than processing artifacts [259, 260]. In contrast, the PCL + Ch-NLCs/CN and no CN + PCL architecture (Figure 19 (C,D)) displayed smoother and more homogeneous fibers, as the second electrospun PCL layer effectively covered and entrapped the previously electrosprayed nanoformulations, reducing the visibility of surface-associated features. All architectures exhibited high porosity, ranging between ≈ 75–80 % for the single-layer PCL + Ch-NLCs systems and slightly lower values of ≈ 70–75 % for the multilayer PCL + Ch-NLCs + PCL configurations. The slight reduction in porosity in the multilayer system can be attributed to the additional PCL layer, which partially covers pore openings and increases the overall packing density of the fibrous network. Despite this decrease, all mats maintained a highly porous and interconnected structure, which is essential for oxygen permeability and exudate management.

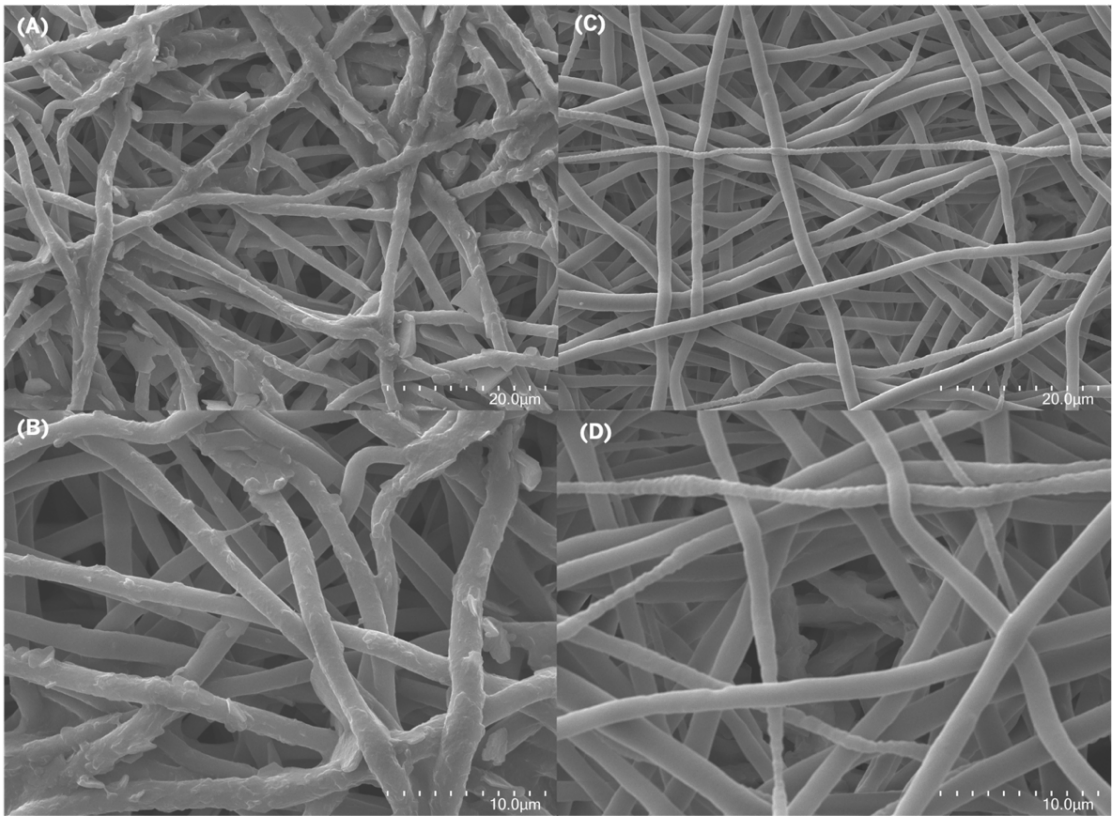


Figure 19 – (A) FEG-SEM micrographs at 5.000× and (B) 10.000 × magnitude of PCL+Ch-NLCs/CN architecture. (C) FEG-SEM micrographs at 5.000× and (D) 10.000 × magnitude of PCL+Ch-NLCs/CN+PCL architecture. Representative micrographs of the corresponding unloaded systems (without CN) exhibited similar morphological features to those presented in (A) and (B), indicating that CN incorporation did not significantly affect fiber morphology. Scale bars in micrographs represent 20 and 10 µm.

The observed morphologies are consistent with the physicochemical properties of the electrosprayed Ch-NLCs/CN dispersions (Table 12), which are characterized by low viscosity, high electrical conductivity, and a strongly positive zeta potential. These properties are particularly favorable for electrospraying, as low viscosity facilitates droplet formation, while high conductivity enhances charge accumulation and promotes fine, uniform deposition onto the fibrous collector [261]. Previous studies have shown that Ch-based or highly charged nanoparticle dispersions can be efficiently electrosprayed onto electrospun mats, leading to homogeneous surface coverage and strong electrostatic interactions with the underlying fibers [262]. The positive surface charge of the Ch-NLCs nanoformulations further supports electrostatic adhesion to the relatively hydrophobic PCL fibers, contributing to the stable immobilization of the nanoparticles observed in the SEM images. From a functional standpoint, the use of electrospray as a post-processing step provides clear advantages for the intended wound dressing application. By avoiding the direct incorporation of nanoparticles into the polymeric solution, potential issues related to jet instability, nanoparticle

degradation, or uneven distribution during electrospinning are minimized. Moreover, surface-localized Ch-NLCs/CN in the PCL + Ch-NLCs/CN mats are expected to promote rapid interaction with the wound environment and efficient antifungal action, while the PCL + Ch-NLCs/CN + PCL configuration offers an additional level of protection and controlled exposure for a more sustained, prolonged nanoparticle-induced bioactivity. Together, these results demonstrate that electrospray-assisted functionalization is a robust and versatile strategy for integrating bioactive nanoformulations into electrospun scaffolds.

Table 12 - PCL and Ch-NLCs loaded and unloaded aqueous solutions viscosity, conductivity, zeta potential, and pH values. Data are reported as mean ± S.D. (n=3).

Solutions	Viscosity (Pa·s)	Conductivity (μS/cm)	Zeta Potential (mV)	pH
PCL	1.577 ± 0.134	0.115 ± 0.005	-11.170 ± 0.001	7.300 ± 0.001
Ch-NLCs	0.081 ± 0.009	930.156 ± 5.871	29.005 ± 0.005	4.544 ± 0.007
Ch-NLCs/CN	0.093 ± 0.004	965.546 ± 3.678	29.157 ± 0.009	4.220 ± 0.007

IV.3.4 Chemical Analysis

ATR-FTIR analysis was performed to confirm the chemical composition of the developed nanoformulations and to verify the successful integration of Ch-NLCs loaded and unloaded onto the electrospun PCL mats without altering the chemical integrity of the individual components. In Figure 20 (A), low-molecular-weight Ch exhibited its characteristic absorption bands, including the broad O–H and N–H stretching vibrations in the 3200-3500 cm^{-1} region, C–H stretching around 2900 cm^{-1}, and amide I and II bands near 1650 and 1580 cm^{-1}, respectively, which are typical of partially deacetylated Ch. After nanoparticle formation, the spectra of unloaded Ch-NLCs retained the main Ch-related bands, although with reduced intensity and slight band broadening, reflecting the presence of the lipid matrix and possible hydrogen bonding interactions between Ch and lipid components at the nanoparticle surface [263]. Moreover, the appearance and increased intensity of bands in the region around 1730-1750 cm^{-1} are associated with the ester carbonyl groups of the lipid components, confirming the successful incorporation of the lipid phase into the nanoformulation. Upon CN loading, the Ch-NLCs/CN spectra showed subtle but visible changes, including increased intensity in the carbonyl stretching region around 1680-1700 cm^{-1}, which can be attributed to the aldehyde group of CN. Minor bands observed in the fingerprint region (approximately 750-900 cm^{-1}) may also be associated with aromatic C–H bending vibrations of CN, further supporting its presence within the nanoformulations. The absence of new peaks or

significant band shifts suggests that CN was physically encapsulated within the lipid matrix rather than chemically reacting with Ch or lipid components, a behavior commonly reported for EO-loaded lipid nanoparticles and desirable for preserving EO bioactivity [264]. Figure 20 (B) presents the ATR-FTIR spectra of neat PCL electrospun mats and mats functionalized by electrospraying Ch-NLCs loaded and unloaded with CN, with and without an additional PCL covering layer. The spectrum of PCL displayed its characteristic absorption bands, including the strong ester carbonyl stretching at approximately 1720 cm^{-1}, C–O–C stretching vibrations in the 1100–1300 cm^{-1} range, and aliphatic C–H stretching bands near 2940 and 2860 cm^{-1}, confirming the chemical integrity of the electrospun fibers. After electrospray deposition of Ch-NLCs nanoformulations, the PCL spectra were largely preserved, with only minor changes in band intensity and baseline shape, particularly in regions associated with O–H/N–H stretching and carbonyl vibrations. A slight increase in absorption in the 3200–3500 cm^{-1} region can be observed, corresponding to the presence of Ch-derived hydroxyl and amine groups, while subtle contributions in the 1650–1700 cm^{-1} region further suggest the presence of CN-loaded nanoparticles at the fiber surface. These subtle variations are consistent with the presence of a thin layer of Ch-coated nanoparticles on the fiber surface and indicate successful surface functionalization without chemical degradation of the polymer. In the PCL + Ch-NLCs/CN + PCL architecture, the spectra closely resembled that of neat PCL, reflecting the dominant contribution of the outer PCL layer and confirming that the additional electrospun layer effectively covered the nanoformulations. The attenuation of Ch and CN-related bands in this configuration supports the interpretation that the nanoformulations are physically encapsulated within the multilayer structure rather than exposed at the surface. Overall, the ATR-FTIR results demonstrate that the electrospray-assisted deposition of CN-loaded Ch-NLCs and unloaded onto electrospun PCL mats did not induce chemical incompatibilities or undesirable interactions, supporting the physical integration of the nanoformulations within the fibrous constructs and preserving the chemical integrity of all components.

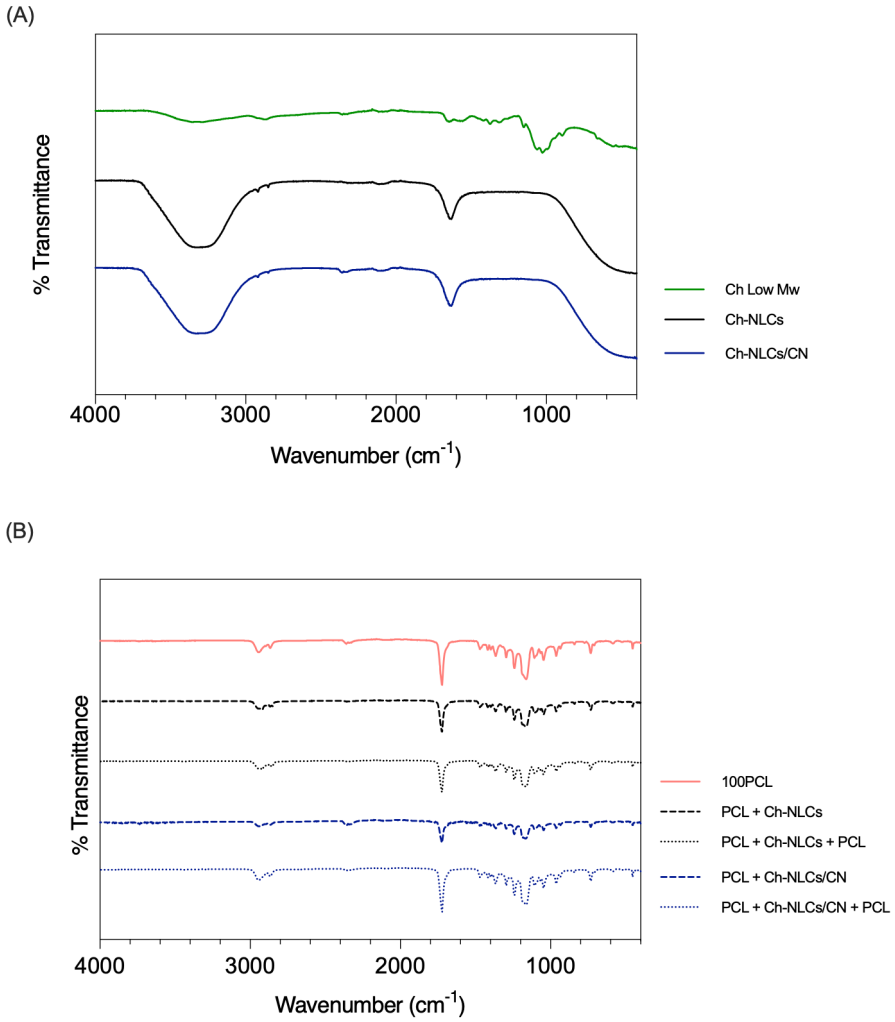


Figure 20 - ATR-FTIR spectra of (A) Ch-NLCs loaded and unloaded with CN, and of (B) PCL electrospun mats electrosprayed with Ch-NLCs loaded with CN and unloaded collected in the range of 4000 to 400 cm^{-1}.

IV.3.5 Mats Thermal Stability

Thermal analysis was carried out to verify whether CN encapsulation and the subsequent electrospray/electrospinning assembly steps affected the thermal integrity of the nanoformulations and of the final PCL-based architectures (Figure 21). In the TGA profiles (Figure 21 (A)), the aqueous dispersions of Ch-NLCs and Ch-NLCs/CN showed an intense mass loss at low temperatures (below ≈ 120 °C), which is consistent with the evaporation of water from the dispersions and is commonly reported for water-containing Ch- or polysaccharide-based systems [265]. After this initial event, only a small residual mass fraction remained, indicating that the dominant contribution to the TGA signal in these samples is indeed the aqueous phase, while the solid fraction (lipids/Ch) represents a minor portion of the total mass. By contrast, the electrosprayed/electrospun mats exhibited the expected high thermal resistance typical of dry PCL

structures: all PCL-containing architectures remained essentially stable up to approximately the 300 °C, followed by a sharp degradation step occurring predominantly between ≈ 350 and 450 °C (Figure 21 (A)). This thermal decomposition window is widely reported for PCL (including electrospun PCL films) and reflects the polymer's main chain scission and volatilization processes [266, 267]. Notably, incorporating the nanoformulations onto the PCL mats did not introduce additional low-temperature weight-loss steps comparable to those observed for the aqueous dispersions, supporting that the final constructs are effectively "dry" systems and that the nanoformulations are immobilized on/within the fibrous structure. The CN-loaded architectures showed only subtle differences relative to their unloaded counterparts, which can be rationalized by the presence of a small amount of CN and by possible plasticization/interfacial effects at the nanoparticle–fiber interface. However, the overall degradation pattern remained governed by PCL, indicating that the thermal robustness of the dressing was preserved. Consistent trends were observed in DSC thermograms (Figure 21 (B)). The aqueous nanoformulations exhibited a dominant endothermic event in the ≈ 100-150 °C region, which is compatible with dehydration/evaporation phenomena in aqueous dispersions and/or with overlapping transitions of the lipid phase. Importantly, CN loading did not generate new thermal events indicative of chemical reaction or incompatibility, supporting that CN is incorporated mainly through physical entrapment within the lipid matrix rather than covalent bonding. This is in line with previous reports where thermal analysis is used as supportive evidence of successful CN encapsulation in lipid nanoparticle systems, typically showing preservation of the carrier transitions and the absence of new reaction-associated peaks [268]. Moreover, lipid nanoparticle systems frequently display broadened or shifted thermal transitions compared with bulk lipids due to nanosizing and reduced crystallinity; these effects are often interpreted as favorable for payload accommodation and retention in NLC/solid lipid nanoparticle (SLN)-type matrices [253]. To complement the TGA data, DSC analysis was performed to assess thermal transitions, crystallinity, and the thermal behavior of individual components, blends, and extract-loaded mats. The resulting thermograms are shown in Figure 21 (B) (Main DSC thermal events: T_o onset temperature, and ΔH enthalpy in SI - Table SD22). For the fibrous constructs, the DSC traces were dominated by the PCL-based architecture, with thermal events occurring at higher temperatures in agreement with the degradation regime observed in TGA. A broad endothermic transition was observed at ≈ 380-420 °C for all PCL-containing samples, corresponding to PCL thermal degradation, with only slight shifts in onset for CN-loaded systems, indicating that EO incorporation does not significantly compromise thermal

stability. At lower temperatures, Ch-NLCs and Ch-NLCs/CN displayed a distinct endothermic peak at ≈ 110–130 °C, attributed to the melting of the lipid phase, confirming the semi-crystalline nature of the NLCs. Slight variations in peak position upon CN loading suggest changes in lipid packing and crystallinity. Additionally, a small thermal event below 100 °C was observed, particularly in Ch-containing systems, which can be associated with water loss or relaxation of chitosan chains. This transition is not evident in TGA due to the minimal mass change involved. In PCL-containing samples, these lipid-related peaks become less pronounced, especially in multilayer architectures, indicating partial masking of the nanoformulations by the PCL matrix. Taken together, the combined TGA/DSC results indicate that (1) CN loading and Ch coating do not compromise the fundamental thermal performance of the carrier materials, (2) the electrosprayed nanoformulations can be integrated into PCL mats without inducing premature thermal instability, and (3) the final dressing-relevant constructs retain the characteristic thermal stability of PCL, an important attribute for handling, storage and processing under conditions well below the polymer's degradation temperature.

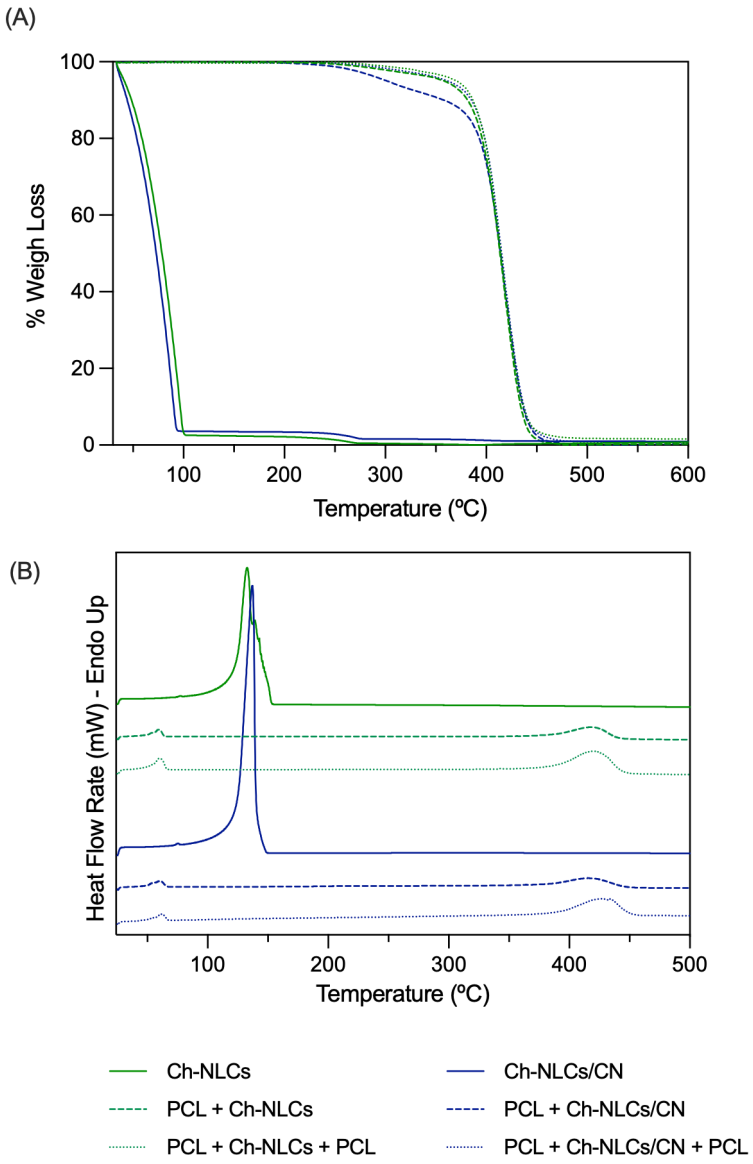


Figure 21 - Thermal stability profiles of Ch-based nanoformulations and electrosprayed/electrospun PCL mats. (A) TGA profiles of unloaded and CN-loaded Ch-NLCs nanoformulations, as well as of CN-loaded and unloaded electrosprayed/electrospun PCL mats for both architectures. (B) DSC thermograms of unloaded and CN-loaded Ch-NLCs nanoformulations and of unloaded and CN-loaded electrosprayed PCL mats for both architectures.

IV.3.6 Mechanical Properties

The mechanical performance of the electrospun mats was evaluated to assess whether the electrospray deposition of Ch-NLCs and the construction of multilayer architectures affected the structural integrity and flexibility required for wound dressing applications (Table 13). Neat PCL mats exhibited a low Young's modulus (≈ 0.17 N/mm), high elongation at break (> 300 %), and relatively low tensile strength, reflecting the intrinsic ductility and elastic behavior of electrospun PCL networks. These properties are characteristic of PCL fibrous mats and are considered

advantageous for skin-contact applications, as they allow the material to conform to irregular wound surfaces while accommodating physiological movements without mechanical failure [269, 270]. Comparable ranges of Young's modulus and elongation at break have been reported for electrospun PCL membranes intended for wound care and soft tissue applications, reinforcing the suitability of the baseline material [270, 271]. The incorporation of Ch-NLCs/CN by electrospray onto the PCL mats did not induce significant changes in stiffness, as evidenced by the nearly unchanged Young's modulus values relative to neat PCL. Similarly, the incorporation of unloaded Ch-NLCs also preserved the stiffness of the mats, with Young's modulus values remaining around ≈ 0.17 N/mm, indicating that the presence of the nanoformulations alone does not affect the elastic response of the fibrous network. This observation indicates that the surface functionalization strategy preserves the bulk mechanical response of the fibrous scaffold, which is expected, given that the nanoformulations are deposited at the surface, rather than embedded within the polymer fibers. A slight reduction in elongation at break was observed for the PCL + Ch-NLCs/CN mats, accompanied by an increase in tensile strength. A comparable trend was also observed for the PCL + Ch-NLCs systems, which exhibited a decrease in elongation at break and an increase in break strength relative to neat PCL, suggesting that the presence of the nanoparticles, independently of CN loading, contributes to limiting fiber mobility while enhancing stress transfer within the network. This trend suggests that the presence of surface-deposited nanoparticles may introduce additional inter-fiber interactions or friction points that limit extreme deformation while improving load transfer across the fibrous network [272]. Similar mechanical responses have been reported in electrospun mats functionalized with nanoparticulate coatings, where surface modifications lead to modest stiffening or strengthening without compromising overall flexibility [273]. The PCL + Ch-NLCs/CN + PCL architecture displayed mechanical properties intermediate between the neat PCL and the single-layer functionalized mats. A similar behavior was observed for the unloaded multilayer system (PCL + Ch-NLCs + PCL), which also presented slightly reduced elongation at break while maintaining Young's modulus values comparable to the other samples and break strength values higher than neat PCL. The additional PCL layer slightly reduced elongation at break while maintaining Young's modulus values comparable to the other samples, and break strength values remained higher than those of neat PCL. This behavior can be attributed to the multilayer structure, in which the outer PCL layer contributes to load bearing and distributes applied stress more evenly across the scaffold, while still retaining the elastic nature of the electrospun network. Overall, the mechanical results demonstrate that the electrospray-assisted functionalization with Ch-NLCs/CN

and unloaded Ch-NLCs, as well as the assembly of multilayer architectures, do not compromise the key mechanical attributes of electrospun PCL mats. The combination of low stiffness, high extensibility, and moderate tensile strength supports their suitability for wound dressing applications, where flexibility, conformability, and resistance to mechanical damage during handling and use are critical requirements.

Table 13 - Young Modulus, elongation at break, and break strength of the two PCL electrosprayed mat architectures and neat PCL mats tested at a displacement rate of 10.0 mm/min (n=3).

Electrospun Mats	Young Modulus (N/mm)	Elongation at break (%)	Break strength (MPa)
PCL	0.174 ± 0.070	313.77 ± 18.112	0.051 ± 0.008
PCL + Ch-NLCs	0.170 ± 0.049	286.176 ± 32.988	0.072 ± 0.033
PCL + Ch-NLCs + PCL	0.173 ± 0.050	280.114 ± 33.456	0.068 ± 0.019
PCL + Ch-NLCs/CN	0.175 ± 0.054	281.778 ± 40.560	0.072 ± 0.019
PCL + Ch-NLCs/CN + PCL	0.178 ± 0.065	276.222 ± 15.313	0.061 ± 0.013

IV.3.7 Wettability

The surface wettability of the electrospun mats was evaluated by static water contact angle (WCA) measurements to assess how electrospray functionalization with Ch-NLCs nanoformulations and the construction of multilayer architectures influenced surface hydrophilicity, a key parameter for wound dressing performance (Figure 22). Neat PCL mats exhibited a high contact angle of 133.95° ± 2.59°, confirming their intrinsically hydrophobic character, which is well documented for PCL due to its aliphatic polyester backbone and low surface energy [274]. Accordingly, neat PCL presented a low total surface free energy of approximately 22-24 mN/m, dominated by its dispersive component, with a negligible polar contribution. Such hydrophobicity, while beneficial for maintaining structural integrity, is generally unfavorable for wound healing applications where moderate wettability is desired to promote fluid absorption and cell interaction [275]. Upon electrospray deposition of Ch-NLCs/CN, a marked reduction in contact angle was observed, with WCA decreasing to 120.24° ± 1.99° for the PCL + Ch-NLCs/CN architecture. A similar reduction was observed for the unloaded system (PCL + Ch-NLCs), which presented a contact angle of 122.05° ± 2.77°, indicating that the presence of CN does not significantly influence surface wettability. This decrease was accompanied by a clear increase in surface free energy, to

approximately 30 mN/m and 29 mN/m, respectively mainly due to an increase in the polar component. This behavior can be attributed to the presence of Ch at the fiber surface, which introduces hydrophilic functional groups such as hydroxyl and protonated amine moieties capable of forming hydrogen bonds with water [263]. The similar wettability values obtained for both loaded and unloaded systems demonstrate that surface properties are primarily governed by the chitosan coating, rather than by the encapsulated CN. This observation further supports that CN remains effectively entrapped within the lipid core, with minimal surface exposure that could otherwise alter surface properties. Similar increases in surface free energy and corresponding reductions in WCA have been reported for electrospun PCL mats functionalized with Ch or Ch-based nanoparticles, demonstrating that even surface-localized modification is sufficient to alter interfacial properties without compromising bulk material characteristics [276–278]. In addition, the surface roughness introduced by the electrosprayed nanoformulations, as observed in SEM analysis, may further enhance apparent wettability by increasing effective surface area and promoting mixed wetting regimes. The PCL + Ch-NLCs/CN + PCL architecture exhibited a further, although modest, decrease in WCA to 118.85° ± 4.37°. In contrast, the corresponding unloaded multilayer system (PCL + Ch-NLCs + PCL) showed a slightly higher contact angle of 124.66° ± 3.78°, which can be attributed to the dominant contribution of the outer PCL layer and the reduced exposure of the underlying nanoformulations. Despite the outermost layer being PCL, the total SFE remained elevated relative to neat PCL, reaching values of approximately 29 mN/m. This indicates that the multilayer assembly does not fully mask the influence of the underlying nanoformulations. Instead, the hierarchical porosity of the fibrous structure, interlayer connectivity, and partial exposure of polar domains contribute to the overall surface energetics. Importantly, these results highlight the role of Ch not only in modulating surface wettability but also in stabilizing the nanoformulations. The presence of Ch at the nanoparticle surface forms a protective hydrophilic shell that reduces the diffusion of CN toward the external environment, minimizing premature release or leakage. Consequently, the absence of significant differences between CN-loaded and unloaded systems in terms of wettability further supports the effective encapsulation and stabilization of CN within the lipid core, preventing its direct interaction with the surface. From a functional perspective, the progressive decrease in WCA from neat PCL to nanoformulation-functionalized architectures indicates a controlled modulation of surface wettability achieved through electrospray-assisted modification. While the mats remain predominantly hydrophobic, the enhanced wettability is advantageous for wound dressing applications.

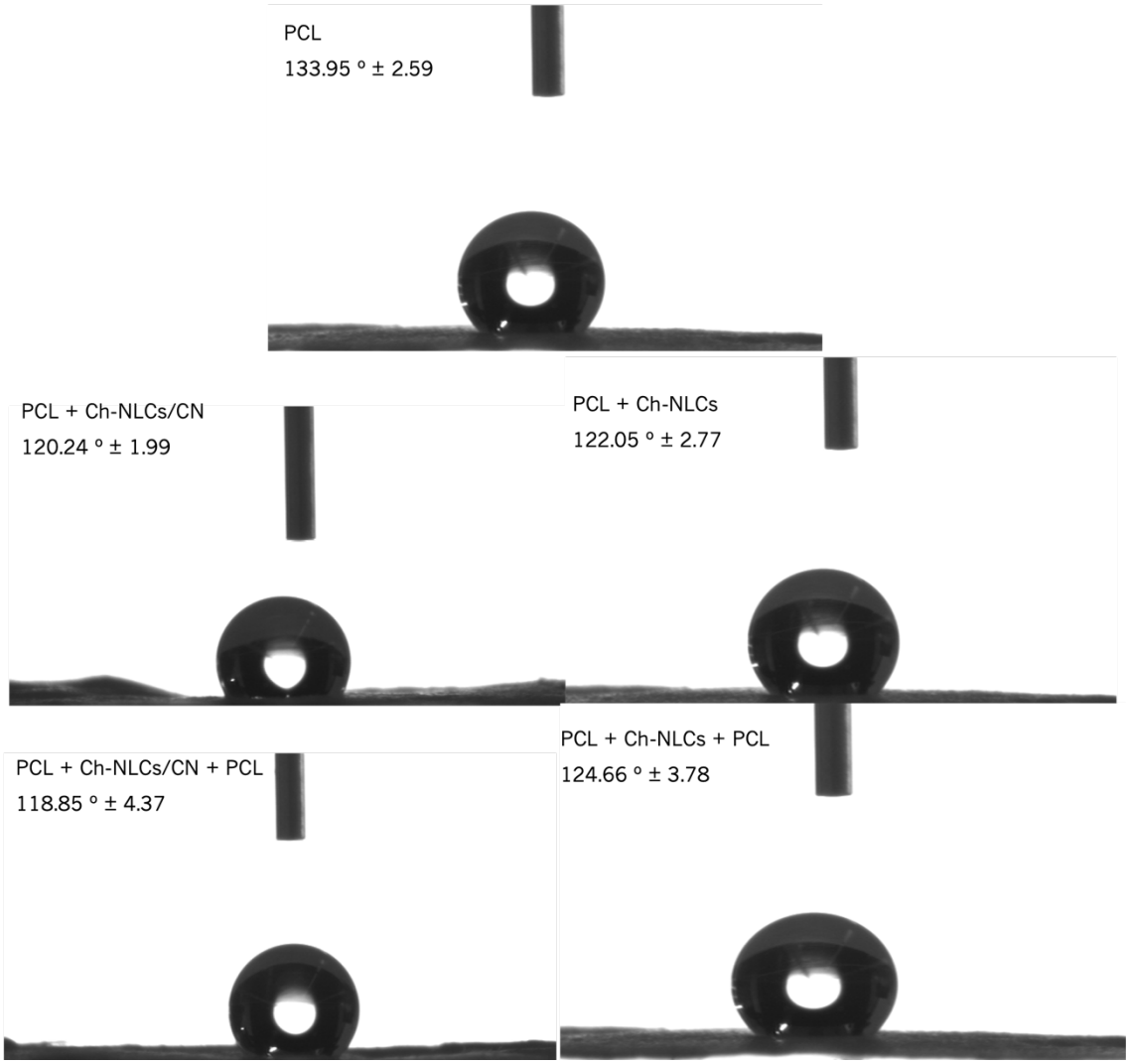


Figure 22 - Wettability of neat PCL and the four PCL electrospun mats architectures electrosprayed with Ch-based nanoformulations by WCA measurements (n=5) using established ASTM standardized methods.

IV.3.8 *In-vitro* Swelling and Degradation

The swelling behavior and mass variation of the electrospun mats were evaluated under physiological-like conditions to further assess their suitability for wound dressing applications (Figure 23). When incubated in PBS at 37 °C, neat PCL mats exhibited a comparatively low degree of swelling over the entire 168 h period (Figure 23 (A)), which is consistent with the intrinsically hydrophobic nature of PCL and its limited affinity for aqueous media. In contrast, all architectures functionalized with Ch-NLCs loaded and unloaded showed a significantly higher degree of swelling at all time points, reaching values close to 80 %. This pronounced increase can be directly associated with the presence of Ch at the fiber surface, introduced via electrospray deposition. Ch contains abundant hydrophilic functional groups, such as hydroxyl and protonated amine groups, which promote water uptake through hydrogen bonding and electrostatic interactions [264]. Similar

enhancements in swelling capacity have been reported for electrospun PCL mats modified with Ch or Ch-based coatings, where even surface-localized modifications substantially alter hydration behavior without requiring bulk blending of hydrophilic polymers [277, 279]. Notably, the swelling profiles of the PCL + Ch-NLCs and PCL + Ch-NLCs + PCL CN loaded and unloaded architectures were comparable, although the multilayer configuration showed a slightly moderated swelling response at some time points. This behavior suggests that the additional PCL layer partially restricts direct water access to the nanoformulation-rich interface, while still allowing fluid penetration through the porous fibrous network. Such moderated swelling is often considered advantageous in wound dressings, as excessive swelling may compromise mechanical stability, whereas insufficient swelling may limit exudate management [280]. The statistically significant differences observed between neat PCL and nanoformulation-functionalized mats at all time points further highlight the effectiveness of electrospray-assisted functionalization in tuning hydration behavior. Mass variation studies over 28 days (Figure 23 (B)) revealed that neat PCL mats exhibited increasingly negative mass loss values over time, indicating progressive water uptake rather than polymer degradation. This behavior is characteristic of PCL, which degrades slowly under physiological conditions due to its semi-crystalline structure and hydrophobicity, often requiring months rather than weeks to show measurable mass loss [275]. The more pronounced negative mass values observed for neat PCL can be attributed to water retention and salt accumulation within the fibrous network, consistent with its swelling profile and limited chain scission over the studied timeframe. In contrast, both Ch-NLCs-functionalized architectures displayed minimal mass variation throughout the 28-day period, with values remaining close to zero or slightly positive. This stabilization effect may result from a balance between water and salts absorption and the possible release or reorganization of surface-deposited nanoformulations, leading to an apparent mass equilibrium. Additionally, the Ch-coated nanoparticles may partially occupy pore spaces or reinforce inter-fiber junctions, reducing excessive water retention within the mat. Comparable mass stability trends have been reported for electrospun systems incorporating surface-modified layers or nanoparticle coatings, where the added components modulate water–material interactions and slow down apparent mass changes without inducing premature degradation [275, 279]. From a functional perspective, the combination of enhanced swelling capacity and minimal mass variation observed for the nanoformulation-functionalized mats is particularly relevant for wound dressing applications. Increased swelling supports effective exudate absorption and maintenance of a moist wound environment, which is beneficial for tissue regeneration, while the absence of significant

degradation over 28 days ensures structural integrity during the typical dressing residence time. The multilayer PCL + Ch-NLCs/CN + PCL architecture further offers a balanced profile, combining controlled hydration with mechanical stability, aligning well with the proposed sandwich-like dressing concept in which different layers are designed to perform complementary roles.

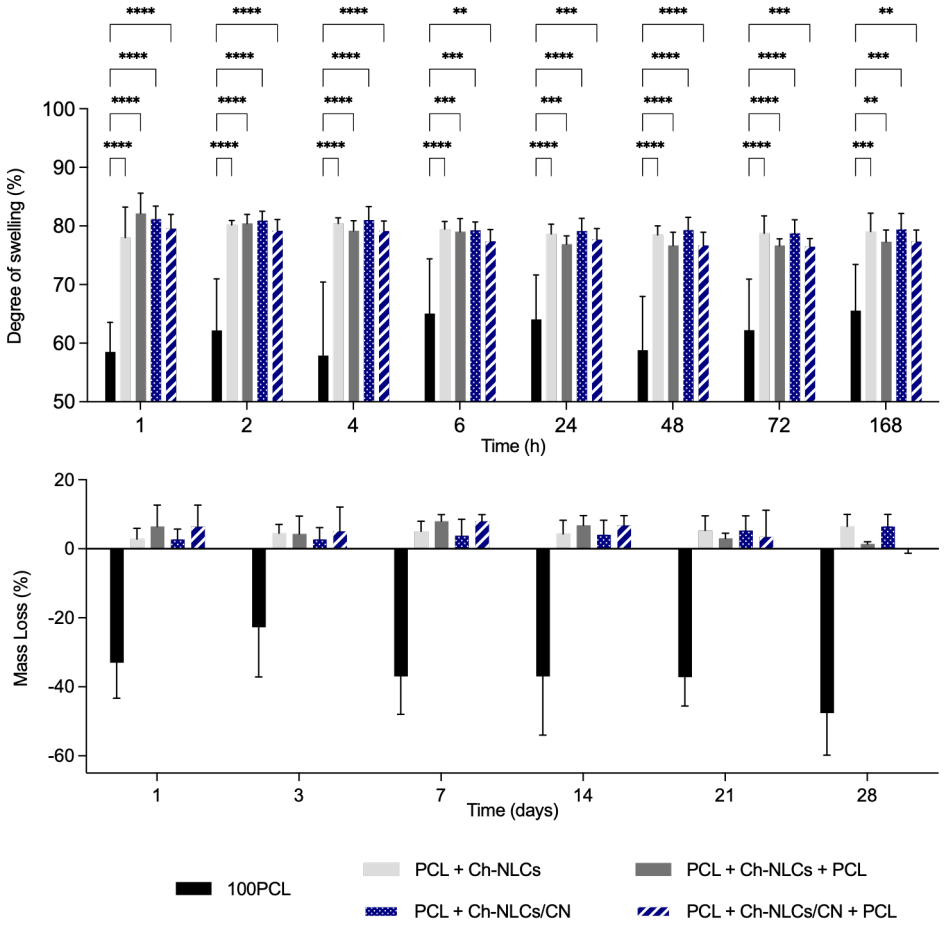


Figure 23 - (A) Degree of swelling (%) of electrosprayed electrospun mats in PBS over 168 hours. All mats were incubated at 37 °C in PBS. Data represent the mean ± SD (n = 4). (B) Mass loss (%) of electrospun mats over 28 days in PBS 1× 0.01M (pH 7.4). Negative values indicate water absorption rather than degradation. Data represent the mean ± SD (n = 4). Statistical significance was determined via the Tukey test, by applying multiple comparisons between all mat types, tested for the same time period (*p < 0.05; **p < 0.01; ***p < 0.001; ****p < 0.0001).

IV.3.9 Air and Water Permeabilities

The barrier and transport properties of the electrospun mats were assessed through water vapor transmission rate (WVTR), water vapor permeability index (I), and air permeability measurements, as these parameters are critical for evaluating the ability of wound dressings to maintain an optimal healing environment (Table 14). Neat PCL mats exhibited relatively low thickness and high WVTR,

reflecting the highly porous structure of electrospun PCL networks (section 3.3) and their intrinsic hydrophobic yet vapor-permeable nature. The high WVTR and permeability index values indicate that neat PCL allows efficient moisture vapor exchange, which can be beneficial for preventing excessive moisture accumulation but may also lead to wound dehydration if not properly balanced. The incorporation of Ch-NLCs nanoformulations by electrospray led to an increase in mat thickness, accompanied by a moderate reduction in WVTR and permeability index. This behavior can be attributed to partial pore filling and surface coverage by the nanoformulations, which slightly restrict vapor diffusion pathways while preserving the overall porous architecture. Importantly, the WVTR values of the PCL + Ch-NLCs loaded and unloaded mats remained within ranges considered suitable for wound dressings, where sufficient vapor transmission is required to prevent maceration while maintaining a moist wound environment [278]. The PCL + Ch-NLCs + PCL loaded and unloaded architecture showed the highest thickness and the lowest WVTR and permeability index values among the tested samples. The additional PCL layer introduces an extra diffusion barrier, further moderating moisture transport through the mat. This reduction in vapor permeability is consistent with multilayer electrospun systems reported in the literature, where stacking or layering fibrous mats leads to increased resistance to vapor flow due to enhanced fiber packing density and reduced interlayer porosity [281, 282]. While excessive reduction in WVTR can be detrimental, the values observed for this multilayer architecture remain within a range compatible with controlled moisture management, suggesting that the system can retain wound exudate without promoting excessive dryness or accumulation. Air permeability measurements followed a similar trend, with all mats exhibiting low but measurable air permeability values. Neat PCL showed the lowest air permeability, whereas PCL + Ch-NLCs displayed a slight increase, possibly due to localized changes in fiber packing or surface roughness introduced by the electrosprayed nanoformulations, as confirmed by the high SD in fiber diameters. The multilayer PCL + Ch-NLCs + PCL mats exhibited intermediate air permeabilities, reflecting a balance between increased thickness and preserved interconnected porosity. Low air permeability is generally desirable in wound dressings to act as a barrier against external contaminants while still allowing limited gas exchange at the wound interface [280]. Taken together, these results demonstrate that electrospray-assisted functionalization with loaded and unloaded Ch-NLCs and the construction of multilayer architectures enable fine-tuning of both water vapor and air transport properties of electrospun PCL mats. The progressive modulation of WVTR, permeability index, and air permeability from neat PCL to nanoformulation-functionalized and multilayer systems aligns with the requirements of advanced

wound dressings, where controlled moisture retention, adequate breathability, and protection from the external environment must be simultaneously achieved.

Table 14 - WVTR, water vapor permeability index (I), air permeability rates, and mat thicknesses (n =3).

Electrospun Mats	Thickness (µm)	WVTR (g/m².day)	I (%)	Air permeability (mL/s)
PCL	96 ± 2 µm	16874.64 ± 981.82	310.89 ± 20.16	1.112 ± 0.05
PCL + Ch-NLCs	130 ± 8 µm	16189.01 ± 900.81	260.54 ± 18.23	1.980 ± 0.23
PCL + Ch-NLCs + PCL	139 ± 13 µm	16067.06 ± 888.96	147.11 ± 22.71	1.860 ± 0.18
PCL + Ch-NLCs/CN	135 ± 13 µm	16016.06 ± 992.69	274.44 ± 10.73	1.893 ± 0.10
PCL + Ch-NLCs/CN + PCL	143 ± 6 µm	15921.77 ± 793.98	141.56 ± 19.71	1.858 ± 0.23

IV.3.10 Antifungal Activity

The antifungal performance of the developed system was evaluated against three clinically relevant *Candida* species, namely *C. albicans*, *C. tropicalis*, and *C. parapsilosis*, to assess the effectiveness of CN-loaded nanoformulations when immobilized on fibrous substrates and to understand the influence of mat architecture on antifungal activity (Figure 24). Overall, mats electrosprayed with unloaded Ch-NLCs showed only modest or transient effects on fungal reduction, confirming that Ch-coated lipid nanoparticles alone were insufficient to induce sustained antifungal activity. Although Ch is known to possess intrinsic antimicrobial and antifungal properties, its mechanism of action differs from that of EOs. Ch is generally believed to interact electrostatically with negatively charged components of fungal cell walls and membranes, leading to increased membrane permeability, disruption of nutrient transport, and inhibition of cell growth. Additionally, Ch may form a polymeric film around fungi cells, limiting oxygen transfer and interfering with cellular metabolism. However, these effects are often dependent on factors such as molecular weight, degree of deacetylation, and environmental conditions, and tend to result in growth inhibition rather than strong fungicidal activity. In contrast, a clear and time-dependent antifungal effect was observed for both CN-loaded architectures, highlighting the key role of CN as the active antifungal agent. These distinct mechanisms help explain why the incorporation of CN generally led to higher antifungal effects compared to unloaded systems. Nevertheless, it is important to note that, in several conditions, the differences between CN-loaded and unloaded

systems are not always statistically significant, suggesting that the contribution of CN depends on factors such as exposure time, fungal species, and the release profile from the fibrous matrix. Therefore, while the presence of CN tends to enhance antifungal performance, particularly at earlier time points, the results should be interpreted as an overall improvement in activity rather than a consistently significant effect across all conditions. For *C. albicans* (Figure 24 (A)), CN-loaded mats induced a pronounced reduction in fungal colonies as early as 4 h, with peak antifungal activity observed at 6 h for both PCL + Ch-NLCs/CN and PCL + Ch-NLCs/CN + PCL architectures. The significant reduction at intermediate time points may suggest a rapid release or surface availability of CN, which is consistent with its low MIC and MFC values determined in the preliminary screening. At 24 h, an apparent loss of antifungal effect was observed, particularly for the single-layer architecture, which may be associated with CN reduction from the surface, volatilization, or adaptation mechanisms of *C. albicans* as referred previously in section 3.1 Comparable time-dependent antifungal profiles have been reported for EO-based systems, where strong early inhibition is followed by reduced activity as the volatile compound dissipates or is consumed [283–285]. A similar trend was observed for *C. tropicalis* (Figure 24 (B)), although the magnitude of fungal reduction was generally lower and more variable. CN-loaded mats still outperformed non-loaded controls at early time points, with statistically significant reductions observed within the first hours of contact. The reduced sensitivity of *C. tropicalis* compared to *C. albicans* aligns with literature reports indicating species-dependent susceptibility to cinnamaldehyde, which has been linked to differences in membrane composition and stress response pathways among *Candida* species [286, 287]. For *C. parapsilosis* (Figure 24 (C)), CN-loaded mats again demonstrated superior antifungal performance compared to unloaded counterparts, mainly at earlier incubation times. Particularly, significant differences were observed at 24 h, where CN-loaded systems maintained measurable antifungal activity while non-loaded systems showed no inhibitory effect. The multilayer PCL + Ch-NLCs/CN + PCL architecture exhibited a slightly moderated but more sustained antifungal response, suggesting that partial coverage of the nanoformulations by the upper PCL layer may slow CN diffusion and volatilization, thereby prolonging antifungal efficacy [288, 289]. Across all three *Candida* species, the differences between single-layer and multilayer CN-loaded mats highlight the importance of architectural design in tuning antifungal performance. While the PCL + Ch-NLCs/CN mats favor rapid CN availability and strong early antifungal action, the PCL + Ch-NLCs/CN + PCL configuration provides a more balanced profile, mitigating rapid CN loss and supporting prolonged activity. From an

application perspective, this behavior is particularly relevant for wound dressings, where an initial reduction of fungal load followed by sustained protection is desirable to prevent infection recurrence.

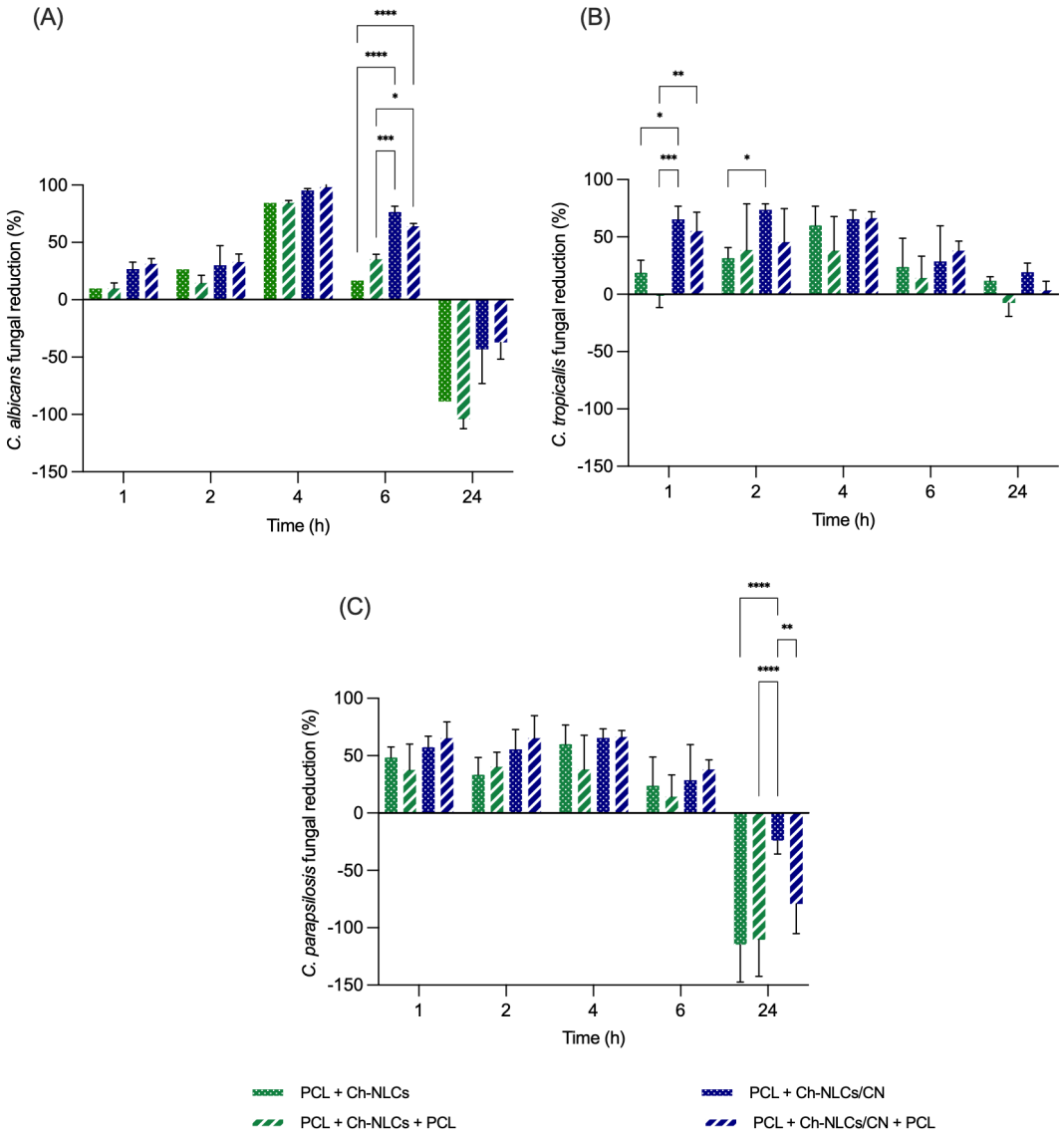


Figure 24 – Reduction of (A) *C. albicans* (B) *C. tropicalis,* and (C) *C. parapsilosis* number of fungi colonies in contact with the electrospun mats electrosprayed with Ch-based nanoformulations loaded and non-loaded with CN after 1, 2, 4, 6, and 24 h of incubation at 28 °C. Data are presented as mean ± standard deviation (n = 3). Statistical significance was determined via Tukey's test applying multiple comparisons between the different combinations at the same time-points (*p < 0.05; **p < 0.01; ***p < 0.001; ****p < 0.0001).

IV.3.11 Cytocompatibility

The cytocompatibility of the developed Ch-based nanoformulations and electrospun mats was evaluated using L929 fibroblasts and HaCaT keratinocytes to ensure their suitability for skin-contact and wound dressing applications (Figure 25). When cells were exposed for 24 h to increasing lipid concentrations of unloaded Ch-NLCs, CN-loaded Ch-NLCs, and free CN (Figure 25 (A, B)), a clear concentration-dependent response was observed. Unloaded Ch-NLCs maintained high cell viability and metabolic activity across the entire tested range for both cell lines, consistently remaining above the 70 % viability threshold defined by ISO 10993-5, and thus confirming the intrinsic cytocompatibility of the lipid–Ch carrier system. CN-loaded Ch-NLCs also exhibited good cytocompatibility at low to intermediate concentrations, with fibroblast viability and keratinocyte metabolic activity remaining close to control levels up to approximately 0.4–0.6 mg/mL. Importantly, in practical terms, the nanoformulations in suspension will never be used at lipid concentrations higher than 0.22 mg/mL, meaning that all realistic application conditions fall well within the non-cytotoxic range [290]. Higher concentrations were deliberately tested to establish safety margins and to identify potential toxicity thresholds; only at these elevated, non-representative concentrations was a reduction in cell viability observed. As expected, free CN induced a much more pronounced decrease in cell viability and metabolic activity at higher concentrations, highlighting the well-known dose-dependent cytotoxicity of CN and reinforcing the protective effect conferred by nanoencapsulation. This cytotoxic effect is mainly associated with the high reactivity of the aldehyde group of CN, which can interact with cellular proteins and enzymes, disrupt mitochondrial function, and induce oxidative stress, ultimately leading to membrane damage and cell death [291]. A differential sensitivity between the two cell lines was also evident, with HaCaT keratinocytes generally showing a higher susceptibility to the treatments than L929 fibroblasts. This behavior is consistent with previous observations and with literature reports indicating that HaCaT cells tend to be more sensitive to chemical and material-induced stress than fibroblast lines [292]. It should also be noted that the use of two distinct cell models, human keratinocytes (HaCaT) and murine fibroblasts (L929), may contribute to this difference, as species-specific responses and metabolic activity can influence cellular sensitivity. These cell lines were selected as complementary models to mimic the main skin components, with keratinocytes representing the epidermal barrier and fibroblasts the dermal layer, thereby providing a more comprehensive assessment of cytocompatibility for wound healing applications. [293, 294]. Therefore, the high tolerance of L929 fibroblasts to both unloaded and CN-loaded nanoformulations

is a positive outcome, as it suggests that the system is unlikely to impair key processes associated with dermal regeneration and extracellular matrix remodeling in wounded tissue. The cytocompatibility of the final electrospun constructs was further confirmed through direct contact assays with L929 fibroblasts and HaCaT keratinocytes (Figure 25 (C, D)), which more closely reflect the intended mode of application of the mats. All tested architectures, including neat PCL, PCL electrosprayed with non-loaded Ch-NLCs, and both CN-loaded configurations, maintained cell viability and metabolic activity well above the 70 % threshold after 24 h of contact, with no statistically significant differences between groups. These results confirm that the electrospray deposition process and the presence of CN-loaded nanoparticles do not compromise cellular response when the nanoformulations are immobilized within the fibrous scaffolds. The combined suspension and direct-contact assays demonstrate that, within all biologically relevant concentration ranges, the developed mats are non-cytotoxic toward both keratinocytes and fibroblasts. This favorable cytocompatibility profile, together with the demonstrated antifungal activity, strongly supports the safety and applicability of the Ch-NLCs/CN-loaded electrospun mats as wound-contact layers in the proposed multifunctional dressing system.

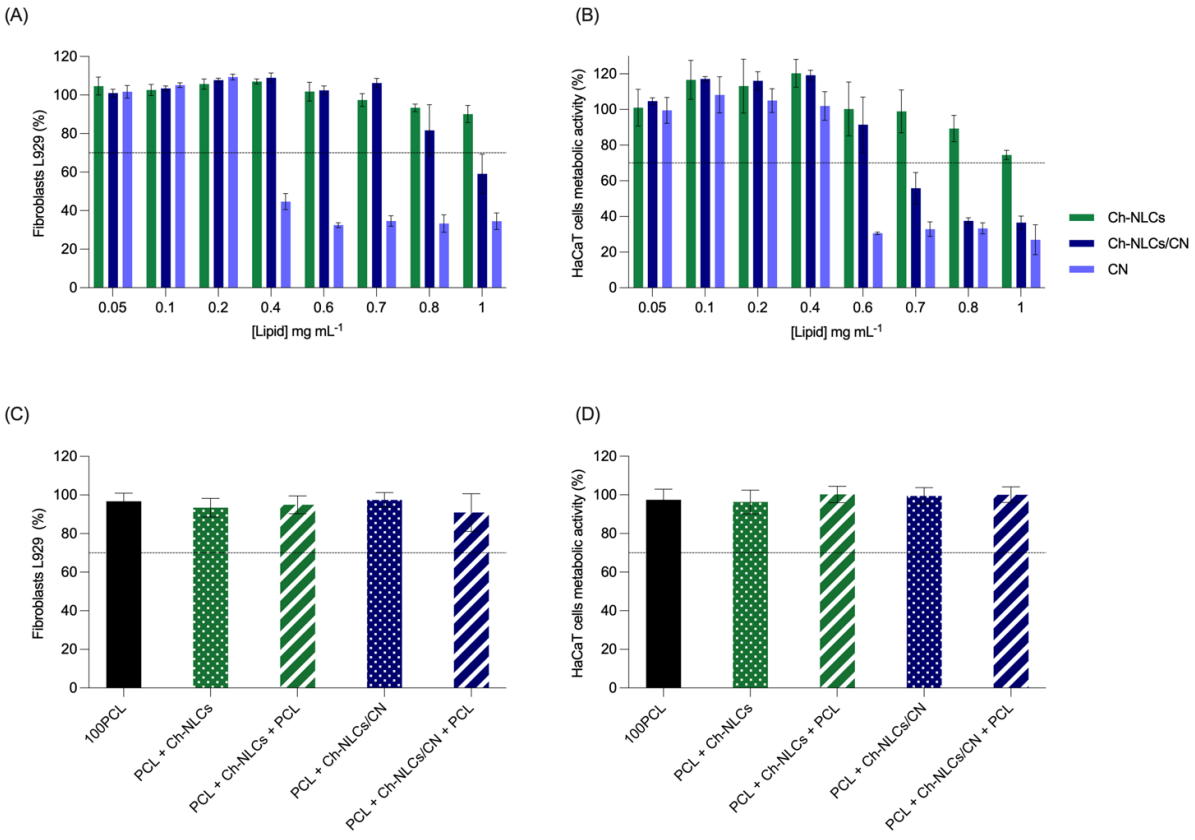


Figure 25 - Cytocompatibility assessment of Ch-based nanoformulations and electrospun mats. (A) Viability of L929 fibroblasts and (B) metabolic activity of HaCaT keratinocytes after 24 h exposure to increasing lipid concentrations of

CN-loaded and unloaded Ch-NLCs and free CN. (C) Viability of L929 fibroblasts and (D) metabolic activity of HaCaT keratinocytes after 24 h of direct contact with electrospun mats, either PCL or PCL incorporating Ch-NLCs and Ch-NLCs/CN for both architectures. Results are expressed as a percentage relative to untreated control cells. Data are presented as mean ± standard deviation (n=9). Statistical significance was determined via Tukey's test, applying multiple comparisons between the different combinations, reporting the absence of significant differences.

IV.4 Conclusions

In this study, a multifunctional electrospun dressing platform was developed by integrating Ch-NLCs/CN onto PCL fibrous mats using an electrospray-assisted approach. A preliminary screening of EO components identified CN as the most suitable antifungal agent, combining strong activity against *Candida* species with acceptable cytocompatibility when nanoencapsulated. The Ch-NLCs exhibited appropriate nanoscale size, stable positive surface charge, and high encapsulation efficiency (≈ 75 %), supporting their use as robust and stable antifungal carriers. The electrospray deposition strategy enabled the immobilization of Ch-NLCs/CN onto pre-formed PCL mats without compromising fiber morphology, mechanical performance, or thermal stability. By exploring two mat architectures, a single antifungal layer and a multilayer configuration with an additional PCL covering, it was possible to modulate surface wettability, swelling behavior, permeability, and antifungal response. The functionalized mats exhibited enhanced hydration capacity and controlled water vapor transport while maintaining low air permeability, properties that are essential for preserving a moist and protected wound environment. Importantly, the mechanical properties of the mats remained within ranges compatible with skin-contact applications, ensuring flexibility, conformability, and resistance to handling-induced damage. Biological evaluation demonstrated that the CN-loaded mats effectively reduced fungal colonization by *Candida species*, with activity profiles that could be tuned by architectural design. At the same time, both suspension-based and direct-contact cytocompatibility assays confirmed that the nanoformulations and final mats were non-cytotoxic to L929 fibroblasts and HaCaT keratinocytes within all biologically relevant concentration ranges. The higher tolerance observed in fibroblasts, together with the acceptable response of keratinocytes, further supports the suitability of the system for wound environments, where both superficial and deeper skin layers may be exposed. Future work should also address the release kinetics of CN from the nanoformulations and from the fibrous matrices, as the low amounts involved require sensitive and quantitative analytical approaches, such as high-performance liquid chromatography (HPLC)-based methods, to accurately characterize the release profile and correlate it with antifungal efficacy. Further studies addressing long-term antifungal

performance and *in vivo* validation will be essential to translate this multifunctional platform toward practical wound care applications.

CHAPTER V

Monitoring cinnamaldehyde fungicidal action in diabetic wound-like environments by means of halochromic multi-layer electrospun/electrospray dressings

CHAPTER V – MONITORING CINNAMALDEHYDE FUNGICIDAL ACTION IN DIABETIC WOUND-LIKE ENVIRONMENTS BY MEANS OF HALOCHROMIC MULTI-LAYER ELECTROSPUN/ELECTROSPRAY DRESSINGS

Abstract

Fungal infections are often early clinical indicators of prediabetic or diabetic conditions. Diabetic foot ulcers (DFUs) are characterized by impaired healing, moisture imbalance, high microbial loads, and an elevated risk of amputation or death. Fungal pathogens, particularly *Candida spp.*, create entry points for secondary bacterial infections, yet are frequently overlooked in standard DFUs treatments. Conventional therapies such as debridement, infection control, and traditional dressings often fall short due to rising antimicrobial resistance. This study aims to develop a multi-layer electrospun dressing for targeted antifungal action and real-time wound monitoring. The inner layer consists of electrospun ε-polycaprolactone (PCL) and electrosprayed nano-lipid carriers coated with chitosan and loaded with cinnamaldehyde (Ch-NLCs/CN), a natural essential oil effective against *Candida spp.*. Nanoparticles exhibited sizes of ≈ 300-350 nm and encapsulation efficiencies around 75 %. The outer layer comprises an electrospun film of a PCL and polyethylene glycol (PEG) blend with high porosity (≈ 80 %), and mechanical properties suitable for skin applications (Young's modulus ≈ 0.17-0.18 N/mm, elongation at break ≈ 270-320 %, and tensile strength ≈ 0.06–0.09 MPa), infused with red radish anthocyanins, halochromic molecules that enable visual tracking of wound healing. *In vitro* evaluations confirmed the dressing's ability to maintain antifungal efficacy against *Candida species* achieving reductions up to 70-90 %. Furthermore, cytocompatibility and cell proliferation studies towards mouse fibroblast cell line (L929) and human keratinocyte cell line (HaCaT) demonstrated high viability (> 90 %) and sustained proliferation over 48 h. This multifunctional dressing proved to reduce fungal infections, promote wound healing. Also, its visual monitoring may minimize dressing changes, potentially preserving newly formed tissue and improving DFUs management.

This chapter is based on the following scientific publication:

- Ana R. M. Ribeiro, Ana Isabel Barbosa, Catarina L. Seabra, Salette Reis, Helena P. Felgueiras, "Monitoring cinnamaldehyde fungicidal action in diabetic wound-like environments by means of halochromic multi-layer electrospun/electrospray dressings", To be submitted.

V.1 Introduction

Diabetic foot ulcers (DFUs) represent one of the most severe complications of diabetes mellitus, often resulting in chronic, non-healing wounds due to impaired vascularization, neuropathy, and altered immune response [295, 296]. They typically develop due to a combination of peripheral neuropathy, ischemia, immune dysfunction, and poor glycemic control, all of which contribute to impaired wound healing and an increased risk of secondary infections [297]. These wounds are particularly prone to microbial colonization, with fungal infections, especially by *Candida* species, frequently serving as early indicators of underlying diabetic pathology [298]. Despite their prevalence and clinical significance, fungal infections in DFUs are commonly overlooked in standard diagnostic and treatment protocols, allowing these infections to act as silent contributors to delayed healing, secondary bacterial infections, and increased risk of limb amputation [299]. Conventional DFU management involves wound debridement, systemic or topical antimicrobials, and passive dressings. However, these strategies often prove inadequate due to the rise of antimicrobial resistance, poor drug penetration, and an inability to maintain optimal moisture balance. Furthermore, frequent dressing changes to assess wound condition can disrupt newly formed tissue and expose the wound to external contaminants, impeding recovery [222, 295, 300]. Consequently, there is a growing need for multifunctional dressings that not only combat infection but also actively support and monitor the healing process.

Natural compounds like cinnamaldehyde (CN), a key element of cinnamon essential oil, have gained attention for their broad-spectrum antimicrobial activity and low propensity to induce resistance [229]. Specifically, CN has shown strong fungicidal action against *Candida spp.*, making it a promising alternative for fungal wound treatment [301]. However, the therapeutic use of essential oils is hindered by volatility, instability, and limited water solubility [229, 233]. Encapsulating CN within nano-structured lipid carriers (NLCs) can address these issues by enhancing its stability, enabling sustained release, and improving delivery to the wound bed [302, 303]. Beyond antifungal therapeutic intervention, diagnostic responsiveness is becoming increasingly important in wound care. Conventional microbiological testing methods are time-consuming and may not detect infections early enough to prevent complications. Thus, integrating biosensing capabilities directly into dressings could transform wound monitoring by offering immediate visual feedback [304, 305]. Local pH is one of the most indicative parameters of wound status; infected and non-healing wounds tend to show more basic shifts due to increased microbiological activity and enzymatic degradation [191]. Halochromic materials such as natural anthocyanins are capable of visually reporting pH

changes via colour transition, offering a low-cost, non-invasive tool to assess wound health in real time [15, 306]. Halochromic materials, such as natural anthocyanins, respond to pH fluctuations by changing colour, offering a non-invasive and visual method to track wound health [14]. Incorporating such sensors into the outer layer of a wound dressing allows caregivers and patients to monitor infection progression without disturbing the wound site.

Electrospinning has emerged as a versatile and scalable technique for fabricating nanofibrous scaffolds that mimic the extracellular matrix (ECM), promoting cell attachment and tissue regeneration [22, 307]. This method enables precise incorporation of both therapeutic agents and diagnostic indicators within discrete layers, allowing controlled release and spatial separation of functionalities [308]. Alongside, electrospray has gained increasing attention as a complementary technique for the deposition of bioactive nanoformulations onto pre-formed fibrous substrates. Unlike conventional blending approaches, electrospray allows the surface functionalization of electrospun mats without compromising fiber morphology or the structural integrity of sensitive compounds [309]. This strategy enables the localized positioning of therapeutic agents at the material interface, enhancing their interaction with the wound environment and improving bioavailability [310]. Therefore, the integration of electrospinning and electrospray techniques represents a novel and powerful approach to engineer multifunctional systems, combining structural support, controlled drug delivery, and responsive sensing capabilities within a single platform. The present study builds upon two previously developed research lines, each addressing a distinct functional layer of the proposed dressing. In the first study, the outer layer with sensing component was established through the development of pH-responsive electrospun PCL/PEG mats incorporating anthocyanin red radish natural extract, demonstrating efficient physicochemical properties, cytocompatibility, antioxidant activity, and halochromic behavior for real-time wound monitoring . In parallel, a second study focused on the therapeutic inner layer, consisting of electrospun PCL mats functionalized with chitosan-coated nanostructured lipid carriers loaded with cinnamaldehyde (Ch-NLCs/CN), which exhibited high encapsulation efficiency (≈ 75 %), and antifungal activity against *Candida* species, alongside with good biocompatibility. While each system independently demonstrated promising performance, their integration into a single multi-layer platform has not yet been explored. Therefore, the present work aims to combine these two complementary strategies into a multi-layered dressing capable of simultaneously providing antifungal treatment and real-time wound monitoring, combining therapeutic action and diagnostic feedback in chronic wound management.

V.2 Materials and Methods

V.2.1 Materials

PCL (Mw 80,000) was purchased from PolySciences, Inc. (Valley Road, Warrington), while PEG (Mw 20,000) was acquired from Sigma-Aldrich (Germany). Chitosan (low molecular weight) was purchased from Sigma-Aldrich (USA). Tween® 80 was purchased from Sigma-Aldrich (USA). Cetyl palmitate pellets were kindly given by Gattefossé SAS (Saint-Priest Cedex, France). Chloroform (CHF) and Dimethylformamide (DMF) were purchased from Riedel-de-Haen (Seelze, Germany) and PanReac AppliChem (Barcelona, Spain), respectively. Acetic acid and ethanol 90 % were purchased from VWR (USA) and Fisher Scientific (Pittsburgh, Pennsylvania, USA), respectively. Red radish natural extract was purchased in powder form from Yunnan Tonghai Yang Natural Products Co., Ltd (Yunnan Province, China). Cinnamaldehyde essential oil, natural ≥ 95 % was purchased from Sigma-Aldrich (USA). Fungal strains, *Candida albicans*, *parapsilosis,* and *tropicalis* were supplied by American Type Culture Collection (ATCC, Virginia, USA). For fungi growth, Sabouraud Dextrose Agar (SDA), Sabouraud Dextrose Broth (SDB) were purchased from HiMedia Laboratories (India). Mouse fibroblast cell line (L929) was purchased from the European Collection of Authenticated Cell Cultures (ECACC, Salisbury, UK) and the human keratinocytes cell line (HaCaT) was purchased from Cell Lines Service GmbH (CLS, Eppelheim, Germany). Dulbecco's Modified Eagle Medium (DMEM, high glucose, GlutaMAX, pyruvate) was puchased to Avantor VWR (Radnor, Pennsylvania, USA); Penicillin-streptomycin (10,000 U/mL), Trypsin-EDTA (0.25 % w/v) were purchased from Gibco Life Technologies (California, USA), Fetal Bovine Serum (FBS) was purchased from Biowest (Missouri, USA), Trypan blue, Sodium resazurin, 3-(4,5-dimethylthiazol-2-yl)-2,5-diphenyltetrazolium bromide assay (MTT), and Triton X-100 were purchased from Sigma-Aldrich (St.Louis, Missouri, USA). All reagents were used without further purification.

V.2.2 Multi-Layer Dressing Production

Separated polymeric solutions of PCL and PEG were prepared at 14 % and 10 % (w/v) respectively, in CHF/DMF (9:1) (v/v). These solutions were continuously stirred at 50 °C for 4 h and 1 h, respectively. PCL and PEG were combined at ratios: 100/0 (also labeled as PCL), and 90:10 (v/v). The natural red radish (RR) halochromic extract was previously dissolved in 1.8 mL DMF and added to the 90:10 polymeric solution at a concentration of 5.0 mg/mL. The solution was stirred at 150 rpm at RT, protected from light and overnight to ensure homogeneity. Viscosity was assessed using a viscometer Brookfield DV-II + Pro (spindle 21, 50 rpm at RT during 5 min, with 30 s time points),

while conductivity was determined using a Thermo Scientific Benchtop Meter (Orion Versa Star Pro) (Chapter III – section 1.14.3). Inner and outer layer were produced by electrospinning, performed with a fixated voltage of 12 kV applied to the steel capillary needle with an inner diameter of 18 Gauge (G). The distance between the needle tip and the aluminum collector was 17 cm. The solution feeding rate was set at 0.7 mL/h. Room temperature (RT) and relative humidity (RH) were controlled and maintained at 20–22 °C and 65–70 %, respectively. On the inner layer of PCL fibers, the electrospray deposition of Ch-NLCs/CN was performed using aqueous suspensions. The electrospray conditions used were a fixated voltage of 16 kV applied to the steel capillary needle with an inner diameter of 20 Gauge (G). The distance between the needle tip and the aluminum collector was 10 cm. The solution feeding rate was set at 1.2 mL/h. Room temperature (RT) and relative humidity (RH) were controlled and maintained in the same conditions as electrospinning (Chapter IV - 1.19.3). After production, the four multi-layer electrospun mats produced (Without Ch-NLCs and anthocyanins: PCL/PEG (90:10) + PCL; With Ch-NLCs/CN but without anthocyanins: PCL/PEG (90:10) + Ch-NLCs/CN + PCL; Without Ch-NLCs/CN but with anthocyanins: PCL/PEG (90:10) – RR + PCL; Complete multi-layer system: PCL/PEG (90:10) – RR + Ch-NLCs/CN + PCL) were stored in a desiccator.

V.2.3 Characterization of Multi-Layer Dressing

V.2.3.1 Field emission gun scanning electron microscopy (FEG-SEM)

Micrographs (NOVA 200 Nano SEM, FEI Company) were collected with an accelerating voltage of 10 kV. Mats were initially coated with a thin film (10 nm) of Au–Pd (80–20 wt. %) using a 208HR high-resolution sputter coater (Cressington Company, Watford WD19 4BX, UK) coupled to an MTM-20 Cressington High-Resolution Thickness Controller. The average fiber diameter was determined by conducting 100 fiber measurements on three micrographs at a magnification of 10.000 ×. Images were processed using the ImageJ® software (version 1.53a, National Institutes of Health, USA). The porosity of the mats was analyzed using the same ImageJ® software and methodology as reported in [170].

V.2.3.2 Fourier-transform infrared spectroscopy in attenuated total reflectance mode (ATR-FTIR)

To examine the chemical structure and identify functional groups of controls and multi-layer system mats, ATR-FTIR spectra were collected using an IRAffinity-1S, SHIMADZU spectrophotometer

(Kyoto, Japan), with a diamond crystal, applied at a spectral resolution of 8 cm^{-1}, for 45 scans, over a range of 4000-400 cm^{-1}.

V.2.3.3 Thermal gravimetric analysis (TGA)

The multi-layer system mats thermal degradation behavior was assessed by weight loss monitoring with the increase of temperature in the range of 25-600 °C, at a heating rate of 10 °C/min under a dynamic nitrogen atmosphere and flow rate of 200 mL/min (inert environment) on a STA 7200 Hitachi® (Fukuoka, Japan), using aluminum pans. The initial mass of each sample was 5 ± 2 mg. Results were plotted as the percentage of weight loss vs temperature.

V.2.3.4 Differential Scanning Calorimetry (DSC)

Thermal properties were also evaluated using a DSC 822 Mettler Toledo (Columbus, USA). Samples were submitted to a first heating step (0-100 °C) (to remove absorbed and adsorbed water), followed by cooling and then to a second heating step from 0 to 500 °C at a rate of 10 °C/min, under a dynamic nitrogen atmosphere, and flow rate of 20 mL/min (inert environment). DSC curves were plotted with heat flow vs temperature.

V.2.3.5 Mechanical testing

Elongations at break and breaking strength of controls (PCL and PCL/PEG (90:10)) and multi-layer system electrospun mats were measured using a uniaxial tensile test. Samples were prepared with dimensions 1 × 3 cm^2 following the standard ASTM D5035–11(2019). The gauge length was set to 25 mm. Hounsfield Universal Testing Machine (Hounsfield UTM) with a 250 N load cell was used to run the tensile test at RT applying displacement rates of 10.0 mm/min. Prior to testing, a low tare load was applied to establish a consistent zero position. Five experiments were conducted for each sample.

V.2.3.6 *In-vitro* Swelling and Degradation

Samples of 11 mm of diameter were cut and dried overnight at 37 °C for complete elimination of water presence. Posteriorly, they were weighted (m_d in m_g) and incubated in 1 mL of phosphate buffer solution 0.01 M (PBS, pH 7.4) at 37 °C for 1, 2, 4, 6, 24, 48, 72, 120 and 168 h under static conditions. At each specified interval, samples were collected, the excess of solution

removed, and the wet weight measured (m_w). The degree of swelling (%) was determined using the following Equation 2:

$$DS\ (\%) = \frac{(mw - md)}{md} \times 100 \qquad \text{Equation 2}$$

where m_W (mg) is the weight of the mats after sample immersion and m_d (mg) is the weight of the dried mats before immersion. Fibers' degradation profile was also assessed in PBS by incubating 11 mm samples of each type of mat, at 37 °C for up to 28 days. After 28 days of incubation, samples were weighted. Mass loss was determined using the following Equation 3 [171]:

$$mass\ loss\ (\%) = \frac{mi - mf}{mi} \times 100 \qquad \text{Equation 3}$$

in which mi (mg) represents the weight of the hydrated mats at time 0 h (fibers were initially hydrated in dH_2O, until saturation) and mf (mg) corresponds to the multi-layer mats weight after each incubation period.

V.2.3.7 Permeabilities

To assess the multi-layer mats' capacity for air exchange and moisture retention, air and water/vapor permeability studies were conducted according to standards ISO 9237 [311]. In the first, air pressure of 100 Pa was applied on the samples in five equidistant points of 5 cm^2, selected transversely along the mats, and the permeability was measured. On the water vapor permeability (WVP) examination, samples were placed on top of cylindrical cups containing 46 mL of dH_2O for 24 h. The evaporation of water through the test membrane was determined by weighing the cup before and after the testing period. Examinations were performed at 37°C and 65 % RH. An open cup was used as reference. Measurements were conducted in triplicate. The water vapor transmission rate (WVTR) and the WVP index (I) were determined using Equations 4 and 5:

$$WVTR = \frac{24\Delta W}{A\Delta t} \qquad \text{Equation 4}$$

$$I = \frac{WVP_S}{WVP_r} \times 100 \qquad \text{Equation 5}$$

where ΔW is the difference in the water weight (g) before and after the 24 h test, A is the inner area of the cup (mm), Δt is the exposure time (h), WVP_s is the water vapor permeability of the

samples and WVP_r is the water vapor permeability of reference (a cup without any sample on top, mimicking a wound without cover and completely exposed to the surrounding environment).

V.2.4 Antioxidant Activity

The free radical scavenging activity was determined using the DPPH assay adapted for a 48-well plate. For this, 11 mm diameter mats were incubated in 150 μL of DPPH stock solution (100 μM, 98 % EtOH), respectively, for 1, 2, 4, 6 and 24 h. The absorbance was measured in the respective time-points at 517 nm with a microplate reader (BioTek, SYNERGY H1M2, UK), to ensure that the reaction was completed (plateau state). The same DPPH solution was used as a negative control, and Trolox was used as a positive control and chemical reference for comparison. All measurements were made in triplicate. The results were expressed in terms of the percentage of reduced DPPH at steady state (% DPPHr) and were calculated following Eq. 6:

$$DPPHr\ (\%) = \frac{A_i - A_r}{A_i} \times 100 \qquad \text{Equation 6,}$$

in which A_r was the absorbance registered at steady state, and A_i was the initial absorbance registered at time 0 h.

V.2.5 Antifungal Efficiency

V.2.5.1 Time-kill Kinetics Evaluation

Multi-layer mats samples of 11 mm of diameter, were tested for their killing abilities against *C. albicans*, *C. parapsilosis* and *C. tropicalis* fungi suspensions, adjusted to 1.0×10^5 CFUs/mL in SDB broth (adaptation of ASTM-E2149–01). Mats samples/fungi solutions were incubated at RT and 150 rpm. After 0 (before agent action), 1, 2, 4, 6 and 24 h of incubation, fungi were serially diluted (10^1 to 10^4 in PBS), cultured on SDA plates and further incubated for another 48 h at 28 °C. Fungi reduction determinations were made between control suspensions (without sample) and the four multi-layer systems. Colonies of surviving fungi were counted and reported as mean ± standard deviation (S.D.).

V.2.6 Cytocompatibility Testing

V.2.6.1 Cell Culture Conditions

The cytocompatibility and cell proliferation of all multi-layer system typologies towards mouse fibroblast cell line (L929) and human keratinocytes cell line (HaCaT) were evaluated using direct

contact assay. The cytocompatibility testing was performed according to the international standard ISO 10993-5:2009. Cells were thawed and sub-cultured in DMEM medium supplemented with 10 % (v/v) FBS and 1 % (v/v) penicillin-streptomycin, at 37 °C in a humidified atmosphere of 5 % CO_2, until reaching 90 % confluence. Thereafter, cells were chemically detached from cell culture flasks using trypsin-EDTA at 0.25 % (w/v). The number of cells was determined using a Neubauer Chamber, labelling cells with trypan blue (ratio 1/1) and cells were counted using a Motic® Inverted Microscope (Motic, Barcelona, Spain). Cells were seeded in 48-well tissue culture polystyrene (TCPS, VWR®, Pennsylvania USA) plates, at the density of 12 $\times 10^4$ cells per well and incubated for 24 h at 37 °C in a humidified atmosphere of 5 % CO_2. The experiments were performed using fibroblast cells in passage 21–26 and keratinocytes cells line in passage 36–41.

V.2.6.2 Cell Viability Assessment

After 24 h of incubation, the metabolic activity of the cells was evaluated by resazurin staining. Briefly, 0.01 mg/mL of sodium resazurin in medium solution was added to the wells and incubated for 2 h at 37 °C and 5 % CO_2 atmosphere. Afterwards, 100 µL of supernatant were transferred to a black 96-well plate (Falcon®, Arizona, USA) and the fluorescence was measured (λ_{ex} =560 and λ_{em} =590 nm) using a microplate fluorometer (Cytation 5 Cell Imaging Reader - BioTek Instruments, Vermont, USA). The percentage of metabolic activity was evaluated by Equation 6 as an indicator of cells' viability:

$$Metabolic\ activity\ (\%) = \frac{Flu_s - Flu_{nc}}{Flu_{pc} - Flu_{nc}} \times 100 \qquad \text{Equation 6}$$

where the Flus is the fluorescence of the samples, Flu_{nc} is the fluorescence of the negative control, the untreated cells, and Flu_{pc} is the fluorescence of the positive control, the treated cells with 2 % (v/v) Triton X-100 solution.

V.2.6.3 Cell Proliferation by MTT quantification

Cell proliferation was evaluated by exposing the multi-layer mats in direct contact with cells for 24h and 48h. The cells were incubated with MTT at 0.5 mg/mL for proliferative profile evaluation. The positive control group (non-exposed cells to mats), negative control (cells exposed to 2 % (v/v) Triton X-100 solution) and the mats control group were incubated with MTT. Cell conversion of MTT was determined for all samples on L929 and HaCaT and compared to control.

V.2.6.4 Cell Morphology observation by Brightfield Microscopy

Cells were visualized at brightfield using an optical microscope. Light microscope images were obtained at the beginning of the experiment (t = 0 h) and after 24 h of incubation in contact with the samples to evaluate the cell morphology and the possible presence of damaged areas. The images were acquired at a 10 x magnification objective of 0.25 N.A. using a MoticTM Camera S12 coupled with Motic Image Plus 3.0 software (Motic, Barcelona, Spain).

V.2.7 Statistical Analysis

Data was treated using GraphPad Prism Software (v10.2.1, GraphPad Software Inc., USA). All assays were conducted three or more times and data was expressed as mean ± standard deviation (SD). Statistically significant was determined as having $p < 0.05$.

V.3 Results and Discussion

The multi-layer electrospun system investigated result from the integration of two previously developed systems: a therapeutic inner layer based on PCL mats functionalized with electrosprayed Ch-NLCs/CN (Chapter IV), and a sensing outer layer composed of PCL/PEG fibers incorporating red radish anthocyanins (Chapter III). The combination of electrospinning and electrospray techniques enabled the independent optimization of each layer prior to assembly, allowing their functionalities to be preserved in the final construct. FEG-SEM micrographs (Figure 26 (A,B)) show the fibrous morphology of PCL mats before and after electrospray deposition, confirming the formation of continuous, bead-free networks and the successful surface localization of nanoformulations. Importantly, no significant alterations in fiber morphology were observed upon incorporation of the nanoformulations, and these images can be considered representative of all developed systems, including those containing anthocyanins. This is further supported by the macroscopic appearance of the final dressing (Figure 26 (C)), where distinct layers can be visually identified, with one side corresponding to the anthocyanin-loaded PCL/PEG layer and the opposite side to the PCL layer containing the nanoformulations, although the internal interface between layers is not directly visible. Based on prior characterization, the individual layers present fiber diameters in the micrometer range (≈ 1 μm) and high porosity (≈ 70-80 %), which are retained after assembly and are relevant for the interpretation of the following results. Therefore, this section focuses on evaluating how the integration of these layers into a multi-layer configuration influences

the overall biological performance of the system, particularly in terms of mechanical features, antifungal activity and cytocompatibility between therapeutic and sensing components.

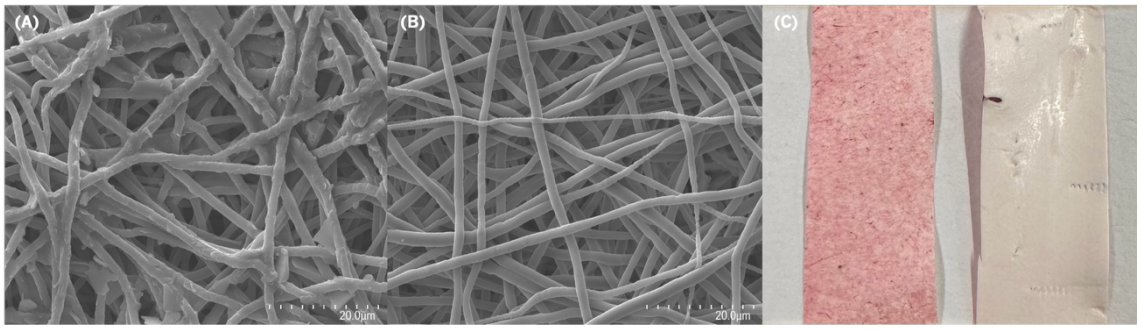


Figure 26 - (A) FEG-SEM micrograph of electrospun PCL fibers after electrospray deposition of Ch-NLCs/CN, showing surface roughness and nanoparticle localization. (B) FEG-SEM micrograph of electrospun PCL fibers without nanoformulations, exhibiting smooth and homogeneous fiber morphology. Both images are representative of all developed systems, indicating that neither nanoformulation incorporation nor multilayer assembly significantly altered the fibrous structure. (C) Macroscopic view of the final multi-layer dressing, displaying the two distinct external surfaces: the anthocyanin-loaded PCL/PEG layer (left) and the PCL layer functionalized with Ch-NLCs/CN (right).

V.3.1 Multi-layer Dressing Characterization

The chemical groups identification of the developed multi-layer electrospun dressing was evaluated by ATR-FTIR to confirm the successful integration of the different functional layers and to assess potential interactions between components (Figure 27). The spectrum of neat PCL (PCL) exhibited the characteristic absorption bands of the polymer, including the strong ester carbonyl stretching at ≈ 1730 cm^{-1} and the aliphatic C–H stretching bands around ≈ 2950 cm^{-1}, confirming the chemical integrity of the electrospun fibers [312]. Similar spectral features were observed for the PCL/PEG (90:10) and PCL/PEG (90:10) + PCL system, indicating that the incorporation of PEG and the formation of multi-layer structures did not alter the fundamental chemical structure of PCL. For the PCL/PEG (90:10) + Ch-NLCs/CN + PCL architecture, the spectra remained largely dominated by PCL bands, with only subtle variations in intensity and baseline, particularly in the fingerprint region (≈ 1000-1500 cm^{-1}). These minor changes can be attributed to the presence of Ch-based nanoformulations, although their spectral contribution is partially masked by the outer PCL layer. This behavior is consistent with previous observations for multi-layer electrospun systems, where the dominant polymer signal can obscure the detection of surface or interfacial components [313, 314]. In the systems containing RR (PCL/PEG (90:10) – RR + PCL and

PCL/PEG (90:10) – RR + Ch-NLCs/CN + PCL), additional small bands and increased signal complexity were observed in the fingerprint region, which can be associated with the presence of RR-derived compounds. However, no significant peak shifts or new bands indicative of chemical reactions were detected, suggesting that RR incorporation occurs through physical entrapment within the fibrous matrix. Similarly, the combined system (RR + Ch-NLCs/CN) did not show evidence of chemical incompatibility, further supporting that both active components are successfully integrated without altering the chemical structure of the polymeric scaffold. Overall, the ATR-FTIR results confirm that the chemical integrity of PCL was preserved while allowing the incorporation of both CN-loaded nanoformulations and RR anthocyanins within the multi-layer system. The absence of significant spectral shifts indicates that the interactions between components are predominantly physical, which is advantageous for maintaining the bioactivity of the incorporated agents and ensuring the stability of the dressing.

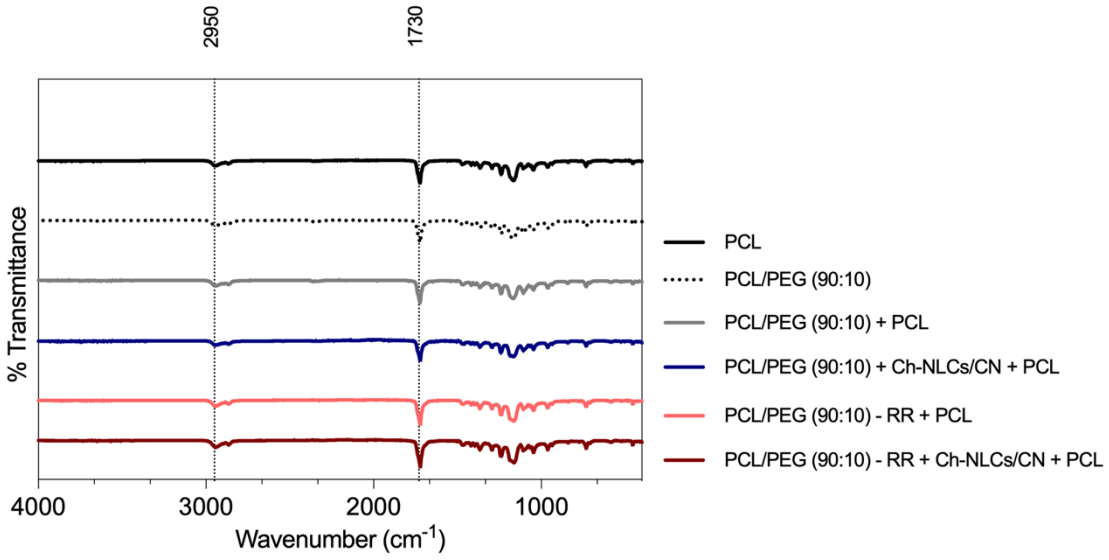


Figure 27 - ATR-FTIR spectra of electrospun mats with different multi-layer architectures collected in the range of 4000–400 cm^{-1}.

V.3.2 Multi-layer System Thermal Behaviour

Through TGA and DSC, the thermal behavior of the developed multi-layer electrospun systems was analyzed to assess the influence of PEG incorporation, RR loading, and Ch-NLCs/CN deposition on the thermal stability of the constructs (Figure 28). All systems exhibited similar degradation profiles, characterized by a major weight loss step occurring between ≈ 300 and 450 °C, which is attributed to the thermal decomposition of the PCL matrix (Figure 28 (A)). Neat PCL showed a single, well-

defined degradation stage (≈ 200 °C), while the multi-layer systems displayed slightly broader degradation regions, suggesting the contribution of additional components such as PEG, RR, and the Ch-based nanoformulations. The incorporation of PEG and RR led to a slight shift of the onset degradation temperature toward lower values, particularly in the PCL/PEG (90:10) – RR + PCL system, which can be associated with the lower thermal stability of PEG and the presence of bioactive compounds [315, 316][31]. However, these differences were not substantial, and all systems maintained degradation temperatures well above the range of physiological and processing conditions. The addition of Ch-NLCs/CN also did not compromise thermal stability, as observed in the PCL/PEG (90:10) + Ch-NLCs/CN + PCL and PCL/PEG (90:10) – RR + Ch-NLCs/CN + PCL systems, which exhibited degradation profiles comparable to their respective controls, with the main thermal degradation occurring in the range of ≈ 300-450 °C and maximum weight loss rates centered around ≈ 390-420 °C. This indicates that the structure remains thermally stable despite the addition of nanoformulations. DSC analysis (Figure 28 (B)) further supported these observations (Main DSC thermal events: T_o onset temperature, and ΔH enthalpy in SI – Table SD23). All systems exhibited an endothermic peak at low temperatures (≈ 60-100 °C), which can be attributed to the evaporation of residual moisture and/or relaxation phenomena associated with PEG and Ch components . At higher temperatures (≈ 400-450 °C), broad thermal events corresponding to polymer degradation were observed, consistent with TGA results [266]. Minor variations in peak shape and intensity among the different architectures suggest subtle changes in crystallinity and phase organization induced by PEG incorporation and the presence of nanoformulations, although without compromising the overall thermal robustness of the system. These differences can be attributed to the intrinsic properties of the components: PEG, being more hydrophilic and less crystalline than PCL, can disrupt the regular packing of PCL chains, leading to slight reductions in crystallinity and broader thermal transitions, as previously inferred from the increased swelling and wettability of PEG-containing systems (Chapter III – section III.3.7). Additionally, the presence of Ch-NLCs/CN, deposited at the fiber surface, may introduce localized heterogeneities and interfacial interactions between the lipid phase, Ch shell, and polymer matrix, which can further influence molecular organization. Despite these localized changes, the dominance of the PCL matrix ensures that the global thermal behavior remains unchanged, preserving the robustness for practical applications.

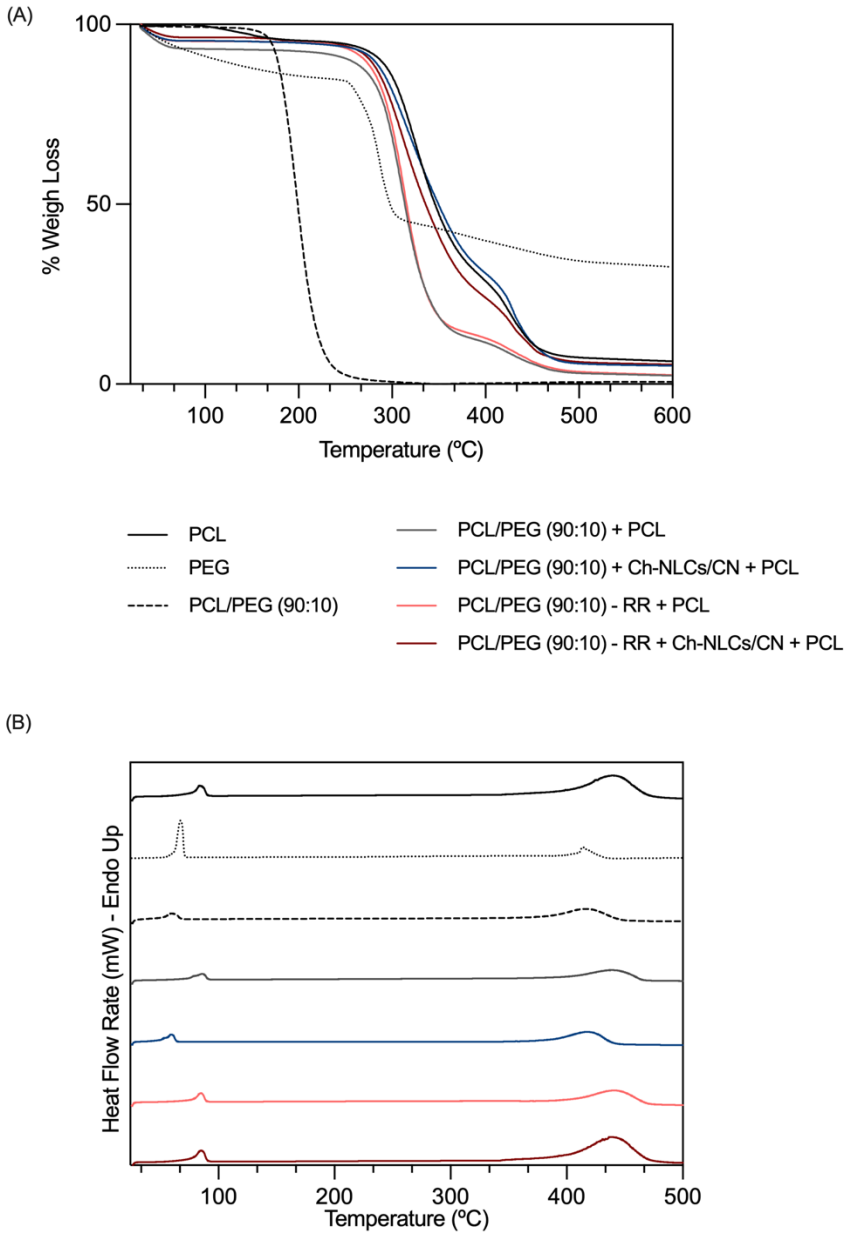


Figure 28 - Thermal stability profiles of multi-layer electrospun mats. (A) TGA profiles of PCL, PEG, PCL/PEG (90:10) and multi-layer electrospun mats. (B) DSC thermograms of PCL, PEG, PCL/PEG (90:10) and multi-layer mats.

V.3.3 Mechanical Stability

The mechanical properties of the multi-layer mats were evaluated to determine the effect of compositional modifications on structural performance (Table 15). Neat PCL mats exhibited a Young's modulus of ≈ 0.165 N/mm, high elongation at break (≈ 322 %), and moderate tensile strength (≈ 0.071 MPa), reflecting the typical ductile behavior of electrospun PCL [317]. The incorporation of PEG (PCL/PEG (90:10) + PCL) resulted in a slight increase in stiffness (≈ 0.180

N/mm) and tensile strength (≈ 0.092 MPa), accompanied by a reduction in elongation at break (≈ 266 %), suggesting increased intermolecular interactions and reduced chain mobility due to PEG presence as described in Chapter III – section III.3.5. The addition of Ch-NLCs/CN (PCL/PEG (90:10) + Ch-NLCs/CN + PCL) maintained similar Young's modulus values (≈ 0.183 N/mm) and slightly improved elongation at break (≈ 280 %), while preserving tensile strength. This indicates that the presence of nanoformulations does not impact negatively on the mechanical integrity of the system and may contribute to improved stress distribution within the fibrous network [318, 319]. Similarly, RR incorporation (PCL/PEG (90:10) – RR + PCL) did not significantly alter stiffness but maintained balanced mechanical properties, with elongation at break around ≈ 281 % and tensile strength (≈ 0.077 MPa). The combined system (PCL/PEG (90:10) – RR + Ch-NLCs/CN + PCL) exhibited mechanical properties comparable to the other multi-layer architectures. These results demonstrate that the simultaneous incorporation of RR and Ch-NLCs/CN does not compromise mechanical performance, highlighting again the robustness of the multi-layer design. All things considered, the developed multi-layer systems exhibit a combination of high thermal stability and suitable mechanical properties, including low stiffness, high extensibility, and adequate tensile strength. These characteristics are essential for wound dressing applications, where flexibility, conformability, and durability under physiological conditions are required [320, 321]. The results further confirm that the incorporation of multiple functional components can be achieved without detrimental effects on the structural integrity of the electrospun mats, supporting their potential as advanced multifunctional wound dressings.

Table 15 - Young Modulus, elongation at break, and break strength of the PCL and PCL/PEG (90:10) mats and multi-layer architectures tested at a displacement rate of 10.0 mm/min (n=3).

Electrospun Mats	Young Modulus (N/mm)	Elongation at break (%)	Break strength (MPa)
PCL	0.165 ± 0.010	322.17 ± 11.129	0.071 ± 0.008
PCL/PEG (90:10)	0.171 ± 0.034	274.44 ± 10.730	0.047 ± 0.011
PCL/PEG (90:10) + PCL	0.180 ± 0.059	266.276 ± 22.488	0.092 ± 0.043
PCL/PEG (90:10) + Ch-NLCs/CN + PCL	0.183 ± 0.050	280.134 ± 20.406	0.088 ± 0.019
PCL/PEG (90:10) – RR + PCL	0.175 ± 0.051	281.448 ± 30.561	0.077 ± 0.029
PCL/PEG (90:10) – RR + Ch-NLCs/CN + PCL	0.173 ± 0.055	286.122 ± 25.013	0.87 ± 0.023

V.3.4 *In-vitro* Swelling and Degradation

The swelling capacity and degradation behavior of the developed multi-layer electrospun systems were evaluated in PBS (pH 7.4). These experiments were conducted to assess the mats' ability to manage wound exudate while maintaining structural integrity over time (Figure 29). As shown in Figure 29 (A), all systems exhibited rapid swelling within the first hours, reaching equilibrium at ≈ 80–85 % for the PCL/PEG-based architectures, whereas neat PCL displayed significantly lower swelling values (≈ 55-65 %). This trend is fully consistent with previous wettability results, where PEG-containing systems exhibited reduced water contact angles and increased surface free energy, promoting water uptake (Chapter III – section III.3.8) [322]. Additionally, the high porosity of the fibrous networks (≈ 70-80 %), also previously confirmed by SEM analysis (Chapter III and IV section III.3.2 And IV.3.3, respectively), further enhances fluid absorption through capillary-driven mechanisms, highlighting the combined influence of chemistry and structure on swelling behavior. The incorporation of Ch-NLCs/CN and/or RR did not significantly alter the overall swelling profile, with all PCL/PEG (90:10)-based systems maintaining similar equilibrium values over 168 h. This observation aligns also with previous morphological results, which showed that electrosprayed nanoformulations are primarily localized at the fiber surface and do not significantly modify the bulk architecture of the scaffold (Chapter IV – section IV.3.3). Therefore, swelling remains predominantly governed by the PEG component and the intrinsic porosity of the electrospun matrix. From a functional standpoint, this is advantageous, as it allows the incorporation of bioactive agents without compromising the fluid-handling capacity of the dressing. The degradation behavior, evaluated through mass loss over 28 days (Figure 29 (B)), further supports the role of composition and architecture. The PCL mats exhibited negative mass loss values (≈ −30 to −50 %), indicating water and salts uptake rather than degradation, which is consistent with the hydrophobic character and slow degradation kinetics of PCL, as previously inferred from wettability and thermal stability analyses (Section III.3.4, III.3.6 and IV.3.5, IV.3.7) [323, 324]. In contrast, PCL/PEG (90:10)-based systems showed positive mass loss values (≈ 10–25 %), reflecting partial material loss over time. This behavior can be attributed to the leaching of PEG, a water-soluble component, which is progressively released into the surrounding medium [315]. Interestingly, the presence of Ch-NLCs/CN and RR slightly reduced mass loss compared to the PCL/PEG (90:10) + PCL system, suggesting a stabilizing effect of the additional components. This may be associated with increased inter-fiber interactions or partial pore filling by the nanoformulations, as suggested by SEM observations (Chapter IV – section IV.3.3), which can limit rapid PEG diffusion. Moreover, the multi-

layer configuration appears to contribute to improved structural integrity, likely due to the additional PCL layer acting as a barrier that modulates water penetration and component release. In general, the results demonstrate that PEG is the primary factor controlling swelling and degradation, while the incorporation of Ch-NLCs/CN and RR enable functionalization without compromising structural performance.

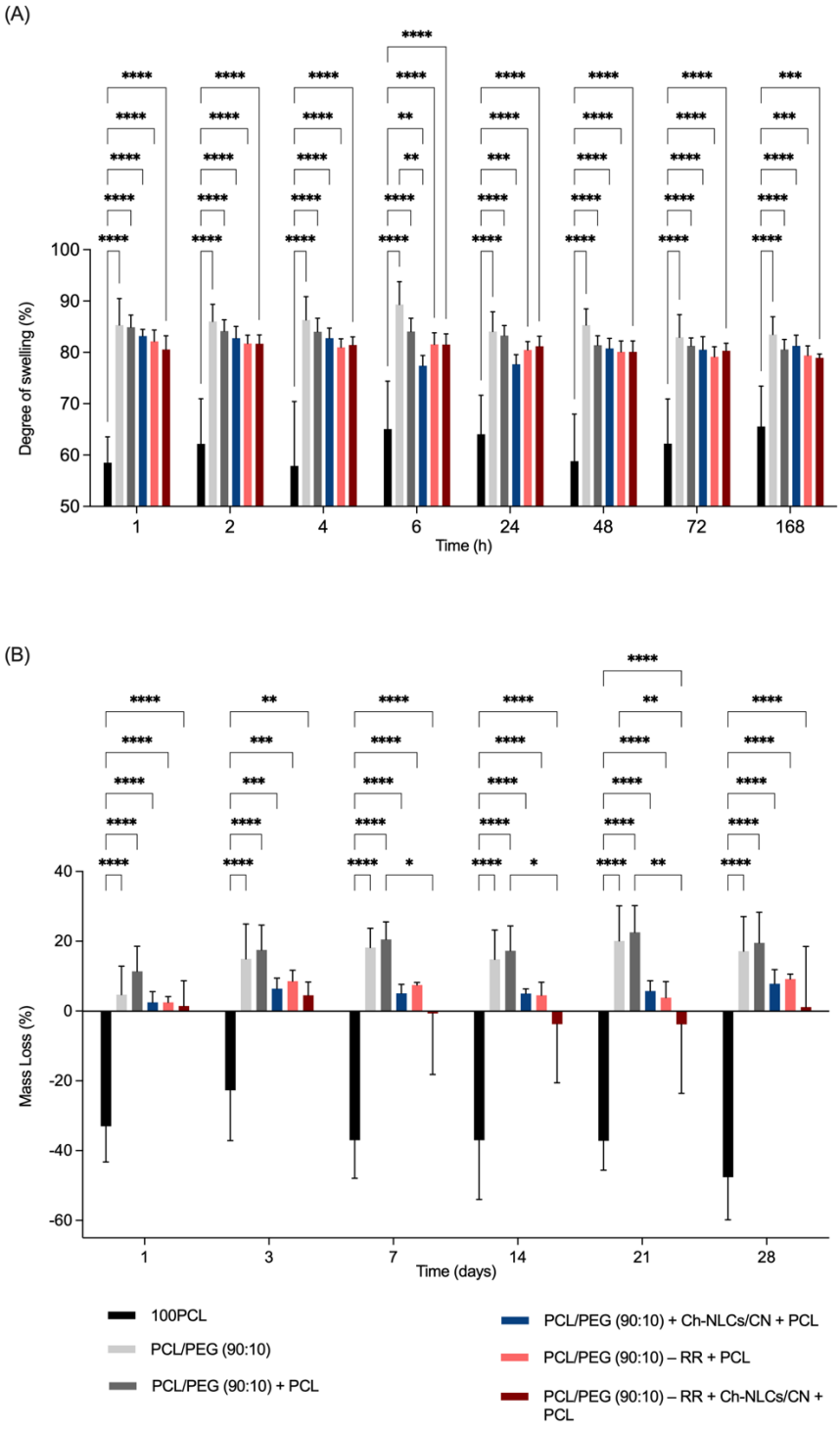


Figure 29 - A) Degree of swelling (%) of controls and multi-layer electrospun mats in PBS over 168 hours. All mats were incubated at 37 °C in PBS. Data represent the mean ± SD (n=4). (B) Mass loss (%) of controls and multi-layer mats over 28 days in PBS 1× 0.01M (pH 7.4). Negative values indicate water absorption rather than degradation. Data represent the mean ± SD (n = 4). Statistical significance was determined via Tukey test, by applying multiple comparisons between all mat types, tested for the same time period (*p < 0.05; **p < 0.01; ***p < 0.001; ****p < 0.0001).

V.3.5 Permeabilities Study

The permeability properties of the developed multi-layer electrospun systems were evaluated in terms of water vapor transmission rate (WVTR), water vapor permeability index (I), and air permeability, as these parameters are critical for maintaining an optimal wound healing environment (Table 16). Measurements were performed at 37 °C to better mimic physiological skin temperature, providing a more realistic assessment of dressing performance under *in vivo*-like conditions. The PCL mats exhibited a WVTR of ≈ 17.100 g/m²/day and relatively low air permeability (≈ 1.09 mL/s), reflecting the intrinsic hydrophobicity and compact fiber packing of PCL, as previously evidenced by wettability and morphological analyses. Upon incorporation of PEG (PCL/PEG (90:10) and PCL/PEG (90:10) + PCL), an increase in WVTR and air permeability was observed, which can be directly correlated with the enhanced hydrophilicity and higher swelling capacity discussed earlier (Chapter III – section III.3.8). PEG promotes water diffusion through the fibrous network, facilitating vapor transport while maintaining structural integrity [325]. The incorporation of Ch-NLCs/CN (PCL/PEG (90:10) + Ch-NLCs/CN + PCL) resulted in a decrease in WVTR (≈ 15.100 g/m²/day) and a reduction in the permeability index, suggesting a more controlled vapor transport. This behavior is consistent with previous SEM observations, where the presence of nanoformulations partially occupied inter-fiber spaces and increased surface roughness, leading to a slight reduction in effective pore size (Chapter IV – section IV.3.3). At the same time, air permeability increased, indicating that the porous architecture remains highly interconnected, allowing gas exchange while moderating moisture loss. A distinct behavior was observed in RR-containing systems. The PCL/PEG (90:10) – RR + PCL configuration exhibited a increase in WVTR (≈ 22.165 g/m²/day), which can be associated with the hydrophilic nature of RR and its influence on fiber morphology and porosity. This result is in line with the swelling data, where RR-containing systems maintained high water uptake capacity, suggesting that RR contributes to enhanced fluid interaction and transport through the scaffold. Similarly, the combined system (PCL/PEG (90:10) – RR + Ch-NLCs/CN + PCL) maintained high WVTR, permeability index and high air permeability (≈ 2.05 mL/s). This indicates that the presence of Ch-NLCs/CN moderates the excessive vapor transport induced by RR, likely through partial pore filling and structural stabilization, as previously suggested in the swelling and degradation analysis (Chapter IV - section IV.3.8). Data showed that PEG and RR promote water vapor transmission and fluid interaction, while Ch-NLCs/CN contribute to a more controlled and balanced permeability

profile. Importantly, all multi-layer systems maintain high air permeability, ensuring adequate oxygen exchange, which is essential for cell metabolism and tissue regeneration [326].

Table 16 - Mat thicknesses, WVTR, water vapor permeability index (I) and air permeability rates (n=3).

Electrospun Mats	Thickness (μm)	WVTR (g/m²/day)	I (%)	Air permeability (mL/s)
PCL	98 ± 2 μm	17124.64 ± 881.02	330.09 ± 10.16	1.092 ± 0.05
PCL/PEG (90:10)	88 ± 1 μm	19181.38 ± 320.90	274.44 ± 10.730	1.017 ± 0.011
PCL/PEG (90:10) + PCL	240 ± 2 μm	18273.66 ± 664.65	260.54 ± 18.23	1.480 ± 0.20
PCL/PEG (90:10) + Ch-NLCs/CN + PCL	199 ± 2 μm	15073.06 ± 455.19	147.11 ± 22.71	2.057 ± 0.18
PCL/PEG (90:10) – RR + PCL	130 ± 4 μm	22165.14 ± 222.77	274.44 ± 10.73	1.810 ± 0.18
PCL/PEG (90:10) – RR + Ch-NLCs/CN + PCL	190 ± 3 μm	21034.27 ± 110.64	241.56 ± 19.71	1.555 ± 0.42

V.3.6 Antioxidant Activity

The antioxidant activity of multi-layer electrospun systems was evaluated using the DPPH radical scavenging assay up to 24 h testing (Figure 30), allowing the assessment of the contribution of RR and Ch-NLCs/CN to the overall radical scavenging capacity of the systems. As expected, systems without RR, namely PCL, PCL/PEG (90:10) and PCL/PEG (90:10) + PCL, exhibited negligible or unstable antioxidant activity, with low %DPPH reduction throughout the assay period. These results confirm that the polymeric matrices themselves do not possess inherent antioxidant properties [327, 328]. In contrast, the incorporation of RR led to a marked increase in antioxidant activity. The PCL/PEG (90:10) – RR + PCL system showed a rapid increase in %DPPH reduction within the first minutes, reaching values close to ≈ 40–50 %, and maintaining relatively stable activity over time. This behavior is consistent with the presence of phenolic compounds in RR, which are known to act as hydrogen or electron donors, effectively neutralizing free radicals such as DPPH [329, 330]. Interestingly, the combined system containing both RR and Ch-NLCs/CN (PCL/PEG (90:10) – RR + Ch-NLCs/CN + PCL) exhibited a similar but slightly more stable antioxidant profile, maintaining values close to the Trolox reference over the entire testing period. This suggests that the presence of Ch-NLCs/CN does not hinder the antioxidant performance of RR and may even contribute to a more sustained activity, potentially due to structural effects such as improved retention or controlled exposure of RR within the fibrous matrix [331]. On the other hand, the system containing only Ch-NLCs/CN (PCL/PEG (90:10) + Ch-NLCs/CN + PCL) showed no

significant antioxidant activity, confirming that CN does not contribute substantially to radical scavenging under these conditions. In fact, a progressive decrease in %DPPH reduction over time was observed, which may be associated with interactions between the nanoformulations and the assay medium rather than true antioxidant effects. These results demonstrate that antioxidant activity in the developed systems is primarily driven by RR incorporation, while Ch-NLCs/CN mainly contribute with the antifungal functionality without interfering with the radical scavenging capacity. The ability to combine antifungal and antioxidant properties within a single multi-layer construct highlights the versatility of the proposed platform and its potential to address multiple aspects of the wound healing process, including infection control and oxidative stress mitigation.

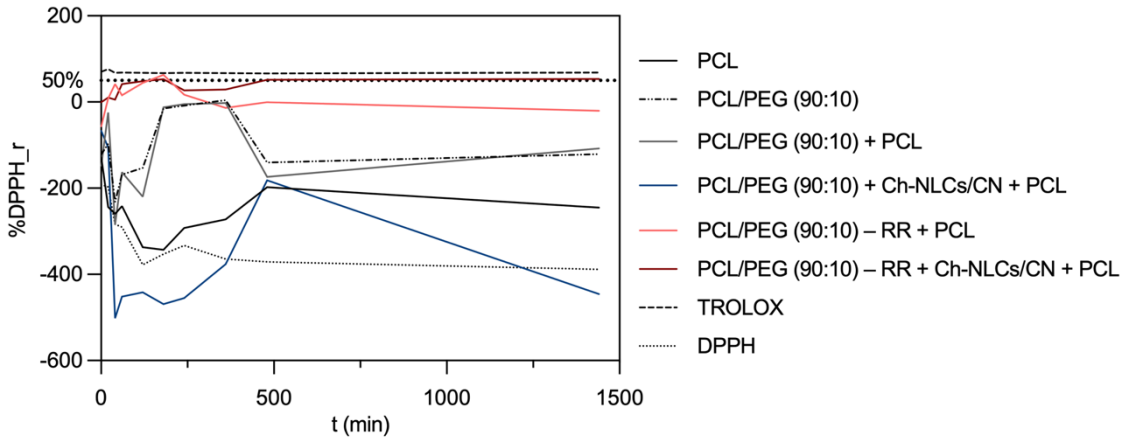


Figure 30 - DPPH scavenging activity (%) at 1, 2, 4, 6, 8 and 24 h. Trolox was used as a positive control and DMSO as a negative control (n=3). Statistical significance was determined via Tukey test, by applying multiple comparisons between timepoints.

V.3.7 Antifungal Activity

The antifungal activity was tested against three clinically relevant *Candida* species (*C. albicans*, *C. tropicalis*, and *C. parapsilosis*) to assess the combined and individual contributions of CN-loaded nanoformulations and RR within the different architectures (Figure 31). All functionalized systems exhibited time-dependent antifungal activity, with more pronounced effects observed in the presence of CN-loaded Ch-NLCs. For *C. albicans* (Figure 31 (A)), moderate fungal reduction was observed at early time points (≈ 30–40 % at 1-2 h), particularly for CN-containing systems. Interestingly, the PCL/PEG (90:10) + PCL control exhibited negative values at 2 h, indicating fungal proliferation in the absence of active agents. In contrast, systems containing CN and/or RR showed improved inhibition, with the combined system (PCL/PEG (90:10) – RR + Ch-NLCs/CN + PCL) generally presenting higher and more consistent antifungal activity over time. However, the

variability observed suggests that the effect is dependent on both exposure time and formulation, likely reflecting differences in release kinetics from the multi-layer structure. For *C. parapsilosis* (Figure 31 (B)), a similar tendency was observed, with higher antifungal activity at early time points, particularly at 1–2 h, where the CN-loaded systems achieved reductions of ≈ 30–40 %. The presence of RR alone also contributed to antifungal effects, although to a lesser extent and with greater variability, including transient negative values at 2 h. The combined system again showed relatively stable performance, although statistical significance was not consistently observed across all time points. The most evident effects were observed for *C. tropicalis* (Figure 31 (C)), where CN-containing systems reached high levels of fungal reduction at intermediate time points (≈ 70-85 % at 2-4 h), followed by a marked decrease at 24 h. Linking these results with previous sections (Chapter IV – section IV.3.10), the observed antifungal performance can be correlated with the structural and physicochemical properties of the multi-layer systems. The surface localization of Ch-NLCs/CN, confirmed by SEM analysis, likely promotes rapid interaction with fungal cells, explaining the higher activity at early time points. In this context, the antifungal effect is expected to be predominantly contact-based, since the nanoformulations are immobilized at the fiber surface, enabling direct interaction between CN and the fungal cell membrane. CN is known to disrupt membrane integrity, increase permeability, and interfere with intracellular processes, leading to cell death, while Ch may further contribute by interacting with negatively charged cell wall components and altering membrane function (Chapter IV – section IV.3.10). Additionally, the permeability and swelling behavior of PEG-containing systems facilitate fluid uptake and diffusion of active agents, further enhancing initial antifungal effects. However, the same properties may also contribute to faster release and depletion, limiting long-term activity. Mechanistically, the antifungal activity of the systems is primarily attributed to CN, which is known to disrupt fungal cell membranes, interfere with intracellular enzymatic activity, and induce oxidative stress, ultimately leading to cell death [332]. In contrast, Ch contributes mainly through membrane interaction and growth inhibition rather than strong fungicidal effects, which explains the more modest activity observed in unloaded systems. The results demonstrate that the incorporation of CN-loaded nanoformulations is essential to achieve effective antifungal activity, while RR can provide complementary functionality without compromising performance. The multi-layer architecture enables tuning of antifungal response, with strong early-stage activity that is particularly relevant for preventing initial fungal colonization in wound environments.

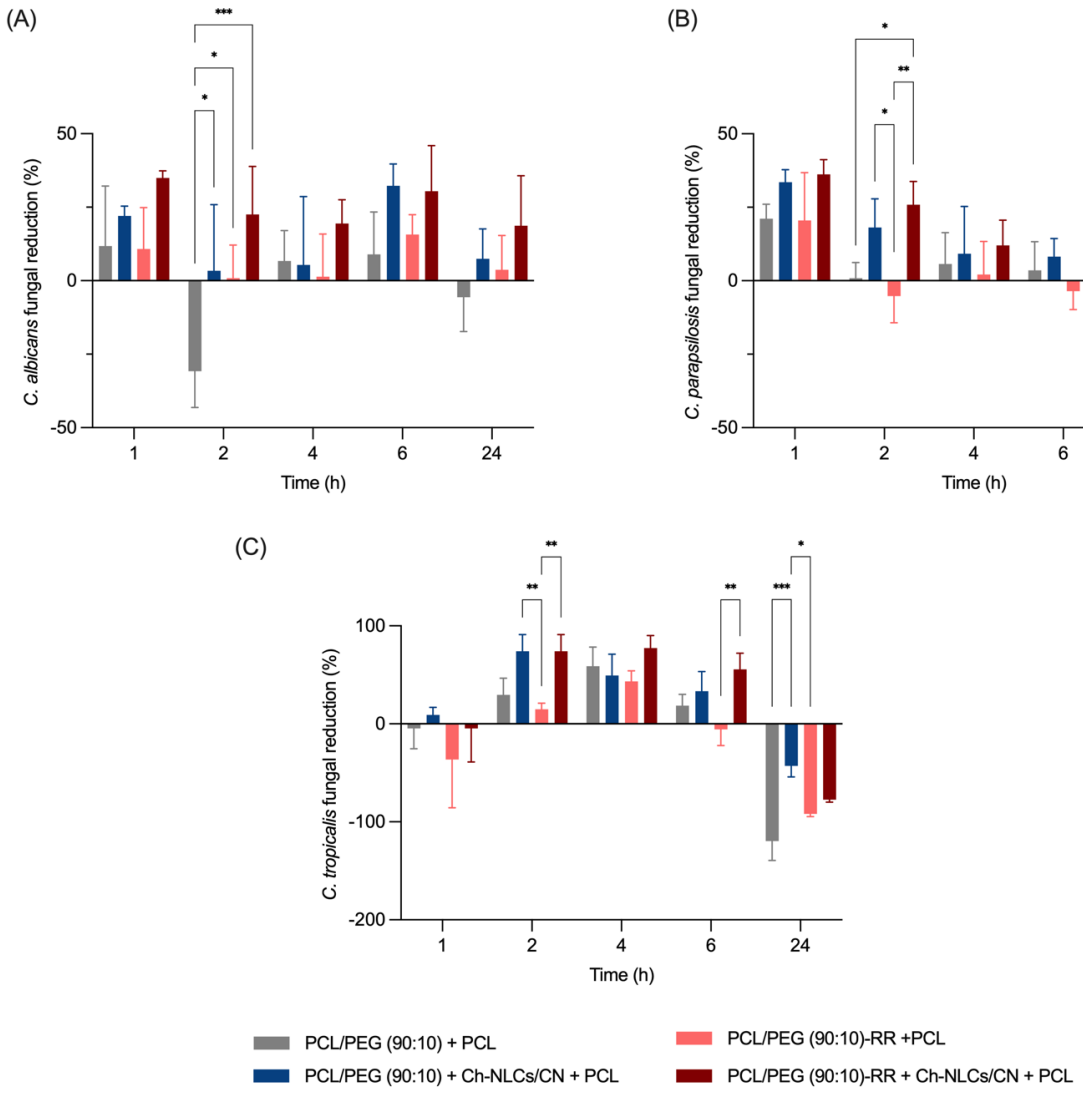


Figure 31 - Reduction of (A) *C. albicans* (B) *C. parapsilosis,* and (C) *C. tropicalis* number of fungi colonies in contact with the electrospun mats after 1, 2, 4, 6, and 24 h of incubation at 28 °C. Data are presented as mean ± standard deviation (n=3). Statistical significance was determined via Tukey's test applying multiple comparisons between the different combinations at the same time-points (*p < 0.05; **p < 0.01; ***p < 0.001; ****p < 0.0001).

V.3.8 Cytocompatibility and Cell Viability

The cytocompatibility was assessed using L929 fibroblasts and HaCaT keratinocytes after 24 h of direct contact to evaluate their suitability for wound dressing applications (Figure 32). In general, all tested systems exhibited high cell viability, with values consistently above 90 % for both cell lines, well above the 70 % threshold defined by ISO 10993-5:2009 for non-cytotoxic materials [169]. These results confirm that the incorporation of PEG, RR, and Ch-NLCs/CN does not induce detrimental cytotoxic effects in the final system. For L929 fibroblasts (Figure 32 (A)), all systems

maintained high viability levels, with values close to or exceeding 100 %, indicating not only cytocompatibility but also a potential proliferative effect. A slight reduction in viability was observed for the PCL/PEG (90:10) – RR + PCL system (≈ 90 %), which was statistically significant compared to the PCL/PEG (90:10) + PCL control. This behavior may be associated with the presence of RR, which, depending on concentration and local availability, can exert mild cytotoxic or stress-inducing effects . However, when RR was combined with Ch-NLCs/CN (PCL/PEG (90:10) – RR + Ch-NLCs/CN + PCL), cell viability increased again (≈ 95–100 %), suggesting that the multi-layer configuration and/or the presence of nanoformulations may modulate the exposure of RR and mitigate potential adverse effects. For HaCaT keratinocytes (Figure 32 (B)), a similar behavior was observed, with all systems maintaining metabolic activity around or above 100 %. The slightly higher variability observed for this cell line is consistent with previous observations, where HaCaT cells tend to be more sensitive to external stimuli compared to fibroblasts [333]. However, no statistically significant cytotoxic effects were detected across the different mats, confirming the overall safety of the developed systems. According to previous sections (Chapter III and IV – section III.3.11 and IV.3.11) , the high cytocompatibility can be attributed to several factors. First, the encapsulation of CN within Ch-NLCs prevents direct exposure of cells to free CN, which cytotoxicity is known to be dose-dependent. Second, the electrospray deposition strategy ensures that nanoformulations are primarily localized at the fiber surface, limiting excessive release and reducing potential cellular stress. Third, the controlled wettability and permeability of the multi-layer systems contribute to a balanced interaction with the biological environment, avoiding excessive accumulation of bioactive compounds. From a biological perspective, the use of both fibroblasts and keratinocytes provides a comprehensive evaluation of the system, as these cell types represent the main components of dermal and epidermal layers, respectively. The high tolerance observed in fibroblasts is particularly relevant, as these cells are critical for extracellular matrix deposition and tissue regeneration in wound healing [334, 335]. At the same time, the good response of keratinocytes supports the compatibility of the system with the outer skin barrier.

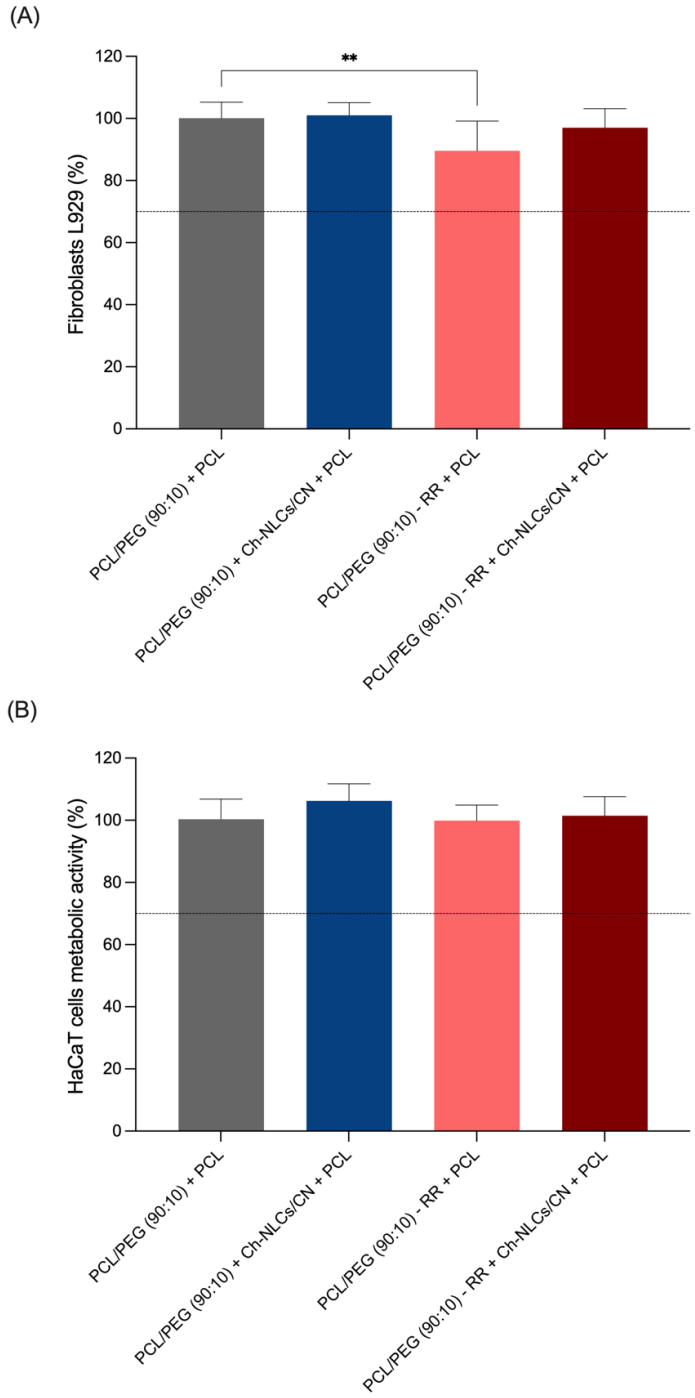


Figure 32 - Cytocompatibility assessment of multi-layer electrospun mats. (A) Viability of L929 fibroblasts and (B) metabolic activity of HaCaT keratinocytes after 24 h of direct contact with the electrospun mats. Results are expressed as a percentage relative to untreated control cells. Data are presented as mean ± standard deviation (n=9). Statistical significance was determined via Sidak's test, applying multiple comparisons between the different combinations. (*$p < 0.05$; **$p < 0.01$; ***$p < 0.001$; ****$p < 0.0001$).

V.3.9 Cell Proliferation

The effect of the developed multi-layer electrospun systems on cell proliferation was assessed using L929 fibroblasts and HaCaT keratinocytes after 24 and 48 h of incubation (Figure 33), providing further insight into the biological response beyond cytocompatibility. Overall, all systems supported cell proliferation, with values generally close to or above the untreated control, confirming that the materials are non-cytotoxic and capable of sustaining cellular metabolic activity over time. For L929 fibroblasts (Figure 33 (A,B)), the PCL/PEG (90:10) + PCL and PCL/PEG (90:10) – RR + PCL systems exhibited proliferation values slightly above the control at 24 h (≈ 100-105 %), suggesting a favorable environment for fibroblast activity. In contrast, systems containing Ch-NLCs/CN showed a moderate decrease in proliferation at 24 h (≈ 65-75 %), which may be associated with the initial exposure to CN released from the nanoformulations. This observation is consistent with previous cytocompatibility results, where CN-containing systems showed slightly reduced, although still acceptable, cell viability at higher exposure levels. Importantly, at 48 h, fibroblast proliferation in all systems recovered to values close to the control (≈ 80–100 %), indicating that the initial effect is transient and that cells adapt to the presence of the nanoformulations over time. For HaCaT keratinocytes (Figure 33 (C,D)), a similar but less pronounced trend was observed. At 24 h, all systems maintained proliferation above ≈ 75 %, with slightly lower values for CN-containing architectures. However, at 48 h, keratinocyte proliferation increased, particularly for the PCL/PEG (90:10) – RR + PCL and PCL/PEG (90:10) + Ch-NLCs/CN + PCL systems, reaching values above 100 %. This suggests that keratinocytes can recover and even benefit from the presence of bioactive components, potentially due to improved surface properties such as wettability and porosity, which were previously shown to favor cell-material interactions [335]. The transient reduction in proliferation observed in CN-containing systems at early time points can be associated with the initial burst release of CN, as suggested by the antifungal activity profiles. However, the encapsulation of CN within Ch-NLCs and its immobilization within the fibrous matrix appears to effectively modulate its release, preventing long-term cytotoxic effects and allowing cell recovery. Additionally, the presence of PEG and the overall porous structure of the mats contribute to a favorable microenvironment that supports cell attachment and proliferation. These results demonstrate that the developed multi-layer systems support both fibroblast and keratinocyte proliferation over time, despite the presence of bioactive agents.

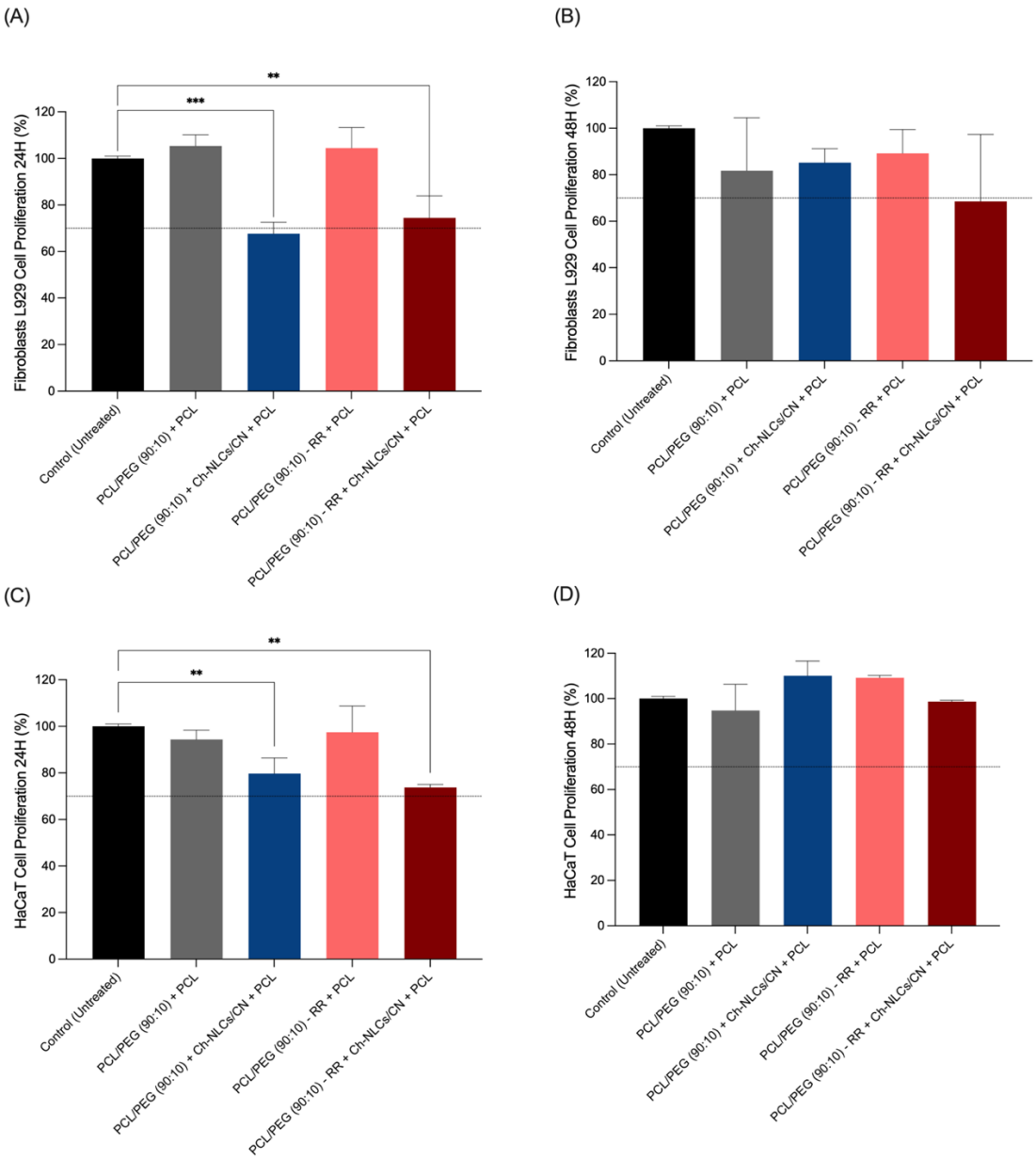


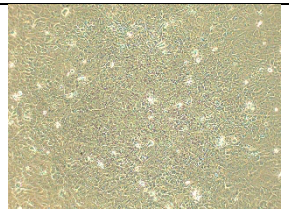
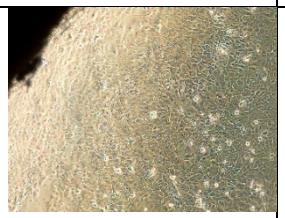
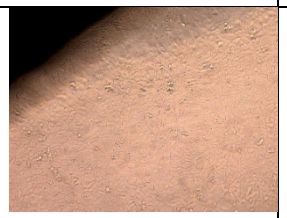
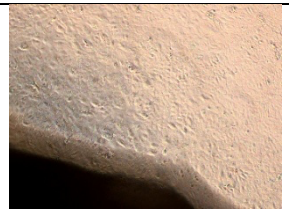
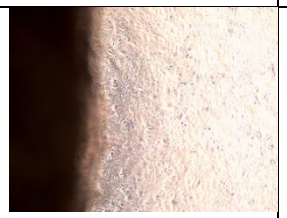
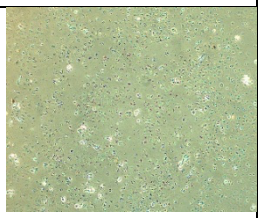
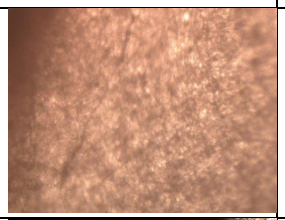
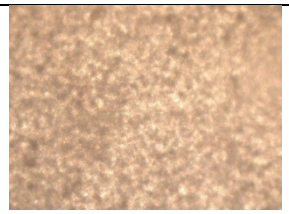
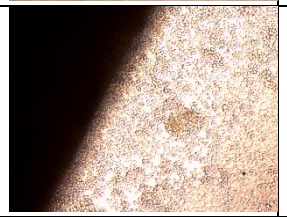
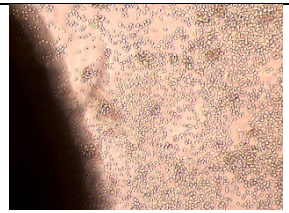
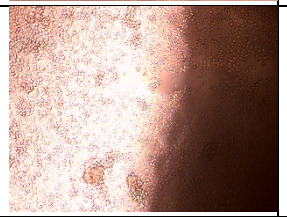
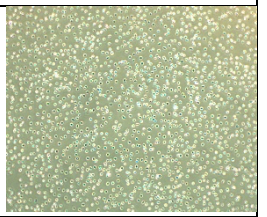
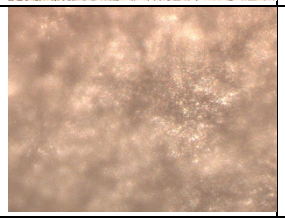
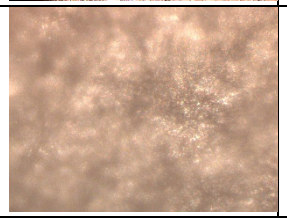
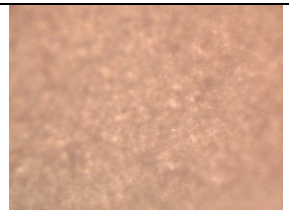
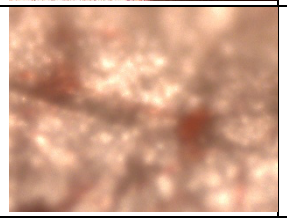
Figure 33 - Cell proliferation of (A, B) L929 fibroblasts and (C, D) HaCaT keratinocytes after 24 h (A, C) and 48 h (B, D) of incubation in the presence of electrospun multi-layer mats. Results are expressed as percentage relative to untreated control cells. Data are presented as mean ± standard deviation (n=9). Statistical significance was determined via Sidak's test applying multiple comparisons between the different conditions (*p < 0.05; **p < 0.01; ***p < 0.001; ****p < 0.0001).

V.3.10 Cell Morphology

Cell morphology was evaluated by optical microscopy to qualitatively assess the interaction between the developed multi-layer electrospun mats and the skin-relevant cell lines (Table 17). Overall, both cell types exhibited normal morphology and confluence patterns when cultured in the presence of all mat formulations, comparable to the untreated control, confirming the absence of

cytotoxic effects and supporting the quantitative cytocompatibility results. For HaCaT cells, a typical epithelial morphology with well-defined cell-cell contacts and homogeneous distribution was observed across all conditions. At the interface between the mats and the cell layer, a clear distinction between the darker regions corresponding to the materials and the lighter regions corresponding to unaffected cells was evident, indicating that the presence of the mats did not induce morphological alterations or detachment [336, 337]. Similarly, L929 fibroblasts maintained their characteristic elongated and spindle-like morphology, with no visible signs of membrane damage, rounding, or loss of adhesion [338]. The systems containing RR and/or Ch-NLCs/CN did not induce noticeable morphological differences compared to the control or PEG-containing systems, suggesting that the incorporation of bioactive components does not negatively affect cell structure. These observations are consistent with the proliferation and viability assays, where only minor and transient effects were detected, particularly in CN-containing systems. Importantly, the Triton X-treated control exhibited clear signs of cell disruption and loss of structural integrity, confirming the sensitivity of the assay and validating the absence of toxicity in the tested materials. The preservation of normal cell morphology in both keratinocytes and fibroblasts reinforces the biocompatibility of the developed multi-layer systems. Combined with the previously demonstrated mechanical, wettability, and permeability properties, these results further support the suitability of the materials for wound dressing applications.

Table 17 - Optical microscopy images of HaCaT keratinocytes and L929 fibroblasts after 24 h of incubation in direct contact with the electrospun multi-layer mats, compared with untreated control and Triton X-treated cells (positive control). Images highlight the interface between the mats (darker regions) and cells (lighter regions).

	Control	PCL/PEG (90:10) + PCL	PCL/PEG(90:10) - RR + PCL	PCL/PEG (90:10) + Ch-NLCs + PCL	PCL/PEG (90:10) - RR + Ch-NLCs + PCL	Triton X treated
HaCaT keratinocytes						
↑TOP - interface between MATs (darker areas) and cells (lighter color, and unaffected) →→→MATs→→						
L929 fibroblasts						
↑TOP - interface between MATs (darker areas) and cells (lighter color, and unaffected) →→→MATs →→						

V.4 Conclusions

In this chapter, a multi-layer electrospun dressing was successfully developed by combining PCL/PEG fibrous matrices with electrosprayed Ch-based nanoformulations loaded with CN and antioxidant RR anthocyanins compounds. The system preserved fiber morphology, high porosity, and suitable mechanical properties, ensuring flexibility and structural integrity for wound dressing applications. The nanoformulations exhibited nanoscale size, stable positive charge, and high encapsulation efficiency (≈ 75 %), confirming their suitability as CN carriers. The resulting systems demonstrated controlled wettability, high swelling capacity, and tunable permeability, enabling effective fluid management while maintaining a moist environment. Thermal analysis confirmed that the materials retain the intrinsic stability of PCL. Biologically, the systems showed antifungal activity against *Candida* species, particularly in CN-containing formulations, while maintaining high cytocompatibility and supporting cell proliferation. The incorporation of RR further introduced antioxidant functionality, allowing the combination of therapeutic effects within a single platform. With that, this study demonstrates the potential of electrospinning and electrospray approaches to design multi-layer wound dressings with tailored properties. Future work should focus on evaluating the release profiles of CN, using sensitive techniques such as HPLC, and on assessing the halochromic response of the dressing under different pH conditions depending on the healing wound phase, for wound monitoring. *In vivo* studies will be essential to validate the performance and clinical relevance of the developed system.

CHAPTER VI

Conclusions and Future Perspectives

CHAPTER VI – CONCLUSIONS AND FUTURE PERSPECTIVES

Chronic wound healing remains a major clinical challenge, often associated with persistent infection, impaired tissue regeneration, and the need for frequent intervention, all of which significantly impact patient quality of life and healthcare systems. In particular, fungal infections, such as those caused by *Candida* species, are frequently overlooked despite their critical role in delaying healing and promoting wound chronicity. To tackle this problematic, the development of multifunctional dressings capable of simultaneously addressing infection, oxidative stress, and wound monitoring represent a promising strategy to improve current therapeutic approaches.

This work addressed these challenges through the development of a novel multi-layer wound dressing integrating three complementary functionalities: (1) a pH-responsive halochromic electrospun layer based on PCL/PEG loaded with anthocyanin-rich extracts, (2) an antifungal therapeutic layer consisting of PCL electrospun mats functionalized with electrosprayed chitosan-coated nanostructured lipid carriers loaded with cinnamaldehyde (Ch-NLCs/CN), and (3) the final integration of both systems into a single platform capable of combining treatment and real-time monitoring.

Individually, each layer demonstrated strong performance. The halochromic system exhibited a clear and reversible color response across a physiologically relevant pH range (4.0-10.0), together with high cytocompatibility, antioxidant activity, and suitable swelling and wettability properties, supporting its role as a non-invasive wound monitoring tool. The therapeutic system confirmed CN as a highly effective antifungal agent against *Candida* species, while its nanoencapsulation into Ch-NLCs enabled high encapsulation efficiency (≈ 75 %), improved stability, and reduced cytotoxicity. The use of electrospray allowed the controlled surface immobilization of nanoformulations onto electrospun PCL mats without compromising fiber morphology, mechanical performance, or thermal stability, while enabling effective antifungal activity.

The main novelty of this work lies in the integration of electrospinning and electrospray techniques to engineer a multi-layer dressing with spatially organized and complementary functionalities. This approach enables the independent optimization of each layer prior to assembly, resulting in a system that combines antifungal activity, antioxidant capacity, and visual pH monitoring within a single construct. The developed systems maintained high porosity, suitable mechanical properties (Young Modulus ≈ 0.17-0.18 N/mm; elongation at break ≈ 270-320 %), controlled wettability, and tunable permeability, all of which are essential for wound healing. Biologically, the dressing

demonstrated antifungal efficacy, high cytocompatibility toward L929 fibroblasts and HaCaT keratinocytes, and the ability to support cell proliferation, highlighting its potential for chronic wound applications.

Overall, this work contributes to the advancement of smart wound dressings by bridging therapeutic and diagnostic functionalities in a single dressing. The proposed system represents a step toward more responsive and personalized wound care strategies, where treatment and monitoring can be achieved simultaneously, potentially reducing dressing changes and improving healing outcomes.

Future work should focus on:

- A detailed evaluation of the release kinetics of CN and other bioactive compounds from both nanoformulations and fibrous matrices, using sensitive analytical techniques such as HPLC to accurately quantify low concentrations and correlate release profiles with biological performance;
- The halochromic response of the anthocyanin-containing layer and CN release kinetics should be further investigated under dynamic and clinically relevant pH conditions to validate its application as a real-time wound monitoring tool;
- Longer stability studies and *in vivo* validation in relevant wound models will be essential to confirm the clinical performance and translational potential of the developed system;

  Evaluation of antifungal efficacy in more complex polymicrobial environments, including mixed fungal populations and bacteria–fungi combinations, to better reflect clinically relevant infection scenarios; A deeper investigation into the mechanisms of antifungal action, comparing free cinnamaldehyde, nanoparticle-loaded systems, and functionalized fibrous matrices, to better understand their interactions with fungal cells at the molecular and cellular levels;
- Exploration of personalized wound care approaches, integrating the developed system with digital health tools (e.g., mobile applications) capable of interpreting colorimetric changes and providing real-time feedback to patients and clinicians on wound status and healing progression.

References

1. Queen D, Harding K (2023) What's the true costs of wounds faced by different healthcare systems around the world? Int. Wound J. 20:3935–3938
2. Sen CK (2025) Human Wound and Its Burden: Updated 2025 Compendium of Estimates. Adv. Wound Care (New. Rochelle).
3. Falcone M, De Angelis B, Pea F, et al (2021) Challenges in the management of chronic wound infections. J. Glob. Antimicrob. Resist. 26:140–147
4. Redmond MC, Gethin G, Finn DP (2025) A Review of Chronic Wounds and Their Impact on Negative Affect, Cognition, and Quality of Life. Int. Wound J. 22
5. Matoori S, Engel E (2025) Emerging Technologies and Solutions for Chronic Wound Care and Diagnosis. ACS Appl. Bio Mater. 8:4413–4415
6. Short B, Bakri A, Baz A, et al (2023) There Is More to Wounds than Bacteria: Fungal Biofilms in Chronic Wounds. Curr. Clin. Microbiol. Rep. 10:9–16
7. Ge Y, Wang Q (2023) Current research on fungi in chronic wounds. Front. Mol. Biosci. 9
8. Beraja GE, Gruzmark F, Pastar I, Lev-Tov H (2025) What's New in Wound Healing: Treatment Advances and Microbial Insights. Am J Clin Dermatol. https://doi.org/10.1007/s40257-025-00953-9
9. El-Tarabily KA, El-Saadony MT, Alagawany M, et al (2021) Using essential oils to overcome bacterial biofilm formation and their antimicrobial resistance. Saudi J. Biol. Sci. 28:5145–5156
10. Nazzaro F, Fratianni F, Coppola R, De Feo V (2017) Essential oils and antifungal activity. Pharmaceuticals 10
11. Touati A, Mairi A, Ibrahim NA, Idres T (2025) Essential Oils for Biofilm Control: Mechanisms, Synergies, and Translational Challenges in the Era of Antimicrobial Resistance. Antibiotics 14
12. Guerini M, Condrò G, Perugini P (2022) Evaluation of the Mucoadhesive Properties of Chitosan-Based Microstructured Lipid Carrier (CH-MLC). Pharmaceutics 14:. https://doi.org/10.3390/pharmaceutics14010170
13. Gonciarz W, Balcerczak E, Brzeziński M, et al (2025) Chitosan-based formulations for therapeutic applications. A recent overview. J. Biomed. Sci. 32
14. Ribeiro ARM, Oliveira BAS, Barbosa AI, et al (2025) Nanomaterial-based scaffolds endowed with halochromic properties for skin healing purposes. J. Drug Deliv. Sci. Technol. 108
15. Zubova G, Melnyk H, Zaets I, et al (2024) Halochromic Bacterial Cellulose/Anthocyanins Hybrid Polymer Film with Wound-Healing Potential. Polymers (Basel) 16:. https://doi.org/10.3390/polym16162327
16. Kim D, Concepcion RS, Agueda JRHS, Martin Mondragon JS (2024) Optimizing Recurrent Neural Network-Based pH Prediction System of Halochromic Film for Chronic Wound Monitoring. IEEE Access 12:88756–88766. https://doi.org/10.1109/ACCESS.2024.3418968
17. Gharibshahian M, Salehi M, Beheshtizadeh N, et al (2023) Recent advances on 3D-printed PCL-based composite scaffolds for bone tissue engineering. Front. Bioeng. Biotechnol. 11

18. Liang HY, Lee WK, Hsu JT, et al (2024) Polycaprolactone in Bone Tissue Engineering: A Comprehensive Review of Innovations in Scaffold Fabrication and Surface Modifications. J. Funct. Biomater. 15
19. Yao X, Qi C, Sun C, et al (2023) Poly(ethylene glycol) alternatives in biomedical applications. Nano Today 48
20. Moayedi S, Xia W, Lundergan L, et al (2024) Zwitterionic Polymers for Biomedical Applications: Antimicrobial and Antifouling Strategies toward Implantable Medical Devices and Drug Delivery. Langmuir 40:23125–23145
21. Dethe MR, A P, Ahmed H, et al (2022) PCL-PEG copolymer based injectable thermosensitive hydrogels. Journal of Controlled Release 343:217–236
22. Luraghi A, Peri F, Moroni L (2021) Electrospinning for drug delivery applications: A review. Journal of Controlled Release 334:463–484. https://doi.org/10.1016/J.JCONREL.2021.03.033
23. Wang J, Windbergs M (2017) Functional electrospun fibers for the treatment of human skin wounds. European Journal of Pharmaceutics and Biopharmaceutics 119:283–299
24. Azari A, Golchin A, Maymand MM, et al (2022) Electrospun Polycaprolactone Nanofibers: Current Research and Applications in Biomedical Application. Adv. Pharm. Bull. 12:658–672
25. Andrew J.M. Boulton et al. (2020) Diagnosis and Management of Diabetic Foot Infections
26. Gubara Musa H, E. Ahmed M (2012) Associated risk factors and management of chronic diabetic foot ulcers exceeding 6 months' duration. Diabet Foot Ankle 3:18980. https://doi.org/10.3402/dfa.v3i0.18980
27. Boateng J, Catanzano O (2015) Advanced Therapeutic Dressings for Effective Wound Healing - A Review. J Pharm Sci 104:3653–3680. https://doi.org/10.1002/jps.24610
28. Burgess JL, Wyant WA, Abujamra BA, et al (2021) Diabetic wound-healing science. Medicina (Lithuania) 57
29. Liu JD, Van Treeck KE, Marston WA, et al (2024) Ultrasound-Mediated Antibiotic Delivery to In Vivo Biofilm Infections: A Review. ChemBioChem 25
30. Baig MS, Banu A, Zehravi M, et al (2022) An Overview of Diabetic Foot Ulcers and Associated Problems with Special Emphasis on Treatments with Antimicrobials
31. Mowafy W (2021) Fungal Diabetic Foot Infections
32. Jneid J, Lavigne JP, La Scola B, Cassir N (2017) The diabetic foot microbiota: A review. Hum Microb J 5–6:1–6. https://doi.org/10.1016/j.humic.2017.09.002
33. Kean R, Rajendran R, Haggarty J, et al (2017) Candida albicans mycofilms support Staphylococcus aureus colonization and enhances miconazole resistance in dual-species interactions. Front Microbiol 8:. https://doi.org/10.3389/fmicb.2017.00258
34. Öztürk AM, Taşbakan MI, Metin DY, et al (2019) A neglected causative agent in diabetic foot infection: A retrospective evaluation of 13 patients with fungal etiology. Turk J Med Sci 49:81–86. https://doi.org/10.3906/sag-1809-74
35. Kandregula S, Behura A, Behera CR, et al (2022) A Clinical Significance of Fungal Infections in Diabetic Foot Ulcers. 14:. https://doi.org/10.7759/cureus.26872
36. Raziyeva K, Kim Y, Zharkinbekov Z, et al (2021) Immunology of acute and chronic wound healing. Biomolecules 11

37. Powers JG, Higham C, Broussard K, Phillips TJ (2016) Wound healing and treating wounds Chronic wound care and management. J. Am. Acad. Dermatol. 74:607–625
38. Tottoli EM, Dorati R, Genta I, et al (2020) Skin wound healing process and new emerging technologies for skin wound care and regeneration. Pharmaceutics 12:1–30. https://doi.org/10.3390/pharmaceutics12080735
39. Felgueiras HP, Amorim MTP (2017) Functionalization of electrospun polymeric wound dressings with antimicrobial peptides. Colloids Surf B Biointerfaces 156:133–148. https://doi.org/10.1016/j.colsurfb.2017.05.001
40. Mangoni ML, Mcdermott AM, Zasloff M (2016) Antimicrobial peptides and wound healing: Biological and therapeutic considerations. Exp Dermatol. https://doi.org/10.1111/exd.12929
41. Vivcharenko V, Przekora A (2021) Modifications of wound dressings with bioactive agents to achieve improved pro-healing properties. Applied Sciences (Switzerland) 11:. https://doi.org/10.3390/app11094114
42. Rezvani Ghomi E, Khalili S, Nouri Khorasani S, et al (2019) Wound dressings: Current advances and future directions. J Appl Polym Sci 136:1–12. https://doi.org/10.1002/app.47738
43. Teixeira MA, Paiva MC, Amorim MTP, Felgueiras HP (2020) Electrospun nanocomposites containing cellulose and its derivatives modified with specialized biomolecules for an enhanced wound healing. Nanomaterials 10:. https://doi.org/10.3390/nano10030557
44. Liakos I, Rizzello L, Hajiali H, et al (2015) Fibrous wound dressings encapsulating essential oils as natural antimicrobial agents. J Mater Chem B 3:1583–1589. https://doi.org/10.1039/c4tb01974a
45. Han Y, Wei H, Ding Q, et al (2024) Advances in Electrospun Nanofiber Membranes for Dermatological Applications: A Review. Molecules 29
46. Imane NI, Fouzia H, Azzahra LF, et al (2020) Chemical composition, antibacterial and antioxidant activities of some essential oils against multidrug resistant bacteria. Eur J Integr Med 35:. https://doi.org/10.1016/j.eujim.2020.101074
47. Yuan X, Cao D, Xiang Y, et al (2024) Antifungal activity of essential oils and their potential synergistic effect with amphotericin B. Sci Rep 14:. https://doi.org/10.1038/s41598-024-82380-0
48. Emami M, Zomorodian K, Yazdanpanah S, et al (2024) Multifunctional Bi-layer collagen nanofiber-collagen/PLLA/Zataria multiflora essential oil nanofiber for wound healing: Antibacterial, antifungal and antioxidant properties. J Drug Deliv Sci Technol 92:. https://doi.org/10.1016/j.jddst.2023.105285
49. S. Sharma, A. Dua AM (2014) Third Generation Materials for Wound Dressings. Int J Pharm Sci Res 5:2113–2124
50. Jeckson TA, Neo YP, Sisinthy SP, Gorain B (2021) Delivery of Therapeutics from Layer-by-Layer Electrospun Nanofiber Matrix for Wound Healing: An Update. J Pharm Sci 110:635–653. https://doi.org/10.1016/j.xphs.2020.10.003
51. Trinca RB, Westin CB, da Silva JAF, Moraes ÂM (2017) Electrospun multilayer chitosan scaffolds as potential wound dressings for skin lesions. Eur Polym J 88:161–170. https://doi.org/10.1016/j.eurpolymj.2017.01.021

52. Saeed SM, Mirzadeh H, Zandi M, Barzin J (2017) Designing and fabrication of curcumin loaded PCL/PVA multi-layer nanofibrous electrospun structures as active wound dressing. Prog Biomater 6:39–48. https://doi.org/10.1007/s40204-017-0062-1
53. Erdogan S, Günes SN, Bulbul YE, et al (2025) Design of multi-layer electrospun poly(ε-caprolactone)/chitosan nanofiber scaffolds loaded with tigecycline for controlled drug release and antibacterial wound healing. Int J Biol Macromol 322:. https://doi.org/10.1016/j.ijbiomac.2025.146955
54. He M, Ou F, Wu Y, et al (2020) Smart multi-layer PVA foam/ CMC mesh dressing with integrated multi-functions for wound management and infection monitoring. Mater Des 194:108913. https://doi.org/10.1016/j.matdes.2020.108913
55. Brooker C, Tronci G (2023) A collagen-based theranostic wound dressing with visual, long-lasting infection detection capability. Int J Biol Macromol 236:. https://doi.org/10.1016/j.ijbiomac.2023.123866
56. Pakolpakçil A, Osman B, Özer ET, et al (2019) Halochromic composite nanofibrous mat for wound healing monitoring. Mater Res Express 6:. https://doi.org/10.1088/2053-1591/ab5dc1
57. Jain R, Shetty S, Yadav KS (2020) Unfolding the electrospinning potential of biopolymers for preparation of nanofibers. J Drug Deliv Sci Technol 57:101604. https://doi.org/10.1016/j.jddst.2020.101604
58. Liu X, Xu H, Zhang M, Yu DG (2021) Electrospun medicated nanofibers for wound healing: Review. Membranes (Basel) 11:. https://doi.org/10.3390/membranes11100770
59. Bhardwaj N, Kundu SC (2010) Electrospinning: A fascinating fiber fabrication technique. Biotechnol Adv 28:325–347. https://doi.org/10.1016/j.biotechadv.2010.01.004
60. Abrigo M, McArthur SL, Kingshott P (2014) Electrospun nanofibers as dressings for chronic wound care: Advances, challenges, and future prospects. Macromol Biosci 14:772–792. https://doi.org/10.1002/mabi.201300561
61. Ibrahim HM, Klingner A (2020) A review on electrospun polymeric nanofibers: Production parameters and potential applications. Polym Test 90:106647. https://doi.org/10.1016/j.polymertesting.2020.106647
62. Thenmozhi S, Dharmaraj N, Kadirvelu K, Kim HY (2017) Electrospun nanofibers: New generation materials for advanced applications. Mater Sci Eng B Solid State Mater Adv Technol 217:36–48. https://doi.org/10.1016/j.mseb.2017.01.001
63. Gul A, Gallus I, Tegginamath A, et al (2021) Electrospun antibacterial nanomaterials for wound dressings applications. Membranes (Basel) 11:1–21. https://doi.org/10.3390/membranes11120908
64. Luraghi A, Peri F, Moroni L (2021) Electrospinning for drug delivery applications: A review. Journal of Controlled Release 334:463–484. https://doi.org/10.1016/j.jconrel.2021.03.033
65. Liu Y, Zhou S, Gao Y, Zhai Y (2019) Electrospun nanofibers as a wound dressing for treating diabetic foot ulcer. Asian J Pharm Sci 14:130–143. https://doi.org/10.1016/j.ajps.2018.04.004
66. Liu M, Duan XP, Li YM, et al (2017) Electrospun nanofibers for wound healing. Materials Science and Engineering C 76:1413–1423. https://doi.org/10.1016/j.msec.2017.03.034

67. Smith S, Goodge K, Delaney M, et al (2020) A comprehensive review of the covalent immobilization of biomolecules onto electrospun nanofibers. Nanomaterials 10:1–39. https://doi.org/10.3390/nano10112142
68. Yoo HS, Kim TG, Park TG (2009) Surface-functionalized electrospun nanofibers for tissue engineering and drug delivery. Adv Drug Deliv Rev 61:1033–1042. https://doi.org/10.1016/j.addr.2009.07.007
69. Sahana TG, Rekha PD (2018) Biopolymers: Applications in wound healing and skin tissue engineering. Mol Biol Rep 45:2857–2867. https://doi.org/10.1007/s11033-018-4296-3
70. Lee EJ, Kasper FK, Mikos AG (2014) Biomaterials for Tissue Engineering. Ann Biomed Eng 42:323–337. https://doi.org/10.1201/b13978
71. Nair LS, Laurencin CT (2007) Biodegradable polymers as biomaterials. Progress in Polymer Science (Oxford) 32:762–798. https://doi.org/10.1016/j.progpolymsci.2007.05.017
72. Schön SM de B (2019) Electrospinning of Polyvinyl alcohol Based Wound Dressing. Universidade de Lisboa - Faculdade de Farmácia
73. Campa-Siqueiros PI, Madera-Santana TJ, Castillo-Ortega MM, et al (2021) Electrospun and co-electrospun biopolymer nanofibers for skin wounds on diabetic patients: An overview. RSC Adv 11:15340–15350. https://doi.org/10.1039/d1ra02986j
74. Christen MO, Vercesi F (2020) Polycaprolactone: How a well-known and futuristic polymer has become an innovative collagen-stimulator in esthetics. Clin. Cosmet. Investig. Dermatol. 13:31–48
75. Mokhena TC, Chabalala MB, Mapukata S, et al (2024) Electrospun PCL-Based Materials for Health-Care Applications: An Overview. Macromol. Mater. Eng. 309
76. Azari A, Golchin A, Maymand MM, et al (2022) Electrospun Polycaprolactone Nanofibers: Current Research and Applications in Biomedical Application. Adv. Pharm. Bull. 12:658–672
77. Satchanska G, Davidova S, Petrov PD (2024) Natural and Synthetic Polymers for Biomedical and Environmental Applications. Polymers (Basel). 16
78. Le YC, Su WT (2025) Aligned Electrospun PCL/PLA Nanofibers Containing Green-Synthesized CeO2 Nanoparticles for Enhanced Wound Healing. Int J Mol Sci 26:. https://doi.org/10.3390/ijms26136087
79. Wang Y, Zhang W, Karamergenova A, Lin L (2025) Fabrication and application of polycaprolactone-based composite scaffolds in tissue engineering: A review. Mater. Today Commun. 49
80. Robles KN, Zahra F tuz, Mu R, Giorgio T (2024) Advances in Electrospun Poly(ε-caprolactone)-Based Nanofibrous Scaffolds for Tissue Engineering. Polymers (Basel). 16
81. Gianino E, Miller C, Gilmore J (2018) Smart wound dressings for diabetic chronic wounds. Bioengineering 5
82. Reyes-Guzmán VL, Villarreal-Gómez LJ, Vázquez-Mora R, et al (2024) Integrating an antimicrobial nanocomposite to bioactive electrospun fibers for improved wound dressing materials. Sci Rep 14:. https://doi.org/10.1038/s41598-024-75814-2
83. Erdogan S, Günes SN, Bulbul YE, et al (2025) Design of multi-layer electrospun poly(ε-caprolactone)/chitosan nanofiber scaffolds loaded with tigecycline for controlled drug

release and antibacterial wound healing. Int J Biol Macromol 322:. https://doi.org/10.1016/j.ijbiomac.2025.146955

84. Ibrahim M, Ramadan E, Elsadek NE, et al (2022) Polyethylene glycol (PEG): The nature, immunogenicity, and role in the hypersensitivity of PEGylated products. Journal of Controlled Release 351:215–230
85. Hu J, Liu S (2022) Emerging trends of discrete Poly(ethylene glycol) in biomedical applications. Curr. Opin. Biomed. Eng. 24
86. Le Khanh HP, Nemes D, Rusznyák Á, et al (2022) Comparative Investigation of Cellular Effects of Polyethylene Glycol (PEG) Derivatives. Polymers (Basel) 14:. https://doi.org/10.3390/polym14020279
87. Wang J, Shi Y, Mao B, et al (2024) Biomaterials for inflammatory bowel disease: treatment, diagnosis and organoids. Appl. Mater. Today 36
88. Gaballa SA, Naguib YW, Mady FM, Khaled KA (2024) Polyethylene glycol: Properties, applications, and challenges
89. Yao S, Yan H, Tian S, et al (2024) Anti-fouling coatings for blood-contacting devices. Smart Mater. Med. 5:166–180
90. Ke W, Li X, Miao M, et al (2021) Fabrication and properties of electrospun and electrosprayed polyethylene glycol/polylactic acid (Peg/pla) films. Coatings 11:. https://doi.org/10.3390/coatings11070790
91. Lobo AO, Afewerki S, de Paula MMM, et al (2018) Electrospun nanofiber blend with improved mechanical and biological performance. Int J Nanomedicine 13:7891–7903. https://doi.org/10.2147/IJN.S175619
92. Alfaro De Pra MA, Coelho DS, Ribeiro-do-Valle RM, et al (2020) The Effect of Polyethylene Glycol on Polycaprolactone Electrospun Scaffolds: Morphology, Mechanical Properties, and Nerve Growth Factor Delivery Profile. Nano Progress 2:. https://doi.org/10.36686/ariviyal.np.2020.02.04.015
93. Yin B, Gosecka M, Bodaghi M, et al (2024) Engineering multifunctional dynamic hydrogel for biomedical and tissue regenerative applications. Chemical Engineering Journal 487
94. Mushtaq F, Ashfaq M, Anwar F, et al (2024) Injectable Chitosan-Methoxy Polyethylene Glycol Hybrid Hydrogel Untangling the Wound Healing Behavior: In Vitro and In Vivo Evaluation. ACS Omega 9:2145–2160. https://doi.org/10.1021/acsomega.3c04346
95. Virijevic K, Živanovic MN, Nikolic D, et al (2024) AI-Driven Optimization of PCL/PEG Electrospun Scaffolds for Enhanced In Vivo Wound Healing. ACS Appl Mater Interfaces. https://doi.org/10.1021/acsami.4c03266
96. Ramlow H, Andrade KL, Immich APS (2021) Smart textiles: an overview of recent progress on chromic textiles. Journal of the Textile Institute 112:152–171. https://doi.org/10.1080/00405000.2020.1785071
97. Peila R, Varesano A, Vineis C, et al (2021) Fabric dyeing with colorimetric pH-responsive colours. Coloration Technology 137:123–133. https://doi.org/10.1111/cote.12511
98. Pakolpakcil A, Karaca E, Becerir B (2018) Investigation of a Natural pH-Indicator Dye for Nanofibrous Wound Dressings. IOP Conf Ser Mater Sci Eng 460:. https://doi.org/10.1088/1757-899X/460/1/012020

99. Dargaville TR, Farrugia BL, Broadbent JA, et al (2013) Sensors and imaging for wound healing: A review. Biosens Bioelectron 41:30–42. https://doi.org/10.1016/j.bios.2012.09.029
100. Gethin G (2007) The significance of surface pH in chronic wounds. Wounds UK 3:52–56
101. Pargai D (2021) Application of Smart and Functional Dyes in Textiles. In: Dyes and Pigments - Novel Applications and Waste Treatment textiles. IntechOpen, p 13
102. Devarayan K, Kim BS (2015) Reversible and universal pH sensing cellulose nanofibers for health monitor. Sens Actuators B Chem 209:281–286. https://doi.org/10.1016/j.snb.2014.11.120
103. Silva S, Costa EM, Calhau C, et al (2017) Anthocyanin extraction from plant tissues: A review. Crit Rev Food Sci Nutr 57:3072–3083. https://doi.org/10.1080/10408398.2015.1087963
104. Mattioli R, Francioso A, Mosca L, Silva P (2020) Anthocyanins: A Comprehensive Review of Their Chemical Properties and Health Effects on Cardiovascular and Neurodegenerative Diseases. Molecules 25:. https://doi.org/10.3390/molecules25173809
105. Pliszka B, Huszcza-Ciołkowska G, Mieleszkoa E, Czaplicki S (2009) Stability and antioxidative properties of acylated anthocyanins in three cultivars of red cabbage (Brassica oleracea L. var. capitata L. f. rubra). J Sci Food Agric 89:1154–1158. https://doi.org/10.1002/jsfa.3565
106. Patil G, Madhusudhan MC, Ravindra Babu B, Raghavarao KSMS (2009) Extraction, dealcoholization and concentration of anthocyanin from red radish. Chemical Engineering and Processing: Process Intensification 48:364–369. https://doi.org/10.1016/j.cep.2008.05.006
107. Abedi-Firoozjah R, Yousefi S, Heydari M, et al (2022) Application of Red Cabbage Anthocyanins as pH-Sensitive Pigments in Smart Food Packaging and Sensors. Polymers (Basel) 14:. https://doi.org/10.3390/polym14081629
108. Chayavanich K, Kaneshige R, Thiraphibundet P, et al (2023) pH-responsive nanofibrous membrane fabricated from gelatin and red radish anthocyanins for meat spoilage monitoring. Dyes and Pigments 216:. https://doi.org/10.1016/j.dyepig.2023.111331
109. Tang C, Han J, Chen D, et al (2023) Recent advances on the biological activities of purple sweet potato anthocyanins. Food Biosci. 53
110. Teng Z, Jiang X, He F, Bai W (2020) Qualitative and Quantitative Methods to Evaluate Anthocyanins. eFood 1:339–346. https://doi.org/10.2991/efood.k.200909.001
111. Tena N, Asuero AG (2022) Up-To-Date Analysis of the Extraction Methods for Anthocyanins: Principles of the Techniques, Optimization, Technical Progress, and Industrial Application. Antioxidants 11:. https://doi.org/10.3390/antiox11020286
112. Wu LP, Wang D, Li Z (2020) Grand challenges in nanomedicine. Materials Science and Engineering C 106:110302. https://doi.org/10.1016/j.msec.2019.110302
113. Elsherbini AM, Sabra SA (2022) Nanoparticles-in-nanofibers composites: Emphasis on some recent biomedical applications. Journal of Controlled Release 348:57–83. https://doi.org/10.1016/j.jconrel.2022.05.037

114. Khursheed R, Dua K, Vishwas S, et al (2022) Biomedical applications of metallic nanoparticles in cancer: Current status and future perspectives. Biomedicine and Pharmacotherapy 150:112951. https://doi.org/10.1016/j.biopha.2022.112951
115. Gao Y, Wu Y (2022) Recent advances of chitosan-based nanoparticles for biomedical and biotechnological applications. Int J Biol Macromol 203:379–388. https://doi.org/10.1016/j.ijbiomac.2022.01.162
116. Antunes JC, Domingues JM, Miranda CS, et al (2021) Bioactivity of Chitosan-Based Particles Loaded with Plant-Derived Extracts for Biomedical Applications: Emphasis on Antimicrobial Fiber-Based Systems. Marine Drugs 2021, Vol 19, Page 359 19:359. https://doi.org/10.3390/MD19070359
117. Wagner AM, Gran MP, Peppas NA (2018) Designing the new generation of intelligent biocompatible carriers for protein and peptide delivery. Acta Pharm Sin B 8:147–164. https://doi.org/10.1016/j.apsb.2018.01.013
118. Kulkarni JA, Witzigmann D, Leung J, et al (2019) On the role of helper lipids in lipid nanoparticle formulations of siRNA. Nanoscale 11:21733–21739. https://doi.org/10.1039/c9nr09347h
119. Mitchell MJ, Billingsley MM, Haley RM, et al (2021) Engineering precision nanoparticles for drug delivery. Nat Rev Drug Discov 20:101–124. https://doi.org/10.1038/s41573-020-0090-8
120. Lakkireddy HR, Bazile D V. (2019) Nano-carriers for drug routeing–towards a new era. J Drug Target 27:525–541. https://doi.org/10.1080/1061186X.2018.1561891
121. Wang W, Lu KJ, Yu CH, et al (2019) Nano-drug delivery systems in wound treatment and skin regeneration. J Nanobiotechnology 17:1–15. https://doi.org/10.1186/s12951-019-0514-y
122. Wathoni N, Suhandi C, Elamin KM, et al (2024) Advancements and Challenges of Nanostructured Lipid Carriers for Wound Healing Applications. Int. J. Nanomedicine 19:8091–8113
123. Farasati Far B, Naimi-Jamal MR, Sedaghat M, et al (2023) Combinational System of Lipid-Based Nanocarriers and Biodegradable Polymers for Wound Healing: An Updated Review. J. Funct. Biomater. 14
124. Lv Y, Zhai C, Sun G, He Y (2024) Chitosan as a promising materials for the construction of nanocarriers for diabetic retinopathy: an updated review. J. Biol. Eng. 18
125. Chuah LH, Loo HL, Goh CF, et al (2023) Chitosan-based drug delivery systems for skin atopic dermatitis: recent advancements and patent trends. Drug Deliv Transl Res 13:1436–1455. https://doi.org/10.1007/s13346-023-01307-w
126. Iacob AT, Lupascu FG, Apotrosoaei M, et al (2021) Recent biomedical approaches for chitosan based materials as drug delivery nanocarriers. Pharmaceutics 13
127. Sun R, Xia Q, Sun Y (2024) A Novel Strategy for Topical Administration by Combining Chitosan Hydrogel Beads with Nanostructured Lipid Carriers: Preparation, Characterization, and Evaluation. Gels 10:. https://doi.org/10.3390/gels10030160
128. Barari F, Maghsoudian S, Alinezhad V, et al (2025) Effective topical delivery of astaxanthin via optimized chitosan-coated nanostructured lipid carriers: A promising strategy for

enhanced wound healing and tissue regeneration. J Drug Deliv Sci Technol 110:. https://doi.org/10.1016/j.jddst.2025.107052

129. Baig MS, Karade SK, Ahmad A, et al (2024) Lipid-based nanoparticles: innovations in ocular drug delivery. Front. Mol. Biosci. 11
130. Chauhan I, Yasir M, Verma M, Singh AP (2020) Nanostructured lipid carriers: A groundbreaking approach for transdermal drug delivery. Adv. Pharm. Bull. 10:150–165
131. Mehta M, Bui TA, Yang X, et al (2023) Lipid-Based Nanoparticles for Drug/Gene Delivery: An Overview of the Production Techniques and Difficulties Encountered in Their Industrial Development. ACS Materials Au 3:600–619
132. Dosler S (2017) Antimicrobial peptides: Coming to the end of antibiotic era, the most promising agents. Istanbul Journal of Pharmacy 47:72–76. https://doi.org/10.5152/istanbuljpharm.2017.0012
133. Yammine J, Chihib NE, Gharsallaoui A, et al (2022) Essential oils and their active components applied as: free, encapsulated and in hurdle technology to fight microbial contaminations. A review. Heliyon 8
134. Pérez-Recalde M, Ruiz Arias IE, Hermida ÉB (2018) Could essential oils enhance biopolymers performance for wound healing? A systematic review. Phytomedicine 38:57–65
135. De Luca I, Pedram P, Moeini A, et al (2021) Nanotechnology development for formulating essential oils in wound dressing materials to promote the wound-healing process: A review. Applied Sciences (Switzerland) 11:1–19. https://doi.org/10.3390/app11041713
136. Kaspute G, Ivaskiene T, Ramanavicius A, et al (2025) Terpenes and Essential Oils in Pharmaceutics: Applications as Therapeutic Agents and Penetration Enhancers with Advanced Delivery Systems for Improved Stability and Bioavailability. Pharmaceutics 17
137. Akombaetwa N, Ilangala AB, Thom L, et al (2023) Current Advances in Lipid Nanosystems Intended for Topical and Transdermal Drug Delivery Applications. Pharmaceutics 15
138. Wen MM, Abdelwahab IA, Aly RG, El-Zahaby SA (2021) Nanophyto-gel against multi-drug resistant Pseudomonas aeruginosa burn wound infection. Drug Deliv 28:463–477. https://doi.org/10.1080/10717544.2021.1889720
139. Hajibonabi A, Yekani M, Sharifi S, et al (2023) Antimicrobial activity of nanoformulations of carvacrol and thymol: New trend and applications. OpenNano 13
140. Rashed AA, Rathi DNG, Nasir NAHA, Rahman AZA (2021) Antifungal Properties of Essential Oils and Their Compounds for Application in Skin Fungal Infections: Conventional and Nonconventional Approaches. Molecules 26
141. Naveedunissa S, Meenalotchani R, Manisha M, et al (2025) Advances in chitosan based nanocarriers for targetted wound healing therapies: a review. Carbohydrate Polymer Technologies and Applications 11
142. Lu T, Zhou X, Jiang SY, et al (2025) Natural Bioactive Compound-Integrated Nanomaterials for Diabetic Wound Healing: Synergistic Effects, Multifunctional Designs, and Challenges. Molecules 30
143. Younis MA, Tawfeek HM, Abdellatif AAH, et al (2022) Clinical translation of nanomedicines: Challenges, opportunities, and keys. Adv. Drug Deliv. Rev. 181

144. Touati A, Mairi A, Ibrahim NA, Idres T (2025) Essential Oils for Biofilm Control: Mechanisms, Synergies, and Translational Challenges in the Era of Antimicrobial Resistance. Antibiotics 14
145. Yu W, Xu H, Yuan X, et al (2025) Cinnamaldehyde promotes diabetic wound healing via synergetic effects of AGE/RAGE-mediated macrophage polarization affecting fibroblast activation and angiogenesis, and Nrf2-dependent antioxidants. Biochem Biophys Res Commun 781:. https://doi.org/10.1016/j.bbrc.2025.152519
146. Akhtari N, Ahmadi M, Kiani Doust Vaghe Y, et al (2024) Natural agents as wound-healing promoters. Inflammopharmacology 32:101–125
147. Majumder J, Taratula O, Minko T (2019) Nanocarrier-based systems for targeted and site specific therapeutic delivery. Adv. Drug Deliv. Rev. 144:57–77
148. Lüdtke FL, Silva TJ, da Silva MG, et al (2025) Lipid Nanoparticles: Formulation, Production Methods and Characterization Protocols. Foods 14
149. Figueiredo CSS e. S, Oliveira PV de, Saminez WF da S, et al (2023) Immunomodulatory Effects of Cinnamaldehyde in Staphylococcus aureus-Infected Wounds. Molecules 28:. https://doi.org/10.3390/molecules28031204
150. Qureshi KA, Mohammed SAA, Khan O, et al (2022) Cinnamaldehyde-Based Self-Nanoemulsion (CA-SNEDDS) Accelerates Wound Healing and Exerts Antimicrobial, Antioxidant, and Anti-Inflammatory Effects in Rats' Skin Burn Model. Molecules 27:. https://doi.org/10.3390/molecules27165225
151. Percival SL, McCarty S, Hunt JA, Woods EJ (2014) The effects of pH on wound healing, biofilms, and antimicrobial efficacy. Wound Repair Regen. 22:174–186
152. Wallace LA, Gwynne L, Jenkins T (2019) Challenges and opportunities of pH in chronic wounds. Ther. Deliv. 10:719–735
153. Mariani F, Serafini M, Gualandi I, et al (2021) Advanced Wound Dressing for Real-Time pH Monitoring. ACS Sens 6:2366–2377. https://doi.org/10.1021/acssensors.1c00552
154. Wang J, Windbergs M (2017) Functional electrospun fibers for the treatment of human skin wounds. European Journal of Pharmaceutics and Biopharmaceutics 119:283–299
155. Sylvester MA, Amini F, Keat TC (2019) Electrospun nanofibers in wound healing. In: Materials Today: Proceedings. Elsevier Ltd, pp 1–6
156. Juncos Bombin AD, Dunne NJ, McCarthy HO (2020) Electrospinning of natural polymers for the production of nanofibres for wound healing applications. Materials Science and Engineering C 114
157. Abrigo M, McArthur SL, Kingshott P (2014) Electrospun nanofibers as dressings for chronic wound care: Advances, challenges, and future prospects. Macromol. Biosci. 14:772–792
158. Kamoun EA, Chen X, Mohy Eldin MS, Kenawy ERS (2015) Crosslinked poly(vinyl alcohol) hydrogels for wound dressing applications: A review of remarkably blended polymers. Arabian Journal of Chemistry 8:1–14
159. Shakiba M, Pourmadadi M, Hosseini SM, et al (2024) A bi-functional nanofibrous composite membrane for wound healing applications. Arch Pharm (Weinheim) 357:. https://doi.org/10.1002/ardp.202400001

160. Rastegar A, Baharifar H, Dabir K, et al (2025) Fabrication and Characterization of ZnO Nanoparticle-Loaded Nanofibers for Diabetic Wound Healing Applications: An in vivo Study. Bionanoscience 15:. https://doi.org/10.1007/s12668-024-01606-7
161. Qamar SUR, Virijević K, Košarić J, et al (2024) Application of biogenic silver nanoparticle incorporated nanofibers in biomedical science. Inorg Chem Commun 170:. https://doi.org/10.1016/j.inoche.2024.113455
162. Kossyvaki D, Contardi M, Athanassiou A, Fragouli D (2022) Colorimetric Indicators Based on Anthocyanin Polymer Composites: A Review. Polymers (Basel). 14
163. Prietto L, Pinto VZ, El Halal SLM, et al (2018) Ultrafine fibers of zein and anthocyanins as natural pH indicator. J Sci Food Agric 98:2735–2741. https://doi.org/10.1002/jsfa.8769
164. Pakolpakçıl A, Osman B, Göktalay G, et al (2021) Design and in vivo evaluation of alginate-based pH-sensing electrospun wound dressing containing anthocyanins. Journal of Polymer Research 28:. https://doi.org/10.1007/s10965-020-02400-1
165. Cui L, Hu J jing, Wang W, et al (2020) Smart pH response flexible sensor based on calcium alginate fibers incorporated with natural dye for wound healing monitoring. Cellulose 27:6367–6381. https://doi.org/10.1007/s10570-020-03219-1
166. Celeiro M, Lamas JP, Arcas R, Lores M (2019) Antioxidants profiling of by-products from eucalyptus greenboards manufacture. Antioxidants 8:1–16. https://doi.org/10.3390/antiox8080263
167. Michiu D, Socaciu MI, Fogarasi M, et al (2022) Implementation of an Analytical Method for Spectrophotometric Evaluation of Total Phenolic Content in Essential Oils. Molecules 27:. https://doi.org/10.3390/molecules27041345
168. Wiegand I, Hilpert K, Hancock REW (2008) Agar and broth dilution methods to determine the minimal inhibitory concentration (MIC) of antimicrobial substances. Nat Protoc 3:163–175. https://doi.org/10.1038/nprot.2007.521
169. European Committee for Antimicrobial Susceptibility Testing (EUCAST) of the European Society of Clinical Microbiology and Infectious Diseases (ESCMID), Determination of minimum inhibitory concentrations (MICs) of antibacterial agents by broth dilution, Clin. Microbiol. Infect. 9 (2003) 1–7.
170. Teixeira MA, Antunes JC, Seabra CL, et al (2022) Tiger 17 and pexiganan as antimicrobial and hemostatic boosters of cellulose acetate-containing poly(vinyl alcohol) electrospun mats for potential wound care purposes. Int J Biol Macromol 209:1526–1541. https://doi.org/10.1016/j.ijbiomac.2022.04.130
171. Huang A, Peng X, Geng L, et al (2018) Electrospun poly (butylene succinate)/cellulose nanocrystals bio-nanocomposite scaffolds for tissue engineering: Preparation, characterization and in vitro evaluation. Polym Test 71:101–109. https://doi.org/10.1016/j.polymertesting.2018.08.027
172. Silva IO, Ladchumananandasivam R, Nascimento JHO, et al (2019) Multifunctional chitosan/gold nanoparticles coatings for biomedical textiles. Nanomaterials 9:. https://doi.org/10.3390/nano9081064
173. Tang B, He Y, Liu J, et al (2019) Kinetic investigation into pH-dependent color of anthocyanin and its sensing performance. Dyes and Pigments 170:. https://doi.org/10.1016/j.dyepig.2019.107643

174. Abedi-Firoozjah R, Yousefi S, Heydari M, et al (2022) Application of Red Cabbage Anthocyanins as pH-Sensitive Pigments in Smart Food Packaging and Sensors. Polymers (Basel). 14
175. Im YR, Kim I, Lee J (2021) Phenolic composition and antioxidant activity of purple sweet potato (Ipomoea batatas (l.) lam.): Varietal comparisons and physical distribution. Antioxidants 10:1–17. https://doi.org/10.3390/antiox10030462
176. Zhang Y, Zhao L, Wang L, et al (2024) Chlorogenic acid compounds from sweetpotato (Ipomoea batatas L.) leaves facilitate megakaryocyte differentiation and thrombocytopoiesis via PI3K/AKT pathway. Front Pharmacol 15:. https://doi.org/10.3389/fphar.2024.1414739
177. Rizk E (2009) Evaluation of red cabbage anthocyanin pigments and its potential uses as antioxidant and natural food colorant
178. Wiczkowski W, Topolska J, Honke J (2014) Anthocyanins profile and antioxidant capacity of red cabbages are influenced by genotype and vegetation period. J Funct Foods 7:201–211. https://doi.org/10.1016/j.jff.2014.02.011
179. Mejias N, Vega-Galvez A, Pasten A, et al (2025) Evaluating the Microstructure and Bioaccessibility of Bioactive Compounds and Antioxidant Activity After the Dehydration of Red Cabbage. Foods 14:. https://doi.org/10.3390/foods14111932
180. Li W, Zhang Y, Deng H, et al (2023) In vitro and in vivo bioaccessibility, antioxidant activity, and color of red radish anthocyanins as influenced by different drying methods. Food Chem X 18:. https://doi.org/10.1016/j.fochx.2023.100633
181. Wang LS, Sun XD, Cao Y, et al (2010) Antioxidant and pro-oxidant properties of acylated pelargonidin derivatives extracted from red radish (Raphanus sativus var. niger, Brassicaceae). Food and Chemical Toxicology 48:2712–2718. https://doi.org/10.1016/j.fct.2010.06.045
182. Sadowska-Bartosz I, Bartosz G (2024) Antioxidant Activity of Anthocyanins and Anthocyanidins: A Critical Review. Int. J. Mol. Sci. 25
183. Khoo HE, Azlan A, Tang ST, Lim SM (2017) Anthocyanidins and anthocyanins: Colored pigments as food, pharmaceutical ingredients, and the potential health benefits. Food Nutr. Res. 61
184. Chandimali N, Bak SG, Park EH, et al (2025) Free radicals and their impact on health and antioxidant defenses: a review. Cell Death Discov. 11
185. Asfaw DE Antioxidant Properties of Phenolic Compounds to Manage Oxidative Stress / A Review
186. Zouine N, Ghachtouli N El, Abed S El, Koraichi SI (2024) A comprehensive review on medicinal plant extracts as antibacterial agents: Factors, mechanism insights and future prospects. Sci. Afr. 26
187. Hosee YN, Farhan MS, Shaban SA (2025) The Potential of Medicinal Plants in Antifungal Drug Development: Mechanisms, Synergies, and Future Directions. J. Mycol. Infect. 30:1–17
188. Vélez MD, Llano-Ramirez MA, Ramón C, et al (2023) Antioxidant capacity and cytotoxic effect of an optimized extract of isabella grape (Vitis labrusca) on breast cancer cells. Heliyon 9:. https://doi.org/10.1016/j.heliyon.2023.e16540

189. Adabavazeh Z, Johari N, Baino F (2025) Electrospun conductive polymer scaffolds: Tailoring fiber diameter and electrical properties for tissue engineering applications. Mater. Today Commun. 46
190. Chinnappan BA, Krishnaswamy M, Xu H, Hoque ME (2022) Electrospinning of Biomedical Nanofibers/Nanomembranes: Effects of Process Parameters. Polymers (Basel). 14
191. Pang Q, Yang F, Jiang Z, et al (2023) Smart wound dressing for advanced wound management: Real-time monitoring and on-demand treatment. Mater Des 229:. https://doi.org/10.1016/j.matdes.2023.111917
192. Suk JS, Xu Q, Kim N, et al (2016) PEGylation as a strategy for improving nanoparticle-based drug and gene delivery. Adv. Drug Deliv. Rev. 99:28–51
193. Rosales-Murillo SS, Sánchez-Bodón J, Hernández Olmos SL, et al (2024) Anthocyanin-Loaded Polymers as Promising Nature-Based, Responsive, and Bioactive Materials. Polymers (Basel). 16
194. Zubova G, Melnyk H, Zaets I, et al (2024) Halochromic Bacterial Cellulose/Anthocyanins Hybrid Polymer Film with Wound-Healing Potential. Polymers (Basel) 16:. https://doi.org/10.3390/polym16162327
195. Felgueiras HP, Homem NC, Teixeira MA, et al (2020) Physical, thermal, and antibacterial effects of active essential oils with potential for biomedical applications loaded onto cellulose acetate/polycaprolactone wet-spun microfibers. Biomolecules 10:1–20. https://doi.org/10.3390/biom10081129
196. Koochakzaei A, Ahmadi H, Achachluei MM (2016) An Experimental Comparative Study on Silicone Oil and Polyethylene Glycol as Dry Leather Treatments. JALCA 111:
197. Stoica R, Ganciarov M, Constantinescu-Aruxandei D, et al (2023) Sustainable Recovery of Anthocyanins and Other Polyphenols from Red Cabbage Byproducts. Foods 12:. https://doi.org/10.3390/foods12224157
198. Souza PP, Robazza WS, Galvão AC (2020) Thermal degradation of the anthocyanins extracts from jabuticaba peels and red cabbage leaves. Scientia Plena 16:. https://doi.org/10.14808/sci.plena.2020.064201
199. De Marchi L, Salemi L, Bellumori M, et al (2024) Thermal degradation of red cabbage (Brassica oleracea L. var. Capitata f. rubra) anthocyanins in a water model extract under accelerated shelf-life testing. Food Chem 440:. https://doi.org/10.1016/j.foodchem.2023.138272
200. ElGamal R, Song C, Rayan AM, et al (2023) Thermal Degradation of Bioactive Compounds during Drying Process of Horticultural and Agronomic Products: A Comprehensive Overview. Agronomy 13
201. Nurazzi NM, Asyraf MRM, Rayung M, et al (2021) Thermogravimetric analysis properties of cellulosic natural fiber polymer composites: A review on influence of chemical treatments. Polymers (Basel). 13
202. Vogel C, Siesler HW (2008) Thermal degradation of poly(ε-caprolactone), poly(L-lactic acid) and their blends with poly(3-hydroxy-butyrate) studied by TGA/FT-IR spectroscopy. In: Macromolecular Symposia. pp 183–194

203. Geisler M, Khan J, Heine T, et al (2025) Analysis of high-molecular weight polyethylene glycol degradation by Pseudomonas sp. Polym Degrad Stab 232:. https://doi.org/10.1016/j.polymdegradstab.2024.111144
204. Matumba KI, Motloung MP, Ojijo V, et al (2023) Investigation of the Effects of Chain Extender on Material Properties of PLA/PCL and PLA/PEG Blends: Comparative Study between Polycaprolactone and Polyethylene Glycol. Polymers (Basel) 15:. https://doi.org/10.3390/polym15092230
205. Tecucianu AC, Draghici O, Oancea S (2020) AN ENZYME-ENHANCED EXTRACTION of ANTHOCYANINS from RED CABBAGE and THEIR THERMAL DEGRADATION KINETICS. Acta Aliment 49:204–213. https://doi.org/10.1556/066.2020.49.2.10
206. Thang NH, Chien TB, Cuong DX (2023) Polymer-Based Hydrogels Applied in Drug Delivery: An Overview. Gels 9
207. Fredi G, Dorigato A (2024) Compatibilization of biopolymer blends: A review. Advanced Industrial and Engineering Polymer Research 7:373–404
208. Pourjavaher S, Almasi H, Meshkini S, et al (2017) Development of a colorimetric pH indicator based on bacterial cellulose nanofibers and red cabbage (Brassica oleraceae) extract. Carbohydr Polym 156:193–201. https://doi.org/10.1016/j.carbpol.2016.09.027
209. Agrawal G, Negi YS, Pradhan S, et al (2017) Wettability and contact angle of polymeric biomaterials. In: Characterization of Polymeric Biomaterials. Elsevier, pp 57–81
210. Guclu N, Duzyer Gebizli S, Orhan M (2023) Development of polycaprolactone-based electrospun pH-sensitive sensors as instant colorimetric indicators for food packaging. Coloration Technology 139:527–543. https://doi.org/10.1111/cote.12701
211. Han G, Ceilley R (2017) Chronic Wound Healing: A Review of Current Management and Treatments. Adv Ther 34:599–610. https://doi.org/10.1007/s12325-017-0478-y
212. Ribeiro ARM, Teixeira MO, Ribeiro L, et al (2024) Sodium alginate-based multifunctional sandwich-like system for treating wound infections. Biomaterials Advances 162:. https://doi.org/10.1016/j.bioadv.2024.213931
213. Huang R, Zhu X, Zhao T, Wan A (2015) Preparation of tissue engineering porous scaffold with poly(lactic acid) and polyethylene glycol solution blend by solvent-casting/particulate-leaching. Mater Res Express 1:. https://doi.org/10.1088/2053-1591/1/4/045403
214. Mostafalu P, Tamayol A, Rahimi R, et al (2018) Smart Bandage for Monitoring and Treatment of Chronic Wounds. Small 14:. https://doi.org/10.1002/smll.201703509
215. Kurek MA, Custodio-Mendoza JA, Aktaş H, Pokorski P (2024) Exploring deep eutectic solvent extraction's impact on anthocyanin degradation kinetics in various conditions. LWT 198:. https://doi.org/10.1016/j.lwt.2024.115994
216. Pachulicz RJ, Yu L, Jovcevski B, et al (2023) Structural Analysis and Identity Confirmation of Anthocyanins in Brassica oleracea Extracts by Direct Injection Ion Mobility-Mass Spectrometry. ACS Measurement Science Au 3:200–207. https://doi.org/10.1021/acsmeasuresciau.2c00058
217. Mejías N, Vega-Galvez A, Gomez-Perez LS, et al (2024) Health-Promoting Properties of Processed Red Cabbage (Brassica oleracea var. capitata f. rubra): Effects of Drying Methods on Bio-Compound Retention. Foods 13:. https://doi.org/10.3390/foods13060830

218. Hamed SH, Azooz EA, Al-Mulla EAJ (2023) Nanoparticles-assisted Wound Healing: A Review. Nano Biomed. Eng. 15:425–435
219. Bowers S, Franco E (2020) Chronic Wounds: Evaluation and Management
220. Frykberg RG, Banks J (2015) Challenges in the Treatment of Chronic Wounds. Adv Wound Care (New Rochelle) 4:560–582. https://doi.org/10.1089/wound.2015.0635
221. Las Heras K, Igartua M, Santos-Vizcaino E, Hernandez RM (2020) Chronic wounds: Current status, available strategies and emerging therapeutic solutions. Journal of Controlled Release 328:532–550
222. Gianino E, Miller C, Gilmore J (2018) Smart wound dressings for diabetic chronic wounds. Bioengineering 5
223. Ge Y, Wang Q (2023) Current research on fungi in chronic wounds. Front. Mol. Biosci. 9
224. Short B, Bakri A, Baz A, et al (2023) There Is More to Wounds than Bacteria: Fungal Biofilms in Chronic Wounds. Curr. Clin. Microbiol. Rep. 10:9–16
225. Hu Y, Yu L, Dai Q, et al (2024) Multifunctional antibacterial hydrogels for chronic wound management. Biomater. Sci. 12:2460–2479
226. Bîrcă AC, Minculescu MA, Niculescu AG, et al (2025) Nanoparticle-Enhanced Collagen Hydrogels for Chronic Wound Management. J Funct Biomater 16:. https://doi.org/10.3390/jfb16030091
227. Saracino IM, Foschi C, Pavoni M, et al (2022) Antifungal Activity of Natural Compounds vs. Candida spp.: A Mixture of Cinnamaldehyde and Eugenol Shows Promising In Vitro Results. Antibiotics 11:. https://doi.org/10.3390/antibiotics11010073
228. Khwaza V, Aderibigbe BA (2023) Antifungal Activities of Natural Products and Their Hybrid Molecules. Pharmaceutics 15
229. Rachel R, Anuradha M, Leela K V. (2024) Evaluating the Antifungal Potential of Cinnamaldehyde: A Study of its Efficacy against Candida Species. J Pure Appl Microbiol 18:2438–2445. https://doi.org/10.22207/JPAM.18.4.16
230. Feng J, Sun L, Zhai T, et al (2023) Preparation of cinnamaldehyde nanoemulsions: Formula optimization, antifungal activity, leaf adhesion, and safety assessment. Ind Crops Prod 200:. https://doi.org/10.1016/j.indcrop.2023.116825
231. Bashiri S, Ghanbarzadeh B, Ayaseh A, et al (2020) Essential oil-loaded nanostructured lipid carriers: The effects of liquid lipid type on the physicochemical properties in beverage models. Food Biosci 35:. https://doi.org/10.1016/j.fbio.2020.100526
232. Wathoni N, Suhandi C, Elamin KM, et al (2024) Advancements and Challenges of Nanostructured Lipid Carriers for Wound Healing Applications. Int. J. Nanomedicine 19:8091–8113
233. Cimino C, Maurel OM, Musumeci T, et al (2021) Essential oils: Pharmaceutical applications and encapsulation strategies into lipid-based delivery systems. Pharmaceutics 13:1–35
234. Khezri K, Farahpour MR, Mounesi Rad S (2020) Efficacy of Mentha pulegium essential oil encapsulated into nanostructured lipid carriers as an in vitro antibacterial and infected wound healing agent. Colloids Surf A Physicochem Eng Asp 589:. https://doi.org/10.1016/j.colsurfa.2020.124414

235. Motsoene F, Abrahamse H, Dhilip Kumar SS (2023) Multifunctional lipid-based nanoparticles for wound healing and antibacterial applications: A review. Adv. Colloid Interface Sci. 321

236. Sotirova Y (2023) Solid Lipid Nanoparticles and Nanostructured Lipid Carriers: Current perspective in wound care. Scripta Scientifica Pharmaceutica 1:24–34. https://doi.org/10.14748/ssp.v9i2.9060

237. Costa-Fernandez S, Matos JKR, Scheunemann GS, et al (2021) Nanostructured lipid carriers containing chitosan or sodium alginate for co-encapsulation of antioxidants and an antimicrobial agent for potential application in wound healing. Int J Biol Macromol 183:668–680. https://doi.org/10.1016/j.ijbiomac.2021.04.168

238. Khan S, Sharma A, Jain V (2023) An overview of nanostructured lipid carriers and its application in drug delivery through different routes. Adv. Pharm. Bull. 13:446–460

239. Rajinikanth B S, Rajkumar DSR, K K, Vijayaragavan V (2024) Chitosan-Based Biomaterial in Wound Healing: A Review. Cureus. https://doi.org/10.7759/cureus.55193

240. Parham S, Kharazi AZ, Bakhsheshi-Rad HR, et al (2022) Antimicrobial Synthetic and Natural Polymeric Nanofibers as Wound Dressing: A Review. Adv. Eng. Mater. 24

241. Zhu J, Xia F, Wang S, et al (2025) Recent advances in nanomaterials and their mechanisms for infected wounds management. Mater. Today Bio 31

242. Barari F, Maghsoudian S, Alinezhad V, et al (2025) Effective topical delivery of astaxanthin via optimized chitosan-coated nanostructured lipid carriers: A promising strategy for enhanced wound healing and tissue regeneration through in vitro and in vivo evaluations. J Drug Deliv Sci Technol 107052. https://doi.org/10.1016/j.jddst.2025.107052

243. Costa-Fernandez S, Matos JKR, Scheunemann GS, et al (2021) Nanostructured lipid carriers containing chitosan or sodium alginate for co-encapsulation of antioxidants and an antimicrobial agent for potential application in wound healing. Int J Biol Macromol 183:668–680. https://doi.org/10.1016/j.ijbiomac.2021.04.168

244. Vieira ACC, Chaves LL, Pinheiro M, et al (2016) Design and statistical modeling of mannose-decorated dapsone-containing nanoparticles as a strategy of targeting intestinal M-cells. Int J Nanomedicine 11:2601–2617. https://doi.org/10.2147/IJN.S104908

245. Vieira ACC, Chaves LL, Pinheiro S, et al (2018) Mucoadhesive chitosan-coated solid lipid nanoparticles for better management of tuberculosis. Int J Pharm 536:478–485. https://doi.org/10.1016/j.ijpharm.2017.11.071

246. Vasconcelos PGS, Lee KM, Abuna GF, et al (2024) Monoterpene antifungal activities: evaluating geraniol, citronellal, and linalool on Candida biofilm, host inflammatory responses, and structure–activity relationships. Front Pharmacol 15:. https://doi.org/10.3389/fphar.2024.1394053

247. Rashed AA, Rathi DNG, Nasir NAHA, Rahman AZA (2021) Antifungal Properties of Essential Oils and Their Compounds for Application in Skin Fungal Infections: Conventional and Nonconventional Approaches. Molecules 26

248. Baghi F, Ghnimi S, Dumas E, Gharsallaoui A (2023) Microencapsulation of Antimicrobial trans-Cinnamaldehyde: Effect of Emulsifier Type, pH, and Drying Technique. Applied Sciences (Switzerland) 13:. https://doi.org/10.3390/app13106184

249. Li Y, Liu Y, Jiang Y, et al (2025) New antifungal strategies and drug development against WHO critical priority fungal pathogens. Front. Cell. Infect. Microbiol. 15
250. Javed S, Mangla B, Almoshari Y, et al (2022) Nanostructured lipid carrier system: A compendium of their formulation development approaches, optimization strategies by quality by design, and recent applications in drug delivery. Nanotechnol. Rev. 11:1744–1777
251. Pitterou I, Kostopoulou I, Karadendrou M-A, et al (2025) Chitosan-Coated Nanostructured Lipid Carriers (NLCs) Incorporating Esters of Ferulic Acid with Photoprotective Activity. Macromol 5:50. https://doi.org/10.3390/macromol5040050
252. Aldayel TS, M. Badran M, H. Alomrani A, et al (2023) Chitosan-Coated Solid Lipid Nanoparticles as an Efficient Avenue for Boosted Biological Activities of Aloe perryi: Antioxidant, Antibacterial, and Anticancer Potential. Molecules 28:. https://doi.org/10.3390/molecules28083569
253. Rabelo RS, Oliveira IF, da Silva VM, et al (2018) Chitosan coated nanostructured lipid carriers (NLCs) for loading Vitamin D: A physical stability study. Int J Biol Macromol 119:902–912. https://doi.org/10.1016/j.ijbiomac.2018.07.174
254. Musielak E, Feliczak-Guzik A, Nowak I (2022) Optimization of the Conditions of Solid Lipid Nanoparticles (SLN) Synthesis. Molecules 27:. https://doi.org/10.3390/molecules27072202
255. Bonaccorso A, Cimino C, Manno DE, et al (2021) Essential oil-loaded nlc for potential intranasal administration. Pharmaceutics 13:. https://doi.org/10.3390/pharmaceutics13081166
256. Chen J, Li S, Zheng Q, et al (2022) Preparation of Solid Lipid Nanoparticles of Cinnamaldehyde and Determination of Sustained Release Capacity. Nanomaterials 12:. https://doi.org/10.3390/nano12244460
257. Ruggeri M, Pollini M, Ricci C, et al (2026) The role of chitosan in modulating physicochemical and biological behavior of solid lipid nanoparticles. Int J Biol Macromol 335:. https://doi.org/10.1016/j.ijbiomac.2025.149153
258. Abdulhussain R, Adebisi A, Conway BR, Asare-Addo K (2023) Electrospun nanofibers: Exploring process parameters, polymer selection, and recent applications in pharmaceuticals and drug delivery. J Drug Deliv Sci Technol 90:. https://doi.org/10.1016/j.jddst.2023.105156
259. Medeiros GB, Lima F de A, de Almeida DS, et al (2022) Modification and Functionalization of Fibers Formed by Electrospinning: A Review. Membranes (Basel). 12
260. Zhou C, Ji Y, Yang A, et al (2025) Surface Functionalization of Electrospun Membranes and Their Biomedical Applications. In: Electrospinning Techniques - Advances, Applications, and Challenges [Working Title]. IntechOpen
261. Faraji S, Sadri B, Vajdi Hokmabad B, et al (2017) Experimental study on the role of electrical conductivity in pulsating modes of electrospraying. Exp Therm Fluid Sci 81:327–335. https://doi.org/10.1016/j.expthermflusci.2016.10.030
262. Farias B, Rizzi F, Gerhardt R, et al (2024) Electrosprayed Chitosan Nanospheres-Based Films: Evaluating the Effect of Molecular Weight on Physicochemical Properties. Coatings 14:. https://doi.org/10.3390/coatings14091159

263. Pitterou I, Kostopoulou I, Karadendrou M-A, et al (2025) Chitosan-Coated Nanostructured Lipid Carriers (NLCs) Incorporating Esters of Ferulic Acid with Photoprotective Activity. Macromol 5:50. https://doi.org/10.3390/macromol5040050
264. Hadidi M, Pouramin S, Adinepour F, et al (2020) Chitosan nanoparticles loaded with clove essential oil: Characterization, antioxidant and antibacterial activities. Carbohydr Polym 236:. https://doi.org/10.1016/j.carbpol.2020.116075
265. Oviedo M, Montoya Y, Alvarez C, Bustamante J (2023) Influence of Electrospinning Parameters on the Physicochemical Properties of Polycaprolactone, Chitosan, and Sericin Membranes. MDPI AG, p 5
266. Kalva SN, Zakaria Y, Velasquez CA, Koç M (2025) Tailoring the mechanical and degradation properties of 3DP PLA/PCL scaffolds for biomedical applications. Reviews on Advanced Materials Science 64:. https://doi.org/10.1515/rams-2025-0098
267. Clerici NJ, Vencato AA, Helm Júnior R, et al (2024) Electrospun Poly-ε-Caprolactone Nanofibers Incorporating Keratin Hydrolysates as Innovative Antioxidant Scaffolds. Pharmaceuticals 17:. https://doi.org/10.3390/ph17081016
268. Chen J, Li S, Zheng Q, et al (2022) Preparation of Solid Lipid Nanoparticles of Cinnamaldehyde and Determination of Sustained Release Capacity. Nanomaterials 12:. https://doi.org/10.3390/nano12244460
269. Azari A, Golchin A, Maymand MM, et al (2022) Electrospun Polycaprolactone Nanofibers: Current Research and Applications in Biomedical Application. Adv. Pharm. Bull. 12:658–672
270. Nejaddehbashi F, Rafiee Z, Orazizadeh M, et al (2023) Antibacterial and antioxidant double-layered nanofibrous mat promotes wound healing in diabetic rats. Sci Rep 13:. https://doi.org/10.1038/s41598-023-30240-8
271. Alexeev D, Tschopp M, Helgason B, Ferguson SJ (2021) Electrospun biodegradable poly(ε-caprolactone) membranes for annulus fibrosus repair: Long-term material stability and mechanical competence. JOR Spine 4:. https://doi.org/10.1002/jsp2.1130
272. Niknejad E, Jafari R, Valipour Motlagh N (2025) Mechanical Properties of Biodegradable Fibers and Fibrous Mats: A Comprehensive Review. Molecules 30
273. Bassey POAO, Oseni BA, Ogundemuren DA, et al (2025) Assessment of microstructural architecture and mechanical properties of levonorgestrel loaded PCL/PLGA/HA nanofibers. Next Materials 8:. https://doi.org/10.1016/j.nxmate.2025.100729
274. Livi G, Fazal F, Barrio-Zhang H, et al (2025) Characterization of Water Adhesion of PCL and PLCL Electrospun Fiber Mats and Their Correlation to Wettability. Macromol Mater Eng 310:. https://doi.org/10.1002/mame.202500189
275. Ahmed MK, Zayed MA, El-dek SI, et al (2021) Nanofibrous ε-polycaprolactone scaffolds containing Ag-doped magnetite nanoparticles: Physicochemical characterization and biological testing for wound dressing applications in vitro and in vivo. Bioact Mater 6:2070–2088. https://doi.org/10.1016/j.bioactmat.2020.12.026
276. de Cassan D, Becker A, Glasmacher B, et al (2020) Blending chitosan-g-poly(caprolactone) with poly(caprolactone) by electrospinning to produce functional fiber mats for tissue engineering applications. J Appl Polym Sci 137:. https://doi.org/10.1002/app.48650

277. Alyamani AA, Al-Musawi MH, Albukhaty S, et al (2023) Electrospun Polycaprolactone/Chitosan Nanofibers Containing Cordia myxa Fruit Extract as Potential Biocompatible Antibacterial Wound Dressings. Molecules 28:. https://doi.org/10.3390/molecules28062501
278. Andrade del Olmo J, Mikeš P, Asatiani N, et al (2024) Alternating Current Electrospinning of Polycaprolactone/Chitosan Nanofibers for Wound Healing Applications. Polymers (Basel) 16:. https://doi.org/10.3390/polym16101333
279. Querido D, Vieira T, Ferreira JL, et al (2022) Study on the Incorporation of Chitosan Flakes in Electrospun Polycaprolactone Scaffolds. Polymers (Basel) 14:. https://doi.org/10.3390/polym14081496
280. Ferraz MP (2025) Wound Dressing Materials: Bridging Material Science and Clinical Practice. Applied Sciences (Switzerland) 15
281. Kamath SM, Sridhar K, Jaison D, et al (2020) Fabrication of tri-layered electrospun polycaprolactone mats with improved sustained drug release profile. Sci Rep 10:. https://doi.org/10.1038/s41598-020-74885-1
282. Tavares TD, Pinho SLC, Delgado-Pujol EJ, et al (2025) Layer-by-layer electrospun PCL/PVA mats loaded with nisin Z for enhanced diabetic foot ulcer treatment. Int J Pharm 685:. https://doi.org/10.1016/j.ijpharm.2025.126208
283. Rachel R, Anuradha M, Leela K V. (2024) Evaluating the Antifungal Potential of Cinnamaldehyde: A Study of its Efficacy against Candida Species. J Pure Appl Microbiol 18:2438–2445. https://doi.org/10.22207/JPAM.18.4.16
284. Schroder T, Gaskin S, Ross K, Whiley H (2017) Antifungal activity of essential oils against fungi isolated from air. Int J Occup Environ Health 23:181–186. https://doi.org/10.1080/10773525.2018.1447320
285. Long Y, Xu J, Hu Z, et al (2024) Antifungal activity of Cinnamaldehyde derivatives against fluconazole-resistant Candida albicans. Microb Pathog 195:. https://doi.org/10.1016/j.micpath.2024.106877
286. Tuan DA, Uyen PVN, Masak J (2024) Unveiling the Antifungal Potential of Trans-Cinnamaldehyde: A Comparative Study Against Biofilm and Planktonic Forms of Candida spp.
287. Tuan DA, Nhan NVT, Uyen PVN, et al (2023) Inhibitory effects of trans-cinnamaldehyde on candida spp. Biofilm and planktonic form compared to nystatin: A comparative analysis. Tạp chí Nghiên cứu Y học 173:167–175. https://doi.org/10.52852/tcncyh.v173i12e13.2178
288. Wang H, Liu Y, Cai K, et al (2021) Antibacterial polysaccharide-based hydrogel dressing containing plant essential oil for burn wound healing. Burns Trauma 9:. https://doi.org/10.1093/burnst/tkab041
289. Zhang T, Luo Y, Wang M, et al (2020) Double-layered microcapsules significantly improve the long-term effectiveness of essential oil. Polymers (Basel) 12:. https://doi.org/10.3390/POLYM12081651
290. Lim SB, Banerjee A, Önyüksel H (2012) Improvement of drug safety by the use of lipid-based nanocarriers. In: Journal of Controlled Release. pp 34–45
291. Mu R, Zhang H, Zhang Z, et al (2023) Trans-cinnamaldehyde loaded chitosan based nanocapsules display antibacterial and antibiofilm effects against cavity-causing

Streptococcus mutans. J Oral Microbiol 15:. https://doi.org/10.1080/20002297.2023.2243067

292. McLean P, Marshall J, García-Bilbao A, et al (2024) A comparison of dermal toxicity models; assessing suitability for safe(r)-by-design decision-making and for screening nanomaterial hazards. Toxicology in Vitro 97:. https://doi.org/10.1016/j.tiv.2024.105792
293. Pastar I, Stojadinovic O, Yin NC, et al (2014) Epithelialization in Wound Healing: A Comprehensive Review. Adv Wound Care (New Rochelle) 3:445–464. https://doi.org/10.1089/wound.2013.0473
294. Dong X, Xiang H, Li J, et al (2025) Dermal fibroblast-derived extracellular matrix (ECM) synergizes with keratinocytes in promoting re-epithelization and scarless healing of skin wounds: Towards optimized skin tissue engineering. Bioact Mater 47:1–17. https://doi.org/10.1016/j.bioactmat.2024.12.030
295. Jiang P, Li Q, Luo Y, et al (2023) Current status and progress in research on dressing management for diabetic foot ulcer. Front. Endocrinol. (Lausanne). 14
296. Deng H, Li B, Shen Q, et al (2023) Mechanisms of diabetic foot ulceration: A review. J. Diabetes 15:299–312
297. Shelar K, Salve PS, Qutub M, et al (2025) Advanced Bioinspired Silver Nanoparticles Integrated into Polyherbal Gel for Enhanced Diabetic Foot Ulcer Regeneration. Biol Trace Elem Res. https://doi.org/10.1007/s12011-025-04666-2
298. Huang F, Lu X, Yang Y, et al (2023) Microenvironment-Based Diabetic Foot Ulcer Nanomedicine. Advanced Science 10
299. Li YR, Lai XS, Cheong HF, et al (2025) Advances in biomaterials and regenerative medicine for diabetic foot ulcer therapy. Ageing Res. Rev. 109
300. Dong R, Guo B (2021) Smart wound dressings for wound healing. Nano Today 41:. https://doi.org/10.1016/j.nantod.2021.101290
301. Tawfeeq Al-Joubouri Z, A Malik Al-Saadi SA, Al-fahham A, et al (2024) The Active Ingredients and Therapeutic Effects of Cinnamon: A Review Article. International Journal of Health & Medical Research 03:2833–2148. https://doi.org/10.58806/ijhmr.2024.v3i08n01
302. Barin R, Machado AK, Silva IZ da, Ourique AF (2022) Healing potential of nanocarriers containing essential oils: a literature review. Disciplinarum Scientia - Ciências Naturais e Tecnológicas 23:129–143. https://doi.org/10.37779/nt.v23i3.4414
303. Nair A, Mallya R, Suvarna V, et al (2022) Nanoparticles-Attractive Carriers of Antimicrobial Essential Oils. Antibiotics 11
304. Basu P, Banerjee A, Okoro PD, et al (2024) Integration of Functional Polymers and Biosensors to Enhance Wound Healing. Adv. Healthc. Mater.
305. Zeng Q, Qi X, Shi G, et al (2022) Wound Dressing: From Nanomaterials to Diagnostic Dressings and Healing Evaluations. ACS Nano 16:1708–1733
306. Alsahag M, Alisaac A, Al-Hazmi GAA, et al (2023) Preparation of carboxymethyl cellulose/polyvinyl alcohol wound dressing composite immobilized with anthocyanin extract for colorimetric monitoring of wound healing and prevention of wound infection. Int J Biol Macromol 224:233–242. https://doi.org/10.1016/j.ijbiomac.2022.10.119
307. Liu Y, Li C, Feng Z, et al (2022) Advances in the Preparation of Nanofiber Dressings by Electrospinning for Promoting Diabetic Wound Healing. Biomolecules 12

308. Xu H, Zhang F, Wang M, et al (2022) Electrospun hierarchical structural films for effective wound healing. Biomaterials Advances 136:. https://doi.org/10.1016/j.bioadv.2022.212795
309. Rodríguez-Tobías H, Morales G, Grande D (2016) Electrospinning and Electrospraying Techniques for Designing Antimicrobial Polymeric Biocomposite Mats. In: Nanofiber Research - Reaching New Heights. InTech
310. Feng K, Huangfu L, Liu C, et al (2023) Electrospinning and Electrospraying: Emerging Techniques for Probiotic Stabilization and Application. Polymers (Basel). 15
311. (1999) ISO 9237; Determination of the Permeability of Fabrics to Air. ISO
312. Phillipson K, Hay JN, Jenkins MJ (2014) Thermal analysis FTIR spectroscopy of poly(ε-caprolactone). Thermochim Acta 595:74–82. https://doi.org/10.1016/j.tca.2014.08.027
313. Tavares TD, Pinho SLC, Delgado-Pujol EJ, et al (2025) Layer-by-layer electrospun PCL/PVA mats loaded with nisin Z for enhanced diabetic foot ulcer treatment. Int J Pharm 685:. https://doi.org/10.1016/j.ijpharm.2025.126208
314. Taskin MB, Ahmad T, Wistlich L, et al (2021) Bioactive Electrospun Fibers: Fabrication Strategies and a Critical Review of Surface-Sensitive Characterization and Quantification. Chem. Rev. 121:11194–11237
315. Ribeiro ARM, Barbosa AI, Celeiro M, et al (2026) Polycaprolactone/polyethylene glycol electrospun mats with pH-responsiveness for real-time sensing in chronic wound healing. React Funct Polym 222:. https://doi.org/10.1016/j.reactfunctpolym.2026.106692
316. Douglas P, Albadarin AB, Sajjia M, et al (2016) Effect of poly ethylene glycol on the mechanical and thermal properties of bioactive poly(ε-caprolactone) melt extrudates for pharmaceutical applications. Int J Pharm 500:179–186. https://doi.org/10.1016/j.ijpharm.2016.01.036
317. Can-Herrera LA, Oliva AI, Dzul-Cervantes MAA, et al (2021) Morphological and mechanical properties of electrospun polycaprolactone scaffolds: Effect of applied voltage. Polymers (Basel) 13:1–16. https://doi.org/10.3390/polym13040662
318. Saha S, Das S, Rahman MZ (2026) Hybridization in natural fiber composites: Enhanced performance and sustainability. Compos. B Eng. 308
319. Ali H, Ali S, Ali K, et al (2025) Impact of the nanoparticle incorporation in enhancing mechanical properties of polymers. Results in Engineering 27
320. Riaz S, Waheed H, Ahmad F, et al (2025) Natural and synthetic biomaterials, structural matrices-based wound dressings: Key properties, material correlation, and adaptability. Regenesis Repair Rehabilitation 1:47–65. https://doi.org/10.1016/j.rerere.2025.10.004
321. Ferraz MP (2025) Wound Dressing Materials: Bridging Material Science and Clinical Practice. Applied Sciences (Switzerland) 15
322. Li K, Qi Y, Zhou Y, et al (2021) Microstructure and properties of poly(ethylene glycol)-segmented polyurethane antifouling coatings after immersion in seawater. Polymers (Basel) 13:1–18. https://doi.org/10.3390/polym13040573
323. Miranda CS, Marinho E, Rocha D, et al (2025) Pioneering wound care solutions: triaxial wet-spun fibers with bioactive agents for chronic wounds - part I (production and characterization of the triaxial fibers). Mater Adv 6:3237–3252. https://doi.org/10.1039/d4ma01105h

324. Miranda CS, Silva AFG, Evenou C, et al (2025) Pioneering wound care solutions: triaxial wet-spun fibers with bioactive agents for chronic wounds, part II (controlled release and biological activity of the active agents). Mater Adv 6:2029–2047. https://doi.org/10.1039/d4ma01104j
325. Checchetto R (2025) Polyethylene Glycol (PEG) Additive in Polymer Membranes for Carbon Dioxide Separation: A Critical Review on Performances and Correlation with Membrane Structure. Separations 12
326. Han X, Ju LS, Irudayaraj J (2023) Oxygenated Wound Dressings for Hypoxia Mitigation and Enhanced Wound Healing. Mol. Pharm. 20:3338–3355
327. Castro-Dominguez B, Gröls JR, Alkandari S, et al (2025) Biopolymers and biocomposites: a comprehensive review of feedstocks, functionalities, and advanced manufacturing techniques for sustainable applications. Biotechnology for Sustainable Materials 2:. https://doi.org/10.1186/s44316-025-00029-y
328. Gulcin İ (2025) Antioxidants: a comprehensive review. Arch. Toxicol. 99:1893–1997
329. Ahmad Z, Rauf A, Orhan IE, et al (2025) Antioxidant Potential of Polyphenolic Compounds, Sources, Extraction, Purification and Characterization Techniques: A Focused Review. Food Sci. Nutr. 13
330. Park CH, Baskar TB, Park SY, et al (2016) Metabolic profiling and antioxidant assay of metabolites from three radish cultivars (Raphanus sativus). Molecules 21:. https://doi.org/10.3390/molecules21020157
331. Behar L, Siddique H (2026) Antioxidant Delivery Revisited: The Promise of Nanostructured Lipid Carriers. Medicines 13:2. https://doi.org/10.3390/medicines13010002
332. Rachel R, Anuradha M, Leela K V. (2024) Evaluating the Antifungal Potential of Cinnamaldehyde: A Study of its Efficacy against Candida Species. J Pure Appl Microbiol 18:2438–2445. https://doi.org/10.22207/JPAM.18.4.16
333. Gabbott CM, Sun T (2018) Comparison of human dermal fibroblasts and hacat cells cultured in medium with or without serum via a generic tissue engineering research platform. Int J Mol Sci 19:. https://doi.org/10.3390/ijms19020388
334. Riaz M, Iqbal MZ, Klar AS, Biedermann T (2025) Immunomodulatory Mechanisms of Chronic Wound Healing: Translational and Clinical Relevance. MedComm (Beijing). 6
335. Qiu Y, Zhu X, Yang X, Wan J (2025) Mechanisms of skin wound healing regulated by fibroblast-derived exosomes. Biochem Biophys Rep 44:. https://doi.org/10.1016/j.bbrep.2025.102371
336. Dey-Rao R, Melendy T (2026) HaCaT Keratinocytes: A Differentiation-Competent Platform for Episomal Replication of HPV Type 11. Viruses 18:. https://doi.org/10.3390/v18020230
337. Colombo I, Sangiovanni E, Maggio R, et al (2017) HaCaT Cells as a Reliable in Vitro Differentiation Model to Dissect the Inflammatory/Repair Response of Human Keratinocytes. Mediators Inflamm 2017:. https://doi.org/10.1155/2017/7435621
338. Correia C, Sousa RO, Vale AC, et al (2022) Adhesive and biodegradable membranes made of sustainable catechol-functionalized marine collagen and chitosan. Colloids Surf B Biointerfaces 213:. https://doi.org/10.1016/j.colsurfb.2022.112409

Supplementary Data

SUPPLEMENTARY DATA

In this section, supplementary results and information are presented to complement the contents discuss in Chapters III, IV, and V.

Table SD18 – Statistical comparison of the three parameters Young Modulus (N/mm), Elongation at Break (%) and Break Strength (MPa) between the selected control (100PCL loaded and non-loaded) (*p < 0.05; **p < 0.01; ***p < 0.001; ****p < 0.0001; ns: non-significant).

	Young Modulus (N/mm)		**Elongation at Break (%)**		**Break strength (MPa)**	
	PCL/PEG 90:10	PCL/PEG 80:20	PCL/PEG 90:10	PCL/PEG 80:20	PCL/PEG 90:10	PCL/PEG 80:20
100 PCL	ns	ns	ns	****	ns	ns
	PCL/PEG 90:10 + RC	PCL/PEG 80:20 + RC	PCL/PEG 90:10 + RC	PCL/PEG 80:20 + RC	PCL/PEG 90:10 + RC	PCL/PEG 80:20 + RC
100 PCL + RC	ns	ns	ns	ns	*	*
	PCL/PEG 90:10 + RR	PCL/PEG 80:20 + RR	PCL/PEG 90:10 + RR	PCL/PEG 80:20 + RR	PCL/PEG 90:10 + RR	PCL/PEG 80:20 + RR
100 PCL + RR	ns	ns	ns	ns	ns	ns

Table SD19 – Statistical comparison of the three parameters Young Modulus (N/mm), Elongation at Break (%) and Break Strength (MPa) between the selected control (non-loaded mats) against loaded mats (*p < 0.05; **p < 0.01; ***p < 0.001; ****p < 0.0001; ns: non-significant).

	Young Modulus (N/mm)		**Elongation at Break (%)**		**Break strength (MPa)**	
	100 PCL + RC	100 PCL + RR	100 PCL + RC	100 PCL + RR	100 PCL + RC	100 PCL + RR
100 PCL	ns	ns	****	****	**	ns
	PCL/PEG 90:10 + RC	PCL/PEG 90:10 + RR	PCL/PEG 90:10 + RC	PCL/PEG 90:10 + RR	PCL/PEG 90:10 + RC	PCL/PEG 90:10 + RR

PCL/PEG 90:10	ns	ns	****	****	ns	ns

	PCL/PEG 80:20 + RC	PCL/PEG 80:20 + RR	PCL/PEG 80:20 + RC	PCL/PEG 80:20 + RR	PCL/PEG 80:20 + RC	PCL/PEG 80:20 + RR
PCL/PEG 80:20	ns	ns	ns	ns	ns	ns

Table SD20 – Main DSC thermal events (T_0 onset temperature, T_{peak} peak temperature and ΔH enthalpy).

	Thermal Event I			**Thermal Event II**		
	T_0 (°C)	T_{peak} (°C)	ΔH (mJ)	T_0 (°C)	T_{peak} (°C)	ΔH (mJ)
100 PCL	51,00	57,44	-346,38	381,37	414,38	-3619,57
PCL/PEG 90:10	51,01	59,45	-363,40	386,41	417,59	-2317,88
PCL/PEG 80:20	60,20	62,14	-331,96	380,28	416,69	-2127,97
100 PCL + RC	54,27	61,38	-142,94	380,62	415,23	-1080,47
PCL/PEG 90:10 + RC	55,06	60,81	-195,86	382,41	417,62	-1523,27
PCL/PEG 80:20 + RC	54,77	59,91	-117,15	384,39	416,35	-657,77
100 PCL + RR	53,65	60,73	-92,79	370,80	414,14	-663,91
PCL/PEG 90:10 + RR	53,98	61,18	-223,24	384,88	416,31	-1450,50
PCL/PEG 80:20 + RR	53,57	60,56	-157,56	378,47	414,46	-920,84

Table SD21 - Detected compounds. Ionization mode, CAS number, retention time and MS/MS transitions.

Ionization mode	**Compound**	**CAS**	**Retention time (min)**	**MS/MS transitions (Collision energy, eV)[a]**
+	3,4-dihydroxybenzoic acid	99-50-3	3.70	152.98 → 109.04 (17) 152.98 → 91.04 (28) 152.98 → 108.03 (26)

+	Chlorogenic acid	327-97-9	5.77	353.00 → 191.07 (22) 353.00 → 85.09 (43) 353.00 → 93.07 (45)
-	Caffeic Acid	331-39-5	5.92	178.98 → 135.03 (19) 178.98 → 134.01 (28)
+	p-coumaric acid	501-98-4	7.12	163.02 → 119.07 (18) 163.02→ 93.07 (37) 163.02 → 117.05 (38)
-	Sinapic acid	530-59-6	7.64	223.00 → 163.90 (23) 223.00 → 192.90 (22)
+	Delphynidin[b]	528-53-0	7.81	303.02 → 229.07 (32) 303.02 → 115.08 (50) 303.02 → 173.07 (33)
-	Trans-ferulic aicd	537-98-4	8.33	192.80 → 177.90 (12) 192.80 → 133.90 (16)
+	Cyanidin[b]	528-58-5	8.87	287.02 → 128.10 (46) 287.02 → 109.06 (39) 287.02 → 115.08 (45)
+	Pelargonidin[b]	7690-51-9	9.20	272.05 → 271.05(15)
-	Kaempferol-O-glucoside	520-18-3	12.27	285.07 → 184.91 (30) 285.07 → 239.12 (35)

[a] eV: Electron-Volt. Underlined MS/MS transition used for quantification purpose.

[b] Anthocyanidins detection after acid hydrolysis.

Table SD22 - Main DSC thermal events (T_0 onset temperature, T_{peak} peak temperature and ΔH enthalpy).

	Thermal Event I			Thermal Event II		
	T_0 (°C)	T_{peak} (°C)	ΔH (mJ)	T_0 (°C)	T_{peak} (°C)	ΔH (mJ)
100 PCL	51.00	57.44	-346.38	381.37	414.38	-3619.57
Ch-NLCs	49.33	110.54	-176.60	-	-	-
Ch-NLCs/CN	51.09	118.23	-136.63	-	-	-
PCL + Ch-NLCs	53.04	59.42	-384.46	385.61	418.98	-2125.59
PCL + Ch-NLCs + PCL	53.35	60.08	-672.77	385.19	419.79	-4350.46
PCL + Ch-NLCs/CN	48.72	60.61	-396.86	382.83	416.00	-2179.03
PCL + Ch-NLCs/CN + PCL	54.10	61.56	-385.51	393.48	426.42	-688.20

Table SD23 - Main DSC thermal events (T_0 onset temperature, T_{peak} peak temperature and ΔH enthalpy).

	Thermal Event I			Thermal Event II		
	T_0 (°C)	T_{peak} (°C)	ΔH (mJ)	T_0 (°C)	T_{peak} (°C)	ΔH (mJ)
PCL	51.00	57.44	-346.38	381.37	414.38	-3619.57
PEG	48.15	68.98	-1183.53	350.31	421.11	-1040.09
PCL/PEG (90:10)	49.33	52.14	-623.36	303.44	418.99	-5712.19
PCL/PEG (90:10) + PCL	47.09	54.13	-404.07	296.87	421.09	-2550.13
PCL/PEG (90:10) + Ch-NLCs/CN + PCL	53.04	54.22	-685.94	250.61	409.18	-6552.83
PCL/PEG (90:10) – RR + PCL	49.35	50.03	-462.73	300.19	419.55	-3105.22
PCL/PEG (90:10) – RR + Ch-NLCs/CN + PCL	48.72	53.61	-386.46	302.83	416.00	-3149.03

Scientific Outputs

Curriculum Vitae

PUBLICATIONS AND COMMUNICATIONS

Papers in peer-reviewed journals

1. Ribeiro A. R. M., Ana Isabel Barbosa, Catarina L. Seabra, Salette Reis, Helena P. Felgueiras, "Integration of Cinnamaldehyde Essential Oil onto Chitosan-coated Nanostructured Lipid Carriers on ε-Polycaprolactone Electrospun Mats: A Novel Approach for Antifungal Chronic Wound Healing". Colloids and Surfaces B: Biointerfaces (In Revision).
2. Ana R. M. Ribeiro, Ana Isabel Barbosa, Maria Celeiro, Marta Lores, Catarina L. Seabra, Salette Reis, Helena P. Felgueiras, "Polycaprolactone/polyethylene glycol electrospun mats with pH-responsiveness for real-time sensing in chronic wound healing". Reactive and Functional Polymers, 222, 2026, https://doi.org/10.1016/j.reactfunctpolym.2026.106692.
3. Ribeiro, Ana R.M.; Oliveira, Bruna A.S.; Barbosa, Ana Isabel; Seabra, Catarina L.; Reis, Salette; Felgueiras, Helena P., "Nanomaterial-based scaffolds endowed with halochromic properties for skin healing purposes". Journal of Drug Delivery Science and Technology 108 (2025): 106950. https://doi.org/10.1016/j.jddst.2025.106950
4. Ribeiro, Ana R.M.; Teixeira, Marta O.; Ribeiro, Lara; Tavares, Tânia D.; Miranda, Catarina S.; Costa, André F.; Ribeiro, Artur; et al. "Sodium alginate-based multifunctional sandwich-like system for treating wound infections". Biomaterials Advances 162 (2024): 213931. http://dx.doi.org/10.1016/j.bioadv.2024.213931.
5. Ribeiro, Ana R. M.; Miranda, Catarina S.; Silva, Ana Francisca G.; Mendes, Filipa D. P.; Silva, Beatriz M.; Oliveira, Bruna A. S.; Paiva, Eduardo D.; et al. "Inhibition of Enzyme and Bacteria Activities in Diabetic Ulcer-like Scenarios via WAAPV-Loaded Electrospun Fibers". Pharmaceutics 16 7 (2024): 911. http://dx.doi.org/10.3390/pharmaceutics16070911.
6. Tavares, Tânia D.; Ribeiro, Ana R.M.; Silva, Carla; Antunes, Joana C.; Felgueiras, Helena P.. "Combinatory effect of nisin antimicrobial peptide with bioactive molecules: A review". Journal of Drug Delivery Science and Technology 91 (2023): 105246. http://dx.doi.org/10.1016/j.jddst.2023.105246.
7. Ribeiro, Ana R. M.; Teixeira, Marta A.; Pereira-Lima, Sílvia M. M. A.; Costa, Susana P. G.; Felgueiras, Helena P.. " Tiger 17 peptide loaded polycaprolactone/cellulose acetate electrospun nanofibrous mats for applications in cutaneous wound dressings. ". Tekstil ve Mühendis 29 128 (2022): 308-314. http://dx.doi.org/10.7216/teksmuh.1222547.

8. Felgueiras, Helena P.; Homem, Natália C.; Teixeira, Marta A.; Ribeiro, Ana R. M.; Antunes, Joana C.; Amorim, Maria Teresa P.. "Physical, Thermal, and Antibacterial Effects of Active Essential Oils with Potential for Biomedical Applications Loaded onto Cellulose Acetate/Polycaprolactone Wet-Spun Microfibers". Biomolecules 10 8 (2020): 1129. http://dx.doi.org/10.3390/biom10081129.
9. Miranda, Catarina S.; Ribeiro, Ana R. M.; Homem, Natália C.; Felgueiras, Helena P.. "Spun Biotextiles in Tissue Engineering and Biomolecules Delivery Systems". Antibiotics 9 4 (2020): 174. http://dx.doi.org/10.3390/antibiotics9040174.

Book Chapter

1. Ribeiro, Ana R. M.; Teixeira, Marta O.; Marinho, Elina; Silva, A. Francisca G.; Costa, Susana P. G.; Felgueiras, Helena P.,"Polymer-Based Nanomaterials Against Multidrug-Resistant Bacteria". In Nanotechnology Based Strategies for Combating Antimicrobial Resistance, 251-289. Springer Nature Singapore, 2024.
2. Ribeiro A. R. M., Tavares T. D., Domingues J. M., Silva C., Antunes J. C., Seabra C. L. and Felgueiras H. P. "Electrospun nanofibrous composites for drug delivery applications". Handbook of Composite Materials for Advanced Biomedical Applications, Springer Nature (In Proof)

Conference Papers

1. Ribeiro, Ana R. M.; Felgueiras, Helena P.; Costa, Susana P. G.; Pereira-Lima, Sílvia M. M. A. "Synthesis of Peptaibolin, an anti microbial peptide". Paper presented in The 1st International Electronic Conference on Pharmaceutics, 2020.
2. Felgueiras, Helena P.; Homem, Natália C.; Ribeiro, Ana R. M.; Teixeira, Marta O.; Teixeira, Marta A.; Antunes, Joana C.; Amorim, M. Teresa P.. "Activity of wet-spun fibers chemically modified with active biomolecules against Gram-positive and Gram-negative bacteria". Paper presented in 2nd International Online-Conference on Nanomaterials, 2020.
3. Felgueiras, H P; Homem, N C; Teixeira, M A; Ribeiro, A R M; Teixeira, M O; Antunes, J C; Amorim, M T P. "Biodegradable wet-spun fibers modified with antimicrobial agents for potential applications in biomedical engineering". Paper presented in 2nd International Conference on Graphene and Novel Nanomaterials (GNN) 2020, 2020.

Oral Presentations

1. Ribeiro, Ana R. M.; Teixeira, Marta A.; Pereira-Lima, Sílvia M. M. A.; Costa, Susana P. G.; Felgueiras, Helena P., "Tiger 17 peptide loaded polycaprolactone/cellulose acetate electrospun

nanofibrous mats for applications in cutaneous wound dressings. ". Presented in the ICONTEX 2022 - 3rd International Congress of Innovative Textiles, Turkey.

Poster Presentations

1. Ana R. M. Ribeiro; Barbosa, Ana Isabel; Catarina L. Seabra; Reis, Salette; Felgueiras, Helena P., "Chitosan Nanoparticle-Loaded Essential Oils Electrosprayed onto Polycaprolactone Microfibers: A Novel Antifungal Therapy for Diabetic Foot Ulcers". Paper presented in The 1st International Online Conference on Functional Biomaterials, 2024.
2. Bruna Oliveira; Marta O. Teixeira; Ana R. M. Ribeiro; Carla Silva; Felgueiras, Helena P.. "Mechanical and biological assessments of braided artificial tendons functionalized with cork extract.". Paper presented in The 1st International Online Conference on Functional Biomaterials, 2024.
3. Ana R. M. Ribeiro; Felgueiras, Helena P.; Reis, Salette; Seabra, Catarina Leal. "Modification of polyvinyl alcohol-based electrospun mats with naturally-derived halochromic molecules for potential applications in wound healing monitoring". Paper presented in 9th International Electronic Conference on Medicinal Chemistry, 2023.
4. Ribeiro, Lara C.; Ribeiro, Ana R. M.; Teixeira, Marta O.; Silva, Carla; Felgueiras, Helena P.. "Fiber-Hydrogel Composites For Chronic Wound Management". Paper presented in The 3rd International Electronic Conference on Antibiotics (ECA 2023), 2023.
5. Ribeiro, Lara C.; Teixeira, Marta O.; Ribeiro, Ana R. M.; Silva, Carla; Felgueiras, Helena P.. "Fiber-Hydrogel Sandwich-Like Composites with Improved Antimicrobial Protection". Paper presented in The 2nd International Electronic Conference on Microbiology, 2023.
6. Helena P. Felgueiras; Natália C. Homem; Ana R. M. Ribeiro; Marta A. Teixeira; Antunes, Joana C.; M. Teresa P. Amorim. "Bactericidal wet-spun cellulose acetate/polycaprolactone fibers: impact of cinnamon, clove and cajeput essential oils loaded onto the surface". Paper presented in The 1st International Electronic Conference on Antibiotics-The Equal Power of Antibiotics And Antimicrobial Resistance, 2021.
7. Helena P. Felgueiras; Homem, Natália C.; Marta A. Teixeira; Marta O. Teixeira; Ana R. M. Ribeiro; Joana C. Antunes. "Biodegradable wet-spun fibers as delivery platforms for the bactericidal effect of the natural-origin biomolecules, cinnamon, clove and cajeput essential oils". Paper presented in 1st International Electronic Conference on Biomolecules: Natural and Bio-Inspired Therapeutics for Human Diseases, 2020.

8. Teixeira, Marta A.; Tavares, Tânia D.; Ribeiro, Ana R. M.; Amorim, M. Teresa P.; Felgueiras, Helena P.. "Development of biodegradable electrospun dressing based on PVA/CA with antimicrobial potential for chronic wounds". Paper presented in 2nd Coatings and Interfaces Web Conference, 2020.

Awards

1. "Luís Marques award" – Portuguese Society of Diabetes (2023)

Participations

1. IMFAHE Program, 2022-2023 - a non-profit, global mentoring program that connects European students in the disciplines of Biomedicine, Engineering, and Entrepreneurship. This international program organizes mentorships, webinars, workshops with the intent to enhance career development.
2. 4th Textile Engineering Conference - University of Minho.
3. Formation of the Electoral College – Technology to Market: How to Create Value from Knowledge, University of Minho, Portugal.
4. UT Austin Portugal Annual Conference 2023 - Modeling the Future
5. Webinar – Nanotechnology: A Revolutionary Approach to Materials Science. Fibrenamics.
6. UT Austin Annual Conference 2022 - International S&T Partnerships: Platforms of Science Diplomacy
7. Sunset Skin Summit Conference – Sustainability in Skin Treatment and Care. University of Lisbon, Faculty of Pharmacy, Portugal
8. Medical Textiles Workshop – 2C2T Medical Textiles Cluster
9. Webinar - " Personalized Medicine: an enabling tool to break down boundaries in chronic skin wound management". Politecnico di Torino, Italy
10. Webinar MRS on Demand - " Career Discovery Series: Focus on Biomaterials". Materials Research Society, United States

Mentoring

1. Bachelor student from Biomedical Engineering course. "Development of Artificial Tendons". Bruna S. Oliveira, September 2023- June 2024.
2. Bachelor student from Biological Engineering course "Production of a Multifunctional Sandwich System to Combat Infections in Chronic Wounds". Lara Ribeiro, January 2023 – October 2023.